Thèse de Doctorat

ZHANG JIAN

Mémoire présenté en vue de l'obtention du
grade de Docteur de l'Université de Nantes
sous le label de l'Université de Nantes Angers Le Mans

École doctorale : ED503 STIM

Discipline : Génie Electrique
Unité de recherche : Institut de Recherche en Énergie Électrique de Nantes Atlantique (IREENA)

Soutenue le 27 Novembre 2015

Optimization design and control strategies of a double stator permanent magnet generator for tidal current energy application

JURY

Président :   **M. Mohamed BENBOUZID**, Professeur des Universités, Université de Bretagne Occidentale
Rapporteurs :   **M. Georges BARAKAT**, Professeur des Universités, Université du Havre
                     M. Michel HECQUET, Professeur des Universités, Ecole Centrale de Lille
Examinateur :   **M. Gang YAO**, Assistant Professor, Shanghai Maritime University, Chine
Invité :   **M. Pascal LE QUÉAU**, Electrical Systems Engineering Manager, Alstom Ocean Energy
Directeur de thèse : **M. Mohamed MACHMOUM**, Professeur des Universités, Ecole Polytechnique de l'Université de Nantes
Encadrant :   **M. Luc MOREAU**, Maître de Conférences, Ecole Polytechnique de l'Université de Nantes

Acknowledgement

4

easier.

Last, but definitely not least, I would like to thank my lovely wife, *Lin DENG*, who resigned her comfortable job in China and came to France to live with me during this thesis. Without her love, continual support and patience this project would not have been possible finished. Furthermore, thanks to her, we have welcomed our first son *Houqian ZHANG (Clément)* in this year and it's him who gives me illimitable motivation to finish this thesis. I also would like to thank my parents *Lianwen ZHANG* and *Yumei DOU* for showing and teaching me man should work harder to make a better life for his family. Thanks are also given to my dear parents in-law, *Zhimin DENG* and *Feng'e YUAN*, for their endeavors help and support especially for the three months in France after *Clément* was born.

Résumé en Français

Ce mémoire de thèse rédigé en langue anglaise est précédé d'un résumé en langue française conformément aux conditions de l'école doctorale Sciences et Technologies de l'Information et Mathématiques (STIM) de l'UNAM.

Dimensionnement optimisé et stratégies de commande d'une génératrice synchrone à double stator pour application hydrolienne

Sommaire

Introduction

1. Etat de l'art de l'énergie hydrolienne
2. Dimensionnement préliminaire et principe de commande d'une génératrice synchrone à double stator
3. Optimisation conjointe de l'ensemble machine synchrone double stator – convertisseur
4. Commande de la génératrice (simple ou à double stator) en mode sain ou en mode défaut
5. Perspectives

Introduction

Les travaux présentés dans cette thèse portent sur l'étude, le dimensionnement, l'optimisation et la commande d'un système machine synchrone à aimants permanents à double stator convertisseurs pour application hydrolienne. Cette thèse s'insère dans le cadre d'un projet de recherche à échelle régionale nommé «Hydrol 44». Ce projet pluridisciplinaire qui regroupe plusieurs acteurs académiques (LHEEA, LBMS, IRENAV, LASQUO et IREENA) et industriels du grand Ouest (Alstom Hydro, Jeumont et EcaEN) est soutenu et financé par la région Pays de la Loire et le C.O.P (Contrat d'Objectifs Partagés : Carene et CCI) et vise à lever des verrous scientifiques et technologiques relatifs à la technologie hydrolienne. Le projet «Hydrol 44» s'intéresse en particulier à la problématique de maintenance des fermes hydroliennes et à la conception de génératrices robustes adaptés à ce contexte et leur intégration sur le réseau. Les travaux de thèse que nous présentons font partie du deuxième work package (WP2).

L'énergie des courants de marée, ou énergie hydrolienne, est considérée comme une source d'énergie renouvelable très prometteuse car elle présente de nombreux avantages tels que la prédictibilité, la haute densité de puissance et un impact visuel négligeable. La machine synchrone à double stator à aimants permanents posés en surface (DSCRPMG) est étudiée car elle présente plusieurs avantages sur la machine simple stator traditionnelle; elle peut fournir une plus grande densité volumique de couple (augmentation de la surface d'entrefer) et présente une meilleure tolérance aux défauts (indépendance magnétique des deux stators).

La DSCRPMG est composée de deux bobinages triphasés. Ces derniers peuvent être connectés en parallèle ou en série. La DSCRPMG est équivalente à deux machines indépendantes magnétiquement. Dans le but d'obtenir une un bon comportement en cas de défauts, nous ne considérons dans le présent document que le système avec les deux stators connectés en parallèle. Chaque stator est connecté à un redresseur à MLI. Les 2 redresseurs sont connectés à un onduleur par un bus continu commun comme présenté sur la Fig. 1.
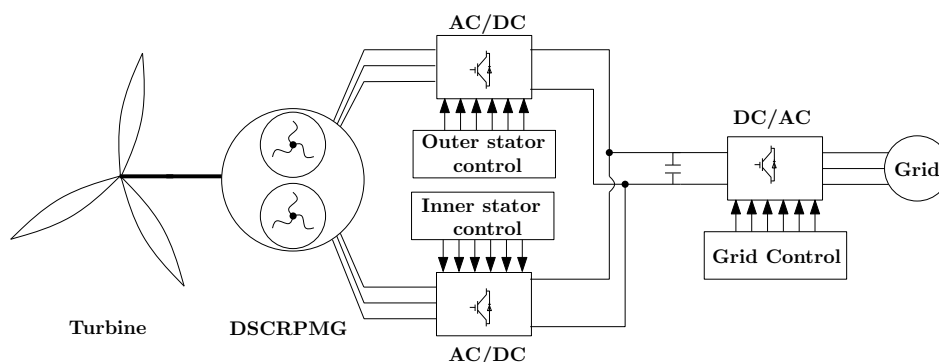

Figure 1 – Structure d'une chaine hydrolienne à base de génératrice synchrone à double stator

Nous étudions un système d'entraînement direct avec une turbine à pas fixe. En effet,

d'une part une turbine à pas fixe est plus robuste qu'une turbine à pas variable et fournit moins d'oscillations de puissance et d'autre part le système d'entraînement direct élimine la boîte de vitesses qui peut entraîner des coûts de maintenance élevés.

Le manuscrit est scindé en quatre chapitres. Le 1$^{\text{er}}$ présente un état de l'art des technologies des hydroliennes et les structures électrotechniques associées. Le 2$^{\text{ème}}$ chapitre présente la comparaison de différentes stratégies de commande en mode de fonctionnement MPPT ou en en mode défluxé pour une génératrice synchrone à double stator pré-dimensionnée. La meilleure stratégie en termes de rendement est retenue pour la suite des travaux. Le 3$^{\text{ème}}$ chapitre montre les résultats de l'optimisation multi-objectif de l'investissement et de l'énergie extraite. Pour ce faire, l'algorithme proposé optimise l'ensemble convertisseur-machine. Une machine est choisie sur le front de Paréto pour le chapitre suivant. Enfin, le chapitre 4 traite de la commande et l'analyse des performances de la chaîne de conversion en mode normal ou en cas de défaut. Trois stratégies de commande sont présentées et évaluées selon des critères tels que la continuité de service, la minimisation des ondulations de couple ou la simplicité d'implémentation.

1. Etat de l'art de l'énergie hydrolienne

Au premier chapitre, nous abordons brièvement les principes, les approches technologiques et les principaux types de machines électriques utilisés dans un système hydrolien.

Les caractéristiques de la ressource sont calculées à partir d'informations océanographiques. Deux modélisations des courants marins sont présentées. Il s'agit des méthodes dites Harmonics Analysis Method (HAM), et SHOM laquelle utilise une équation semi-expérimentale simple. Ensuite, on montre le lien entre la puissance extraite et les caractéristiques de la turbine, la vitesse de rotation de la turbine et la vitesse du fluide. Un tableau récapitule les différents prototypes en cours d'essais en précisant le type de technologie; axe vertical ou horizontal ou bien système oscillant.

Enfin, les différents choix d'ensemble convertisseur machine sont présentés. La DSCRPMG, à attaque directe et connectée au réseau via un convertisseur de puissance back to back, est proposée comme une alternative aux solutions de la littérature car, comme indiqué plus haut, elle peut fournir une plus grande densité volumique de couple et présente a priori une meilleure tolérance aux défauts que les machines à simple stator.

2. Dimensionnement préliminaire et principe de commande d'une génératrice synchrone à double stator

Le deuxième chapitre a un objectif double. Il s'agit dans un premier temps d'expliciter le modèle analytique de la machine synchrone à double stator puis, dans un second temps de comparer différentes stratégies de commande usuelles et proposer une nouvelle réalisant le
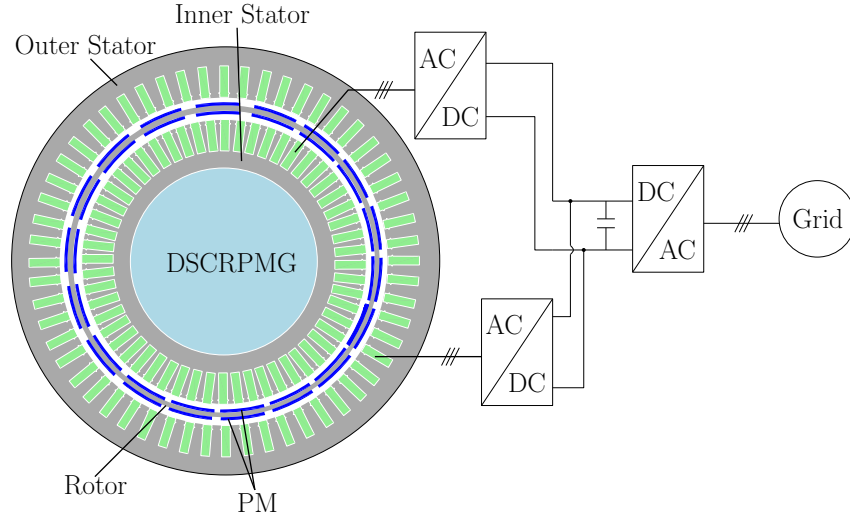
Figure 2 – Connexion des 2 stators au même bus DC

meilleur compromis en termes de rendement en mode de fonctionnement MPPT ou en mode de fonctionnement en défluxé.

La machine est composée de deux stators, l'un externe et l'autre interne, et d'un rotor avec des aimants posés sur ses surfaces externes et internes. Une structure mécanique en forme de coupe (rotor cup) assure la cohésion mécanique de l'ensemble. La géométrie de la machine est définie par les paramètres géométriques présentés sur la Fig. 3. Nous présentons une modélisation analytique qui permet de déterminer des grandeurs externes telles que les inductances et fem, les coûts matière et de structure, les pertes dans la machine (Joule et fer) et les pertes convertisseur (par conduction et par commutation).
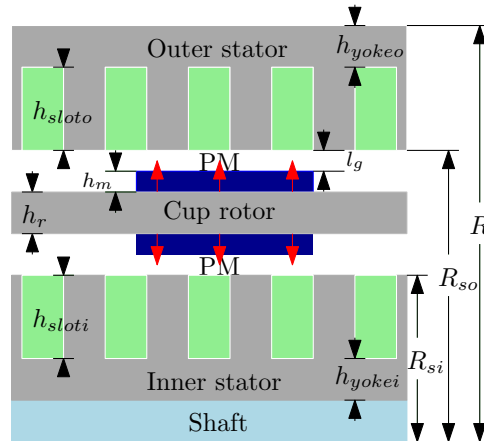
Figure 3 – Paramètres géométriques de la machine synchrone double stator étudiée

L'ensemble des paramètres géométriques est déterminé avec des règles de prédimensionnement communément admises, et ce pour un cahier des charge défini au point de fonctionnement nominal ($1MW$, $21.5tr/min$).

Un modèle de Park pour les machines externe (indice o) et interne (indice i) est élaboré en vue de la commande. Ce modèle utilise les grandeurs calculées par modèle analytique

développé auparavant. Les équations des tensions et du couple sont données ci-dessous:

$$\begin{cases} \begin{bmatrix} v_{do} \\ v_{qo} \end{bmatrix} = R_{cuo} \begin{bmatrix} i_{do} \\ i_{qo} \end{bmatrix} + \begin{bmatrix} L_{do}\frac{d}{dt} & -L_{qo}\omega_e \\ L_{do}\omega_e & L_{qo}\frac{d}{dt} \end{bmatrix} \begin{bmatrix} i_{do} \\ i_{qo} \end{bmatrix} + \omega_e\psi_{PMo} \begin{bmatrix} 0 \\ 1 \end{bmatrix} \\[3ex] \begin{bmatrix} v_{di} \\ v_{qi} \end{bmatrix} = R_{cui} \begin{bmatrix} i_{di} \\ i_{qi} \end{bmatrix} + \begin{bmatrix} L_{di}\frac{d}{dt} & -L_{qi}\omega_e \\ L_{di}\omega_e & L_{qi}\frac{d}{dt} \end{bmatrix} \begin{bmatrix} i_{di} \\ i_{qi} \end{bmatrix} + \omega_e\psi_{PMi} \begin{bmatrix} 0 \\ 1 \end{bmatrix} \end{cases}$$

$$\begin{cases} T_{eo} = \frac{3}{2}pi_{qo}\left[i_{do}(L_{do} - L_{qo}) + \psi_{PMo}\right] \\[1.5ex] T_{ei} = \frac{3}{2}pi_{qi}\left[i_{di}(L_{di} - L_{qi}) + \psi_{PMi}\right] \\[1.5ex] T_e = T_{eo} + T_{ei} \end{cases}$$

La caractéristique de fonctionnement (puissance-vitesse de rotation) d'une hydrolienne est présentée en Fig. 4. Elle comprend deux zones principales: la région MPPT (Maximum Power Point Tracking) pour laquelle l'énergie extraite est maximisée jusqu'à la puissance et la vitesse de rotation nominales, puis la région dite d'écrêtage de puissance en raison des limites des organes (générateur et électronique de puissance).
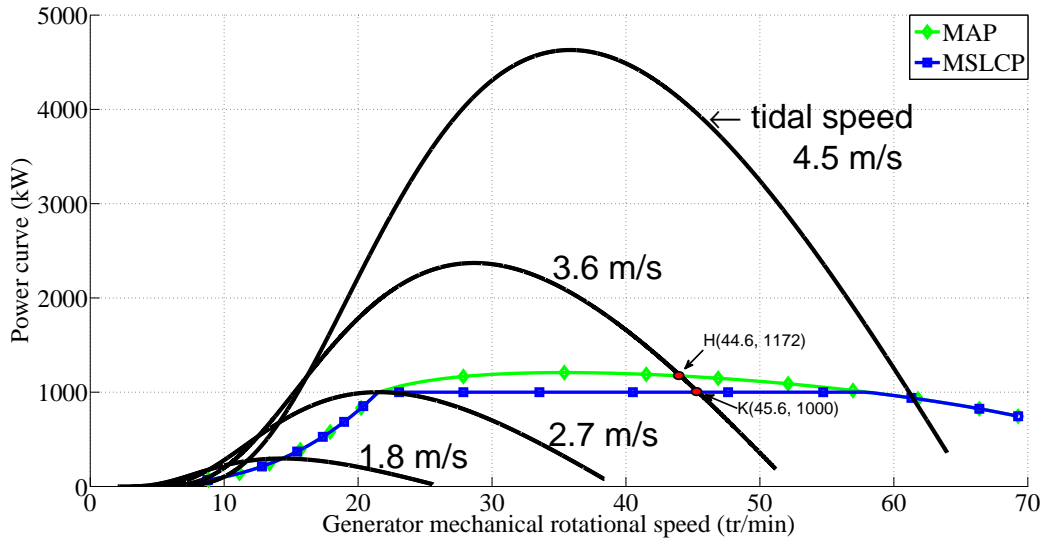
Figure 4 – Courbes de puissance en mode MAP ou MSLCP

Dans la zone MPPT, pour chaque point de fonctionnement, le courant i_q, à l'image du couple, est le même quelque que soit la stratégie de commande adoptée. En sus, la commande par un convertisseur MLI autorise le réglage de i_d, et laisse ainsi un degré de liberté. C'est ce degré de liberté qui permet d'implémenter des stratégies de commande différentes. Trois stratégies de commande sont étudiées: commande à facteur de puissance unitaire, commande à flux constant (tension de sortie égale à la fem) et la commande à couple max ($i_d = 0$). Chacune permet de balancer différemment la répartition des pertes Joule et pertes fer de la machine. Nous

montrons aussi la stratégie MSL, i.e. Minimum System Losses Control, qui calcule le courant i_d de façon à minimiser à la fois les pertes de la machine mais aussi celles du convertisseur. La prise en compte des pertes convertisseur est une originalité de notre travail. Nous montrons que cette stratégie conduit à un meilleur rendement.

Ensuite, la zone de défluxage est examinée. Il s'agit de respecter des contraintes de tenue en tension et thermiques (machine et convertisseur). On distingue deux façons de procéder: travailler à la puissance maximale admissible, le système est alors en limite de tension et thermique ou bien maintenir la puissance constante à la valeur nominale, il y a alors une liberté sur le courant i_d. Dans le premier cas une seule stratégie est disponible consistant à maintenir la tension et le courant à leurs valeurs maximales alors que la seconde autorise l'optimisation du rendement via le réglage de i_d. La figure ci-dessous illustre la plage de variation du courant i_d. Celui-ci appartient au segment AB. Comme pour la région MPPT, deux méthodes de la littérature (point A et B) sont comparées à notre algorithme qui maximise le rendement de l'ensemble convertisseur machine (point C).
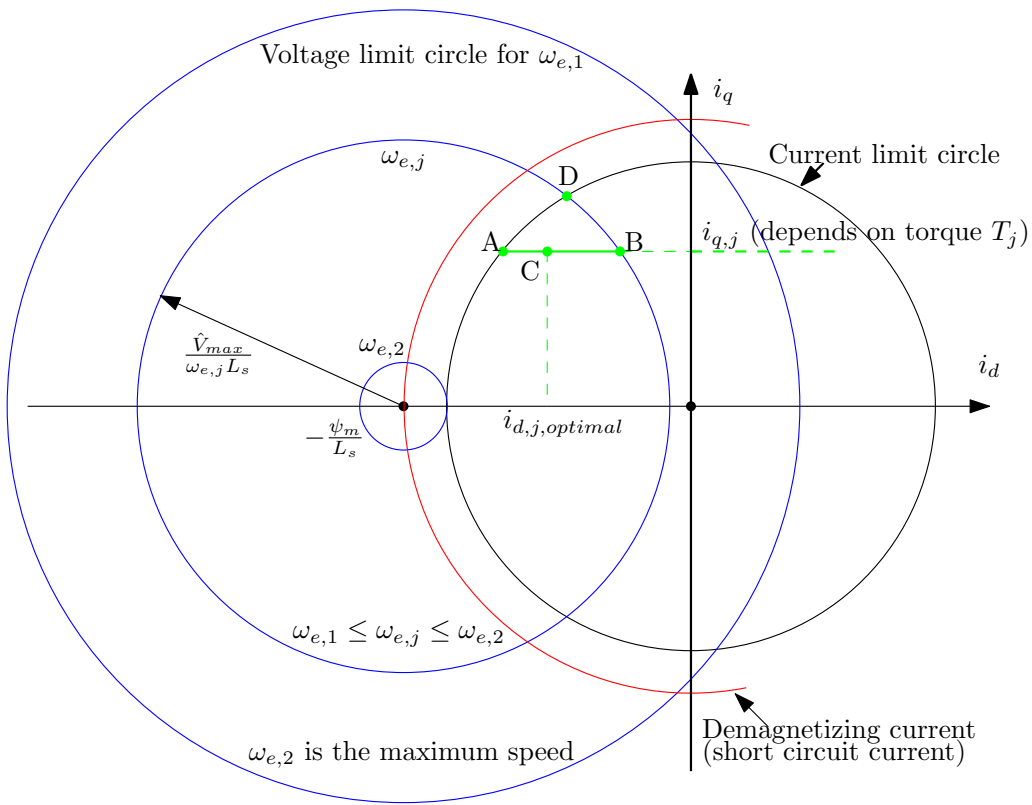

Figure 5 – Illustration de la stratégie MSL

La stratégie de commande proposée en mode MPPT (MSL) et en défluxage (MSLCP) maximise le rendement de l'ensemble convertisseur machine et sera utilisée pour la suite des travaux.

3. Optimisation conjointe de l'ensemble machine synchrone double stator–convertisseur

On s'intéresse à l'optimisation de l'ensemble convertisseur machine en vue de minimiser l'investissement et maximiser l'énergie extraite sur une durée d'exploitation de vingt ans. L'inve -stissement est calculé à partir des coûts suivants: matières actives de la machine, la structure mécanique, et le convertisseur. L'énergie extraite est évaluée en intégrant les caractéristiques vitesse du courant marin vs puissance, vitesse du courant vs vitesse de rotation de la génératrice ainsi que les probabilités d'apparition de vitesse du courant, telles que représentées ci-dessous:
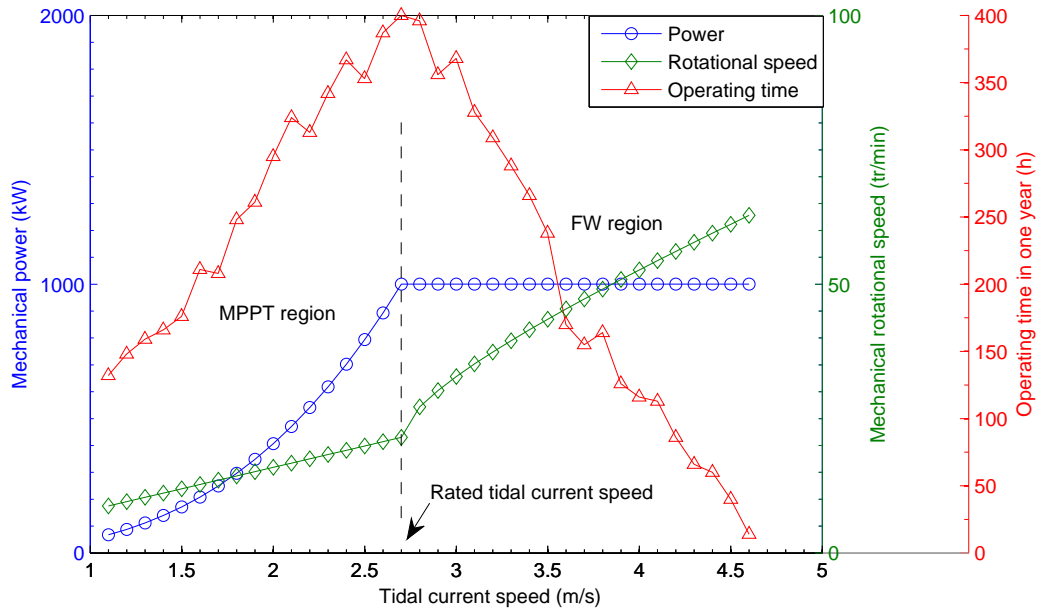
Figure 6 – Points de fonctionnement de la turbine

Afin de dégager des fronts de Pareto, un algorithme multicritère de type essaimage particulaire est mis en œuvre pour d'optimiser 16 paramètres. Le modèle de la machine et du convertisseur sont ceux développés au chapitre 2 tandis que la stratégie de commande est celle proposée au chapitre précèdent (MSL).

Le front de Pareto est un guide pour le choix d'une structure, car il donne les compromis disponibles entre l'investissement et le revenu. Néanmoins, ce choix n'est pas aisé. Dès lors, nous définissons deux critères secondaires qui permettent chacun de dégager une machine particulière sur le front de Pareto. La première fonction $F_{obj,final1}$ est calculée par la différence entre le revenu obtenu en 20 ans et les coûts en incluant celui de la turbine estimé à $1M€$. La seconde, $F_{obj,final2}$ se détermine par le quotient des coûts par l'énergie extraite en 1 an.

Le front de Pareto obtenu est présenté Fig. 7.

Ce front montre les machines A et B prédimensionnées au 2ème chapitre, lesquelles sont logiquement dominées par le front de Pareto optimisé. On voit aussi apparaitre les machines déterminées par $F_{obj,final1}$ et $F_{obj,final2}$. On pourrait croire que la meilleure machine est la plus

Figure 7 – Pareto front

compacte, avec un grand nombre de pôles et en limite thermique (machine le plus à gauche du front). Or il n'en est rien. En effet, en passant à la machine choisie par $F_{obj,final2}$ on augmente très légèrement l'investissement, mais on accroit de façon significative l'énergie extraite sur une durée de 20 années et donc les revenus.

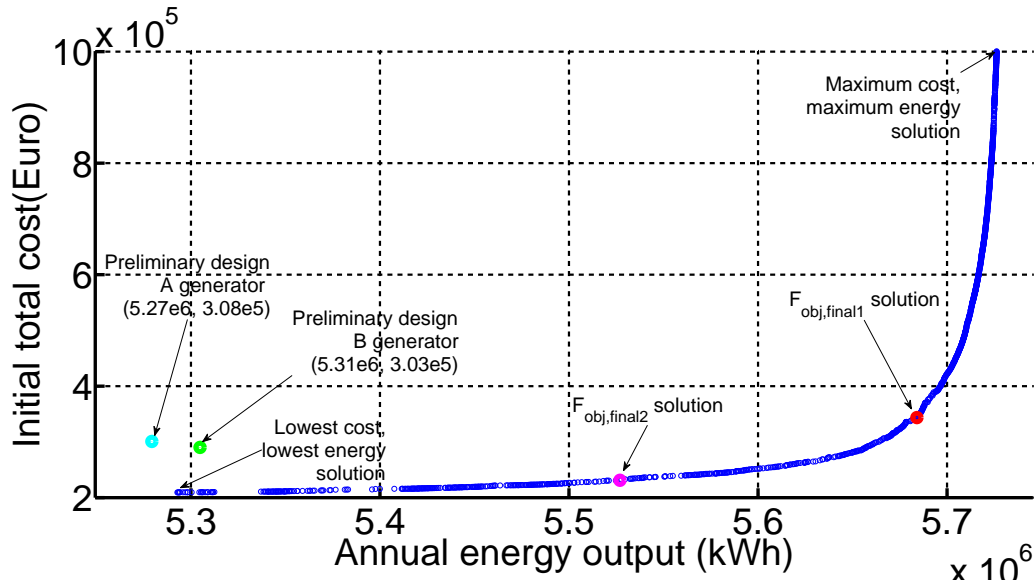On présente aussi les évolutions des paramètres (géométriques et externes) de la machine sur ce front dans l'optique de dégager des règles de dimensionnent. Par exemple, le nombre de paires de pôles est compris entre 12 et 54; la machine externe produit de l'ordre de 57% de la puissance totale; la réactance unitaire est stable et très proche de 80%. En outre, les paramètres des machines externes et internes sont similaires.

Une étude de sensibilité est menée sur quelques paramètres géométriques, la qualité du refroidissement, la nature et le coût des matériaux utilisés. On montre ainsi par exemple que l'augmentation du diamètre extérieur conduit à un meilleur rendement annuel en contrepartie d'un investissement accru ou que le type de tôlerie a une faible influence sur le dimensionnement.

Une validation par la méthode des éléments finis du modèle électromagnétique analytique développé sur trois machines particuliaires du front est ensuite effectuée. Il en découle que le calcul des inductances est précis à environ 5% près et les déterminations des fem et du couple font apparaitre des erreurs de moins de 1.5% et 2.0% respectivement. Notre modèle analytique donne donc une bonne estimation du comportement électromagnétique de la machine.

Enfin, nous effectuons une comparaison des résultats d'optimisation entre la machine double stator et la machine simple stator. Il apparait que la machine double stator donne une nette amélioration du couple volumique (+65%) en contrepartie d'une légère dégradation du couple massique (-1%). Ceci permet de réduire les dimensions du générateur à attaque directe et ainsi de réduire son impact sur les écoulements du fluide. En effet, contrairement à l'éolien, le di-

amètre du générateur à attaque directe n'est pas négligeable devant les dimensions de la turbine hydrolienne. Un autre avantage de la structure à double stator est sa redondance naturelle.

4. Commande de la génératrice (simple ou à double stator) en mode sain ou mode défaut

Le dernier chapitre traite d'abord la commande de la machine synchrone simple ou à double stator en mode normal. Les stratégies de contrôle des deux convertisseurs côté machine et côté réseau sont détaillées et validés pour des conditions d'écoulement de fluide réalistes. L'accent est ensuite mis sur la commande de la DSCRPMG en mode défaut, en particulier le cas de l'ouverture d'une phase du stator externe. Trois stratégies sont élaborées et testées pour assurer une continuité de service et minimiser les ondulations de couple. La plus simple consiste à déconnecter le stator externe défaillant et fournir le couple uniquement avec le stator interne sain en tenant compte de ses limites thermiques. La 2$^{\text{ème}}$ consiste à élaborer des consignes de courants adéquates pour le pilotage du stator défaillant et la 3$^{\text{ème}}$ s'appuie sur un estimateur des ondulations de couple permettant par la suite de les compenser par action sur le stator interne (Fig. 8). Ces approches sont comparées en termes de simplicité d'implémentation et efficacité de compensation des ondulations de couple montrant ainsi les possibilités offertes par la DSCRPMG. La figure 9 illustre les résultats de simulation obtenus avec la méthode basée sur l'estimateur de couple. Après compensation, le couple est quasi constant. Le taux d'ondulation de la vitesse est de l'ordre de $0,1\%$ alors que l'oscillation de couple n'excède pas les 5%.
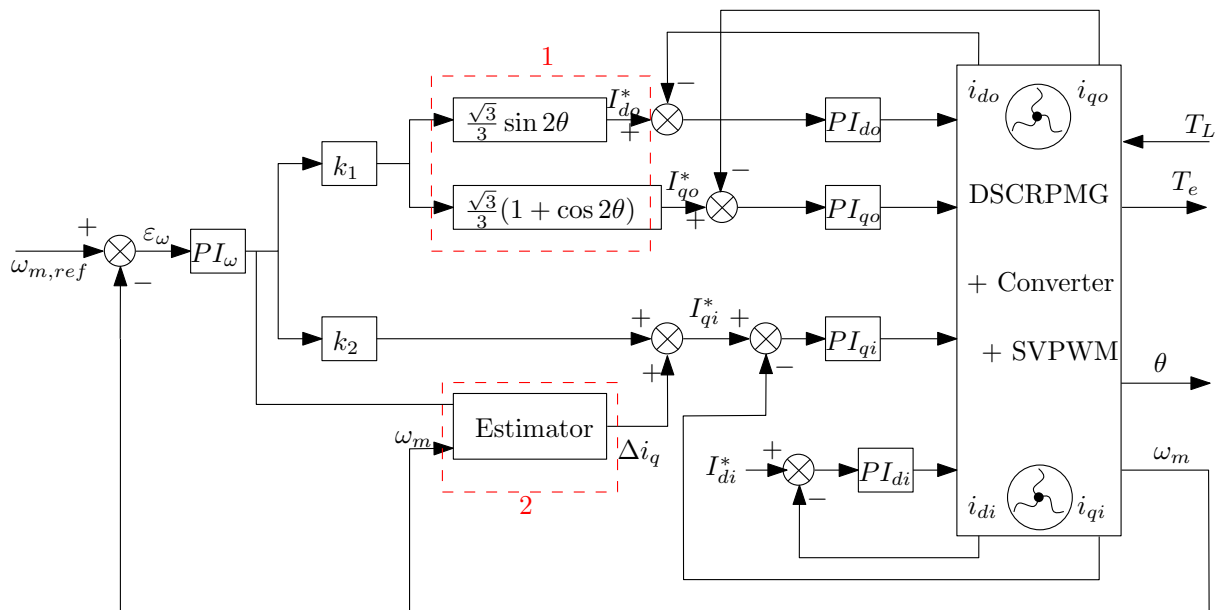
Figure 8 – Commande de la DSCRPMG en mode défaillant, méthode avec estimateur

14
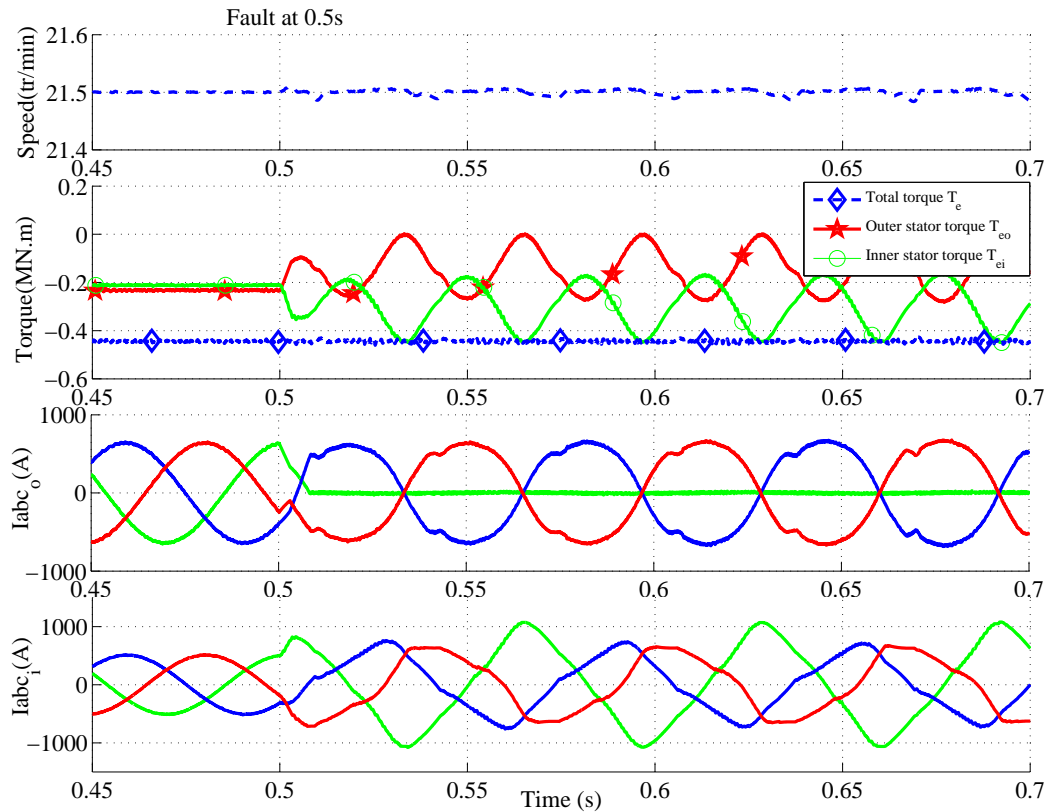
Figure 9 – Performances de la DSCRPMG obtenues en mode défaut avec l'estimateur

5. Perspectives

Nous donnons ci-dessous quelques perspectives envisageables:

— Amélioration du modèle thermique: si le modèle analytique de la machine a pu être validé avec la MEF, le modèle thermique implémenté est relativement simple et nécessiterait d'être affiné et confirmé par des essais expérimentaux. Ceci est d'autant plus critique que le «rotor cup» pourrait conduire à des systèmes de refroidissement spécifiques, en particulier pour une machine de grande dimension.

— Intégration de la valeur nominale de la vitesse du courant dans le processus d'optimisation;

— Etude du décalage entre les stators externes et interne en vue de réduire le cogging et/ou les ondulations de couple;

— Prise en compte du modèle de la turbine hydrolienne dans l'étude de l'ensemble de la chaîne de conversion allant de la ressource jusqu'à l'intégration au réseau.

— Poursuivre les travaux relatifs à la tolérance aux défauts en intégrant d'autres topologies de convertisseurs.

— Validation expérimentale des travaux réalisés dans cette thèse.

Contents

List of Symbols

β	Turbine blades pitch adjustment angle, °; The magnet arc angle, °.
ϵ	Short pitching.
γ	The ratio between coil pitch and pole pitch.
$\hat{B}_g$	Air-gap max fundamental flux density, T.
$\hat{B}_m$	Maximum flux density, T.
$\hat{B}_s$	Saturation flux density, T.
κ_c	Carter coefficient.
λ	Tidal current turbine tip speed ratio.
λ_s	The slot permeance factor.
λ_s	Tooth tip permeance factor.
μ_o	The permeability of free space, H/m.
μ_{rm}	The permeability of magnet, H/m.
ω_e	Electrical rotational speed of generator, rad/s.
ω_m	Mechanical rotational speed of turbine rotor, rad/s.
$\omega_{e,b}$	Base (rated) electrical rotational speed of generator, rad/s.
Φ_z	Common factor of tides harmonics.
ψ_{PM}	The max fundamental flux in the air gap, Wb.
ρ	The density of tidal current, kg/m^3.
ρ_{cu}	The electrical resistivity of copper, Ω/m.
σ_z	Circular frequency of tides, Hz.
τ_d	The tooth pitch, m.
τ_p	Pole pitch, m.
θ_{ele}	Electrical angle, °.
φ	Power factor angle, °.
A	The electric linear current loading, A/m.
A_z	Amplitude of tides harmonics, m.
B_r	Magnet remanence, T.
C	Tide coefficient; Cost of material, €.
C_p	Tidal power coefficient.

C_z	Latitude factor of tides harmonics.
d	Density of material, $\mathrm{kg/m^3}$.
D_o	Bore diameter of the outer stator lamination, m.
E	RMS value of the stator fundamental induced EMF, V.
E_{tidal}	Kinetic energy contained in the tidal current, J.
f	Frequency of a synchronous generator, Hz.
g	Gravitational acceleration, $\mathrm{m/s^2}$.
H	Height of the tides, m.
h	Heat exchange coefficient, $\mathrm{W/m^2K}$.
H_0	Mean sea level, m.
h_m	The thickness of the magnet, m.
h_r	The thickness of rotor, m.
h_{slot}	The height of slot, m.
h_{yoke}	The thickness of yoke, m.
i	Phase current, A.
$i_{d,q}$	The current in d and q axis, A.
I_s	RMS value of the stator nominal RMS phase current, A.
J	Current density, $\mathrm{A/mm^2}$; Rotor inertia, $\mathrm{kg\,m^2}$.
j	Tidal turbine operation point number.
k_f	The winding fill factor.
k_h	The specific loss coefficients for hysteresis.
K_L	Effective loss coefficient of the channel; Coefficient for end winding.
K_T	Turbine quantity coefficient.
k_t	The teeth open ratio.
k_{d1}	Winding distribution factor of the fundamental harmonic.
k_{ec}	The specific loss coefficients for eddy currents.
k_{Fe}	Iron lamination factor.
k_{p1}	Winding pitch factor of the fundamental harmonic.
k_{w1}	Winding factor of the fundamental harmonic.
L	Length of the stator lamination, m.
L_σ	Air-gap leakage inductance, H.
l_g	Mechanical air-gap length, m.
$L_{d,q}$	Direct-axis and quadrature-axis inductance, H.
L_{eff}	Effective machine length, m.
$L_{md,mq}$	The direct-axis and quadrature axis magnetizing inductance, H.
$L_{s\delta}$	The leakage inductance, H.

L_{slot}	Slot leakage inductance, H.
L_{tooth}	Tooth tip leakage inductance, H.
M	Mass of material, kg.
m	Number of slots per pole per phase.
N	Number of turns per phase.
n	Turbine rotor turning speed, r/min; The order of the harmonics.
N_c	Number of conductors in one slot.
P	Extracted power from tidal power, W.
p	The number of pole pairs.
P_i	Inner stator power of the generator, W.
P_n	Total power of the generator, W.
P_o	Outer stator power of the generator, W.
P_{conv}	Converter losses, W.
P_{culoss}	Total copper power loss, W.
P_{iron}	Total core power loss, W.
P_{tidal}	Power of tidal current, W.
q	The number of phase.
Q_s	The number of slots.
R	The generator outer surface radius, m.
R_b	Turbine blades radius, m.
R_{cu}	Winding resistance for one phase, Ω.
R_{shaft}	Generator shaft radius, m.
R_{so}	Bore radius of the outer stator lamination, m.
S	Rotational area of turbine blades, m^2.
S_d	Heat exchange surface, m^2.
S_i	Inner stator apparent power, VA.
S_o	Outer stator apparent power, VA.
S_{cu}	The surface of copper conductor, m^2.
t	Time, s.
T_A	Ambient temperature, °C.
T_e	Electric torque, Nm.
T_L	Turbine torque, N m.
T_{cu}	Winding temperature, °C.
T_{iron}	Iron temperature, °C.
V	Tidal current volume pass through the turbine blades or volume of material, m^3; Root mean square value of phase terminal voltage, V.

v	Phase voltage, V.
v_c	Cut-out or Furling tidal speed, m/s.
v_i	Cut-in tidal speed, m/s.
v_r	Rated tidal speed, m/s.
v_t	Tidal current velocity, m/s.
V_z	Initial phase of tides when $t = 0$, rad.
$v_{d,q}$	The voltage in d and q axis, V.
v_{fi}	The surface tide velocity, m/s.
V_{nt}	Neap tide current velocities, m/s.
V_{st}	Spring tide current velocities, m/s.
v_{th}	Theoretical tide velocity, m/s.
V_{tide}	Tidal current velocity for a choosing site , m/s.
w_{slot}	The width of slot, m.

Acronyms

Symbol	Description
CCCP	Constant Current Constant Power
CMF	Constant Mutual Flux
CP	Constant Power
CVCP	Constant Voltage Constant Power
DC	Direct Current
DSCRPMG	Double Stator Cup Rotor Permanent Magnet Generator
FEA	Finite Element Analysis
FEMM	Finite Element Method Magnetics
FW	Flux Weakening
MAP	Maximum Active Power
MML	Minimize Machine Losses
MOPSO	Multi-Objective Particle Swarm Optimization
MPPT	Maximum Power Point Tracking
MSL	Minimize System Losses
MSLCP	Minimize System Losses Constant Power
PMSG	Permanent Magnet Synchronous Generator
UPF	Unity Power Factor
ZDC	Zero D-aixs Current

List of Tables

List of Figures

Introduction

There is worldwide agreement on the need to reduce greenhouse gas emissions, and different policies are evolving both internationally and locally to achieve this. This kind of world trend drives people to explore different kinds of renewable energy such as wind power, solar power and ocean power. Wind power and solar power have been industrialized and successfully integrated to the grid in large scale for many years. More and more organizations, companies and laboratories start to focus on exploring ocean power. More than 70% of the earth area is covered by ocean and in which stored a vast of energy. The oceans represent an energy resource which is theoretically far larger than the entire human race could possibly use. The existed various forms in ocean power are namely tidal rise & fall energy, tidal (ocean) current energy, wave energy, salinity gradient and thermal gradient energy. Among them, tidal current energy [1] has obtained a strong increasing interest due to the advantages of predictable, high power density and huge potential characteristics in the last decade.

Tidal current energy has been regarded as the most closely commercialized resource and the method to harness tidal current energy has some similarities with wind power technology. An abundant of tidal current turbines have been originally designed by different universities and industries. Some of them have realized to transfer electricity to the customer. In Europe, many countries and company are scheduled to build several megawatt range tidal current energy farm and to supply electricity for coastal areas or remote islands in the near coming future. However, there are still some difficulties before commercialization in large scale of the tidal current energy system. The investment cost of tidal current energy is still very high comparing with wind energy even with the tax deduction and exemption by government. This thesis work mainly focuses on two sides to improve the tidal current energy system cost performance which are generator optimization design and fault tolerant control. Fixed pitch direct drive system with Double Stator Cup Rotor Permanent Magnet Generator (DSCRPMG) is adopted in this thesis. Fixed pitch system is robust and provides less power oscillation. Direct drive system eliminates the gear-box which may lead high maintenance cost and long downtime. As the tidal current speed profile is predictable for a selected tidal site for a long term, DSCRPMG design will take full consideration of the operation point and its corresponding operation time. Fault tolerant control is researched to reduce the system downtime.

---

1. It is also called marine current energy or ocean current energy

The structure of this thesis is:

— The first chapter presents the state of art of tidal current energy. Tidal current source modeling and power extracting are briefly discussed. The up to date hopeful tidal turbines are shown in the classification of tidal turbine type. The advantages and disadvantages of the possible generator system for tidal current energy application are also summarized. Some introductions of the researched double stator PM generator are given at the end of this chapter.

— The second chapter discusses the design of a DSCRPMG at the rated power condition. Then, a comprehensive comparison of different current vector control strategies are made through evaluating the generator converter system efficiency both in Maximum Power Point Tracking (MPPT) region and Flux Weakening (FW) region. Several control strategies (zero d-axis current control (ZDC), constant mutual flux (CMF) and minimize machine loss (MML)) are analysed and compared. An approach minimising all system loss (machine and converter) and allowing to maximise efficiency is adopted.

— The third chapter presents a methodology of DSCRPMG optimization design which takes into account the control strategy and predicted tidal current frequency into consideration using Multi-Objective Particle Swarm Optimization (MOPSO) tool. 16 variable parameters including DSCRPMG geometry parameters and converter size parameters are to be optimized under the mechanical, magnetic, electrical and thermal constraints. The two optimization objectives are maximizing the annual energy output and minimizing the investment for the specific tidal energy site. Comparison between PMSG and DSCRPMG optimization design for the same turbine and torque speed profile are discussed in this chapter.

— The fourth chapter researches the control system design of PMSG and DSCRPMG for health and open circuit fault conditions. The health condition operation systems are firstly designed. The performances under constant tidal speed or variable tidal speed are presented and discussed. In the open circuit fault condition, three control strategies are proposed for DSCRPMG to remedial the torque and speed oscillation. The results show that DSCRPMG system has much better fault tolerant performance than PMSG system.

— The final chapter is the general conclusion and perspective of this thesis.

1

State of art in tidal current energy extracting technologies

1.1 Introduction

The potential of electric power generation from tidal currents is enormous. Tidal currents are being recognized as a resource to be exploited for the sustainable generation of electrical power. The high ocean water density leads to that tidal current turbine blades size are much smaller than wind turbine blades for the same power level. Additionally, tidal source is highly predictable for long time. Those characteristics make tidal current extremely promising and advantageous for power generation when compared to other renewable energy resources. The technology used for harnessing tidal current energy mainly based on the relevant work which has been carried out on ship's propellers, wind turbines and on hydro turbines. This chapter reports tidal power fundamental concepts and two currently used source modeling methods. The most promising tidal turbine projects worldwide are classified depending on the structure of turbine and some brief notes are given. The possible generator choices and system topologies are presented. Furthermore, the introduction of the researched DSCRPMG characteristics are briefly introduced.

1.2 Tidal current resource modeling and energy extraction

The technologies used to extract most of renewable energy are closely depending on the characteristics of the resource. Undoubtedly, some basic understanding of the resource dy-

namics is therefore one of the first steps to be considered before exploiting it. This section will discuss the formation reasons and model methods of tidal current firstly and then the tidal power harness principles.

1.2.1   Tidal current principle

The global tidal current or marine current energy resources are the horizontal movement of water mostly driven by tides which caused by gravitational interactions between sun, moon, and earth. In some cases the tidal currents are also caused by thermal gradient and salinity gradient effects. The tides can be classified into three types: semi-diurnal, diurnal and mixed tide. Semi-diurnal tide causes water to flow both inwards (flood tide) and seawards (ebb tide) twice each day with a cycle period approximately 12 hours and 24 minutes. Diurnal tide flows once both inwards and seawards each day with a cycle period approximately 24 hours and 48 minutes. Mixed tide is a combination result of the semi-diurnal and diurnal effects and which is the most dominant type in the world. Tides are generated by gravitational forces of the sun and moon on the ocean waters of the rotating earth. The strength of the currents varies, depending on the distance of the moon and the sun relative to the earth. The magnitude of the tide-generating force is about 68% moon and 32% sun due to their respective masses and distance from Earth. The sun's and moon's gravitational forces create two "bulges" in the earth's ocean waters: one directly under or closest to the moon and other on the opposite side of the earth. These "bulges" are the two tides a day observed in many places in the world. Unfortunately, this simple concept is complicated by the fact that the earth's axis is tilted at 23.5 degrees to the moon's orbit; the two "bulges" in the ocean are not equal unless the moon is over the equator. This difference in tidal height between the two daily tides is called the diurnal inequality or declination tides and they repeat on a 14 day cycle as the moon rotates around the earth. Where the semi-diurnal tide is dominant, the largest marine currents occur at new moon and full moon (high tides), which is when the sun and moon's gravitational pull are aligned. The lowest, occurs at the first and third quarters of the moon (low tides), where the sun and moon's gravitational pull are 90 degrees out of phase as shown in Fig. 1.1 [1]. With diurnal tides, the current strength varies with the declination of the moon (position of the moon relative to the equator). The biggest currents appear at the extreme declination of the moon and lowest currents at zero declination. Therefore differences in currents occur due to changes between the distances of the Moon and Sun from Earth, their relative positions with reference to Earth and varying angles of declination. These positions occur with a periodicity of two weeks, one month, one year or longer, and are entirely predictable [2]. This means that the strength of the tidal currents generated by the tide varies, depending on the position of the site on the earth. Other factors such as the shape of the coastline and the bathymetry (shape of the sea bed) also affect the strength of tidal currents. Along straight coastlines and in the middle of deep oceans, the tidal
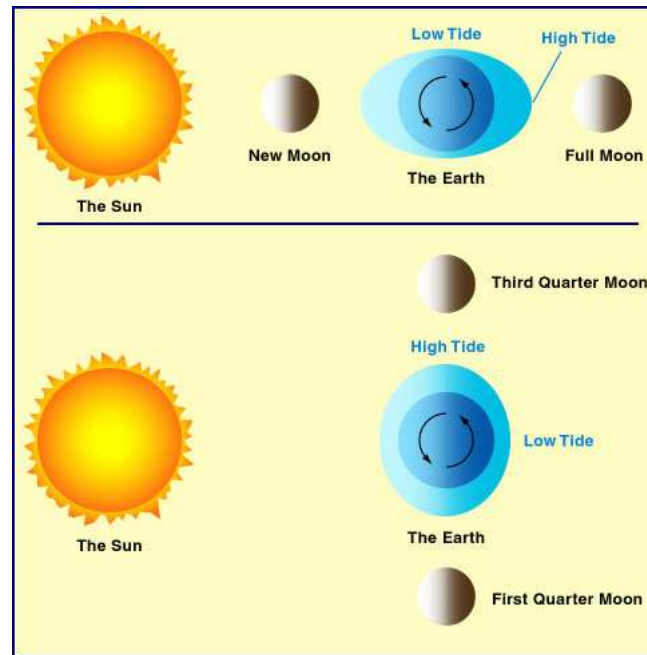
Figure 1.1 – Formation of tides

range and marine currents are typically low.

To estimate one location whether it is suitable to build a tidal turbine farm or not, the resource should be assessed thanks to oceanographic databases. The main key criteria are: maximum spring current velocity; maximum neap current velocity; seabed depth; maximum probable wave height in 50 years; seabed slope; significant wave height; and the distance from land [3] [4].

1.2.2 Modeling of tidal current speed modeling

Tides and tidal current are periodically in motion as a result of Sun-Moon-Earth gravitational system interaction. In fact, it is not easy to get the exact behavior. In any hydrodynamic model for tidal current flow in a channel, there is a requirement for accurate water height data and channel parameters. For any subsequent resource evaluation and site capacity estimation there must be a large amount of data available (usually at least 1 year). Currently, there are several ways to model the tidal current velocity. At the same time, the modeling of the tidal channel is also very important. Different shape of channel change tidal current velocity sharply. All of the model methods depend on the marine meteorology data measured in the past years. In this part we will mainly present two method called Harmonics Analysis Method (HAM) and Practical Model (SHOM) [1](French Navy Hydrographic and Oceanographic Service, Brest, France) [5]. There are also other kinds of methods to simulate tidal current model such as Tide 2D and Double Cosine Method [6].

---

1. This method is mainly used in France to model tidal current velocity

Harmonics Analysis Method (HAM)

The tide change at any location can be divided into many tidal harmonic constituents (partial tides), then calculate the tidal amplitudes and phases of each partial tide according to the tidal observations. Tide can be considered as a superposition of many simple waves. This method is usually called Harmonics Analysis Method (HAM). Each single simple wave corresponds to an object called imaginary celestial body. So the whole tide caused by the tidal force can be written as [6, 7]:

$$H = C_z \sum_z A_z \Phi_z \cos(\sigma_z t + V_z) \qquad (1.1)$$

Where:

H: Height of the tide (m);

σ_z: Circular frequency (rad/hour);

t: Time (hour);

V_z: Initial phase (rad) when $t = 0$;

C_z: Latitude factor;

Φ_z: Common factor;

A_z: Amplitude (m);

In order to build the tidal current model, there are 11 very important harmonic tides needed:

— 4 semi-diurnal partial tides: $M2$ (Principal Lunar Semi-diurnal Constituent), $S2$ (Principal Solar Semi-diurnal Constituent), $N2$ (Large Lunar Elliptic Semi-diurnal Constituent), $K2$ (Luni-solar Semi-Diurnal Constituent);

— 4 diurnal partial tides: $K1$ (Luni-solar Diurnal Constituent), $O1$ (Principal Lunar Diurnal Constituent), $P1$ (Principal Solar Diurnal Constituent), $Q1$ (Large Lunar Elliptic Diurnal Constituent);

— 3 shallow water constituents (due to the topography and effect of interference): $M4$ (Lunar 1/4 Diurnal Shallow Water Constituent), $MS4$ (Lunisolar 1/4 Diurnal Shallow Water Constituent), $M6$ (Lunar 1/4 Diurnal Shallow Water Constituent).

The initial phase V_z, Amplitude A_z and factors depend on the choosing site.

Approximately, choosing some of the very important harmonic tides to build the tidal current model we can acquire relatively high accuracy. In order to simplify the equation Eq.1.1 and the calculation, we just choose some of the tides: $M2$, $N2$, $S2$, $K1$, $O1$, $M4$ and $M6$ and their values are shown in Table. 1.1. Then the whole formulation Eq.1.1 for the tide height can be rewritten as follow:

$$
\begin{aligned}
H(t) = & H_0 + A_{M2} \cos(\sigma_{M2} t + V_{M2}) + A_{N2} \cos(\sigma_{N2} + V_{N2}) \\
& + A_{S2} \cos(\sigma_{S2} t + V_{S2}) + A_{K1} \cos(\sigma_{K1} t + V_{K1}) \\
& + A_{O1} \cos(\sigma_{O1} t + V_{O1}) + A_{M4} \cos(\sigma_{M4} t + V_{M4}) \\
& + A_{M6} \cos(\sigma_{M6} t + V_{M6})
\end{aligned}
\qquad (1.2)
$$

z Harmonic Constituent	Definition	σ_z(rad/hour)
$M2$	Principal Lunar Semi-diurnal	0.5059
$N2$	Large Lunar Elliptic Semi-diurnal	0.4964
$S2$	Principal Solar Semi-diurnal	0.5236
$K1$	Luni-solar Diurnal	0.2625
$O1$	Principal Lunar Diurnal	0.2434
$M4$	First overtide of $M2$	1.0117
$M6$	Second overtide of $M2$	1.5176

Table 1.1 – Principal tidal harmonic constituents

$H(t)$=mean sea level + contribution from sum of harmonic constituents;

Where: A is the amplitude of each harmonic constituent; H_0 is mean sea level.

As the tidal height is predicted by specific method, such as HAM mentioned above, it allows us to deduce the tidal current velocity. It should be noticed that the velocity of the tidal current is the final key criteria to assess tidal current location. Tidal currents flow in channel. Each channel is of course unique in terms of its width and depth variations, roughness etc. The basic premise of the channel model method is therefore to take a real channel and idealize it into a simple mathematical model. Water height level data from two reservoirs on either end of the channel need to be obtained. The tidal height at the first reservoir is at a height h_1 and the second is at a height h_2. A Side-view and a top-view of the channel model are shown in Fig. 1.2. So
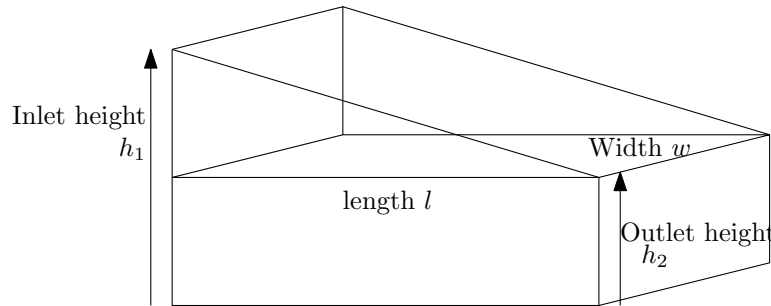
Figure 1.2 – Tides channel model

the theoretical tide velocity is:

$$v_{th} = \sqrt{2g|(h_1 - h_2)|} \tag{1.3}$$

Where g is gravitational acceleration equal to $9.8m/s^2$, h_1 and h_2 can be calculated by Eq.1.2 with a constant time difference between two tide height. But, due to the Law of Conservation of Mechanical energy and take into account the effect of material in the seabed as well as effect of channel blockage [6], the final velocity equation can be written as:

$$v_{fi} = \sqrt{\frac{2g|(h_1 - h_2)|}{1 + K_L + K_T}} \tag{1.4}$$

Where K_L is an effective loss coefficient of the channel; K_T is a turbine quantity coefficient
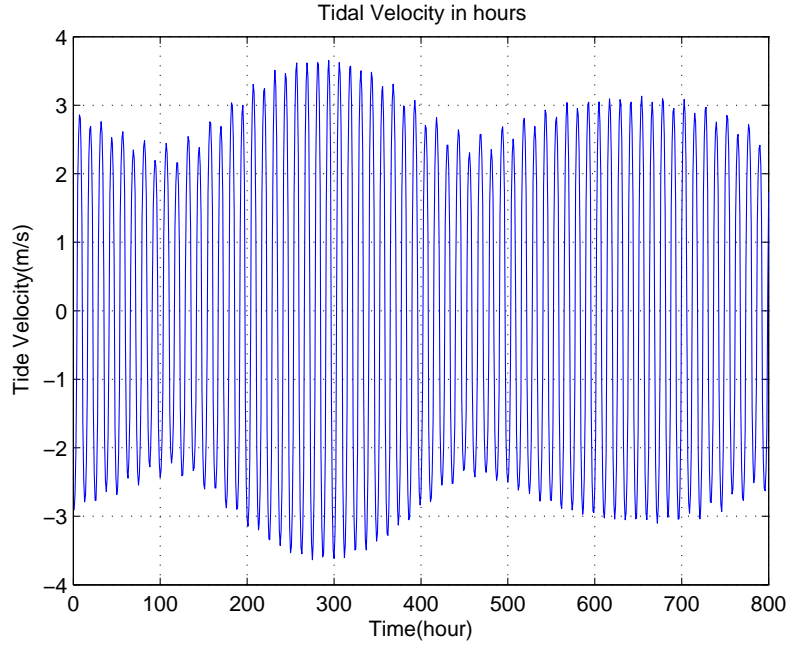
Figure 1.3 – Tidal velocity example (HAM)

which represented in terms of number of turbines. Something should be emphasized is that v_{fi} is the surface tidal current velocity. The calculation methods of the coefficient K_L and K_T are showed in the literature [6]. Fig. 1.3 shows the HAM simulation result for the choosing tidal harmonics parameter. This method is used to model a tidal current speed for the following generator design Chapter. Once the tidal current speed profile is obtained, the tidal current speed frequency is consequently obtained. The generator optimization design will take this tidal speed frequency into consideration.

Practical Model (SHOM)

The tidal current data used in this method is provided by the SHOM [8]. For a specific site, it needs the current velocities for spring and neap tides. These values should be given at hourly intervals starting at 6 hours before high waters and ending 6 hours after. Therefore, knowing tide coefficients, it is easy to derive a simple and practical model for tidal current velocities V_{tide} as follow:

$$V_{tide} = V_{nt} + \frac{(C - 45)(V_{st} - V_{nt})}{95 - 45} \tag{1.5}$$

Where C is the tide coefficient which characterize each tidal cycle (95 and 45 are respectively the spring and neap tide medium coefficient). The value of tide coefficient C for different France tidal locations can be find on the website [8]. This coefficient is determined by astronomic calculation of earth and moon positions. V_{st} and V_{nt} are respectively the spring and neap tide current velocities for hourly intervals starting at 6 hours before high waters and ending 6 hours after. For example, 3 hours after the high tide, $V_{st} = 1.8$ knots and $V_{nt} =0.9$ knots. Therefore,
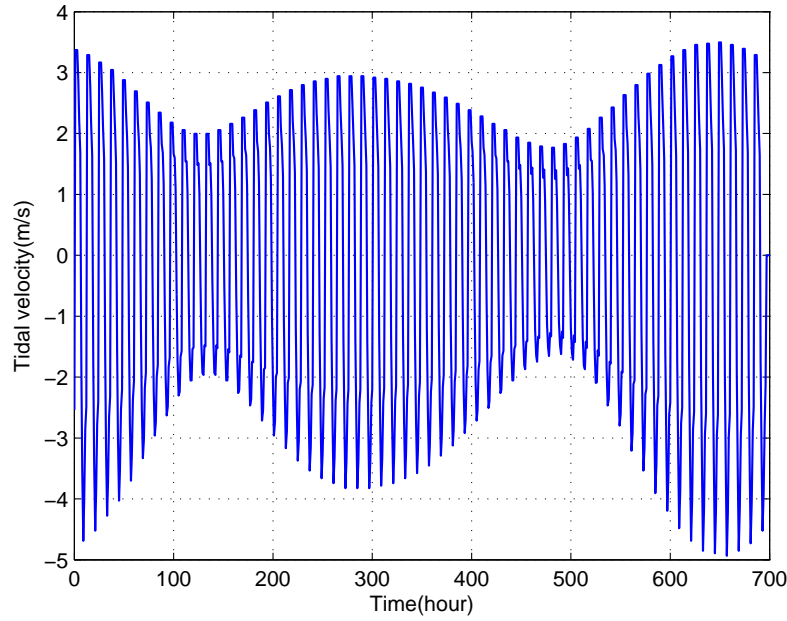
Figure 1.4 – Tidal velocity example (SHOM)

for a tide coefficient C=80, V_{tide}=1.53 knots. However,this method is the ideal current velocity model. In practice, the speed of the tidal current will fluctuates with swells which are considered as the main disturbance of the tidal current velocity. Normally, high tidal speed sites are often located at shallow water sites with typical sea depth about 30-50m. And for this depth the fluctuation caused by underwater propagation of swells can not be negligible when use SHOM method to model the tidal current velocity. The author (Zhibin Zhou) discussed the power fluctuation caused by the influence of swells and the modeling method of swells in detail [9]. Fig. 1.4 shows the SHOM simulation result for tidal location Penmarc'h, France in Sept.2011.

1.2.3 Kinetic energy extraction

The energy in the tidal current is in the form of kinetic energy like wind power. Kinetic energy contained in the tidal current is characterized by the equation:

$$E_{tidal} = \frac{1}{2}mv_t^2 \tag{1.6}$$

Where the mass of tidal current $m = \rho V$, ρ is the density of the ocean water ($1025kg/m^3$) and $V = Sv_t t$ is the tidal current volume pass through the turbine blades in time t. v_t is the tidal current velocity and S is rotational area of turbine blades. For the chosen turbine blades radius R_b, so the turbine blades swept area $S = \pi R_b^2$. Consequently the power of the water flow is given by:

$$P_{tidal} = \frac{E_{tidal}}{t} = \frac{1}{2}\rho S v_t^3 \tag{1.7}$$

The kinetic energy contained in tidal current can't be totally extracted by the turbine blades because the tidal current on the back side of the blades must have a high enough velocity to move away and allow more tidal current flow through the plane of the blades. The question that how much of the tidal energy can be transferred to the blade as mechanical energy has been answered by the Betz'law. Betz'law states that only a maximum of 59.25% of the kinetic power in the fluid can be converted to mechanical power using turbine blades. That number is the so called maximum power coefficient or Betz-Number.

The ratio between the rotor blades extracted power P and the power contained in the tidal current P_{tidal} is given by the power coefficient C_p:

$$C_p = \frac{P}{P_{tidal}} \tag{1.8}$$

C_p is a function of tip speed ratio λ and turbine blades pitch adjustment angle β. The tip speed ratio is defined as:

$$\lambda = \frac{R_b \omega_m}{v_t} \tag{1.9}$$

Where $\omega_m(rad/s)$ is the mechanical rotational speed of rotor. Fig. 1.5 is an example to show
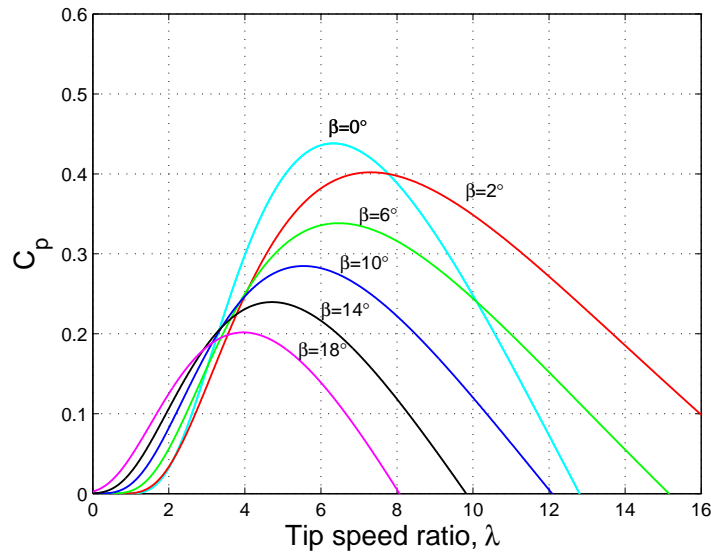
Figure 1.5 – Relationship between C_p, λ and β

the characteristics of one turbine [10]. For every pitch angle β, there is a tip speed ratio λ which corresponds to the maximum power coefficient and hence the maximum efficiency. It can be seen that the power efficiency significantly depends on the pitch angle and the tip speed ratio. Therefore, the pitch angle of the blade has to be changed mechanically in respect to the actual tip speed ratio in order to capture maximum tidal power. This is the theoretical basis for the tidal power maximum efficiency controlling. C_p curve is strongly dependent on the production process of the blades and so the $C_p(\lambda, \beta)$ equation changed.

By combining equation Eq.1.7 and equation Eq.1.8, the power P extracted by turbine blades can be rewritten as:

$$P = C_p P_{tidal} = \frac{1}{2} \rho C_p \pi R_b{}^2 v_t^3 \tag{1.10}$$

For wind generators, C_p has typical values in the range 0.25∼0.5. The upper limit is for highly efficient machines with low mechanical losses. For marine turbines, C_p is estimated to be in the range 0.35∼0.5. The C_p equation used in this thesis is:

$$C_p = 0.3171[116(\frac{1}{\lambda} - 0.035) - 5]e^{-15.45(\frac{1}{\lambda} - 0.035)} \tag{1.11}$$

As turbine pitch is fixed, the pitch angle β is set as 0. It is not showed in the C_p equation.

1.2.4 Optimal regime characteristics and power curve

Optimal regime characteristics

As we discussed before, power coefficient $C_p(\lambda, \beta)$ is a function of tip speed ratio and pitch angle. The Maximum value of $C_p(\lambda, \beta)$ can be achieved through adjusting the value of tip speed ratio λ and pitch angle β. Therefore, for a certain pitch angle β, $\beta = 0$ and fixed in our case, the rotational speed of the turbine needs to be changed to keep the generator work at the maximum power point as the tidal current speed varies.
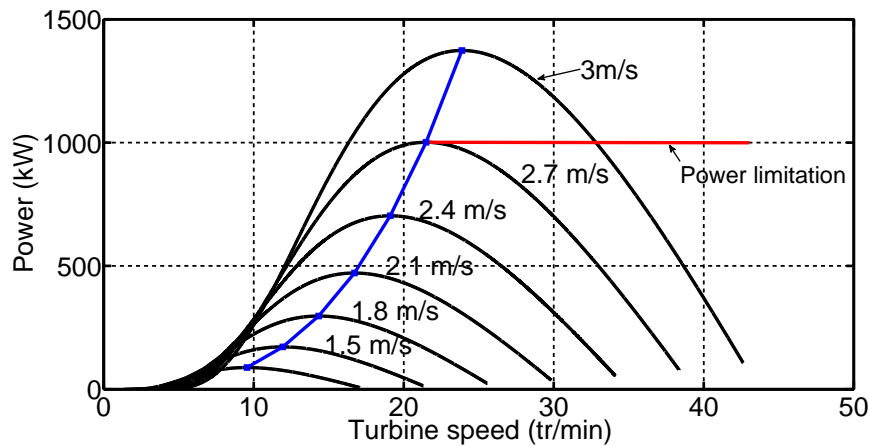
Figure 1.6 – Optimal regime characteristics

Fig. 1.6 shows that for each tidal current speed there is a best rotational speed to extract maximum power in the tidal current energy. All these maximum points determine a so-called "Optimal Regimes Characteristics". It is hoped to absorb maximum power in the flow, so the turbine rotational speed should be keep around its optimal point. In a tidal power system we can use some control methods to find these optimal points, such as MPPT (Maximum Power Point Tracking). The rotation speed of generator is controlled to enable the operation of the turbine at its maximum power coefficient over a wide range of tidal current velocity (blue curve

in Fig. 1.6). In order to keep maximum C_p, the tip speed ratio λ is controlled as a constant. Therefore, the rotational speed of turbine linearly increases with tidal current speed. When the current speed is too high which is more than the rated operational speed and in order to avoid the generator operated under over-rated situation, the maximum power point is no longer need to be tracked. The power will be limited at the rated power level (red line in Fig. 1.6). The rated tidal current speed is $2.7m/s$ in this thesis. When tidal current speed is $3m/s$, if the turbine is still controlled with the manner MPPT, the abstract power will around $1.4MW$ which is much bigger than the designed $1MW$ power rated. There are two rotational speed for $3m/s$ can obtained $1MW$. One is the rotational speed lower than the rated speed and the other is higher than the rated speed. For direct drive turbine generator system, the rotational speed bigger than the rated speed is the proper one to limit the power. Because deceasing the generator rotational speed to have the same power, the torque needs to be increased which will bigger than the rated torque. It is bad for the generator efficiency and thermal limitation. Therefore, increasing the rotational speed and decreasing the torque to achieve constant power limitation will be adopted in this thesis. This manner is call Flux Weakening and it is applied for the power limitation region.

Power curve

The power curve of a tidal current turbine is a graph that indicates which electrical power output will be available at different current speeds. Fig. 1.7 shows the shape of a theoretical power curve of a tidal current turbine.
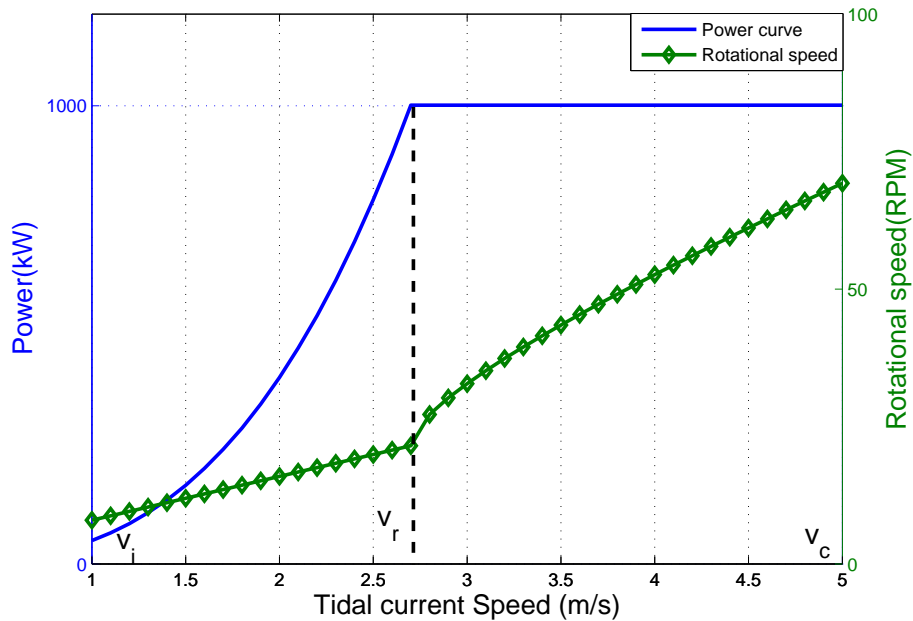
Figure 1.7 – Theoretical power and speed curve for a fixed pitch turbine with power limitation

— **Cut-in tidal speed** v_i**:** Low-speed tidal may not have enough power to overcome friction in the turbine drive train and, even if it does and the generator is rotating, the generated electrical power generated may not be enough to offset the power required by the system. The cut-in tidal speed v_i is the minimum value needed to generate net power. Normally, this value is equal to $1m/s$.

— **Rated tidal speed** v_r**:** As velocity increases above the cut-in tidal speed, the power delivered by the generator tends to increase proportionally to the cubed tidal speed. When marine current speed reach the rated tidal speed v_r, the generator is delivering as much power as rated power P_R. Above v_r, there must be some way to shed some of the tidal power otherwise the generator may be damaged. Three approaches are common on large machines to limit the power on the turbine: an active pitch-control system, a passive stall-control design, and a combination of the two. For fixed pitch turbine, increasing the turbine rotational speed through generator flux weakening control is normally used to limit the turbine power.

— **Cut-out tidal speed** v_c**:** At some point the marine current speed is so strong that there is real danger for the tidal current turbine. At this tidal speed v_c, called the cut-out tidal speed or the furling one, the machine must be shut down. Above v_c, output power obviously is zero.

Fig. 1.6 and Fig. 1.7 are obtained by modeling an assumption tidal current location project with the parameters showed by Table. 1.2:

v_i	v_r	v_c	R_b	P_R
$1m/s$	$2.7m/s$	$5m/s$	$8.4m$	$1MW$

Table 1.2 – Supposed tidal current location project parameters

1.3 Difference between wind energy and tidal current energy

Both wind turbine and tidal current have the same essential principle that extracting kinetic energy from a moving fluid. Wind energy system has been discussed many decades and it has achieved relatively mature stage. Tidal current turbine designs based on those developed technology by wind energy industry has firstly applied. Certainly the basic theory, such as blade element momentum theory and turbine design basic theory, can be equally applicable. Certain major components or subsystems, such as gear box (if needed), could be directly installed into tidal current system with little or no modification. However, tidal turbine design has many differences comparing to wind turbine design because of the different working condition and fluid source despite their apparent similarities. Table. 1.3 shows the main differences between wind turbine and tidal current turbine.

Feature	Wind Turbine	Tidal Current Turbine
Fluid density	$\sim 1.25 kg/m^3$	$\sim 1025 kg/m^3$
Rated speed	$\sim 12 m/s$	$2 \sim 5 m/s$
Cut out speed	$\sim 25 m/s$	$\sim 5 m/s$
Variation of velocity with time	Stochastic variation all the time	Predictable for given location over periods of years (except swell effect)
Visual impact	Yes	No
Cavitation	Yes	Yes
Turbulence	Yes	Yes, stronger than wind turbine because of the high water density.
Rotor diameter (typical)	$90 \sim 120 m$	$15 \sim 30 m$
Corrosion	Salt spray by rain and fog	Immersion in salt ocean water requires careful consideration of material
Erosion	Unlikely to be a serious problem	Potential for serious problem, may exacerbate corrosion
Maintenance access	Weather dependent	Depends on deployment method but probably more difficult than wind turbine
Site limit	Much more place can be chosen in the world than tidal current energy site.	A few locations in the world where the tidal currents can be economically exploited.
Fouling	Unlikely to be a serious problem	Marine growth and biofouling can decrease the efficiency of turbine.
Stress	Tower stress limits the power rate. Turbine blade stress is smaller than tidal turbine.	Tower stress can be reduced by using buoyant material. Higher water density gives high strain on the turbine. The anchoring structure of turbine must resists this force.

Table 1.3 – Comparison of the differences between wind turbine and tidal turbine

Because of those different characteristics, tidal current turbine has its advantages and disadvantages. Tidal turbine size can be designed much smaller. For the same obtained power with the same power coefficient C_p in wind power and tidal power turbine, the blades radius of wind turbine is around 2.6 times of tidal current turbine [11]. That indicates that even the wind speed is much higher than tidal current speed, for the same power level, tidal current turbine blades radius are much smaller than wind turbine because of the higher water density. The predictable tidal current speed and huge tidal power potential quantity are the other important advantage for extracting tidal current energy. Fixed turbine pitch control is recommended because of the big thrust and fluctuation caused by higher water density [12]. A small perturbation can lead

high torque oscillation. Because of the problem of corrosion in the salt water, the requirement of material for tidal turbine is higher than wind turbine. In addition, the auxiliary devices such as electrical cable, nacelle and turbine foundation have higher requirement comparing to wind turbine because of the serious operation environment.

1.4 Hopeful turbine prototypes
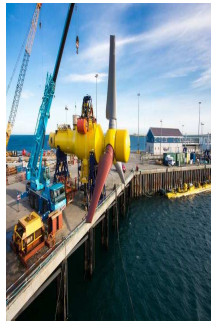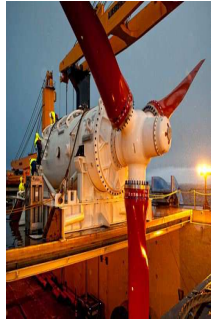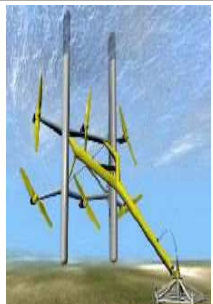
Tidal current turbine is a device which used for harnessing the kinetic energy in a tidal flow and then transforming the energy into the motion of a mechanical shaft, which can then drive a generator. Both wind and tidal current are in the form of fluid. Therefore, it is not too surprising that many wind turbine design technology which has been successfully utilized to harness the wind power can be used to harness tidal energy. Most tidal devices can be characterized as belonging to four fundamental types. They are:

— Horizontal Axis Turbine Systems

— Ducted Turbine System

— Vertical Axis Turbines Systems

— Oscillating Hydrofoil Turbines System

In the following introduction, some brief information of the pre-commercial turbine prototype are given. More details can be found through the corresponding references. Furthermore, all the tidal current energy projects and test sites information around the world are shown in the marine renewable energy world map by Open Ocean [13].

1.4.1 Horizontal axis turbine systems

Horizontal axis turbine rotate around a horizontal axis which is parallel to the current stream. The majority of the tidal current devices to date are horizontal axis turbine. Multi-bladed devices are favorable as they generate greater starting torque and reduce balancing problems encountered with single-blade devices. However, hydrodynamic losses are greater with the use of a greater number of blades. Like wind turbine, three blades turbine type are the most common choice for the industries. Depending on turbine design, the blades can either have a fixed pitch or variable pitch to enable the turbine to operate during flow in both directions. Table. 1.4 summarizes the main horizontal axis turbine projects existed in the world.

Horizontal Axis Turbines			
Company	*Devices*	*Features and Notes*	*Illustration*
Verdant Power Ltd (USA) [14]	KHPS	Three-bladed fixed pitch, gearbox connected turbines are installed in East river New York 2007. Currently, it moves to develop the 5th Generation turbine.	
Tidal stream turbines-Alstom (France) [15]	Oceade	1 MW tidal current turbine was successfully installed at EMEC in 2013. In 2014, Alstom has been chosen by GDF to equip 4 Oceade^{TM} 18 (1.4MW) turbines at raz Blanchard tidal pilot farm. Pitch-able blades, gearbox, induction generator and buoyant material are used to reduce the installation and maintenance costs.	
Andritz Hydro Hammerfest (Norway) [16]	E-Tide, HS1000	A 300kW(HS300) system was tested in Kvalsundet and a 1MW(HS1000) precommercial tidal turbine with induction generator was tested at EMEC in 2011. 10 MW commercial array turbines are intended to be installed in Islay site with companmy Meygen and 95 MW for Duncansby Head site.	
Marine Current Turbine (UK) [17]	Seagen	Twin horizontal-axis rotors each one with two variable-pitch blades and induction generator, 2*600 kW was installed at May 2008 in Strangford Lough, Northern Ireland and generated 8 GWh electricity since the installation. 2 MW SeaGen S systems will be installed in UK from 2015.	
Tidal Stream Energy (UK) [18]	Triton (3 or 6)	An array of turbines (3 or 6) fixed on the same shelf. Scaled T3 was tested in 2011 . Scaled T6 was undertaken in the deep water ocean basin near Brest, France, from 2009. Currently, platform with 25 or 36 small turbines which announced have lower cost are under developing.	

Tocardo tidal turbine (Nether-lands) [19]	Tocardo	The first Tocardo turbine was tested in 2005, followed by the installation of a commercial turbine in 2008 and fully commercial since 2012. This concept turbine is very suitable for shallow tidal sites and existing structures as well, like dams, bridges and barrages.	
Atlantis Resources (UK) [20]	AR1000, AR1500	AR-1000 turbine was successfully deployed in August 2011 and produced first power to the Orkney grid. AR1500 is a pitch-able, gearbox integrated and permanent magnet generator system. It will be test at the end of 2015.	
Sabella (France) [21]	D3, D10, D12, D15	6 blades design. Installed and tested the first French tidal stream turbine (10kW) near Brest in 2008. It is 100% made in France turbine. Type D10 1MW turbine has been installed in the Fromveur Strait on June 2015. Larger turbines D12 and D15 with power capacities of $1 \sim 2$ MW are under design.	
Voith Hydro(Germany) [22]	Voith Hytide	The first test turbine of 110 kW has been in operation near the South Korean island of Jindo since 2011. The up-scaled version of 1 MW turbine is now installed and tested at EMEC tidal test site. GDF Suez has recently confirmed to use Voith Hydro HyTide for the Raz Blanchard project.	

Table 1.4: Main projects of horizontal axis turbines

1.4.2 Ducted turbine system

Ducted turbine can be essentially classified in horizontal axis turbines. It has been firstly discussed for wind energy extracting with unidirectional type and yaw system. However, this structure doesn't gain recommendation in wind energy system because the cost of the complete structure normally outweighs the benefits of flow speed augmentation for these type of devices [23]. However, a wide range of ducted tidal turbine have been suggested. The main advantage is that it can produce higher tidal velocity [24]. Table. 1.5 shows the most hopeful horizontal

ducted turbine.
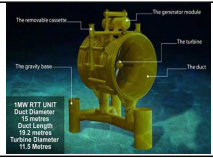
Ducted Turbine System			
Company	*Devices*	*Features and Notes*	*Illustration*
Lunar Energy (UK) [25]	Lunar	A $1/20^{th}$ model was tested in 2004, and a 1MW is testing in Korea. It is planed first commercial Lunar Energy field in 2015.	
Open-Hydro Ltd (Ireland) [26]	Open Centre Turbine	Rim driven generator is normally used. It is the most well known ducted turbine. Installed at the EMEC off Orkney in Scotland. Connected to UK national grid in May 2008. It is chosed by EDF to build the first tidal current demonstration farm at Paimpol-Bréhat in France. 4 turbines (each one 500kW) are reported to be connected to the power grid in 2018.	
Clean Current (Canada) [27]	Clean Current Turbine	Segmented generator is adopted. It's bi-directional ducted horizontal axis turbine. Commercial river turbine has been deployed in Manitoba, Canada in the spring of 2013 and shallower tidal projects is under testing from 2014. The turbine was tested even in severe winter conditions in November, 2014.	

Table 1.5: Main projects of ducted turbines

1.4.3   Vertical axis turbines system

Vertical axis turbines that operate in marine currents are based on the same principles as the land based Darrieus turbine. The Darrieus turbine is a cross flow machine, whose axis of rotation meets the flow of the working fluid at right angles. In marine current applications, cross flow turbines allow the use of a vertically orientated rotor which can transmit the torque directly to the water surface without the need of complex transmission systems or an underwater nacelle. The vertical axis design permits the harnessing of tidal flow from any direction, facilitating the extraction of energy not only in two directions, the incoming and outgoing tide, but making use of the full tidal ellipse of the flow. In this kind of turbines as in the horizontal axis ones the rotation speed is very low (around 15 rpm). Table. 1.6 shows the main vertical turbine project existed in the world.
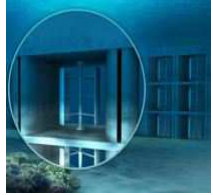
Vertical Axis Turbines System			
Company	*Devices*	*Features and Notes*	*Illustration*
GCK Technology (USA) [28]	Gorlov helical turbine	Self-starting, it always rotates in the same direction, even when tidal currents reverse direction.	
Blue Energy (Canada) [29]	Blue Energy turbine	A unit turbine is expected about 200 kW. Blue Energy plans to build a 120km tidal energy bridge across the Bohai Strait, China. This project would generate over 70,000MW of power.	

Table 1.6: Main projects of vertical axis turbines

1.4.4 Oscillating hydrofoil turbines system

The oscillating hydrofoil induces hydrodynamic lift and drag forces due to a pressure difference on the foil section caused by the relative motion of the tidal current over the foil section. These forces induce a resultant tangential force to the fixing arm which by driving reciprocating hydraulic rams pump, high pressure hydraulic fluid to turn a hydraulic motor and electrical generator. There are not so many proposed system existed in tidal current energy and normally it is used for wave energy. Table. 1.7 shows two projects as example.
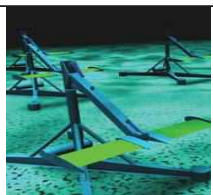
Oscillating Hydrofoil Turbines System			
Company	*Devices*	*Features and Notes*	*Illustration*
BioPower (Australia) [30]	bioSTREAM	Based on the swimming propulsion of some swimming species, such shark. Systems are being developed for 500W, 1 and 2MW capacities to match conditions in various locations	
Engineering Business Ltd (UK) [24]	Stingray turbine	It weighs 180 tonnes and is capable of generating 150kw. The system was tested at Yell Sound off Shetland in 2002. In 2005, this project was put on hold.	

Table 1.7: Main projects of oscillating hydrofoil turbines

1.5   Generator choices

A generator is mounted on the turbine shaft to convert mechanical power generated by the turbine blades into electric power. More than one option is available. However, the generator information is not readily available from all existing projects. Some industry share their generator information while for some, it is impossible to find. Information on type of gear and gear ratio is almost non-existent. Tidal energy has closely followed the development of wind energy and both of them has similar technologies. Therefore, many wind turbine generator topologies could be used for tidal current turbines. In this section, different tidal generator system topologies are summarized based on the publications [7, 13].

1.5.1   Squirrel cage and wound rotor induction generator

Induction generators may generally be set in two categories, those with squirrel cage (SCIG), and those with wound rotor (WRIG). They are widely used since they are relatively inexpensive, robust and they require low maintenance. Fig. 1.8(a) illustrates a fixed speed tidal generator systems with a multiple-stage gearbox and a SCIG connects to the grid through a soft stater and a transformer. WRIG has a similar topology. The difference is that the rotor resistance is controllable as shown in Fig. 1.8(c). Since the SCIG and WRIG always draws reactive power from the grid, a compensator should be used. In order to avoid compensator and soft stater problem, a generator system with gearbox and full scale power converter has been proposed as illustrated in Fig. 1.8(b).

(a) SCIG fixed speed topology

(b) SCIG variable speed topology

(c) WRIG topology
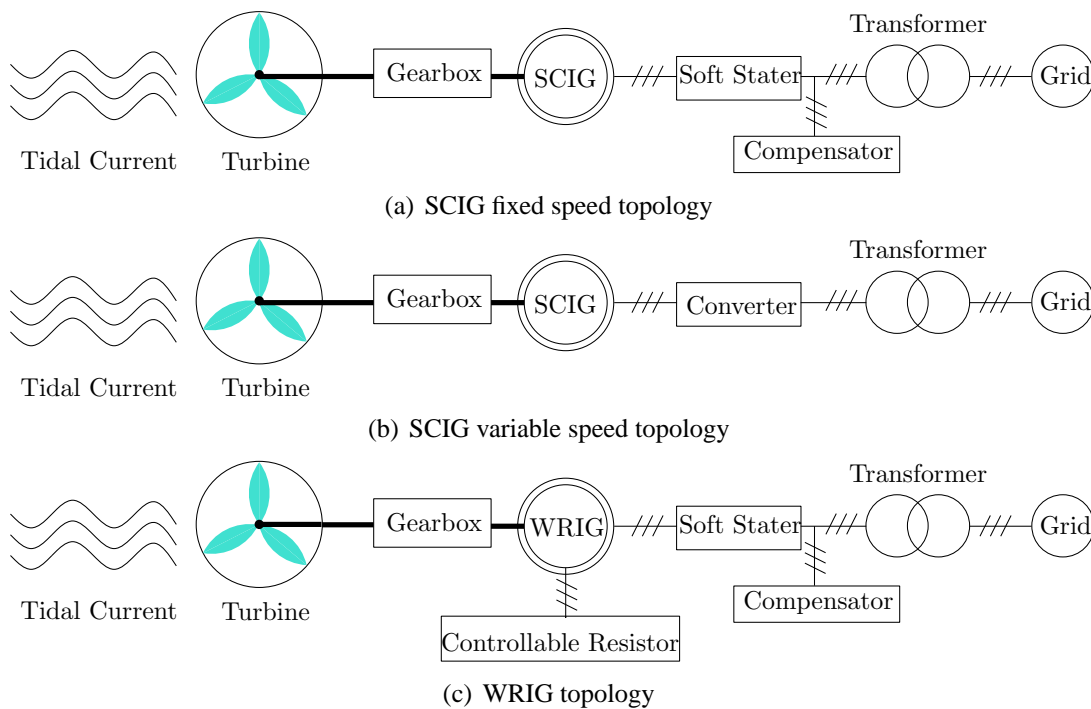
Figure 1.8 – Induction generator topology

1.5.2 Doubly fed induction generator

Fig. 1.9 is known as the DFIG concept. The stator is directly connected to the grid, whereas the wound rotor is connected through a power electronic converter. The variable speed range is $\pm 30\%$ around the synchronous speed [31]. The rating of the power electronic converter is only 25∼30% of the generator capacity, which makes this concept attractive and popular from an economic point of view. The DFIG is the most commonly used one for wind integration due to its high efficiency, fast reaction and robustness during faults. However, DFIG is probably not the case in tidal turbine applications except in special cases comparing to PMSG direct drive system [32].
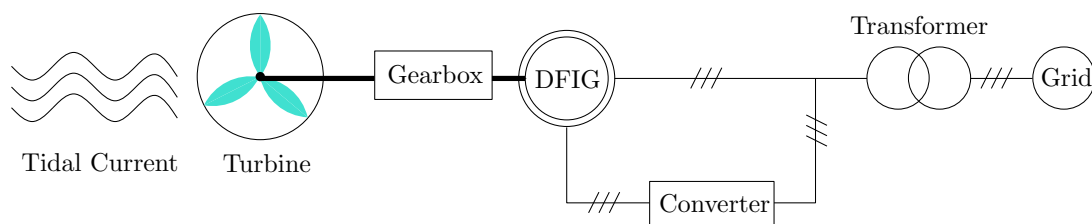
Figure 1.9 – DFIG topology

1.5.3 Permanent magnet and electrically excited synchronous generator

PMSG and EESG are normally used in direct drive train option with full scale power converter connect to the grid as Fig. 1.10 showed. PMSG system has high potential for the tidal current turbines because of its reduced failure, increased energy yield and reliability. The structure, merits and shortages of PMSG are discussed in [33]. The EESG is usually built with a rotor connected to excitation converter and the stator is quite similar to the induction machine. EESG has no demagnetizing risk compared with permanent magnet.

(a) PMSG topology

(b) EESG topology
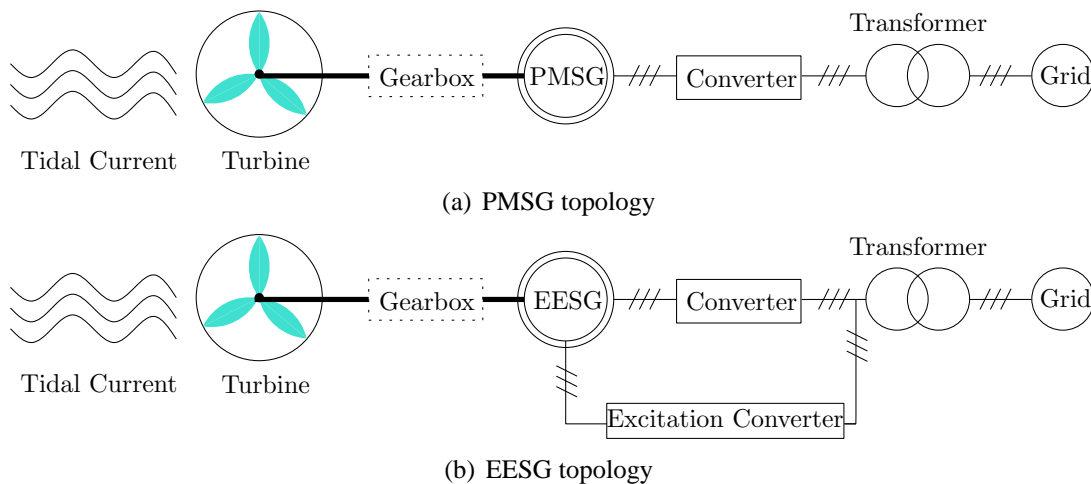
Figure 1.10 – Synchronous generator topology

Both gearbox or direct drive system now are using in the new energy market. However, in direct drive system, the low rotational speed characteristic leads to bigger pole pairs generator design and then leads to bigger system volume and mass. In order to reduce the size and mass of system, a gearbox can be introduced as the dotted line shown in Fig. 1.10. Especially for floating platform turbines, this seems to be the trend even that gearbox system needs high maintenance cost. For the direct-drive and oscillating hydrofoil systems, particularly for the horizontal ducted turbines, PMSG are preferred. SCIG is now in the trend of abandonment by the wind energy industry because of its poor fault ride-through capability and significant deterioration of power quality of the local network, therefore, it is a second choice for tidal energy applications.

1.5.4   Special tidal generator researched by laboratory IREENA

IREENA laboratory (ST Nazaire, France) is currently carrying an inter-regional project called Hydrol 44 involving academic partners (LHEEA, LBMS, IRENAV, LASQUO and IREENA) and industrial partners (Alstom Hydro, Jeumont and Eca-EN) whose purpose is to organize a "task force" in the West region dedicated to the study of marine current energy conversion chains. This thesis is proposed as a part of the project Hydrol 44.

The researches carried-out in the laboratory IREENA are focused on special direct drive permanent magnet generators design and control, such as Doubly Salient Permanent Magnet Generator (DSPMG) , five phase permanent magnet generator and Double Stator Cup Rotor Permanent Magnet Generator (DSCRPMG).

The studied DSPMG is a doubly salient machine with 4 permanent magnets on the stator. The stator includes 48 small teeth distributed on 12 stator big teeth and the rotor 64 teeth as Fig. 1.11 shown. Advantages of this structure are simple and robust construction, high reliability, low cost and high mass torque [34]. Moreover, PMs are located in the stator, easier to cool than in the rotor. This machine has very specific characteristics and researches in the laboratory IREENA are focused on the design optimization, saturated inductance calculation [35], and control strategies [7].

Five phase permanent magnet generator research are mainly focused on converter design, control strategy and fault tolerant control for tidal current energy application [36, 37].

DSCRPMG is studied in this thesis and it will presented in the following section.

1.6   Double stator cup rotor permanent magnet generator

DSCRPMG has been firstly designed to serve as the integrated starter generator for Hybrid Electrical Vehicles(HEVs) [38] and wind energy application [39], which is claimed to offer much higher power density than traditional PMSG. Actually, DSCRPMG has much more mer-
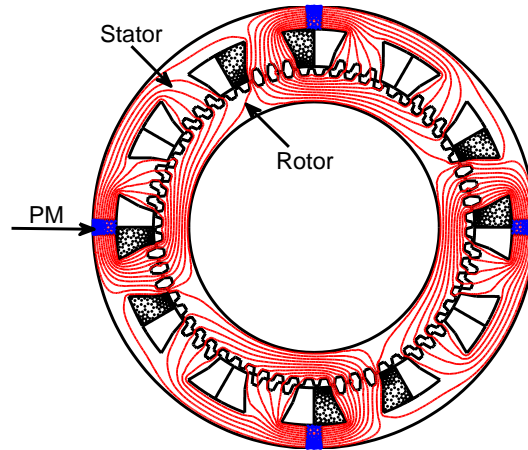
Figure 1.11 – Doubly salient permanent magnet generator

its such as smaller cogging torque, smaller rotor inertia and higher redundancy comparing with traditional PMSG. Based on those advantages, DSCRPMG can be well suited for tidal current energy extracting. Fig. 1.12 shows one possible system topology of DSCRPMG. The two stators are connected to two back-to-back converters independently. The total torque of the generator is the superposition of the torque of inner and outer stator. DSCRPMG also can be controlled in series using one back-to-back converter with the phase windings of the two stators are connected in series. In this thesis report, the topology that the two stators are connected in parallel with independent control system are researched because this topology can provide better fault tolerant control performance.
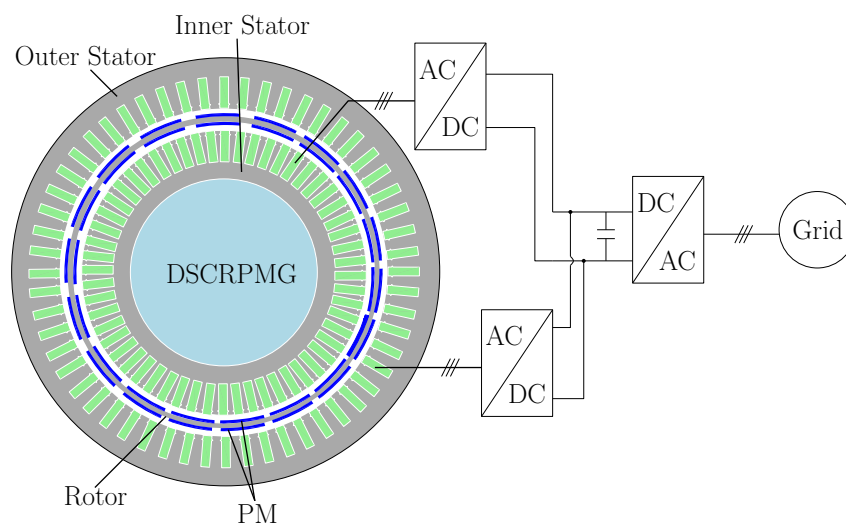
Figure 1.12 – Two stators are connected independently to DC-bus

1.6.1   DSCRPMG configurations

Double stator PM generator is classified in two main categories according to the flux direction in air-gap as radial-flux and axial-flux generator. Transverse flux generator exists, but do not seem to have gained a foothold in tidal power generation or in wind power generation. Some literature introduce three kinds of radial-flux double stator generators as Fig. 1.13 shows below [39, 40]:

(a) Flux path in series   (b) Flux path in parallel

(c) Interior PM
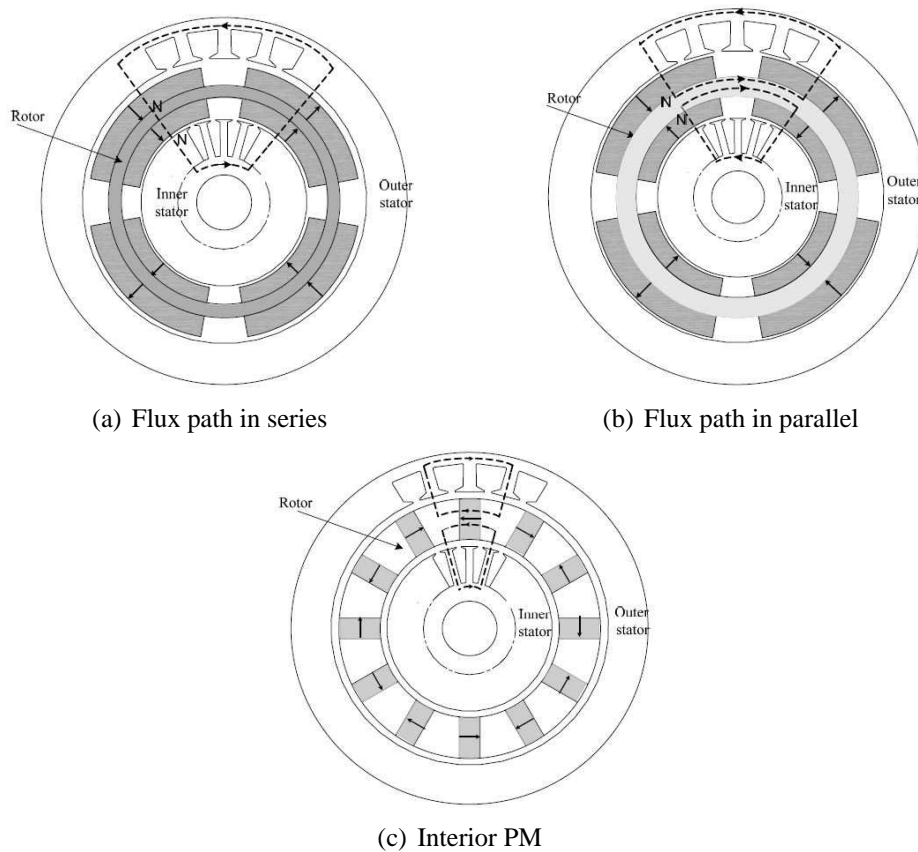
Figure 1.13 – Radial-flux double stator PM generator configuration

PMs surface mounted on the two sides of rotor with the same polarized direction is shown in Fig. 1.13(a). The magnetic flux will passes directly from the inner stator, through the inner air-gap and outer air-gap, to the outer stator. Because there are no magnetic flux travels through the rotor core. Hence, the cup rotor core, which is mainly used to mechanically fix the inner and outer PMs, can be designed very thin. The total volume of machine can be reduced and torque density can be improved consequently. Also, this kind of topology reduced the moment of inertia. Another configuration with opposite polarized direction PMs is shown in Fig. 1.13(b), the flux paths are in parallel between the two stators. Magnetic flux will travel from single side of stators, namely through the same side air-gap and the rotor core, and then return to the initial stator. And the two flux paths will pass parallel inside of the rotor core. In order to avoid magnetic saturation, the thickness of rotor should around 2 times bigger than the thickness of the yoke in stator for a compact generator design. Fig. 1.13(c) demonstrates the type of interior

permanent magnet generator. Actually, the magnets can be embedded on the surface of rotor or buried into the rotor. The flux path is also in parallel.

The author Niu Shuangxia [41] quantitatively compares both steady and dynamic performances of the double stator surface mounted PM generator, double stator interior PM generator and traditional single stator PM generator. The comparison results confirms that double stator surface mounted PM generator has relatively better performance with higher torque density and lower cogging torque. In the mechanical point of view, interior PM generator is suitable for high rotational speed application. However, for tidal current turbine application which normally rotates at low speed, surface mounted PM generator is robust enough. This report will mainly focus on the preferred surface mounted PM double stator generator with flux path in parallel as shown in Fig. 1.13(b) because this topology can provide a good independence of the two stators.

1.6.2 DSCRPMG mechanical assembly
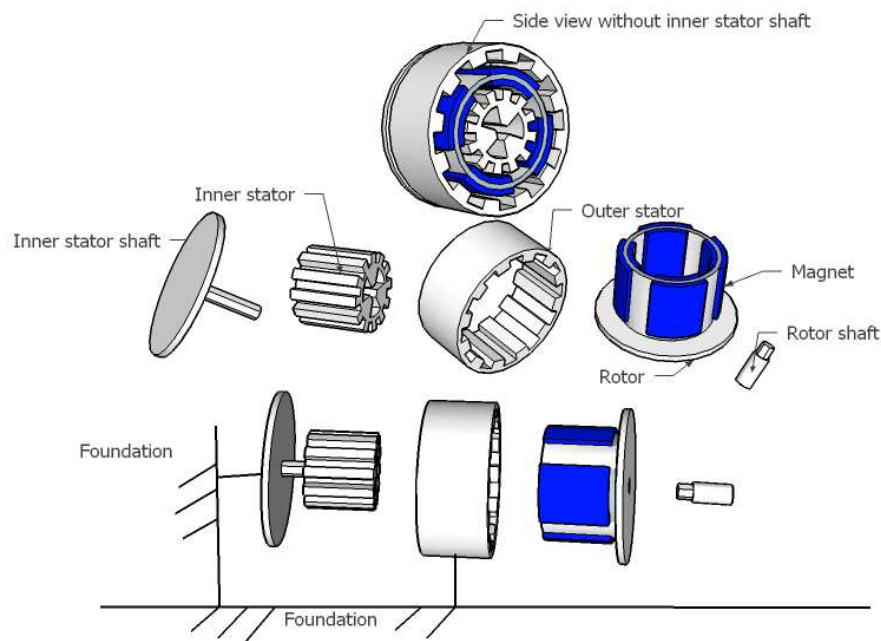
Figure 1.14 – 3D mechanical assembly illustration of a simple DSCRPMG

Fig. 1.14 shows a simple example of DSCRPMG mechanical assembling. The outer stator surface can be fixed to a foundation. Inner stator can be designed with or without shaft. One side of the inner stator is fixed to the foundation. Cup shape rotor inserts into the gap between outer stator and inner stator. The bottom of the cup rotor connected to the shaft axis which can be connected to the gear box or directly to the turbine. Ball bearing is needed to fix the rotor shaft. Ball bearing can be fixed to the same foundation as outer stator. Then the length of the

inner stator shaft and cup rotor should be relatively longer than the effective length of the two stators. The aim longer length is to left enough space for the end winding. As the rotor and inner stator are fixed with one side, the fixed side should have enough strength to support the gravity force of the other side. Therefore, the machine can't be designed too long or two small air gap. The exact limitation depends on the mechanical engineering and the characteristics of the used material. There is also possibility to fix the inner stator and rotor for two sides. However, it needs more ball bearings and more complicate mechanical assembling.

1.7   Summary

This Chapter has reviewed the tidal current energy extracting principle and introduced the up to date promising tidal current turbines. Horizontal axis turbine is the main type turbine adopted in current research and tidal current energy farm. Tidal energy technology is based on wind energy concepts. However, there are also many differences and advantages comparing to wind energy. Tidal current is predictable and sustainable. The tidal turbine has high power density, smaller size, no view impact. Those advantage make it really promising source to produce renewable energy. Like every has two sides, tidal current energy also face many difficulties such as high investment, fouling, erosion, corrosion, strong turbulence. The possible generator choice are also discussed. Many prototypes adopt induction generator because it is simple and robust such as Alstom tidal turbine, Marine Current Turbine and Andritz Hydro Hammerfest turbine. Permanent magnet generator can be also find in many hopeful projects such as the turbines of the company Open-Hydro, Tocardo, Sabella D10, Voith Hydro and Atlantis Resources. It seems like that permanent magnet generator is the trend in tidal current energy application because it is possible to avoid gear box which may cause high maintenance cost and long downtime. Some introductions of the the researched DSCRPMG are given at the last part of this Chapter.

2

DSCRPMG preliminary design and control principle

2.1 Introduction

This chapter focuses on the generator design and vector current control strategies comparison. An analytical model of a DSCRPMG is firstly presented. The generator is designed at the rated power condition with some experience machine design rules. Generator external diameters fixed and the other parameters vary with the generator outer stator bore radius in this preliminary design model. The power losses model, material cost model and thermal model are also presented.

Vector current control strategies are comprehensively studied not only in MPPT region but also in FW (Flux Weakening) region. For the above chosen generator, the output system efficiency is evaluated when it is controlled under different vector current control strategies. Converter losses are taken into consideration to calculate the output system (converter and machine) efficiency.

An control approach minimizing all machine and converter losses is developed (MSL in MPPT region and MSLCP in FW region). This approach is then applied to the above preliminary designed maximum efficiency generator and another one having lower efficiency at rated power. The global performances of both machines are compared to explain the reason why optimal machine design should take into account the predicted current frequency.

2.2   Generator preliminary design Model

2.2.1   Mathematical analysis of generator design model

Fig. 2.1 shows a part of the double stator PM generator configuration in tangent plane. PMs in inverse polarized direction are mounted on both of inside and outside surface of the cup-rotor. The cup-rotor is manufactured with ferromagnetic steel material which inherits the property of high mechanical strength and high magnetic permeability. Hence, both the inner stator and outer stator share the same rotor for torque production. The flux path will go through in parallel in the two stators. The total output torque is the summation of their torque components.
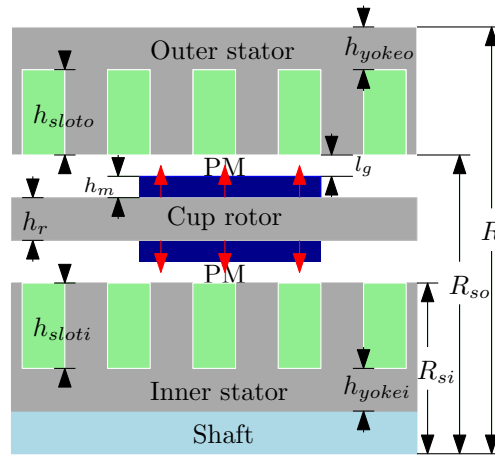
Figure 2.1 – Double stator permanent magnet machine structure

In this section, the machine design analytical model is divided in the following parts: **1). Generator main dimensions**. The generator geometry parameters (such as thickness of yoke, slot height and width, magnet thickness, air gap length and rotor thickness, phase conductor turns) are calculated based on the preliminary machine design assumptions in this part. **2). Inductance calculation**. Based on the generator main dimensions, the method for calculating the magnetizing inductance and leakage inductance are presented. **3). Copper and iron losses model**. Power losses model is used to calculate the system efficiency and winding temperature. **4). Thermal model**. The adopted thermal model is based on the generator power losses and heat dissipation surface. **5). Generator volume and mass calculation**. Generator volume and active material mass calculation provides possibility to calculate the generator cost and torque density. **6). Cost model**. Generator cost model is based on the active used material mass. A converter cost model based on the apparent power rate is also presented.

For first approximately design, some assumptions should be firstly emphasized:

— Two stators phase wingdings are star connected and independently connected to the DC-bus, line to line effective voltage $U = 690V$.

— Total rated power $P_n = 1MW$.

Symbol	Description	Value
Thermal		
h	Heat exchange coefficient	$100W/(m^2K)$
t_{iso}	Thickness of isolation	$1mm$
T_A	Ambient temperature	$20°C$
T_{max}	Admissible temperature in winding (Class F)	$155°C$
Losses		
ρ_{cu}	Resistivity of copper @ $115°C$	$2.4 \times 10^{-8}\Omega m$
k_{ec}	Eddy currents loss coefficient(M400-50A)	$0.00019293W/(kg.T^2.Hz^2)$
k_h	Hysteresis loss coefficient(M400-50A)	$0.021631W/(kg.T^2.Hz)$
Material		
d_{iron}	Density of iron(M400-50A)	$7870kg/m^3$
d_{PM}	Density of magnet	$7400kg/m^3$
d_{copper}	Density of copper	$8960kg/m^3$
C_{iron}	Specific cost of iron	$3€/kg$
C_{PM}	Specific cost of magnet	$30€/kg$
C_{copper}	Specific cost of copper	$6€/kg$
Magnet (NdFeB N35SH)		
B_r	Remanence @ $80°C$	$1.14T$
β	Magnet arc electrical open angle	0.85π
$\mu_{r,PM}$	Magnet relative permeability	1.05
H_c	Intrinsic coercive force	$876kA/m$
Converter		
$V_{0,IGBT}$	Threshold voltage of IGBT	$2V$
$V_{0,diode}$	Threshold voltage of diode	$1.7V$
$r_{d,IGBT}$	Resistance of IGBT	$1500m\Omega/A$
$r_{d,diode}$	Resistance of diode	$1000m\Omega/A$
f_{sw}	Switching frequency	$2kHz$
$B_{sw,rec}$	Switching, recovery losses factor	$3mJ/A$
Others		
μ_0	Air permeability	$4\pi \times 10^{-7}$
$P_{price/kWh}$	Price of electricity per kWh	$0.14€/kWh$
$C_{turbine}$	Turbine cost	$1M€$

Table 2.1 – Constant parameters used in the model

— Rated rotational speed $n = 21.5rpm$.

— Rated power factor $cos\varphi = 0.8$, typical value for machine preliminary design [42].

— Number of phase in each stator $q = 3$.

— Number of pole pairs $p = 40$. Inner stator and the outer stator have the same number of pole pairs.

— Number of slot per pole per phase $m = 1.25$.

— Slot fill factor $k_f = 0.65$ [43].

— External stator radius $R = 1.5m$.

— Teeth open ratio $k_t = 0.5$ (ratio between width of teeth and slot pitch).

— The fundamental peak air gap flux density $\hat{B}_g = 0.8T$.

— The outer and inner PMs thickness are identical. The outer and inner air gap length also have the same value.

— Iron type M400-50A (saturation flux density $\hat{B}_s = 1.4T$) is used. Neodymium-Iron-Boron Magnets type is N35SH $B_r = 1.14T$ @80°C. Intrinsic coercive force $H_c = 876kA/m$.

— Iron lamination factor or stacking factor is fixed as $k_{Fe} = 0.97$. Normally it is between 0.95 and 1 [44].

— Generator design and control are based on the fundamental flux density harmonic.

The constant parameters used in the analytical model are given in Table. 2.1.

In the following equations, the subscript o and i refers to outer stator and inner stator respectively. In some equations, in order to simplify the formulation, the subscribe k is used to represent the outer stator (o) or inner stator (i). Both outer stator and inner stator have similar model equations.

1). Generator main dimensions

Double stator generator can be roughly treated as a combination of two PM synchronous generators. Therefore, the total power of the generator P_n can be expressed as:

$$P_n = P_o + P_i = S_o \cos\varphi + S_i \cos\varphi \tag{2.1}$$

where S_o and S_i are outer and inner stator apparent power respectively. It is assumed that the power factors $\cos\varphi$ for inner stator and outer stator are identical. The apparent power can be expressed as:

$$S_k = qE_k I_{sk} \tag{2.2}$$

where E_k is the RMS value of the fundamental component induced EMF in a phase wingding and I_{sk} is the stator nominal RMS phase current, q is number of phase. The EMF E_k can be calculated by the following equation:

$$E_k = \frac{1}{\sqrt{2}}\omega_e k_{w1,k} N_k \psi_{PMk} \tag{2.3}$$

where ψ_{PMk} is the peak fundamental flux in air gap, N_k the number of turns per phase and ω_e the electrical rotational speed with: $\omega_e = p\omega_m$ (where ω_m is the mechanical rotational speed and p is the number of pole pair).

Three factors which influence the value of winding factor $k_{w1,k}$ are distribution factor $k_{dn,k}$, pitch factor $k_{pn,k}$ and skew factor $k_{sk,k}$ [45]. As the machine is not skewed in our design model,

the skew factor is not considered.

$$k_{dn,k} = \frac{\sin(n\pi/6)}{(Q_s/6p)\sin(np\pi/Q_s)} \tag{2.4}$$

$$k_{pn,k} = \sin(n\gamma\pi/2) \qquad \text{with} \qquad \gamma = \frac{coil \quad pitch}{pole \quad pitch} \tag{2.5}$$

In the formulation, Q_s is the number of stator slots; $Q_s = 2pqm$. m is the number of slots per pole and per phase. n represents the harmonics order which is integer number. The shorten pitch factor γ is fixed to $\frac{5}{6}$ because this value can minimize the $(6w \pm 1)^{th}$ (5,7,11,13 ...) harmonics [46]. For fundamental EMF, $n = 1$. Therefore,

$$k_{w1,k} = k_{d1,k}k_{p1,k} \tag{2.6}$$

As the inner stator and outer stator have the same number of pole pair, slot and shorten pitch factor, it is obtained that the winding factor for inner and outer stator are identical.

The stator peak fundamental flux is:

$$\psi_{PMk} = \frac{2}{\pi}\tau_{pk}L_{eff}\hat{B}_{gk} \tag{2.7}$$

where L_{eff} is the effective length of the stator lamination assembled in a stack and it is expressed as $L_{eff} = L + 2l_g$ [42, 47]. L is the length of the stator lamination. $\hat{B}_{gk}$ is the stator air gap maximum value of fundamental flux density in the air gap. It is naturally preferred to design a generator with air gap length l_g as small as possible to minimize the amount of permanent magnets needed [47]. However, when the air gap length is too small, obviously, mechanical problem will come out. In the thesis the following relation is used:

$$l_g = \frac{2R_{so}}{500} \tag{2.8}$$

The pole pitch τ_{pk} is defined by:

$$\tau_{pk} = \frac{\pi R_{sk}}{p} \tag{2.9}$$

The magnets arc defined by the angle β. Its flux density have a constant magnitude of B_e over β in the positive half cycle and $-B_e$ over β in the negative half cycle as shown in Fig. 2.2 for a surface mounted magnet rotor. The air-gap maximum fundamental flux density $\hat{B}_g$ can be obtained by using Fourier analysis as follows:

$$\hat{B}_{gk} = \frac{4}{\pi}B_{ek}\sin(\frac{\beta}{2}) \tag{2.10}$$

The value B_{ek} is deduced from the magnet thickness h_m, equivalent air gap length l_{geqk} and
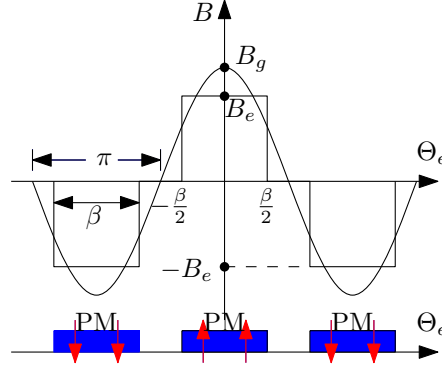
Figure 2.2 – Approximately air gap flux density for surface mounted magnet generator

permanent magnet remanence B_r [48, 49].

$$B_{ek} = \frac{B_r}{1 + \frac{l_{geqk}}{h_m}} \tag{2.11}$$

$$l_{geffk} = l_g + \frac{h_m}{\mu_{r,PM}} \tag{2.12}$$

$$l_{geqk} = l_g + (\kappa_{ck} - 1)l_{geffk} \tag{2.13}$$

κ_{ck} is the Carter's factor [50, 51]:

$$\kappa_{ck} = \frac{\tau_{toothk}}{\tau_{toothk} - \kappa_k w_{slotk}} \tag{2.14}$$

where κ_k is:

$$\kappa_k = \frac{2}{\pi} \left[\arctan(\frac{w_{slotk}}{2l_{geffk}}) - \frac{2l_{geffk}}{w_{slotk}} \ln \sqrt{1 + \frac{w_{slotk}}{2l_{geffk}}} \right] \tag{2.15}$$

w_{slotk} can be calculated as:

$$w_{slotk} = (1 - k_t)\tau_{slotk} = (1 - k_t)\frac{\pi D_k}{Q_s} \tag{2.16}$$

k_t is the teeth open ratio which is the ratio between teeth width and slot pitch. D_k is the bore diameter which equal to $2R_{sk}$.

Combining the equations Eq.2.3 and Eq.2.7, the equation Eq.2.2 can rewritten as:

$$S_k = qE_kI_{sk} = 1.11k_{w1,k}D_k^2L_{eff}\omega_m\hat{B}_{gk}A_k \tag{2.17}$$

where A_k is the ampere turns per meter or the electric specific linear load. A typical value for machine with bore diameter $D \approx 2 \sim 3m$ is around $80kA/m$. It depends on the cooling system [42]. It can be expressed as:

$$A_k = \frac{2qN_kI_{sk}}{\pi D_k} \tag{2.18}$$

For the preliminary design, A_o is considered equal to A_i. Apparent power can also be written as follows:

$$S_k = C_k D_k^2 L_{eff} \omega_m \tag{2.19}$$

The machine constant C_k is:

$$C_k = 1.11 k_{w1,k} \hat{B}_{gk} A_k \tag{2.20}$$

The power ratio of the two stator can be express as following:

$$\frac{P_o}{P_i} = \frac{S_o \cos \varphi}{S_i \cos \varphi} = \frac{C_o D_o^2}{C_i D_i^2} \tag{2.21}$$

The machine constant C_k for inner stator and outer stator can be approximately treated as identical value because the max air gap flux density for inner and outer stator is almost the same. Therefore, the power ratio of the two stators is:

$$\frac{P_o}{P_i} = \frac{R_{so}^2}{R_{si}^2} \tag{2.22}$$

From the equations Eq.2.2 and Eq.2.22, it is assumed that

$$\frac{E_o}{E_i} = \frac{R_{so}}{R_{si}} \tag{2.23}$$

and

$$\frac{I_{so}}{I_{si}} = \frac{R_{so}}{R_{si}} \tag{2.24}$$

In order to get the target EMF, the number of turns per phase N_k is calculated by:

$$N_k = \frac{E_k}{4.44 k_{w1,k} f \psi_{PMk}} \tag{2.25}$$

where f is the generator frequency. The number of conductors per slot N_{ck} is:

$$N_{ck} = \frac{N_k}{pm} \tag{2.26}$$

As the slot shape is considered as rectangular, For outer stator, the height of slot is:

$$h_{sloto} = R - h_{yoke} - R_{so} \tag{2.27}$$

where h_{yokeo} is the thickness of outer stator yoke and R is the out generator radius. It is assumed that the $h_{sloti} = h_{sloto}$. Therefore, the cross section of copper conductor S_{cuk} can be calculated as:

$$S_{cuk} = \frac{w_{slotk} h_{slotk} k_f}{N_{ck}} \tag{2.28}$$

with k_f the slot fill factor. w_{slotk} is the width of the slot.

The outer stator current density in the copper wire is:

$$J_k = \frac{I_{sk}}{S_{cuk}} \tag{2.29}$$

The minimum thickness of yoke h_{yokeo} is normally decided to avoid excessive flux saturation [42].

$$(h_{yokeo})_{min} = \frac{\hat{\psi}_{mo}}{2Lk_{Fe}\hat{B}_{ys}} = \frac{\frac{2}{\pi}\tau_{po}L_{eff}\hat{B}_g}{2Lk_{Fe}\hat{B}_{ys}} \tag{2.30}$$

$\hat{B}_{ys}$ is the iron flux saturation value. k_{Fe} is the lamination factor or stacking factor. For core material M400-50A, $\hat{B}_{ys} = 1.4T$. Hence,

$$(h_{yokeo})_{min} \approx 0.2\tau_{po} \tag{2.31}$$

In the generator preliminary design stage, the following relationship is applied:

$$h_{yokeo} = 0.3\tau_{po} \tag{2.32}$$

The thickness of cup rotor h_r is designed as two times thickness of h_{yokeo} in order to avoid saturation in the rotor.

$$h_r = 2h_{yokeo} \tag{2.33}$$

Inner stator radius R_{si} can be obtained:

$$R_{si} = R_{so} - 2l_g - 2h_m - h_r \tag{2.34}$$

Applying the same process to calculate the inner stator dimension parameters, the inner stator pole pitch is:

$$\tau_{pi} = \frac{\pi R_{si}}{p} \tag{2.35}$$

Inner yoke thickness:

$$h_{yokei} = 0.3\tau_{pi} \tag{2.36}$$

Inner stator flux linkage:

$$\psi_{PMi} = \frac{2}{\pi}\tau_{pi}L_{eff}\hat{B}_{gi} \tag{2.37}$$

2). Inductance calculation

The inductance is one of the most important information that generator designers should provide it to power conversion and control designers.

The direct-axis synchronous inductance L_{dk} consists of the direct-axis magnetizing induc-

tance L_{mdk} and the leakage inductance $L_{s\delta k}$:

$$L_{dk} = L_{mdk} + L_{s\delta k} \tag{2.38}$$

The direct-axis magnetizing inductance L_{mdk} is defined as the phase inductance due to resultant *mmf* from excitation in all phases. The difference between L_{mdk} and the self-inductance is that the resultant *mmf* in a three-phase machine is equal to 1.5 times the value of single-phase *mmf* [45]. The self inductance is expressed as:

$$L_{sk} = \frac{4}{\pi} \mu_o \frac{L_{eff} R_{sk}}{l_{geqk} + h_m} \left[\frac{k_{w1,k} N_k}{p} \right]^2 \tag{2.39}$$

where μ_o is the permeability of vacuum. The calculation detail are discussed in the books [42, 52]. The direct-axis magnetizing inductance L_{mdk} is 1.5 times self inductance in three phase generator, thus:

$$L_{mdk} = \frac{6}{\pi} \mu_o \frac{L_{eff} R_{sk}}{l_{geqk} + h_m} \left[\frac{k_{w1,k} N_k}{p} \right]^2 \tag{2.40}$$

The second part of d-axis inductance is the leakage inductance $L_{s\delta k}$ which normally is neglected and is often considered as a negative phenomenon by the generator designer. However, leakage flux in some cases has a positive role also. For instance, if the target is to filter the motor current of a pulse-width-modulated (PWM) AC inverter drive, the stator flux leakage of the machine can be increased intentionally. In addition, for big number of pole pair machine, the height of slot normally will much bigger than the width of slot, therefore, the leakage inductance can't be neglected. Finally, leakage inductance can influence the machine flux weakening region and even influence the efficiency. It is important to design a machine with suitable inductance value. According to the electrical motor design tradition, leakage inductance $L_{s\delta k}$ mainly consist of two important parts [50]:

— slot leakage inductance L_{slotk};

— tooth tip leakage inductance L_{toothk};

The leakage inductance can be written in terms of specific permeance coefficients with the dominant leakage flux paths of the stator. Hence,

$$L_{s\delta k} = L_{slotk} + L_{toothk} = \frac{4q}{Q_s} \mu_o L_{eff} N_k^2 (\lambda_{sk} + \lambda_{tk}) \tag{2.41}$$

λ_{sk} is the slot leakage flux specific permeance coefficient. For the double-layer winding slot shape showed in Fig. 2.3, it can be expressed as:

$$\lambda_{sk} = k_1 \frac{y_1 - y_4}{3x_1} + k_2 \left(\frac{y_2}{x_1} \right) + \frac{y_5}{4x_1} \tag{2.42}$$

The factors k_1 and k_2 can also be calculated with the aid of the amount of short pitching ϵ given

by

$$\epsilon = 1 - \gamma \tag{2.43}$$

γ is the ratio between coil pitch and pole pitch. Juha Pyrhönen [42] gives out the equation to calculate the factors k_1 and k_2 for three phase winding and two phase winding.

$$k_1 = 1 - \frac{9}{16}\epsilon \qquad \text{and} \qquad k_2 = 1 - \frac{3}{4}\epsilon \tag{2.44}$$

Figure 2.3 – Double-layer winding slot tooth dimensions

The tooth tip leakage inductance is determined by the magnitude of leakage flux flowing in the air gap outside the slot opening. The tooth tip leakage inductance permeance factor λ_t is

$$\lambda_{tk} = k_2 \frac{5 \left(\frac{l_{gefk} + h_m}{x_1} \right)}{5 + 4 \left(\frac{l_{gefk} + h_m}{x_1} \right)} \tag{2.45}$$

where $k_2 = 1 - \frac{3}{4}\epsilon$ is calculated from equation Eq.2.44.

The studied machine has surface mounted PM, hence, the *d-axis* and *q-axis* inductance are the same (the *d-axis* and *q-axis* magnetic air gap length are the same). The inductance calculation of inner stator machine is similar to the outer stator one.

3). Copper and iron losses model

1. **Copper (winding in stator) losses**

   By neglecting both skin effects and eddy currents in the conductor (copper) and with number of turns N_{ck} in one slot, copper cross-section S_{cuk}, the armature winding resistance for one phase can be expressed in the form:

   $$R_{cuk} = \frac{2pmN_{ck}K_{Lk}L\rho_{cu}}{S_{cuk}} \tag{2.46}$$

   ρ_{cu} is the electrical resistivity of copper. It will vary with the temperature and it increase obviously as the temperature increases. In machine design, engineers usually take the

value ρ_{cu} equal to

$$\rho_{cu,T=T_1} = \rho_{cu,T=T_A} \times \frac{(235 + T_1)}{(235 + T_A)} \tag{2.47}$$

T_A and T_1 are ambient temperature and the average temperature in winding respectively. From standard IEC 60034-1, for thermal class F [53], $\rho_{cu,T=T_A} = 1.75 \times 10^{-8}\Omega/m$, where $T_A = 20°C$ and $T_1 = 115°C$.

End winding coefficient K_{Lk} can be calculated as:

$$K_{Lk} = \left[L + 6\pi \left(R_{sk} + \frac{h_{slotk}}{2} \right) / Q_s \right] / L \tag{2.48}$$

Therefore, the total copper losses in the stator k is:

$$P_{culossk} = 3I_{sk}^2 R_{cuk} \tag{2.49}$$

2. **Iron (core) losses**

For the iron losses, the principle of separation of losses is applied, including both hysteresis losses and eddy current losses. Hysteresis losses in the core material is the energy expended to magnetize and demagnetize the core. The eddy currents are currents that are induced in the electric conducting core material when it is exposed to a varying magnetic field. These currents causes resistive losses in the core material which can be minimized either by increasing the resistance in the iron material and/or by laminating the core material [54].

The total core losses should be calculated separately in the part of yoke and teeth because their flux density are different. Iron losses for a core with mass M under a sinusoidal flux density is calculated using the following classical formula [51, 54, 55]:

$$P_{iron} = (k_{ec}f^2 + k_h f)M\hat{B}_m^2 \tag{2.50}$$

where f is the operation frequency. $\hat{B}_m$ is the maximum flux density pass through the core. k_{ec} and k_h are the specific loss coefficients for eddy currents and hysteresis, respectively. Their value can be approximately estimated from the data sheet of core material [56]. The date sheet normally gives out the unit power losses for a certain core type under a certain frequency and flux density. Then, curve fitting method can be used to get those loss coefficient. Fig. 2.4 shows the loss curve fitting for generally used core type M400-50A. By using the polynomial equation Eq.2.50, it can be found that the best fitting curve which is almost superposition with the manufacture provides data points. The loss coefficients for core type M400-50A are found as $k_{ec} = 0.00019293 W/(kg.T^2.Hz^2)$ and $k_h = 0.021631 W/(kg.T^2.Hz)$. Losses in both the yoke ($P_{ironyokek}$) and teeth ($P_{ironteethk}$) have been considered. The transverse component of flux density in the yoke ($\hat{B}_{myokek}$), as
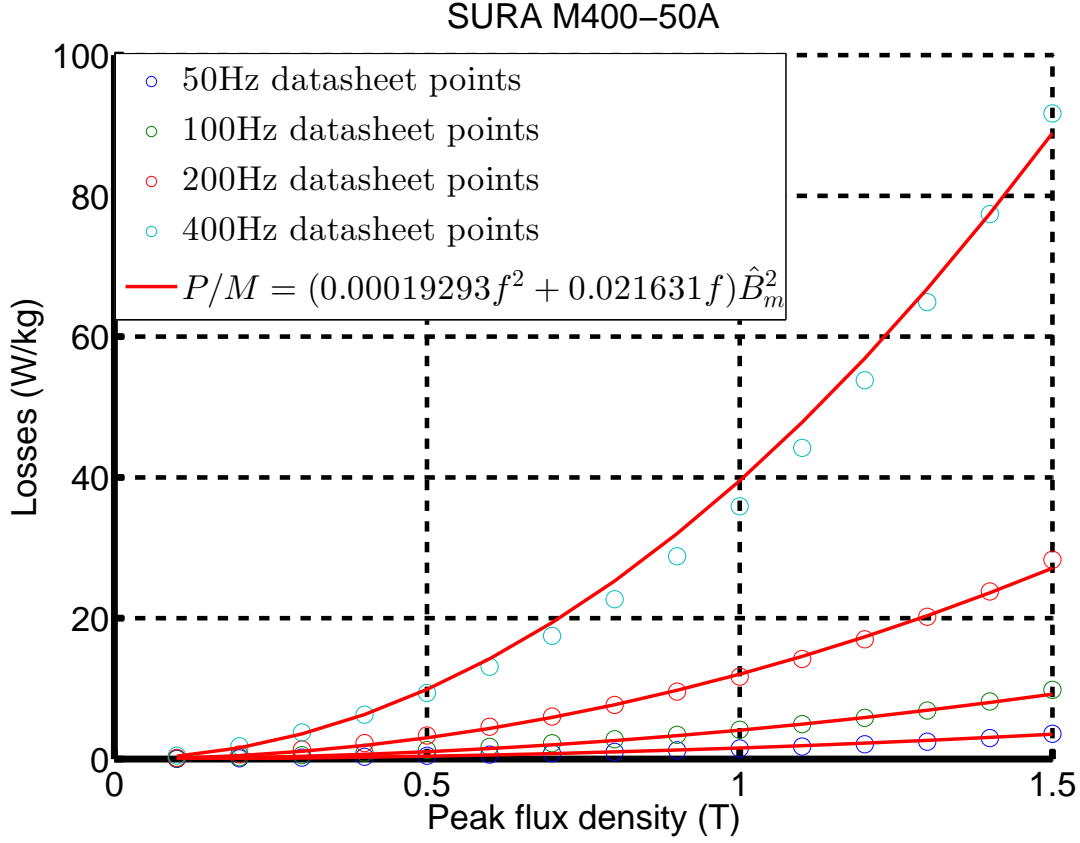
Figure 2.4 – SURA-M400-50A loss curve fitting

well as radial component in the teeth ($\hat{B}_{mteethk}$), have been incorporated and calculated using Gauss's Law [57]:

$$\hat{B}_{myokek} = \frac{R_{sk}L_{eff}\hat{B}_{gk}}{Lk_{Fe}(H_{yokeo})p} \tag{2.51}$$

$$\hat{B}_{mteethk} = \frac{\hat{B}_{gk}}{k_t} \tag{2.52}$$

The total iron losses are the sum of the two parts, $P_{ironyokek}$ and $P_{ironteethk}$, so the iron losses in the outer stator are:

$$\begin{aligned}
P_{irontotalk} =& P_{ironyokek} + P_{ironteethi} \\
=& (k_{ec}f^2 + k_h f)(\hat{B}_{myokek}^2 M_{yokek} + \hat{B}_{mteethk}^2 M_{teetho})
\end{aligned} \tag{2.53}$$

4). Thermal model

It is important to understand the principle and complexities of thermal modeling of electric machines. The temperature rise of the machine is due to several losses components including copper losses, iron losses and frictional losses. The heat can be radiated naturally or with cooling system. The complexity of thermal modeling is due to the materials which are used to

design machine including iron type, copper, isolation paper, slot shape and cooling system. In cooling system, fluid flow phenomenon, *i.e.* laminar, vortex or turbulent, has a great influence on convection heat transfer. Therefore, it's very difficult to have a very precise thermal model [49,50,58]. In this thesis, a simple thermal model is used to evaluate the temperature in winding and iron.

The heating of conductors in one slot is modeled by the principle of heat conduction [59]. The ratio between unit copper losses p_{cuk} in one outer slot and a unit length L_u can be expressed as

$$\frac{p_{cuk}}{L_u} = \frac{\rho_{cu}}{S_{cuk}N_{ck}}(N_{ck}I_{sk})^2 = \rho_{cu}J_k A_{mk} \tag{2.54}$$

with $I_{sk} = J_k S_{cuk}$. A_{mk} is *mmf* in one slot and it equals $N_{ck}I_{sk}$. The heat transfer in the air gap is neglected and it is assumed that the temperature is uniform in iron and winding.

The heating surface for a unit length in one slot is $S_{unitk} = (2h_{slotk} + w_{slotk})L_u$. The heating in conductors can expressed as:

$$\Delta\theta_{cuk} = R_{th}\frac{p_{cuk}}{L_u} = \frac{1}{\lambda_e}\frac{t_{is}}{\frac{S_{unitk}}{L_u}}\frac{p_{cuk}}{L_u} \tag{2.55}$$

where R_{th} is thermal resistance of a unit length isolation. λ_e is the thermal conductivity of isolation. t_{is} is the thickness of isolation, considered equal to $1mm$ [47]. Combining Eq.2.54, Eq.2.55 can be rewritten as:

$$\Delta\theta_{cuk} = KA_{mk}J_k\frac{t_{is}}{2h_{slotk} + w_{slotk}} \tag{2.56}$$

The coefficient $K = \frac{\rho_{cu}}{\lambda_e}$. It varies between 0.25×10^{-6} and 0.6×10^{-6} (SI) which depends on the material of isolation [60,61]. In this thesis, $K = 0.6 \times 10^{-6}$ is used. This equation indicates that the heating of conductor is proportional to the product of $A_{mk}J_k$.

For the thermal model of stator iron , the temperature is assumed uniform. The losses to be evacuated are the copper losses and iron losses. The friction losses are neglected. The heating of stator iron can be expressed as

$$\Delta\theta_{ironk} = \frac{1}{h}\frac{P_{culossk} + P_{irontotalk}}{S_{dk}} \tag{2.57}$$

where $h(W/m^2K)$ is the heat exchange coefficient. For air natural convection and radiation, $h = 10W/m^2K$; for air forced convection, h is between $50 \sim 300W/m^2K$ [50]. The used value of h is given in Table. 2.1. S_{dk} is the heat exchanging surface of inner and outer stator, and S_{do} and S_{di} can be calculated by:

$$S_{do} = 2\pi RL + 2\pi(R^2 - R_{so}^2) \tag{2.58}$$

$$S_{di} = 2\pi R_{shaft} L + 2\pi (R_{si}^2 - R_{shaft}^2) \tag{2.59}$$

where $R_{shaft} = R_{si} - h_{sloti} - h_{yokei}$. $2\pi (R^2 - R_{so}^2)$ and $2\pi (R_{si}^2 - R_{shaft}^2)$ represent the surface of two sides of outer and inner stator respectively.

The temperature of the winding T_{cuk} is the sum of temperature in conductor $\Delta\theta_{cuk}$, stator iron $\Delta\theta_{ironk}$ and ambient temperature T_A. T_A is normally around $40°C$ (IEC 60034-1). However, for tidal energy application, $T_A = 20°C$ is taken because the generator is operated under the sea water.

$$T_{cuk} = \Delta\theta_{cuk} + \Delta\theta_{ironk} + T_A \tag{2.60}$$

The temperature of stator iron

$$T_{ironk} = \Delta\theta_{ironk} + T_A \tag{2.61}$$

5). Generator volume and mass calculation

In this part the material volume and mass for the active parts of the generator is calculated. The symbol d here is the density of the materials, not the resistivity. The subscribe symbol indicates the relative material. V represents volume and M means Mass. When calculating the total volume of generator, the end winding length is not considered.

$$V_{PM} = 2ph_m L\beta\tau_{po} + 2ph_m L\beta\tau_{pi} \tag{2.62}$$

$$M_{PM} = d_{PM} V_{PM} \tag{2.63}$$

$$V_{copper} = 2qpm N_{co} k_{Lo} L S_{cuo} + 2qpm N_{ci} k_{Li} L S_{cui} \tag{2.64}$$

$$M_{copper} = d_{copper} V_{copper} \tag{2.65}$$

$$V_{teetho} = 2pqm w_{sloto} h_{sloto} L k_{Fe} \tag{2.66}$$

$$M_{teetho} = d_{iron} V_{teetho} \tag{2.67}$$

$$V_{teethi} = 2pqm w_{sloti} h_{sloti} L k_{Fe} \tag{2.68}$$

$$M_{teethi} = d_{iron} V_{teethi} \tag{2.69}$$

$$V_{yokeo} = \pi \left[R^2 - (R - h_{yokeo})^2 \right] L k_{Fe} \tag{2.70}$$

$$M_{yokeo} = d_{iron} V_{yokeo} \tag{2.71}$$

$$V_{yokei} = \pi \left[(R_{si} - h_{sloti})^2 - (R_{si} - h_{sloti} - h_{yokei})^2 \right] L k_{Fe} \tag{2.72}$$

$$M_{yokei} = d_{iron} V_{yokei} \tag{2.73}$$

$$V_{rotor} = \pi \left[(R_{so} - h_m - l_g)^2 - (R_{si} + h_m + l_g)^2 \right] L k_{Fe} \tag{2.74}$$

$$M_{rotor} = d_{iron} V_{rotor} \tag{2.75}$$

$$M_{iron} = M_{rotor} + M_{yokei} + M_{yokeo} + M_{teethi} M_{teetho} \tag{2.76}$$

$$V_{generator} = \pi R^2 L \tag{2.77}$$

$$M_{generator} = M_{PM} + M_{copper} + M_{iron} \tag{2.78}$$

6). Cost model

The material cost of generator is estimated from the weights of active parts including copper, iron and magnets.

$$C_{generator} = C_{PM} M_{PM} + C_{copper} M_{copper} + C_{iron} M_{iron} \tag{2.79}$$

where C_{PM}, C_{copper} and C_{iron} are the specific cost of the material permanent magnets, copper and iron respectively. Those value are given in Table. 2.1.

For the cost of converter, most works suggest that it is based on the apparent rated power. The majority converter cost model is obtained by using curve fitting method to the manufacture data. For the converter used for MW range machine, the cost model

$$C_{conv} = 6.3 S_{conv}^{0.7} \tag{2.80}$$

is well suited for the cost estimation [62]. The unit of S_{conv} is VA. This three phase AC-DC-AC converter cost model include the cost of auxiliary systems, such as modules, drivers, filters, control circuit and processor.

2.2.2 Preliminary design results

In this section, we will discuss how the generator parameters changing with the generator bore radius R_{so}(or called air gap radius) at rated power. This parameter has great importance for machine design. A small R_{so} variation can lead to significant changes of the efficiency, cost, inductance and temperature of the machine. Furthermore, the variation of inductance will lead to changing of generator control performance and it will be addressed in the next part. For a given bore radius R_{so} value, the generator parameters can be calculated from the Table. 2.2. It is noticed that all the other parameters will vary with the bore radius R_{so} in our preliminary design stage. Table. 2.1 gives out the constant parameters used in the analytical model and the nominal power is always keep at $1MW$.

Fig. 2.5 is the generator efficiency and losses plotted as a function of the bore radius R_{so}. Because the machine outer radius R, the ratio between pole pitch and thickness of yoke are fixed, the smaller R_{so} results bigger height of slot. As a consequence, the current density will be smaller. The iron losses are much bigger than copper losses in the small R_{so} region. In the higher R_{so} value region, copper losses become the dominant losses of the generator. That can

Dimensions	Outer stator	Inner stator
Pole pitch	$\tau_{po} = \frac{\pi R_{so}}{p}$	$\tau_{pi} = \frac{\pi R_{si}}{p}$
Slot pitch	$\tau_{sloto} = \frac{2\pi R_{so}}{Q_s}$	$\tau_{sloti} = \frac{2\pi R_{si}}{Q_s}$
Yoke thickness	$h_{yokeo} = 0.3\tau_{po}$	$h_{yokei} = 0.3\tau_{pi}$
Height of slot	$h_{sloto} = R - h_{yokeo} - R_{so}$	$h_{sloti} = h_{sloto}$
Width of slot	$w_{sloto} = (1 - k_t)\tau_{sloto}$	$w_{sloti} = (1 - k_t)\tau_{sloti}$
Air gap length	$l_g = \frac{2R_{so}}{500}$	
Magnet thickness	Obtain h_m from Eq.2.11 to Eq.2.15	
Cup rotor thickness	$h_r = 2h_{yokeo}$	
Inner stator radius	$R_{si} = R_{so} - 2l_g - 2h_m - h_r$	
Generator length	Eq.2.19 and Eq.2.20	

Table 2.2 – Analytical expressions for the machines basic dimensions

be explained by the increasing of current density as Fig. 2.6 shows. When the iron losses and
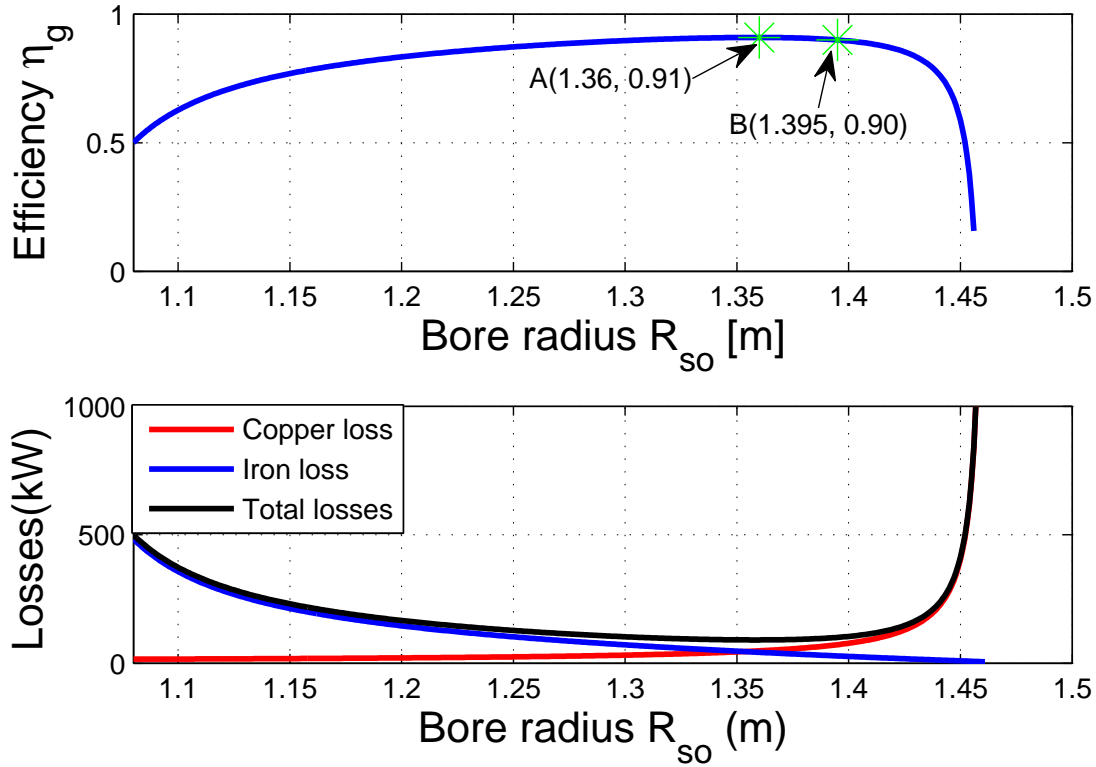
Figure 2.5 – Efficiency and losses variation

copper losses have across point, the generator achieves maximum efficiency. This generator is named as generator "A". In order to understand better what parameters changed because of the changing of R_{so}, we chose another generator and call it as generator "B". The R_{so} of generator "B"($1.395m$) is $35mm$ bigger than that of generator "A"($1.36m$). The efficiency of generator "A" is 1% bigger than that of generator "B". However, the generator "B" is $23k€(-18.7\%)$ less expensive than generator "A", shown in Fig. 2.7.

In figure Fig. 2.8, the length of generator is plotted as a function of bore radius R_{so}. It shows
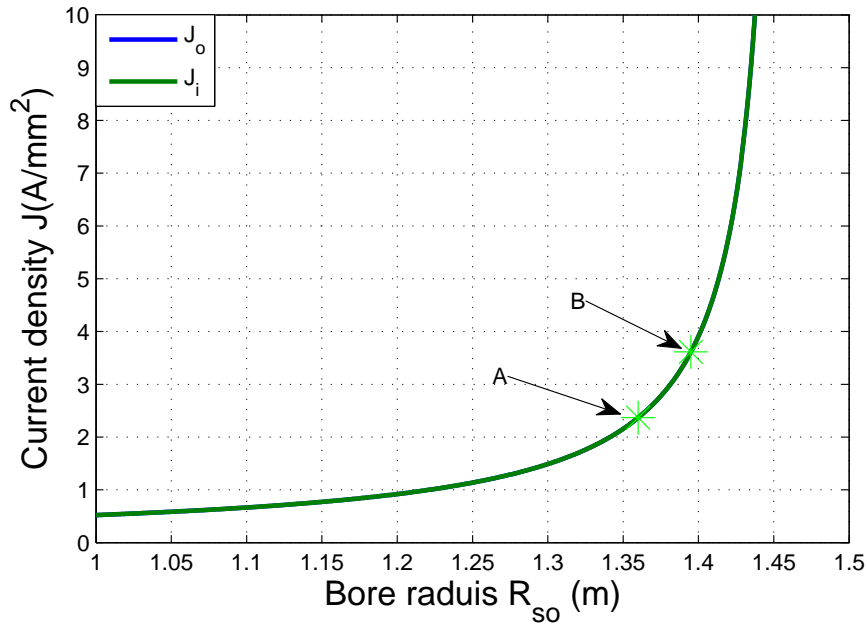
Figure 2.6 – Current density varying with R_{so}
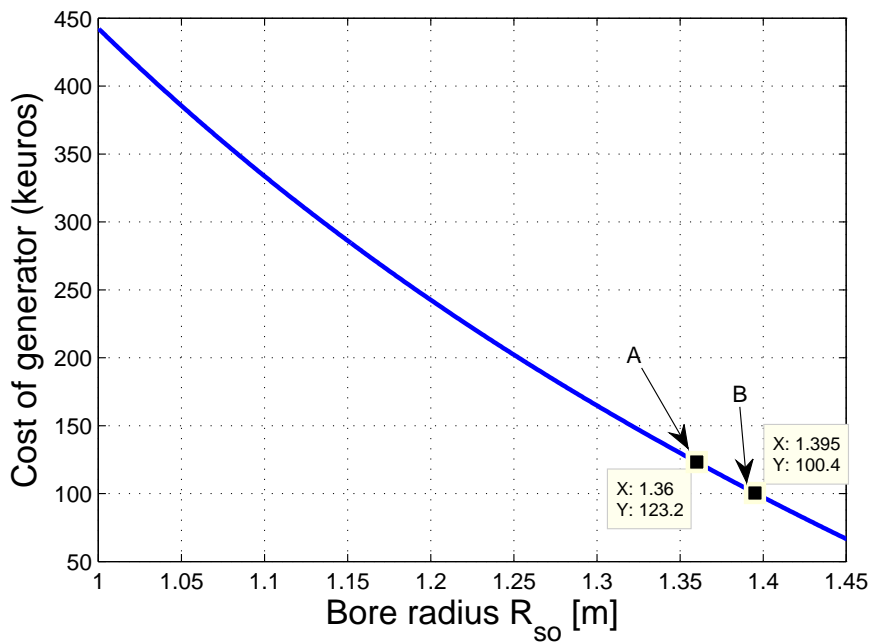
Figure 2.7 – Cost of generator varying with R_{so}

that the generator length will decrease with the increasing of R_{so}. This figure also reveals the basic principle of machine design that the length L and the bore radius R_{so} has inverse proportion relationship. From the length comparison of the two generator, it is known that the torque active mass density and torque volume density of generator "B" will be bigger than that of generator "A". They are illustrated by the Fig. 2.9 and Fig. 2.10 respectively. From the Fig. 2.5 and Fig. 2.9, it can be seen that R_{so} is a parameter which needs to be optimized. Higher
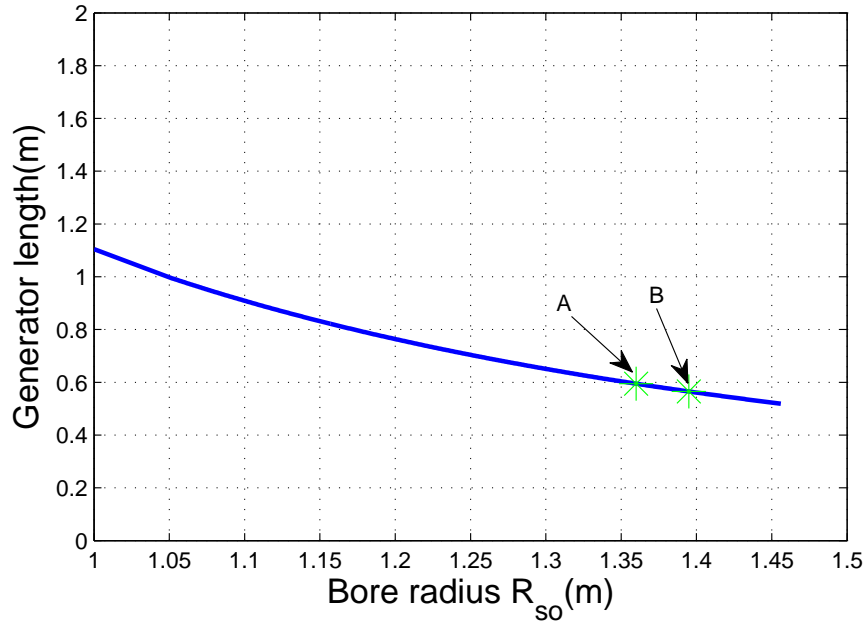
Figure 2.8 – Generator length varying with R_{so}
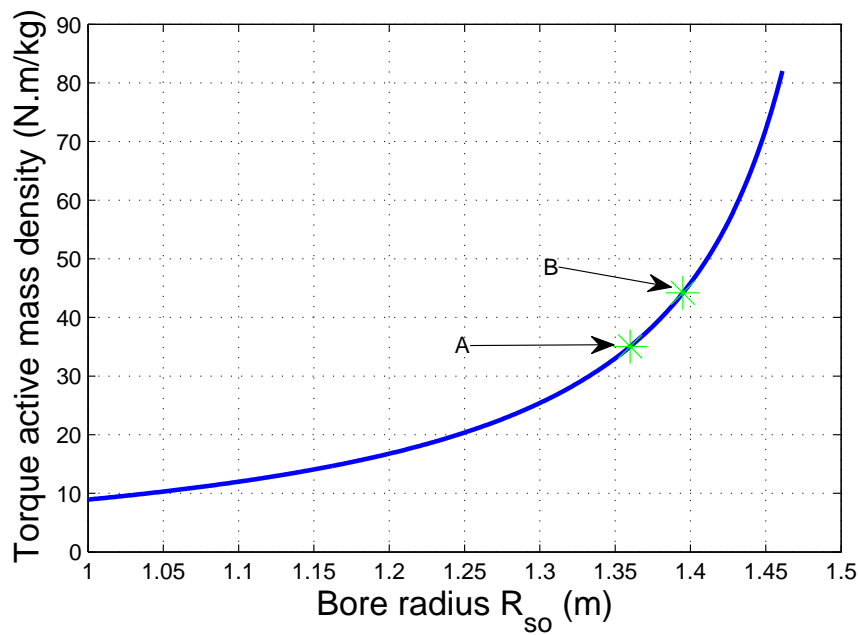
Figure 2.9 – Torque active mass density

torque active mass density machine will has worse efficiency. The optimal bore radius R_{so} should be a compromise result between efficiency and torque active mass density.

In addition, the generator bore radius R_{so} changing will lead to the generator inductance varying as shown in Fig. 2.11. This figure shows the outer stator inductance varying trends. For the inner stator, the inductance varying trends has the same conclusion as outer stator. The total inductance will decrease with the increasing of bore radius R_{so}. This decreasing is caused by the decreasing of leakage inductance. As we discussed before, the smaller R_{so} leads to bigger
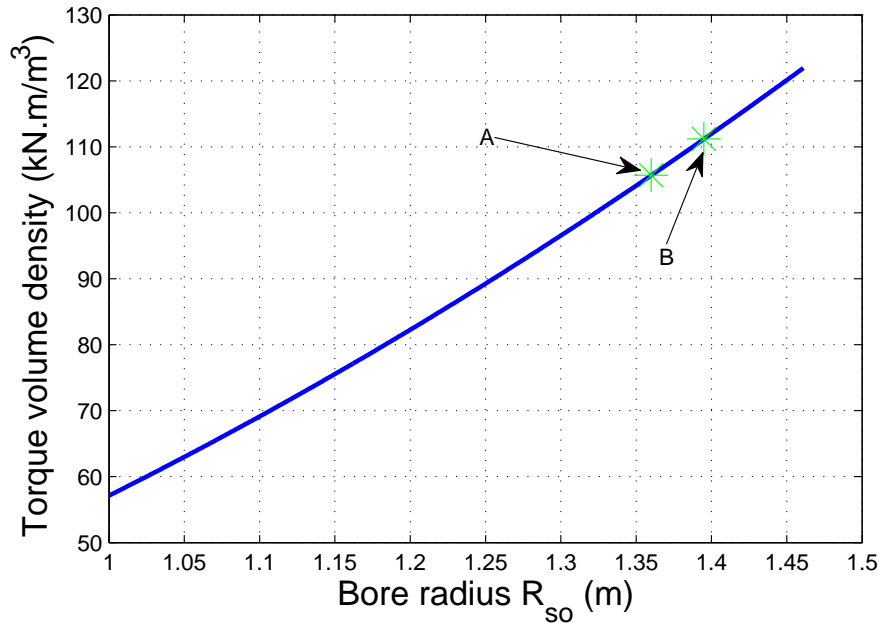
Figure 2.10 – Torque volume density
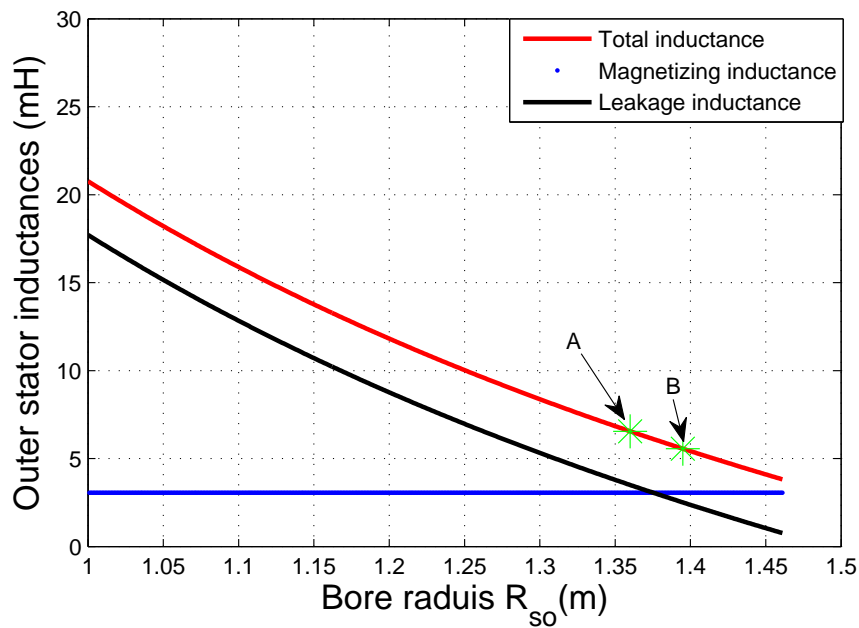
Figure 2.11 – Inductance varies with the outer bore radius R_{so}

height of slot h_{sloto}. The smaller R_{so} can also lead to a bigger ratio between the height of slot and width of slot. Fig. 2.12 shows the inductance as a function of the ratio between the height of slot and width of slot. When the ratio is bigger than 6, leakage inductance becomes bigger than the magnetizing inductance of the generator. When this ratio is very small, around or less 1, the leakage inductance can be neglect. The leakage inductance should be taken into account to analyze the generator performance. It is suggested that this ratio should be less than 10 for the mechanical constrains [43]. The generator "A" has bigger height to width slot ratio, hence,
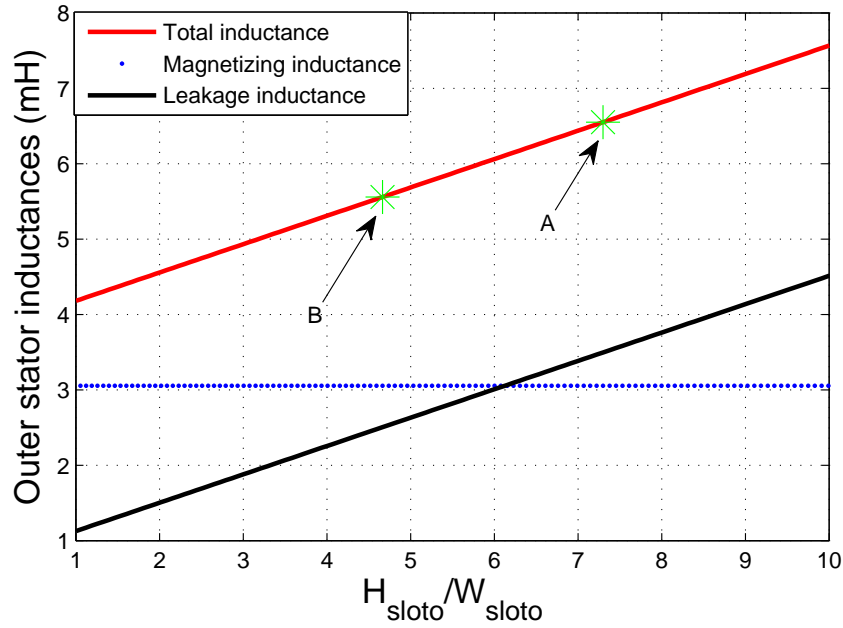
Figure 2.12 – Inductance varies with the ratio between slot height and slot width
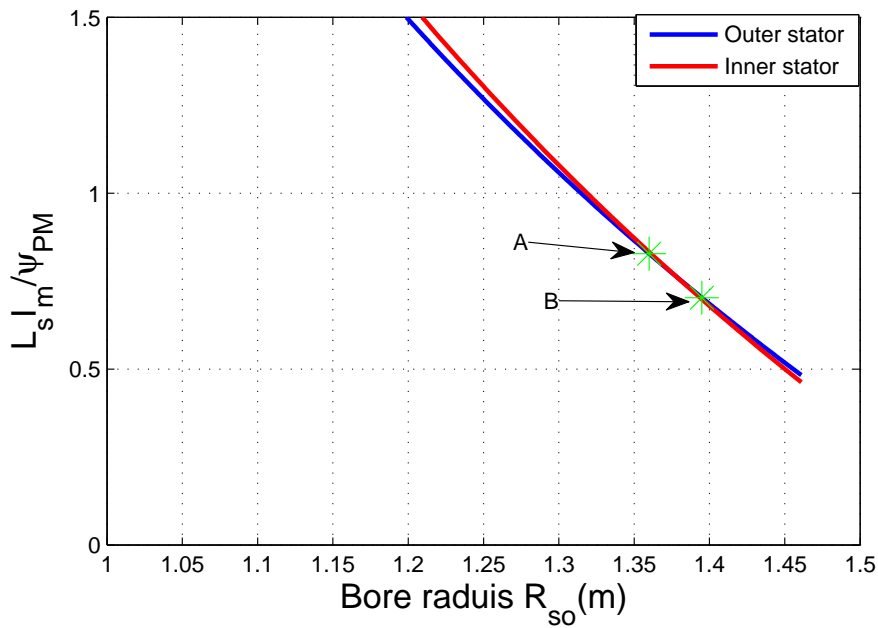
Figure 2.13 – Ratio between armature and permanent magnet flux linkage

the inductance of generator "A" is bigger than that of generator "B" both for inner and outer stator inductance.

In Fig. 2.13, the ratio between armature flux linkage $L_s I_m$ and permanent flux linkage ψ_{PM} is plotted as a function of R_{so}. This ratio is also called the pu reactance (X_{pu}). It indicates the capability of flux weakening. When this value is equal or bigger than 1, theoretically, the machine can achieve infinite speed by flux weakening control [63]. Bigger inductance machine have stronger capability of flux weakening, however, the power factor of the machine
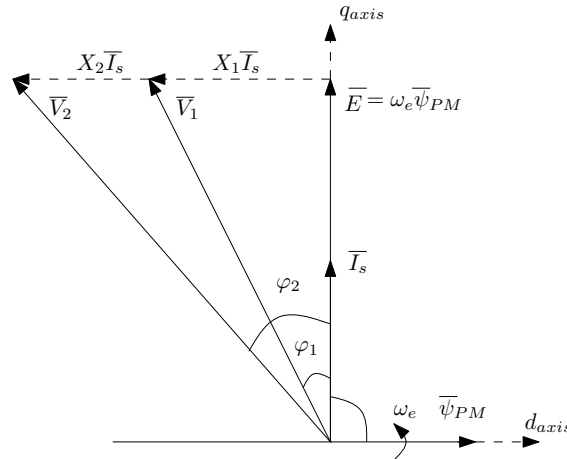
Figure 2.14 – Phasor-diagram for PM machine with different inductance
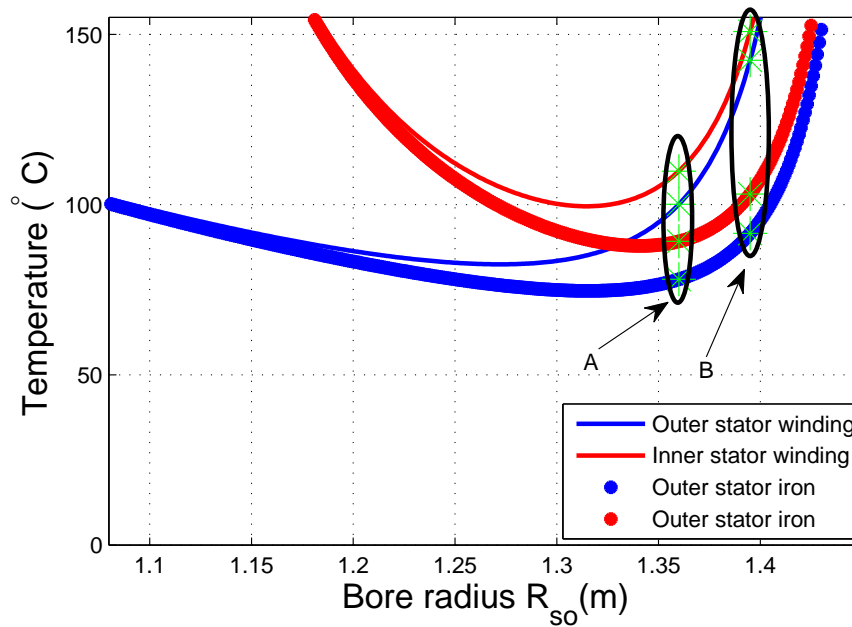
Figure 2.15 – Iron and winding temperature varying with R_{so}

will be smaller. Fig. 2.14 shows the phase diagram of two machines with different inductance ($X_1 < X_2$) and same magnet flux linkage ψ_{PM} in steady state. In this phase diagram, the resistance influence is neglected. For bigger inductance, the terminal voltage is bigger and the angle between the current and terminal voltage is also better. It means that bigger inductance machine will has bigger iron losses and smaller power factor. However, as the needed terminal voltage is bigger, the capability of flux weakening is also stronger. The detail influence of this phenomenon will be developed in the next section.

Fig. 2.15 shows the generator inner and outer stator winding and iron temperature variation with R_{so}. In the small R_{so} region, the winding temperature and iron temperature is almost the same because the copper losses is relatively small as shown in Fig. 2.5. When the copper losses become the dominant losses of the generator in big R_{so} region, the temperature of winding is

always higher than the iron one. When R_{so} is bigger than $1.4m$, the inner and outer winding temperature is rising over than $155°C$ which is the machine design limit temperature for Class F. Through our design model, we know that the rated power of inner stator is smaller than outer stator. However, from this figure, it can be seen that the temperature of inner stator is always higher than outer stator. That's because the inner stator has much smaller heat transfer surface than outer stator. It means the cooling system of DSCRPMG should be carefully designed for inner stator. This characteristic is regarded as a disadvantage of double stator permanent magnet machine by some author [64, 65].

	A	B
Efficiency	🙂	🙁
Cost	🙁	🙂
Torque mass density	🙁	🙂
Torque volume density	🙁	🙂
Flux weakening capability	🙂	🙁
Power factor	🙁	🙂
Winding temperature	🙂	🙁

Table 2.3 – A and B generator performance comparison at rated power

Table. 2.3 summarizes the performance of A and B generators. It indicates that the generator which has better efficiency, better winding temperature margin maybe worse for cost, torque density, flux weakening capability and power factor. In order to design a generator which has the characteristics of satisfying the temperature limitation, acceptable power factor, strong enough flux weakening capability, high efficiency and relatively low cost, the bore radius R_{so} can't be chosen with a simple standard such as maximum efficiency. In conclusion, generator parameters design is a compromised process. It's impossible to design a machine with best efficiency and low cost at the same time. In the next section, different control strategies will be applied to the generator "A" to analyze how the vector current control strategies influence the performance of the machine for tidal energy application.

2.3 Mathematical modeling of double stator permanent magnet machine

2.3.1 DSCRPMG model in rotating reference frame

Based on the space vector theory, sinusoidal abc frame can be decomposed into two components perpendicular to each other in the stationery $\alpha\beta0$ reference frame, where the α axis is

aligned with vector a and the β axis is leading the α axis by 90 degrees. For balanced three phase system, there is on zero sequence component. Through this transformation, the three axis time variables in abc stationery frame can be equivalently treated as two axis time variables in $\alpha\beta0$ stationery frame:

$$f_{\alpha\beta0} = \mathbf{T}_{abc \to \alpha\beta0} f_{abc} \tag{2.81}$$

where the transformation matrix $\mathbf{T}_{abc \to \alpha\beta0}$ is written as:

$$\mathbf{T}_{abc \to \alpha\beta0} = \frac{2}{3} \begin{bmatrix} 1 & -\frac{1}{2} & -\frac{1}{2} \\ 0 & \frac{\sqrt{3}}{2} & -\frac{\sqrt{3}}{2} \\ \frac{1}{2} & \frac{1}{2} & \frac{1}{2} \end{bmatrix} \tag{2.82}$$

This transformation is known as the Clarke Transformation. Reversely, a vector can be converted from the $\alpha\beta0$ stationery reference frame to the three-phase abc stationery reference frame by the following equation,

$$f_{abc} = \mathbf{T}_{\alpha\beta0 \to abc} f_{\alpha\beta0} \tag{2.83}$$

where the transformation matrix $\mathbf{T}_{\alpha\beta0 \to abc}$ is the inverse matrix of $\mathbf{T}_{abc \to \alpha\beta0}$,

$$\mathbf{T}_{\alpha\beta0 \to abc} = \begin{bmatrix} 1 & 0 & 1 \\ -\frac{1}{2} & \frac{\sqrt{3}}{2} & 1 \\ -\frac{1}{2} & -\frac{\sqrt{3}}{2} & 1 \end{bmatrix} \tag{2.84}$$

It is necessary to point out that three-phase voltage, current, flux linkage and inductance in an AC rotating machine still remain dependent of rotor position and time variation in the $\alpha\beta0$ reference frame. The $dq0$ rotating reference frame is then introduced to transfer the sinusoidal variables in the stationery reference frame into variables independent of the rotor position of the electric machine.

$$f_{dq0} = \mathbf{T}_{\alpha\beta0 \to dq0} f_{\alpha\beta0} \tag{2.85}$$

where the transformation matrix $\mathbf{T}_{\alpha\beta0 \to dq0}$ is:

$$\mathbf{T}_{\alpha\beta0 \to dq0} = \begin{bmatrix} \cos\theta & \sin\theta & 0 \\ -\sin\theta & \cos\theta & 0 \\ 0 & 0 & 1 \end{bmatrix} \tag{2.86}$$

Similarly, the transformation from the dq0 rotating reference frame to the $\alpha\beta0$ stationery reference frame is expressed as,

$$f_{\alpha\beta0} = \mathbf{T}_{dq0 \to \alpha\beta0} f_{dq0} \tag{2.87}$$

where

$$\mathbf{T}_{dq0\to\alpha\beta0} = \begin{bmatrix} \cos\theta & -\sin\theta & 0 \\ \sin\theta & \cos\theta & 0 \\ 0 & 0 & 1 \end{bmatrix} \tag{2.88}$$

From Eq.2.81 and Eq.2.85, we can transform abc stationery reference to $dq0$ rotating reference frame:

$$f_{dq0} = \mathbf{T}_{\alpha\beta0\to dq0}\mathbf{T}_{abc\to\alpha\beta0}f_{abc} \tag{2.89}$$

where $\mathbf{T}_{\alpha\beta0\to dq0}\mathbf{T}_{abc\to\alpha\beta0}$ can be expressed as $\mathbf{T}_{abc\to dq0}$:

$$\mathbf{T}_{abc\to dq0} = \frac{2}{3}\begin{bmatrix} \cos\theta & \cos(\theta - \frac{2\pi}{3}) & \cos(\theta + \frac{2\pi}{3}) \\ -\sin\theta & -\sin(\theta - \frac{2\pi}{3}) & -\sin(\theta + \frac{2\pi}{3}) \\ 1/2 & 1/2 & 1/2 \end{bmatrix} \tag{2.90}$$

Inversely, the variables in the rotating $dq0$ reference frame are transformed to the stationary abc rotating reference using the inverse matrix:

$$\mathbf{T}_{dq0\to abc} = (\mathbf{T}_{abc\to dq0})^{-1} = \begin{bmatrix} \cos\theta & -\sin\theta & 1 \\ \cos(\theta - \frac{2\pi}{3}) & -\sin(\theta - \frac{2\pi}{3}) & 1 \\ \cos(\theta + \frac{2\pi}{3}) & -\sin(\theta + \frac{2\pi}{3}) & 1 \end{bmatrix} \tag{2.91}$$

It is noticed that sinusoidal quantities in the abc frame appear as dc quantities in the dq frame under steady-state operation. In addition to the mathematical simplification, obtaining linear equations, it becomes feasible the decoupled control of torque and flux in the machine. Those are the main advantages of the transformation.

Mathematical modeling of double stator permanent magnet machine is needed to formulate and theoretically analyze the control strategies and generator performance. Fig. 2.16 shows the flux density map of the generator "A" with Finite Elements Analyze (FEA) method. From the figure, it can be seen that there is no cross flux line between the two stators. This figure confirms that double stator permanent magnet machine can be treated as two magnetically independent machine. There is no mutual inductance between the outer stator phase winding and inner stator phase winding [66]. This is a very important difference comparing with six phases in one stator machine. As a consequence, the mathematical model of double stator generator can be simply written as the combination of two conventional single stator PMSG models.

The basic equations for phase winding voltages in abc stationary reference of DSCRPMG
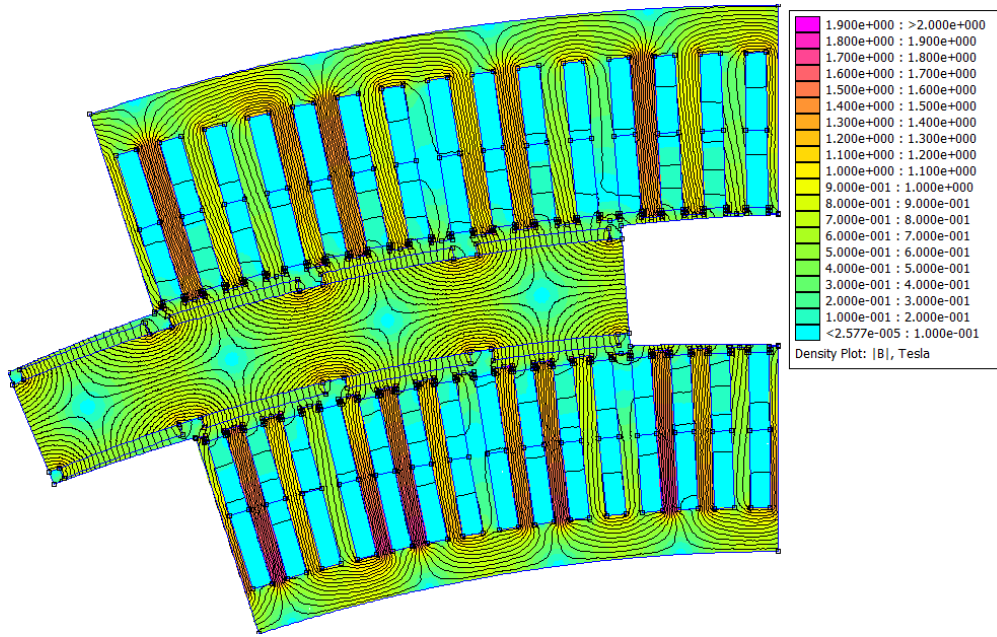
Figure 2.16 – Generator A flux lines with load current

are:

$$
\begin{cases}
\begin{bmatrix} v_{ao} \\ v_{bo} \\ v_{co} \end{bmatrix} = R_{cuo} \begin{bmatrix} i_{ao} \\ i_{bo} \\ i_{c} \end{bmatrix} + \frac{d}{dt} \begin{bmatrix} \psi_{ao} \\ \psi_{bo} \\ \psi_{co} \end{bmatrix} \\[4ex]
\begin{bmatrix} v_{ai} \\ v_{bi} \\ v_{ci} \end{bmatrix} = R_{cui} \begin{bmatrix} i_{ai} \\ i_{bi} \\ i_{ci} \end{bmatrix} + \frac{d}{dt} \begin{bmatrix} \psi_{ai} \\ \psi_{bi} \\ \psi_{ci} \end{bmatrix}
\end{cases}
\tag{2.92}
$$

In Eq.2.92, ψ is flux linkage and can be expressed as:

$$
\begin{cases}
\begin{bmatrix} \psi_{ao} \\ \psi_{bo} \\ \psi_{co} \end{bmatrix} = \begin{bmatrix} L_{ao} & M_{abo} & M_{aco} \\ M_{bao} & L_{bo} & M_{bco} \\ M_{cao} & M_{cbo} & L_{co} \end{bmatrix} \begin{bmatrix} i_{ao} \\ i_{bo} \\ i_{co} \end{bmatrix} + \psi_{PMo} \begin{bmatrix} \cos(\theta_r) \\ \cos(\theta_r - \frac{2}{3}\pi) \\ \cos(\theta_r + \frac{2}{3}\pi) \end{bmatrix} \\[6ex]
\begin{bmatrix} \psi_{ai} \\ \psi_{bi} \\ \psi_{ci} \end{bmatrix} = \begin{bmatrix} L_{ai} & M_{abi} & M_{aci} \\ M_{bai} & L_{bi} & M_{bci} \\ M_{cai} & M_{cbi} & L_{ci} \end{bmatrix} \begin{bmatrix} i_{ai} \\ i_{bi} \\ i_{ci} \end{bmatrix} + \psi_{PMi} \begin{bmatrix} \cos(\theta_r) \\ \cos(\theta_r - \frac{2}{3}\pi) \\ \cos(\theta_r + \frac{2}{3}\pi) \end{bmatrix}
\end{cases}
\tag{2.93}
$$

where θ_r is rotatinal electrical angle. It must be noticed that as the machine windings are symmetrical, the corresponding mutual inductance are equal: $M_{abo} = M_{bao} = M_{bco} = M_{bco} = M_{aco} = M_{cao} = M_o$ and $M_{abi} = M_{bai} = M_{bci} = M_{bci} = M_{aci} = M_{cai} = M_i$. M_o and M_i are outer stator and inner stator mutual inductance respectively.

For surface mounted permanent magnet machine, our case, the inner and outer inductance

are:

$$\begin{cases} L_{ao} = L_{bo} = L_{co} = L_{\delta o} + L_{mo} \\ L_{ai} = L_{bi} = L_{ci} = L_{\delta i} + L_{mi} \end{cases} \tag{2.94}$$

where $L_{\delta o}$ and $L_{\delta i}$ are outer stator and inner stator leakage inductances respectively. L_{mo} and L_{mi} are outer stator and inner stator magnetizing inductances respectively. Due to the angular displacement of the phase windings ($\frac{2}{3}\pi$), the mutual inductances can be calculated as:

$$\begin{cases} M_o = -\frac{L_{mo}}{2} \\ M_i = -\frac{L_{mi}}{2} \end{cases} \tag{2.95}$$

Replacing the inductance values Eq.2.94 and Eq.2.95 into Eq.2.92 and Eq.2.93 and applying the space vector transformation abc to $dq0$ Eq.2.90, the voltage equation in the rotating frame dq are:

$$\begin{cases} \begin{bmatrix} v_{do} \\ v_{qo} \end{bmatrix} = R_{cuo} \begin{bmatrix} i_{do} \\ i_{qo} \end{bmatrix} + \begin{bmatrix} L_{do}\frac{d}{dt} & -L_{qo}\omega_e \\ L_{do}\omega_e & L_{qo}\frac{d}{dt} \end{bmatrix} \begin{bmatrix} i_{do} \\ i_{qo} \end{bmatrix} + \omega_e\psi_{PMo} \begin{bmatrix} 0 \\ 1 \end{bmatrix} \\ \begin{bmatrix} v_{di} \\ v_{qi} \end{bmatrix} = R_{cui} \begin{bmatrix} i_{di} \\ i_{qi} \end{bmatrix} + \begin{bmatrix} L_{di}\frac{d}{dt} & -L_{qi}\omega_e \\ L_{di}\omega_e & L_{qi}\frac{d}{dt} \end{bmatrix} \begin{bmatrix} i_{di} \\ i_{qi} \end{bmatrix} + \omega_e\psi_{PMi} \begin{bmatrix} 0 \\ 1 \end{bmatrix} \end{cases} \tag{2.96}$$

Here, $L_{do} = L_{\delta o} + \frac{3}{2}L_{mo}$, $L_{di} = L_{\delta i} + \frac{3}{2}L_{mi}$. For surface mounted permanent magnet topology, $L_{do} = L_{qo}$ and $L_{di} = L_{qi}$. The method to calculate dq axis inductance is explained in machine preliminary design.

The electromagnetic torque as a function of the stator current in the dq axes is given by:

$$\begin{cases} T_{eo} = \frac{3}{2}pi_{qo}\left[i_{do}(L_{do} - L_{qo}) + \psi_{PMo}\right] \\ T_{ei} = \frac{3}{2}pi_{qi}\left[i_{di}(L_{di} - L_{qi}) + \psi_{PMi}\right] \end{cases} \tag{2.97}$$

For the studied permanent magnet surface mounted machine, $L_{dk} = L_{qk}$. Then, the torque equation can be rewrote as:

$$\begin{cases} T_{eo} = \frac{3}{2}pi_{qo}\psi_{PMo} \\ T_{ei} = \frac{3}{2}pi_{qi}\psi_{PMi} \end{cases} \tag{2.98}$$

The total torque is

$$T_e = T_{eo} + T_{ei} \tag{2.99}$$

The modeling of the DSCRPMG is completed by the mechanical equation given by:

$$Te = T_L + J\frac{d\omega_m}{dt} + f_v\omega_m \tag{2.100}$$

where J is the rotor inertia and f_v is the viscous damping. The relationship between electrical rotational angle and mechanical speed is:

$$\frac{d\theta_r}{dt} = \omega_e = p\omega_m \tag{2.101}$$

The resulting model is a second order system, where the rotor permanent magnet flux of inner and outer stator are constant parameters.

2.4 Vector current control strategies in Maximum Power Point Tracking (MPPT) region

In DSCRPMG, the outer and inner stator can be regarded as two independent PMSGs with mechanical connection. Each stator has one set of full controllable rectifier and which are connected to the same DC bus as shown in Fig. 1.12. The generator performance can be controlled through controlling the two rectifiers. DC bus has the function of decoupling between the generator side and grid side. The control method is similar to PMSG system with back to back converter.

The converter is controlled with aims of harness the maximum power from the tidal current and delivering it to the grid with the best power quality possible. Maximum power extracting can be achieved by adjusting the generator speed through controlling the generator side rectifier for direct drive system. Power quality issues are fulfilled by controlling the dc-link voltage, regulating the power factor and frequency, and ensuring low harmonic distortion in compliance with the grid codes. In order to satisfy those goals, the open loop control schemes (Scalar or Volt/Hertz control) is no longer suitable as it has no signal feedback. Then, the control method with close loop scheme, such as vector current control, is a better choice for high performance PMSG drive. Vector control (also known as Field Oriented Control - FOC) was proposed to control torque and flux independently, emulating the separately excited DC machine operating principle [67, 68]. The flux and torque are naturally coupled in a three phase AC machine. However, through Park's transformation, the natural reference frame abc can be transformed into rotating reference frame dq and then the flux and torque are decoupled in dq frame. The AC machine is similarly controlled as DC machine. In this chapter, we will mainly focus on the generator side vector control. Different control strategies are discussed and compared in detail.

The DSCRPMG torque is produced by the sum of outer and inner stator torque as shown in Eq.2.99. Both the outer and inner stator are controlled in the same way. Therefore, in order simplify the formulation, only the control strategy of the outer stator will be detailed. In the control strategy analysis, generalized control equations are formulated with inductance L_d and L_q. Those principles can be applied to the machine with different L_d and L_q, for instance, PM interior buried machine (IPM). In our generator case, $L_d = L_q$ for inner and outer stator.

The most important objective of high performance control strategies is to maintain linear control over torque. For the demanded torque T_{eo}, i_{do} and i_{qo} must be coordinated to satisfy the equation given in Eq.2.98. Obviously, a wide range of i_{do} and i_{qo} values can allow to obtain the same torque. Utilizing the available degree of freedom under the current limitation, a number of control strategies can be proposed to satisfy a particular objective [69]. In the following section, four control strategies will be presented and analyzed in detail. They are:

1. Zero D-axis Current Control (ZDC)

2. Unity Power Factor Control (UPF)

3. Constant Mutual Flux Control (CMF)

4. Minimize System Losses Control (MSL)

To simplify the analysis, the voltage drop caused by the stator resistance is neglected and all analysis are based on steady state.

2.4.1   Zero D-axis Current Control (ZDC)

ZDC control strategy is the most commonly utilized control strategy by industry because it simplifies the relationship between torque and current amplitude. The torque will linear increasing or decreasing with the phase current no matter for salient or non-salient pole machine. In fact, for the smooth permanent magnet generator topology (permanent magnets surface mounted on the rotor), the reluctance torque part equals zero as reason of $L_{do} = L_{qo}$. Therefore, the torque is linearized with *q-axis* current amplitude. If the *d-axis* current is controlled as zero for non-salient pole machine, ZDC control strategy has the same performance as the Maximum Torque Per Ampere (MTPA) control strategy which is usually researched for salient pole machine. The idea of MTPA control strategy is that the d-axis current are controlled as non-zero value to utilize the reluctance torque with the possible minimum phase current amplitude for salient pole machine. In this report, MTPA will not be detailed because surface mounted permanent magnet generator (non-salient) is adopted in our case. The authors in papers [70] has explained clearly for MTPA control strategy for IPM.

Fig. 2.17 shows the vector diagram of smooth PM generator with ZDC control in d-q plane. The torque angle, δ_1, is maintained at $90°$. As the generator torque and speed increasing, the power factor angle φ_1 and terminal voltage V_1 will change. When the generator is operated at low speed and small load region, a very high power factor can be achieved. When the maximum converter voltage is achieved, demagnetizing current should be applied to decrease the *d-axis* flux linkage. This is realized by giving a negative *d-axis* current. For non-salient pole generator, ZDC control strategy minimize the copper loss because that it minimize the phase current for a needed torque.
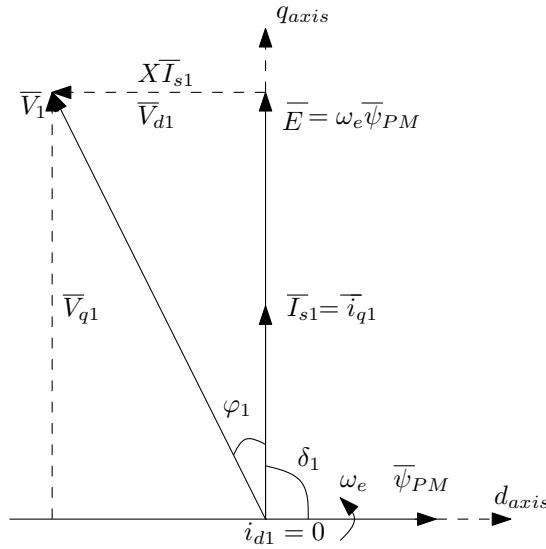
Figure 2.17 – Vector diagram of non-salient PM generator with ZDC control

2.4.2 Unity Power Factor Control (UPF)

In UPF control, the current and the terminal voltage are controlled in the same phase which results in $cos\varphi = 1$. This control strategy minimizes the machine apparent power. Fig. 2.18 shows the vector diagram of PM generator with UPF control in d-q plane. Negative *d-axis* current is needed to decrease the flux linkage so as to decrease the terminal voltage. From the vector diagram, we can obtain the voltage and current components relationship as:

$$\frac{V_{d2}}{V_{q2}} = \frac{i_{d2}}{i_{q2}} = \frac{-\omega_e L_q i_{q2}}{\omega_e \psi_{PM} + \omega_e L_d i_{d2}} \tag{2.102}$$
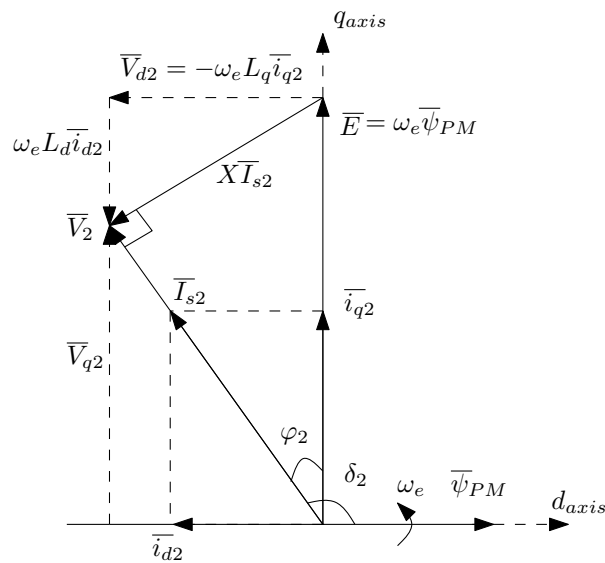
Figure 2.18 – Vector diagram of non-salient PM generator with UPF control

For the non-salient pole generator, the quadrature-axis current i_{q2} can be directly solved from the needed torque, but in the case of the salient pole machine, the quadrature-axis current

i_{q2} must be iterated. Once the value of i_{q2} is solved, the d-axis current can be deduced from Eq.2.102. This equation can be rewritten as:

$$L_d i_{d2}^2 + i_{d2}\psi_{PM} + L_q i_{q2}^2 = 0 \tag{2.103}$$

Solving the above equation with variable i_{d2}, we get

$$i_{d2} = \begin{cases} \frac{-\psi_{PM}+\sqrt{\psi_{PM}^2-4L_dL_qi_{q2}^2}}{2L_d} & (a) \\ \frac{-\psi_{PM}-\sqrt{\psi_{PM}^2-4L_dL_qi_{q2}^2}}{2L_d} & (b) \end{cases} \tag{2.104}$$

The smallest real and negative solution is the right choice to reduce the copper losses. In addition, the solution Eq.2.104(b) normally or easily exceeds current rated value. Therefore, solution (a) in Eq.2.104 will be chosen as *d-axis* current reference.

UPF can be realized if the root of Eq.2.104(a) is positive. So the *q-axis* current must satisfy the following constraint:

$$|i_{q2}| \leq \frac{\psi_{PM}}{2\sqrt{L_dL_q}} \tag{2.105}$$

This control strategy may not be applicable in full speed range for variable speed energy conversion system when the needed *q-axis* current is too big. It is noted that the generator can be specially designed to achieve the full speed range operation with UPF control strategy, if needed.

2.4.3   Constant Mutual Flux Control (CMF)

In this strategy, the stator terminal voltage amplitude V_3 is controlled to be at the same value as E. That means the resultant flux linkage of rotating frame *dq-axes* and rotor PM, known as the mutual flux linkage, is maintained constant which equals to PM flux linkage ψ_{PM}. Fig. 2.19 shows the vector diagram of PM generator with CMF control in d-q plane. The current vector is in the middle between vector E and V_3. Negative *d-axis* current is also needed to reduce the *d-axis* flux linkage. The flux linkage relationship can be expressed as:

$$\psi_{PM} = \sqrt{(\psi_{PM} + L_d i_{d3})^2 + (L_q i_{q3})^2} \tag{2.106}$$

Solving this equation with variable i_{d3},

$$i_{d3} = \begin{cases} \frac{-\psi_{PM}+\sqrt{\psi_{PM}^2-L_q^2i_{q3}^2}}{L_d} & (a) \\ \frac{-\psi_{PM}-\sqrt{\psi_{PM}^2-L_q^2i_{q3}^2}}{L_d} & (b) \end{cases} \tag{2.107}$$

The solution has similar form like the solution in UPF control. Therefore, Eq.2.107(a) is chosen as the right current reference with the similar reason that the demagnetizing *d-axis* current is
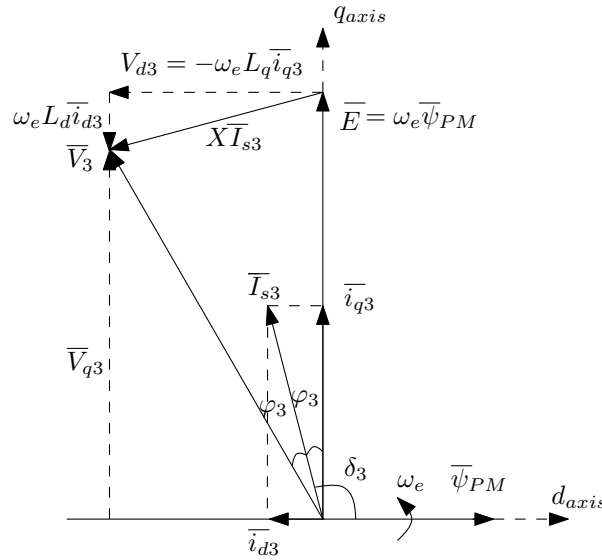
Figure 2.19 – Vector diagram of non-salient PM generator with CF control

much smaller so as to the copper losses. The realization of this control strategy is also based on the load torque, *q-axis* inductance and rotor PM flux linkage. For the non-salient pole generator, the quadrature-axis current i_{q3} can be directly solved from the needed torque, but in the case of the salient pole machine, the quadrature-axis current i_{q3} must be iterated with the torque equation. The value of i_{q3}, L_q, and ψ_{PM} should satisfy the constraint that the radicand in Eq.2.107(a) is positive. The *q-axis* current should satisfy the relation:

$$|i_{q3}| \leq \frac{\psi_{PM}}{L_q} \tag{2.108}$$

Comparing this equation with the constraint equation Eq.2.105 of UPF control, it is known that the possible operating torque range with CMF control is two times bigger than that with UPF control for non-salient pole generator ($L_d = L_q$). For salient pole generator, the conclusion that which control strategy has bigger torque range will strongly depends on the deference between direct-axis inductance L_d and quadrature-axis inductance L_q.

2.4.4 Minimize System Losses Control (MSL)

This control strategy minimize the total electrical losses (machine iron and copper losses, converter losses) at all operating points. It can be a preferable choice in many applications where a maximum efficiency operation is required. It is not so obvious to illustrate the vector diagram for this control. However, this problem can be expressed as the following formula:

$$i_d \rightarrow min(P_{copper}(i_d, i_q) + P_{iron}(i_d, i_q) + P_{rectifier}(i_d, i_q)) \tag{2.109}$$

Taking outer stator as an example. The losses expression of $P_{copper}(i_d, i_q)$,

$$P_{copper}(i_{do}, i_{qo}) = \frac{3}{2}R_{cuo}\hat{I}_o^2 = \frac{3}{2}R_{cuo}(i_{do}^2 + i_{qo}^2) \qquad (2.110)$$

For the iron loss $P_{iron}(i_{do}, i_{qo})$, the key issue is to obtain the flux density in air gap. In a simplified approach, the terminal voltage amplitude is used to calculate the fundamental air gap flux density:

$$\begin{cases} \hat{V}_o = \sqrt{V_{do}^2 + V_{qo}^2} = \sqrt{(-\omega_e L_{qo}i_{qo})^2 + (\omega_e\psi_{PM} + \omega_e L_{do}i_{do})^2} \\ \hat{B}_{go} = \hat{V}_o/(\frac{2}{\pi}k_w N_o\omega_e\tau_{po}L_{eff}) \end{cases} \qquad (2.111)$$

This simplified approach method is confirmed with FEM [66]. Once we get the air gap flux density $\hat{B}_{go}$ through the generator terminal voltage $\hat{V}_o$, the flux density in teeth and yoke can be calculated using Eq.2.52. Then, the generator iron losses are calculated by Eq.2.53. Hence, for a given rotational speed, the generator iron losses can be expressed as a function which varies with i_{do} and i_{do}.

The rectifier losses calculations are detailed in Appendix. A. Fig. 2.20 shows the principle of MSL. The black circle is the current limitation circle ($\hat{I}_{max}$) and the blue circle is the voltage limitation circle $\hat{V}_{max}$. In dq current plan, the machine operating point should satisfy the equation below:

$$\begin{cases} i_d^2 + i_q^2 \le \hat{I}_{max}^2 & within \quad black \quad circle \\ (-\omega_e L_q i_q)^2 + (\omega_e\psi_{PM} + \omega_e L_d i_d)^2 \le \hat{V}_{max}^2 & within \quad blue \quad circle \end{cases} \qquad (2.112)$$

For a specific machine rotational speed $\omega_{m,j}$ (j present the operating point), there is a voltage limitation circle. Current and voltage limitation are posed by converter. For example, for the machine operating condition (T_j, $\omega_{m,j}$), the *q-axis* current value can be directly solved by the needed torque as $i_{q,j}$. For *d-axis* current, it can be chosen between the point A (current limitation) and point B (voltage limitation). However, there is a optimal value (point C) which will result in minimum system power losses. Searching the optimal value in the range AB, then this value is named as $i_{d,j,optimal}$. Using those d, q current references ($i_{d,j,optimal}$ and $i_{q,j}$) to control the machine for operating point (T_j, $\omega_{m,j}$), maximum system efficiency can be obtained.

In literature, many authors has researched Minimize Machine Losses (MML) control [71–74]. The difference between our proposed control model and theirs is that the electronics device losses are taken into consideration in our study. In MML control strategy, the *d-axis* current reference i_d can be directly calculated by solving the equation following:

$$\frac{d(P_{copper}(i_d, i_q) + P_{iron}(i_d, i_q))}{di_d} = 0 \qquad (2.113)$$
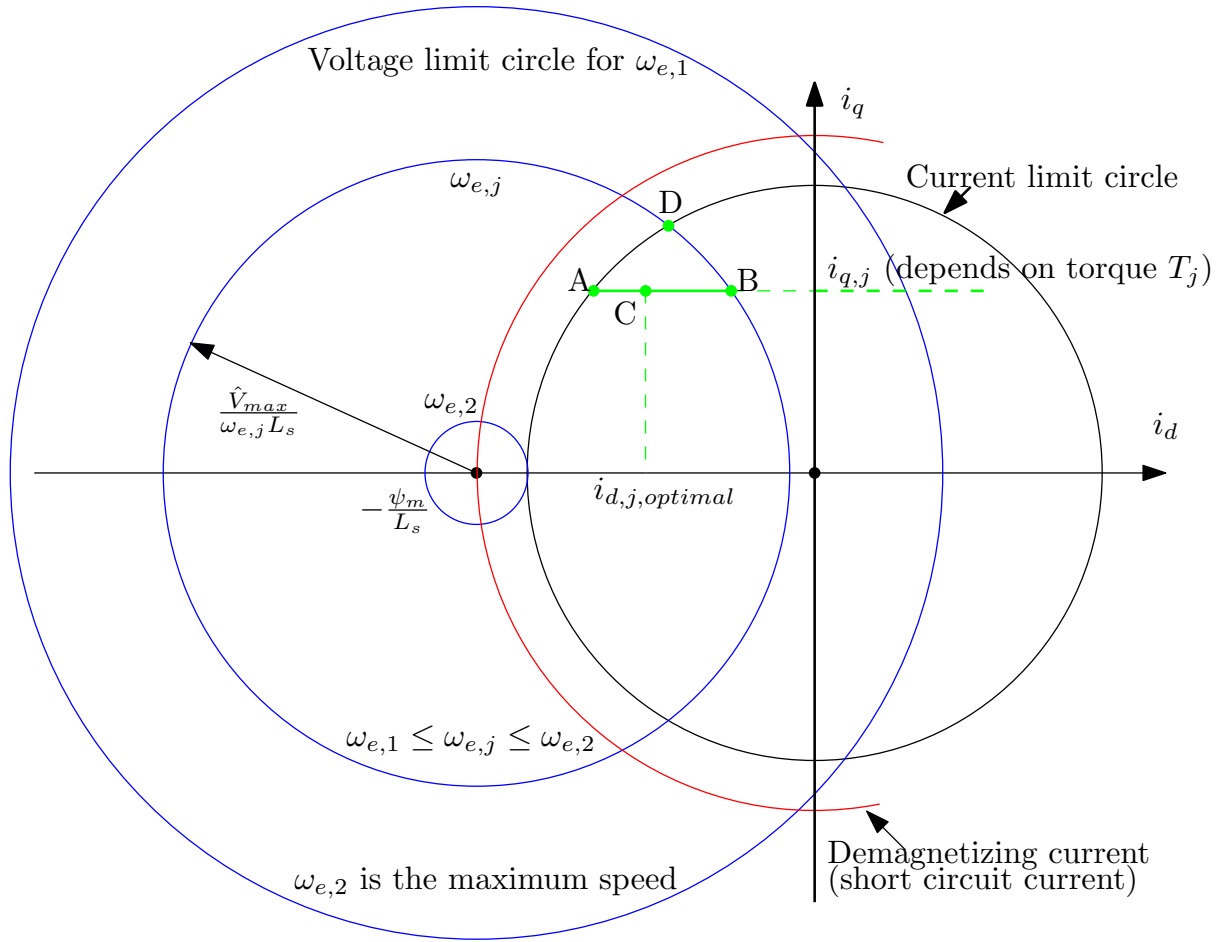
Figure 2.20 – Illustration of minimize system losses control strategy

However, for our MSL control strategy, it is difficult to solve the differential losses equation to get *d-axis* current reference i_d when the converter losses is taken into consideration because of the complexity of converter losses model. The optimal *d-axis* current reference is obtained by a losses comparison loop in MSL control strategy. In the results part, we will also present the efficiency difference between MML and the developed MSL.

2.5   Control strategies in Flux Weakening (FW) region

The turbine power curve shows that the tidal turbine produced power is supposed to be limited to a constant power at over rated current speed region. This power is the generator designed nominal power. For variable pitch turbine system, changing the pitch to reduce the tidal current attack angle can reduce the harness power. The power limitation can also be realized by turbine mechanical design which called stall control [75]. However, for the fixed pitch tidal turbine, most fluently used method to limit the power is to operate the turbine at over rated speed in over rated tidal speed region for reducing the turbine power coefficient and the extracting power. As the generator is directly coupled with the turbine, over rated speed operating will lead to high

electromotive force of the PM generator. Machine output voltage needs to be limited because of voltage limitation of both generator and converter. It can be done by mean of proper control strategy to provide a negative *d-axis* current i_d.

In the last section, the vector current control strategies in MPPT region have been discussed. The majority control strategies need a negative *d-axis* current except ZDC control. Nevertheless, when the generator operated under the rated speed, they can't be classified in flux weakening control even their effect is to reduce the *d-axis* flux linkage. Because the terminal voltages of those control strategies don't reach the limitation of converter voltage.

In flux weakening region, two possible operation modes, named Constant Power (CP) and Maximum Active Power (MAP) [76] are detailed below. The power curve of the two modes are shown in Fig. 2.21. MAP mode keeps the converter current and voltage at the limitation value. CP mode control the power as a constant. The point M in the figure is the point that the converter can't transfer the constant power. It will be explained in the following section. For Constant Power (CP) mode, three control strategies named Constant Current Constant Power (CCCP), Constant Voltage Constant Power (CVCP) and Minimize System Losses Constant Power (MSLCP) are detailed.
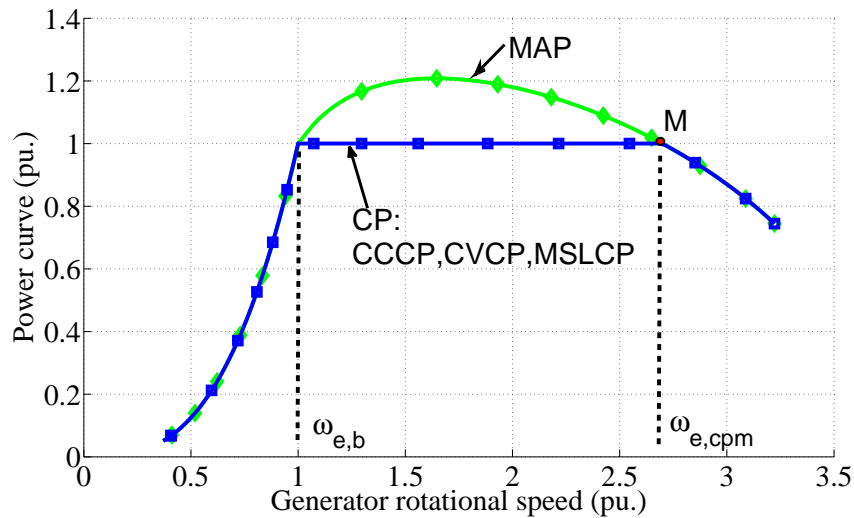
Figure 2.21 – CP and MAP mode in FW region. Three control strategies (CCCP,CVCP,MSLCP) are presented in CP mode

2.5.1 Constant Power (CP) mode

In CP mode, one given generator rotational speed high than rated speed, we need to reduce the torque to keep the power constant. Then the relative *q-axis* current can be calculated with the needed torque. This current normally will not achieve the current and voltage limitation at the same time. That the main difference between the MAP mode. For needed current reference i_q, there are two commonly used strategies to obtain the *d-axis* reference current:

Constant Current Constant Power (CCCP) control

This control strategy keeps the current as a constant value, normally the current limit. In Fig. 2.20, point A is obtained with this control strategy. When the machine operated at nominal torque and nominal rotational speed, it is assumed that the current reached the limitation. At this point, we name the *q-axis* current as $i_{q,b}$ and the *d-axis* current as $i_{d,b}$. b represent the base operation point (rated torque operation point). The nominal rotational speed is normally called base speed $\omega_{e,b}$. The limitation current $\hat{I}_{max}$ is equal to $\sqrt{i_{d,b}^2 + i_{q,b}^2}$. For a given rotational speed $\omega_{e,j}$ which is bigger than $\omega_{e,b}$, there is a needed torque which is smaller than the rated torque to keep the power as a constant (rated power). The q-axis current should obey the following relation to keep the power constant:

$$i_{q,j} = \frac{\omega_{e,b}}{\omega_{e,j}} i_{q,b} \tag{2.114}$$

As constant current constant power control keeps a constant phase current, the *d-axis* current can be written as follows:

$$i_{d,j} = -\sqrt{\hat{I}_{max}^2 - i_{q,j}^2} \tag{2.115}$$

Constant Voltage Constant Power (CVCP) control

This control strategy keeps the voltage as a constant value, normally the voltage limit. In Fig. 2.20, point B is obtained with this control strategy. In order to keep the power at the rated power in flux weakening region, the product of torque and speed should satisfy the following relationship:

$$\frac{\omega_{e,j}}{p} T_j = \frac{\omega_{e,b}}{p} T_{rated} \tag{2.116}$$

For PM surface mounted machine, Eq.2.116 can be rewritten as follow:

$$\omega_{e,j} i_{q,j} = \omega_{e,b} i_{q,b} \qquad constant \tag{2.117}$$

Therefore,

$$i_{q,j} = \frac{\omega_{e,b}}{\omega_{e,j}} i_{q,b} \tag{2.118}$$

In steady state, the *d-axis* voltage equation is:

$$v_{d,j} = -\omega_{e,j} L_s i_{q,j} \qquad constant \tag{2.119}$$

From the Eq.2.117, it is known that $v_{d,j}$ is a constant value. In order to keep the phase voltage as a constant, $v_{q,j}$ should be also a constant value which is equal to $v_{q,b}$:

$$v_{q,b} = \omega_{e,b}(\psi_{PM} + L_s i_{d,b}) \qquad constant \tag{2.120}$$
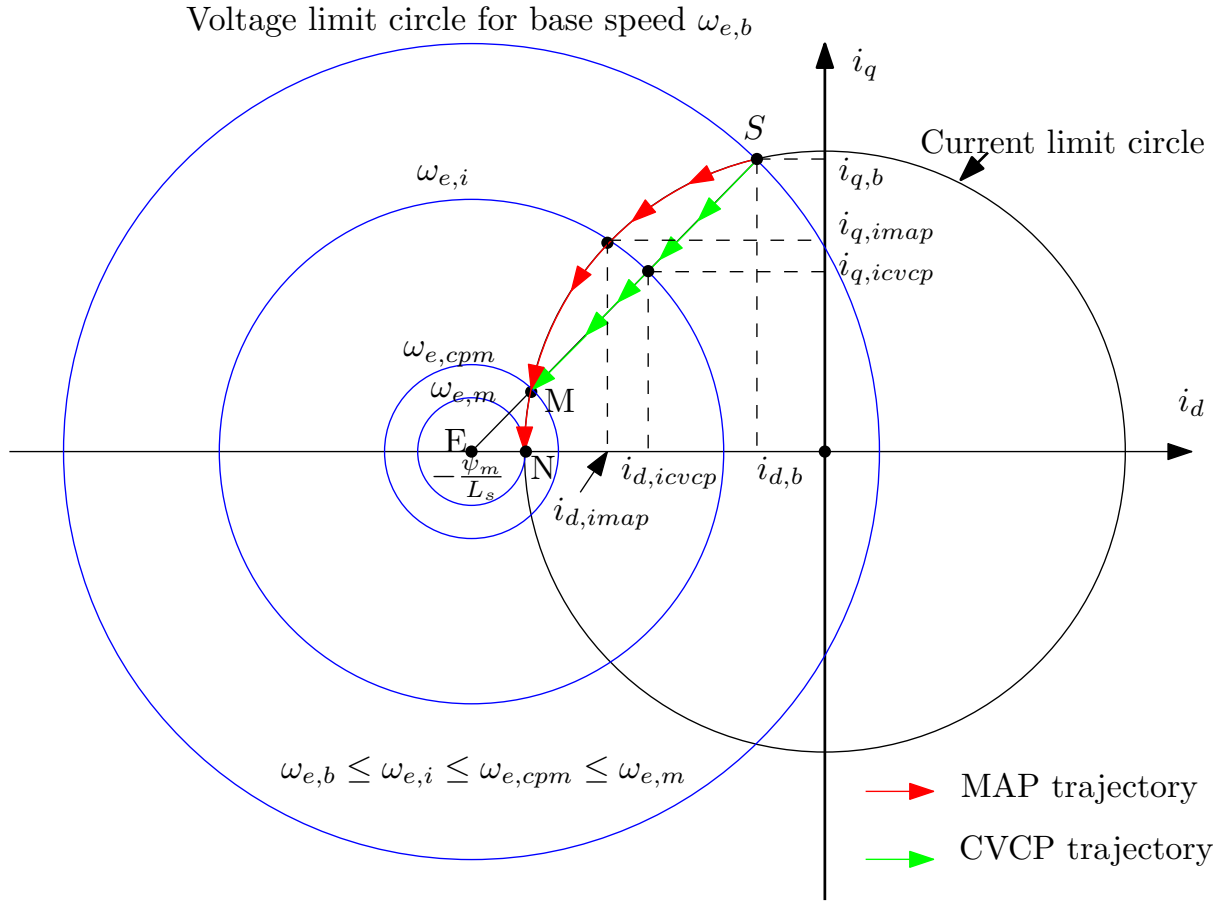
Figure 2.22 – MAP and CVCP trajectory.

$$v_{q,j} = \omega_{e,j}(\psi_{PM} + L_s i_{d,j}) \qquad constant \qquad (2.121)$$

From the relation of Eq.2.120 and Eq.2.121, the *d-axis* reference current can be calculated as:

$$i_{d,j} = \frac{\omega_{e,b}}{\omega_{e,j}}(\frac{\psi_{PM}}{L_s} + i_{d,b}) - \frac{\psi_{PM}}{L_s} \qquad (2.122)$$

From Eq.2.118 and Eq.2.122, we can write the relationship between $i_{d,j}$ and $i_{q,j}$ as follow:

$$i_{d,j} = \frac{i_{q,j}}{i_{q,b}}(\frac{\psi_{PM}}{L_s} + i_{d,b}) - \frac{\psi_{PM}}{L_s} \qquad (2.123)$$

It is noted that $i_{q,b}$ and $i_{d,b}$ can be obtained from the base speed operation condition. Hence, it is obvious that the *d, q-axis* current components are linearly related to each other. The CVCP trajectory can be drown as depicted in Fig. 2.22, which is the lime SE.

It should be noticed that the intersection point, M, between the line SE and the current-limiting circle, represents the boundary of the CP mode control. When the speed is higher than $\omega_{e,cpm}$, the converter can't transfer the constant power. In order to maximize the power, CP mode need to change to MAP mode (it will be discussed in next section). This point is the point which we achieve the limitation of current and voltage circle at the same time for constant power

control. At this speed condition, the control strategies MAP, CCCP and CVCP will give out the same *d-q axis* current reference. The ratio between $\omega_{e,cpm}$ and $\omega_{e,b}$ is a very important parameter for the system. It is called Constant Power Speed Ratio (CPSR) in some reference [77–79]. As we discussed before, the CCCP and CVCP control has the same current reference for $\omega_{e,cpm}$. Therefore, we can calculate the CPSR from the equivalent of d-axis current which are obtained by CCCP and CVCP (Eq.2.115 and Eq.2.122).

$$\sqrt{\hat{I}_{max}^2 - (\frac{\omega_{e,b}}{\omega_{e,cpm}})^2 i_{q,b}} = \frac{\omega_{e,b}}{\omega_{e,cpm}}(\frac{\psi_{PM}}{L_s} + i_{d,b}) - \frac{\psi_{PM}}{L_s} \tag{2.124}$$

Combining with:

$$\hat{I}_{max}^2 = i_{d,b}^2 + i_{q,b}^2 \tag{2.125}$$

leads to the CPSR ($\frac{\omega_{e,cpm}}{\omega_{e,b}}$) as:

$$\frac{\omega_{e,cpm}}{\omega_{e,b}} = \frac{\psi_{PM}^2 + 2\psi_{PM}L_s i_{d,b} + (L_s\hat{I}_{max})^2}{\psi_{PM}^2 - (L_s\hat{I}_{max})^2} \tag{2.126}$$

In order to get a more generalized CPSR expression, we multiply $\omega_{e,b}^2$ to the numerator and denominator of Eq.2.126. Then, the generalized CPSR is:

$$CPSR = \frac{\hat{V}_{max}^2}{\omega_{e,b}^2 \left[\psi_{PM}^2 - (L_s\hat{I}_{max})^2\right]} \tag{2.127}$$

with

$$\hat{V}_{max}^2 = \omega_{e,b}^2 \left[\psi_{PM}^2 + 2\psi_{PM}L_s i_{d,b} + (L_s\hat{I}_{max})^2\right] \tag{2.128}$$

From Eq.2.127, it is clear that for a given machine, in order to increase CPSR: firstly, increasing the voltage limitation value $\hat{V}_{max}^2$ to increase the numerator. Secondly, increasing the current limitation $\hat{I}_{max}$ can decrease the denominator. That means converter with bigger apparent power has bigger CPSR. CPSR can also be increased through the machine design as it has been presented in the generator preliminary design. Designing the generator with bigger inductance L_s will increase the CPSR. However, as the too big inductance will cause bad system power factor, the inductance should be designed properly to have the enough capability of flux weakening. If we design a generator with big CPSR, the converter cost will increase sharply and even the generator cost will increase as it has been shown before. Therefore, for tidal energy or wind energy system, it needs to design the generator combining with the converter capability to satisfy the turbine power characteristic curve.

Minimize System Losses Constant Power (MSLCP) control

Another control method is proposed in this thesis. It minimizes the system losses in CP mode called MSLCP. The principle is the same as MSL control in MPPT region. The *q-axis* is calculated from the needed torque for a certain speed. Then the d-axis current reference $i_{d,j,optimal}$ is calculated from the system minimize losses. In this region, it is really important to take the power electronics device losses into account. Because the current and voltage are normally around the limit value and so as to the losses is important. In some well designed machine, the converter losses is almost equal or even bigger than the iron losses. Therefore , we should calculate the optimal *d-axis* current reference including the converter losses. In fact, in Fig. 2.20, the point A which is obtained with control strategy CCCP will just minimize the iron losses of the machine. And the point B which obtained with control strategy CVCP will just minimize the copper loss of the machine. The point C is the point which can minimize the system losses with an optimal *d-axis* current $i_{d,j,optimal}$. It is a compromised result of copper loss, iron losses and power electronics device losses.

2.5.2   Maximum Active Power (MAP) mode

MAP control follows the current limitation and voltage limitation cross point (point D in Fig. 2.20). That means the converter will always operated at the maximum apparent power $S_{conv} = \frac{3}{2}\hat{V}_{max}\hat{I}_{max}$. In PM surface mounted machine, $L_d = L_q = L_s$. For a given generator electrical rotational speed $\omega_{e,j}$, the *d-q axis* flux weakening reference can be calculated by solving the following equations:

$$\begin{cases} (L_s i_{q,jmap})^2 + (L_s i_{d,jmap} + \psi_{PM})^2 = \frac{\hat{V}_{max}^2}{\omega_{e,j}^2} \\ i_{d,jmap}^2 + i_{q,jmap}^2 = \hat{I}_{max}^2 \end{cases} \tag{2.129}$$

The solution of current references are obtained as:

$$\begin{cases} i_{d,jmap}^2 = \frac{\hat{V}_{max}^2 - (\omega_{e,j} L_s \hat{I}_{max})^2 - (\omega_{e,j}\psi_{PM})^2}{2\psi_{PM} L_s \omega_{e,j}^2} \\ i_{q,jmap}^2 = \hat{I}_{max}^2 - i_{d,jmap}^2 \end{cases} \tag{2.130}$$

The MAP trajectory can be drown as depicted in Fig. 2.22. With the speed increasing, the voltage limitation circle will shrink and the *d-q axis* current reference is always obtained at the cross point of the current and voltage limit circle. The voltage limitation circle center is located at the point E ($-\frac{\psi_{PM}}{L_s}, 0$). When this point E is located inside or on the current limit circle, theoretically, the machine can achieve infinite speed operation. However, when point E is outside of current limit circle, there exist a speed that the generator can't harness any power. The current limit circle and voltage circle has just one common intersection (point N). All the

phase current is in *d-axis* and it is used to weak the permanent magnet flux. This speed is called maximum generator speed ($\omega_{e,m}$) and it is calculated as following:

$$\omega_{e,m} = \frac{\hat{V}_{max}}{\psi_{PM} - L_s \hat{I}_{max}} \qquad (2.131)$$

2.6 System efficiency evaluation in MPPT and FW region

In this section, the efficiency evolution under different control strategies in MPPT region will be firstly presented. Then, the FW region efficiency evolutions are discussed under the three constant power control strategies with one selected converter size. Finally, CP and MAP model performances are compared in detail.

Symbol	Description	Value
ψ_{PMo}	Outer stator magnet flux linkage	$6.26Wb$
ψ_{PMi}	Inner stator magnet flux linkage	$5.85Wb$
L_{do}, L_{qo}	Outer stator *dq-axis* inductance	$6.73mH$
L_{di}, L_{qi}	Inner stator *dq-axis* inductance	$6.77mH$
R_{cuo}	Outer stator resistance	0.028Ω
R_{cui}	Inner stator resistance	0.029Ω
p	Pole pair	40

Table 2.4 – Control parameters of generator "A"
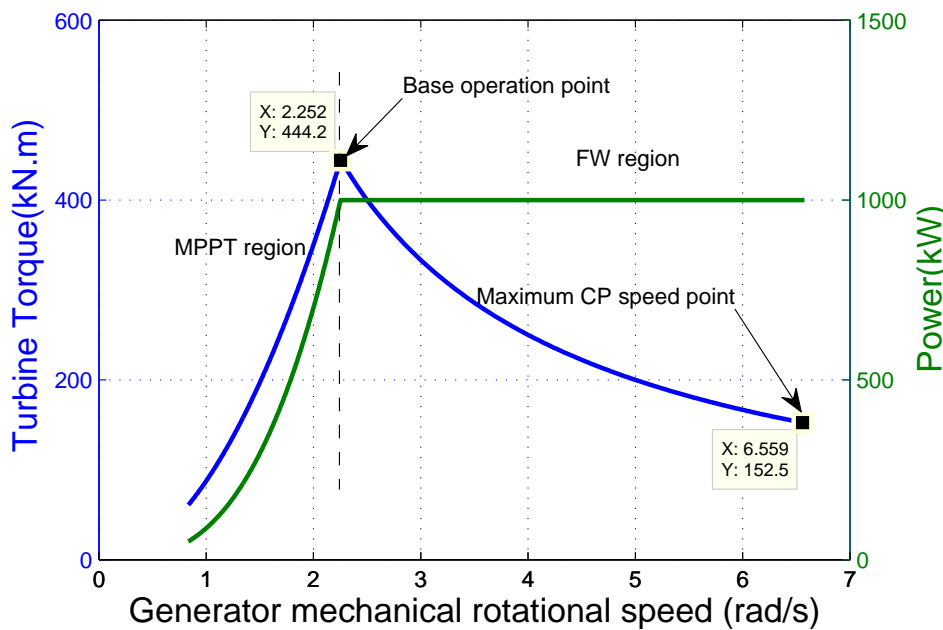
Figure 2.23 – Classical power torque curve of tidal current turbine

For the full speed region operation, the generator control method can be any combination of the control strategies in MPPT region (ZDC, UPF, CMF, MSL) and control strategies in FW

region (CCCP, CVCP, MSLCP, MAP). In this section, the efficiency evolution under different control strategies will be presented separately for MPPT and FW region. We will apply the different control strategies to the generator "A" which is the maximum efficiency generator as obtained through preliminary design process. The parameters used for control of the generator "A" are showed in the Table. 2.4.

Fig. 2.23 shows the classical power torque curve for a specific tidal current turbine. In FW region, CP mode is considered. MAP mode will be further studied and compered in the next section. The generator operates with different control strategies to follow the torque speed curve. For different operating point (T_j, ω_j), the system will have different efficiency for different control strategies.

2.6.1   System efficiency for different control strategies in MPPT region

Fig. 2.24 shows the efficiency curve in full tidal current speed range. From this figure we can see that MSL control strategy always has better efficiency than other control strategies in MPPT region. The most frequently applied control strategy ZDC has smallest system efficiency
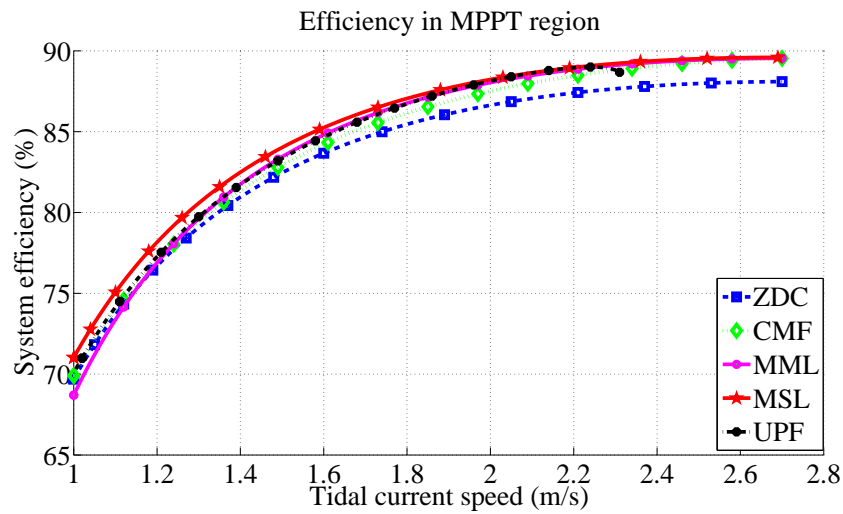
Figure 2.24 – System efficiency operated with different control strategies in MPPT region

in majority MPPT speed region ($1.2m/s \sim 2.7m/s$). The efficiency difference between MSL and ZDC control strategies is more than 1% and it achieves 1.6% at rated speed (2.7m/s) region. For MW range generator, improving more than 1% the system efficiency in renewable energy system through control strategy is a valuable solution to increase the annual energy output.

The black line shows the UPF control which can't be applied to the base operation point for generator "A". The needed *q-axis* current for outer and inner stator are $631.7A$ and $589.9A$ to provide the rated torque respectively. Those value are bigger than $\psi_{PMo}/(2L_{so}) = 476.2A$ and $\psi_{PMi}/(2L_{si}) = 436.6A$. Therefore, from the Eq.2.105, it is known that the generator can't operated with UPF at high speed region. However, from the efficiency evolution, it can be seen that in low speed region UPC has better efficiency than ZDC and CMF. The UPF will not be

analyzed and compared in detail with other control strategies because for generator "A" UPF can't operated in full tidal speed range.

The control strategy MML which optimizes the machine losses without taking converter losses into consideration almost have the same efficiency in the high tidal speed region ($2m/s \sim 2.7m/s$). However, in low speed region (below $1.4m/s$), MSL results more than 1% comparing to MML.

CMF control strategy results a efficiency curve between the control strategies ZDC and MSL. In high speed region ($2.2m/s \sim 2.7m/s$), CMF, MML and MSL almost have the same efficiency. For the machine system which always operated at rated condition, CMF can achieve a good system efficiency as MSL control strategy. This control strategy can be used in industry application because it is simple and has good system efficiency. However, for variable speed drive system like in our case, MSL is a better choice because in large tidal speed range ($1m/s \sim 2.2m/s$) MSL has better efficiency than CMF.
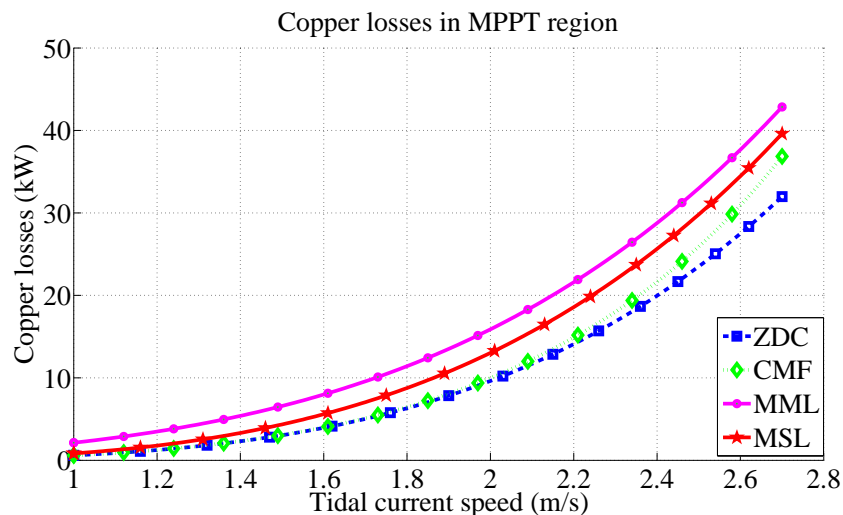
Figure 2.25 – Copper losses in MPPT region under different control strategies

The system copper, iron and converter losses variations lead to the system efficiency evolution. The evolution of those losses under different control strategies are shown in Fig. 2.25, Fig. 2.26 and Fig. 2.27 respectively. ZDC control strategy results minimum copper losses in MPPT region because it needs smallest current for the same torque. However, the iron losses of this control strategy are much bigger than the others. Because in low speed region, generator iron losses are much important than copper loss. MML strategy tends to have bigger value of *d-axis* current to reduce the terminal voltage, so as to reduce the iron losses. Bigger current will also cause the higher converter losses. As MML doesn't take consideration of converter losses to calculate the *d-axis* current reference, it will result out much bigger converter losses than MSL control strategy. That's the reason that MML has a little smaller efficiency than MSL. Losses evolution curves (copper, iron and converter) of control strategy MSL are always between the corresponding maximum and the minimum losses curves of the other control strategies. That
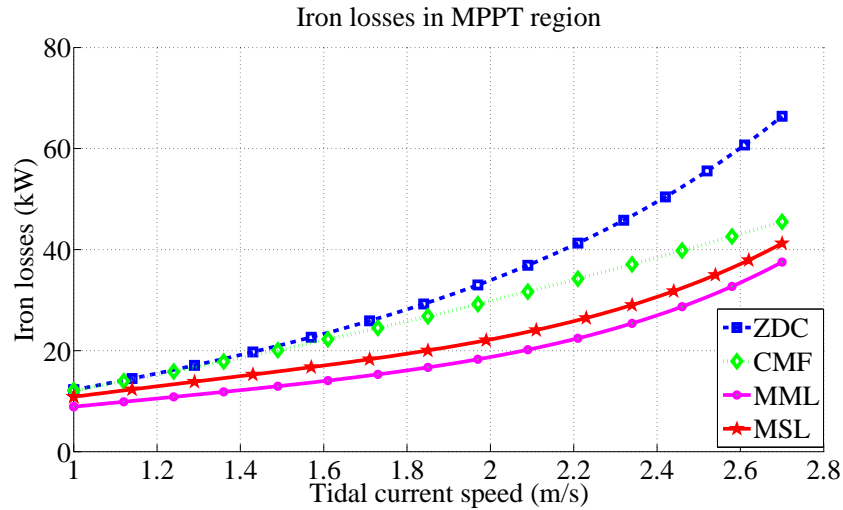
Figure 2.26 – Iron losses in MPPT region under different control strategies

means MSL control strategy can provide an optimal *d axis* current reference $i_{d,optimal}$ which compromises between those losses to have minimum system losses.
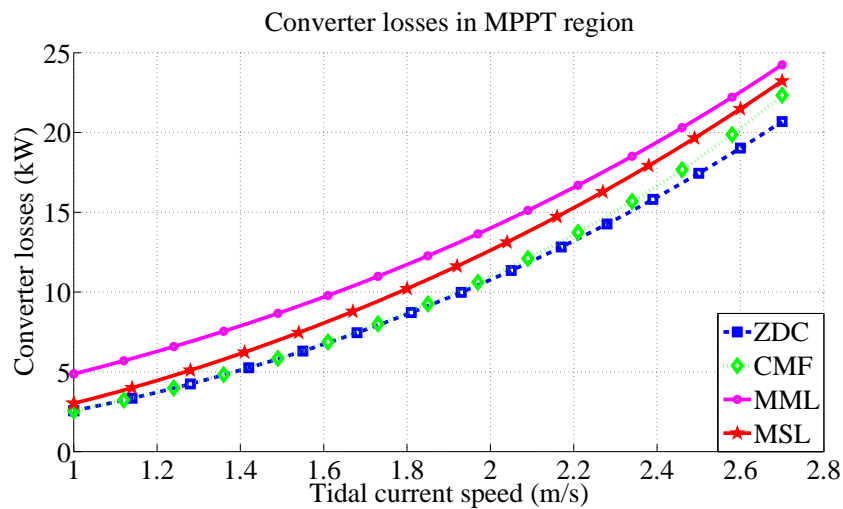
Figure 2.27 – Converter losses in MPPT region under different control strategies

Fig. 2.28 illustrates the power factor of outer stator for different control strategies in MPPT region. In the speed which around the cut in speed $(1m/s)$, ZDC and CMF have power factor almost equal to 1. It is logical that ZDC has always smaller power factor than CMF in MPPT region. Because the phase current vector is in the middle of EMF and terminal voltage for CMF. However, the current vector of ZDC is in the same axis of EMF. MML has the smallest power factor at cut in speed. For the base operation point, ZDC has smallest power factor. From the power factor curve, it is known that ZDC should have bigger minimum converter size than other control strategies.

Table. 2.5 summarized the advantages and disadvantages between the different control strategies.

Table. 2.6 gives out the operation voltage and current for the base operation point (rated
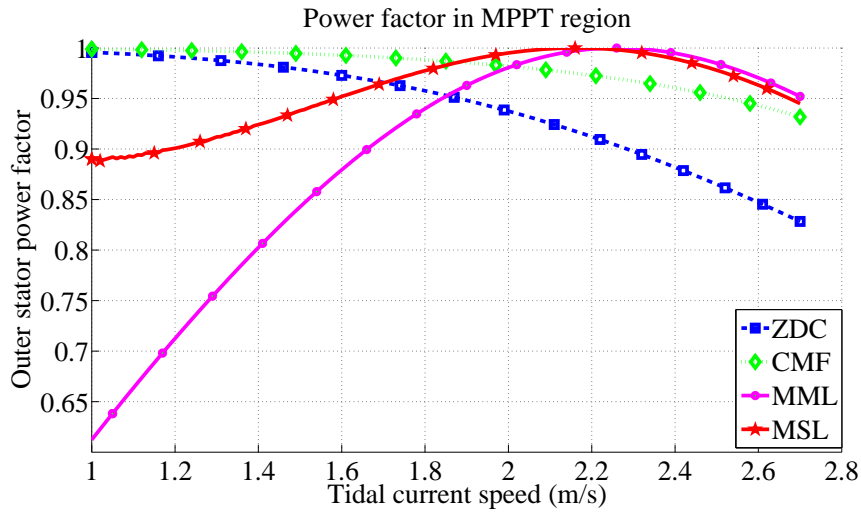
Figure 2.28 – Power factor in MPPT region under different control strategies

	Copper losses	Iron losses	Converter losses	Converter size	Efficiency
ZDC	🙂	😣😣😣	🙂	😣	😣😣
CMF	😐	😣😣	😐	🙂	😣
MML	😣	🙂🙂	😣	🙂	🙂
MSL	😐	🙂	😐	🙂	🙂🙂

Table 2.5 – Summary of the different control strategies (ZDC, CMF, MML, MSL) in MPPT region for the generator "A".

Strategy	$i_{d,b}\,(A)$		$i_{q,b}(A)$		$\hat{I}_{max}(A)$		$\hat{V}_{max}(V)$		$S_{conv}(MVA)$	
	o	i	o	i	o	i	o	i	o	i
ZDC	0	0	631.7	589.9	631.7	589.9	**680.6**	**636.5**	**0.64**	**0.56**
CMF	-246	-231	631.7	589.9	677.9	633.6	563.8	526.5	0.57	0.50
MSL	-300.3	-268.5	631.7	589.9	699.5	648.2	540.1	510.1	0.57	0.49
MML	-359	-323.6	631.7	589.9	**726.6**	**672.9**	515.6	486.8	0.56	0.49

Table 2.6 – Generator "A": Base operation point current and voltage. S_{conv} are the minimum apparent needed for corresponding control strategies. $\hat{I}_{max} = \sqrt{i_{d,b}^2 + i_{q,b}^2}$ and $\hat{V}_{max} = \sqrt{(-\omega_e L_q i_{q,b})^2 + (\omega_e \psi_{PM} + \omega_e L_d i_{d,b})}$.

torque and rated speed) for different control strategies. It also confirms that ZDC will have maximum voltage and minimum current. MML control strategy has much bigger *d-axis* current absolute value at base operation point to reduce the iron losses.
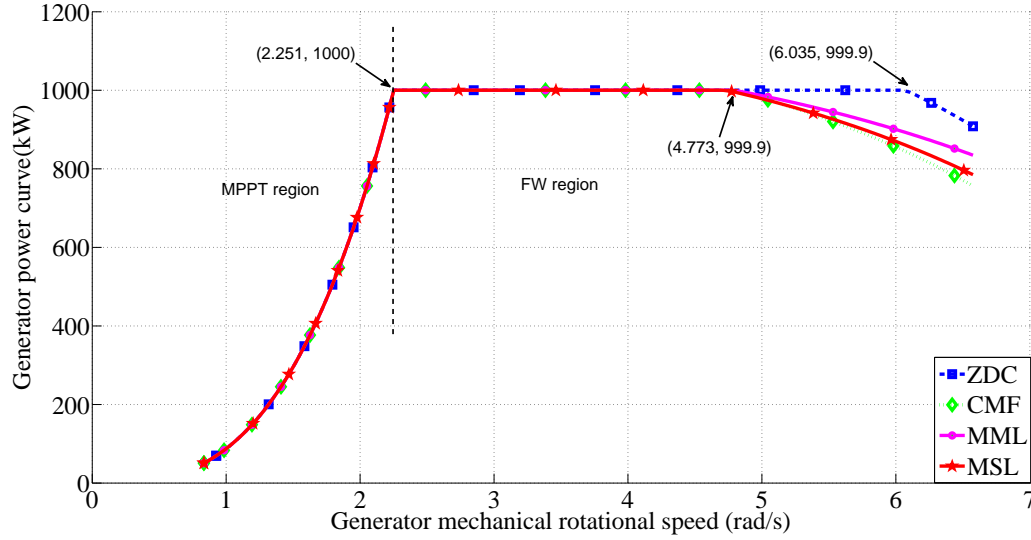
Figure 2.29 – Generator "A": Extractable power curve for different control strategies with the minimum needed converter rated current and voltage which are calculated at base (rated) operation point respectively.

The apparent power values S_{conv} for different control strategies in the Table. 2.6 are calculated based on the rated operation point. Fig. 2.29 shows the extractable power of the generator and converter system using the converter size in Table. 2.6 for each control strategy. It is clearly shown that for every control strategy, there is a certain rotational speed that the generator can't keep constant power. Using the generator parameters in Table. 2.4 and converter parameters Table. 2.6 to the Eq.2.131 and Eq.2.127, the generator maximum CP operation rotational speed and maximum generator operating rotational speed is obtained as shown in the Table. 2.7. From the table, it confirms that ZDC has bigger flux weakening capability. When the generator speed is bigger than maximum constant power operation speed, CP control mode will change to MAP mode control.

Strategy	$\omega_{m,cpm}$		$\omega_{m,m}$		CPSR
	o	i	o	i	Min(o,i)
ZDC	6.04	6.04	8.39	8.38	2.68
CMF	4.75	4.74	8.20	8.20	2.11
MSL	4.70	4.70	8.58	8.46	2.09
MML	4.76	4.73	9.26	9.07	2.10

Table 2.7 – Generator "A": Maximum CP speed and maximum operational speed of generator

From the above discussion, it is know that constant power limitation control mode can't be achieved for full FW region if the converter size is too small. In the next section, converters

with bigger apparent power which can operate constant power mode until cut out tidal current speed ($4.6m/s$) will be selected to compare the efficiency evolution.

2.6.2 System efficiency for different control strategies in FW region (constant power mode)

In FW region, three control strategies are presented in the former section for constant power control mode which are CCCP, CVCP and MSLCP. The efficiency evolutions in FW under the three control strategies strongly depends on the converter size (current and voltage limitation circle). In this section, in order to study the whole FW region for CP mode, the converter size is selected bigger than the based operation point converter power rate. The peak current and voltage of the converter are chosen as $750A$ and $700V$ respectively to have CPSR bigger than $2.92(\frac{6.576}{2.252})$. The converter apparent power is $770kVA$. This CPSR is needed by the turbine control to have constant power in high tidal current speed region($2.7m/s \sim 4.6m/s$).
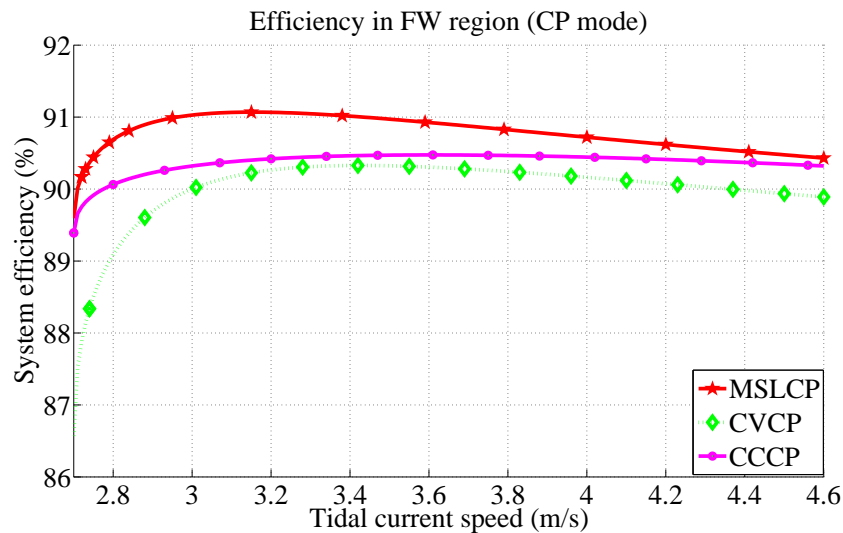
Figure 2.30 – System efficiency operated with different control strategies in FW region(CP mode)

Fig. 2.30 shows the efficiency variations in FW region for the three control strategies. MSLCP control method has undoubtedly better efficiency than the other two control strategies (CCCP and CVCP) because it minimize the summation of system losses (copper, iron and converter losses). CVCP has the smallest efficiency curve. The generator is operated at point B in Fig. 2.20. This control strategy keeps the phase voltage as a constant as the voltage limitation. It results biggest phase voltage and smallest current compared to the MSLCP and CCCP. High phase terminal voltage causes the iron losses very big. Smaller current leads to smaller copper losses. However, smallest copper losses doesn't lead to higher efficiency because the iron losses are much bigger than the copper losses. The generator is operated at point A in Fig. 2.20 with control method CCCP. It minimizes the iron losses. However, the current keeps at the limitation

value and then it results maximum copper losses. The converter losses have very strong proportional relationship with the phase current. Biggest current will also cause biggest converter losses. Better efficiency of MSL is a compromise result of the three part losses (copper, iron and converter losses) comparing to CCCP and CVCP which are just better for one part losses.

Fig. 2.31, Fig. 2.32 and Fig. 2.33 show the copper, iron and converter losses variations respectively. CCCP has constant and biggest copper losses because the current is keep at a constant as the current limitation. CVCP has the smallest copper losses and much bigger iron losses than the other two control strategies. It keeps the voltage at a constant as the voltage limitation. The iron losses will not keep at a constant value because the speed is not constant. The converter losses almost have the same form of the current losses. It means that the converter losses model has stronger relationship with the phase current. The voltage and power factor have smaller influence to the converter losses.
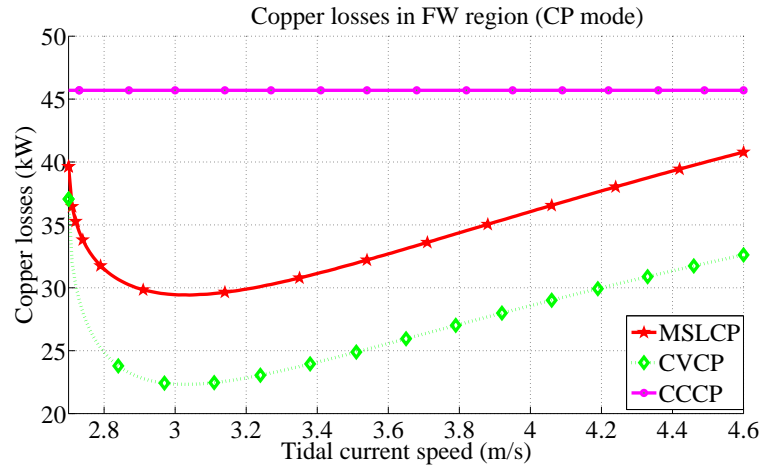
Figure 2.31 – Copper losses in FW region under different control strategies(CP mode).
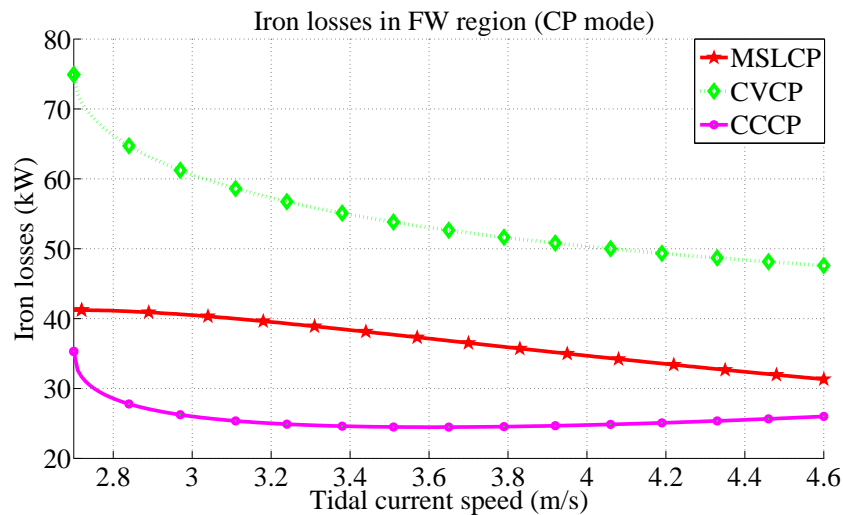
Figure 2.32 – Iron losses in FW region under different control strategies(CP mode).
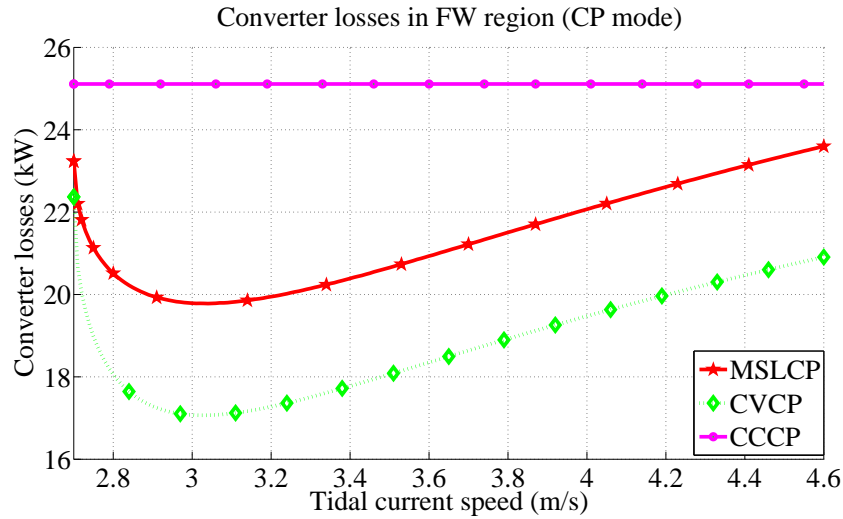
Figure 2.33 – Converter losses in FW region under different control strategies(CP mode).

	Copper losses	Iron losses	Converter losses	Efficiency
CCCP	🙁	🙂🙂🙂	🙁	🙂
CVCP	🙂	🙁🙁🙁	🙂	🙁
MSLCP	😐	🙂🙂	😐	🙂🙂

Table 2.8 – Summary of the different control strategies (CCCP, CVCP, MSLCP) for FW region with CP mode.

Table. 2.8 summarized the three CP mode control strategies in FW region. CCCP is bad for converter and copper losses. CVCP is bad for iron losses as it always keep the terminal voltage as limitation value. However, it results less copper and converter losses. As the iron losses is the majority losses of this generator, CVCP has smallest efficiency because it has very big iron losses. MSLCP leads to better efficiency. The total losses is a compromise result between the three parts losses.

From the discussion of efficiency variation in MPPT and FW region, it is known that MSL and MSLCP are better control strategy for improving the system efficiency.

2.6.3 Comparison between MAP mode and CP mode

In FW region, the generator can also be controlled in MAP mode. In this section, the efficiency of the generator when it operates with MAP mode and MSLCP mode are compared. The converter size (current and voltage limitations) is the same for the two control mode in the comparison. ZDC control minimum converter size in Table. 2.6 is taken as a example ($\hat{I}_{max} = 631.7A$, $\hat{V}_{max} = 680.6V$ for outer stator, $\hat{I}_{max} = 589.9A$, $\hat{V}_{max} = 636.5V$ for inner stator). In reality, the converter limit current and voltage can't be as precise as it has been calculated in the model. However, it will not change the conclusion the this comparison if a bigger or real converter size is used.

Fig. 2.34 shows the power curve of turbine and power curves of generator under MAP and MSLCP control mode. The black lines shows the turbine extracted power varying with the rotational speed for different tidal speed value. As we can see that, each tidal speed curve has its maximum power point. When the tidal current speed is under the rated value, we will control the rotational speed to have the maximum power coefficient so as to obtained the maximum power. When the tidal speed is bigger than rated speed, the flux weakening mode will start. For the same generator rotational speed, MAP can provide more power to the DC-bus than generator is controlled under the MSLCP mode. For one tidal current speed, the needed rotational speed is different to reach the MAP and MSLCP control. For example, the tidal speed $3.6m/s$, if we operate the generator in MSLCP mode, the rotational speed should be controlled at $45.6tr/min$ as point K shown. If the generator is operated with MAP mode, the rotational speed should be controlled at $44.6tr/min$ as point H shown. When the tidal current speed is too big, such as $4.5m/s$, the turbine can produce $1MW$ or more power, however the machine converter system can't deliver this power because of the limitation of converter current and voltage. If we assume that the turbine rotational speed is controlled correctly with the tidal current speed, MAP mode is better than CP mode because of the power production. However, because the maximum power achieved by this control mode is bigger than $1MW$, the generator should have the capability to operated in over-rated condition.
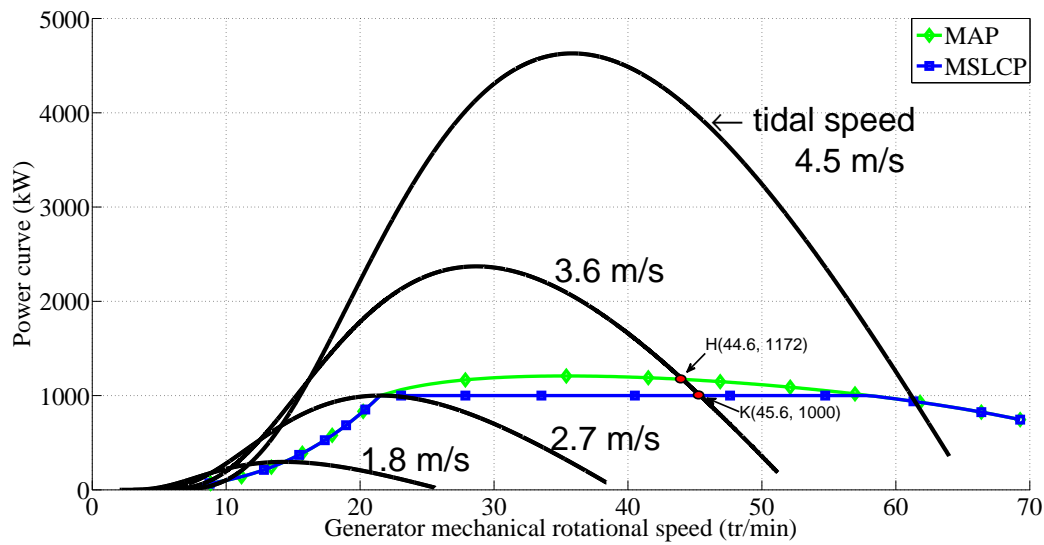
Figure 2.34 – Power curve for MAP and MSLCP

Fig. 2.35 shows the efficiency curves of the generator "A" when it is operated in MAP mode and MSLCP mode in FW region. The figure shows that MAP mode has better efficiency than MSLCP in majority speed range of flux weakening region. It should be addressed that better efficiency dose not mean smaller losses here. Because the machine total harnessed power is bigger than constant rated power. Fig. 2.36 shows the machine losses in FW region with the control mode of MAP and MSLCP. The iron losses of MAP mode is much bigger than that of

MSLCP mode. The copper loss will not change in FW region for MAP mode because it always operated at the current limit.
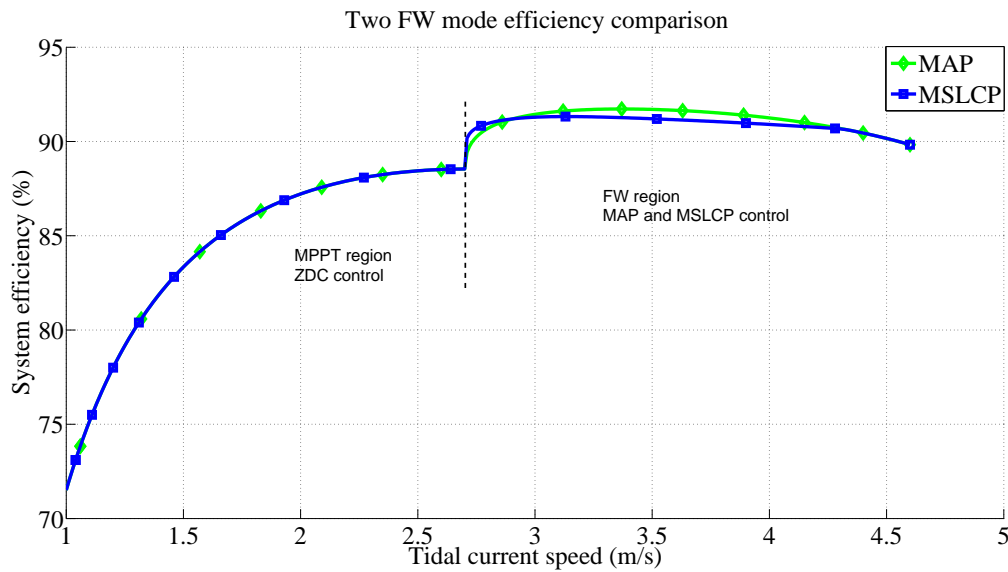
Figure 2.35 – Efficiency comparison of MAP and MSLCP
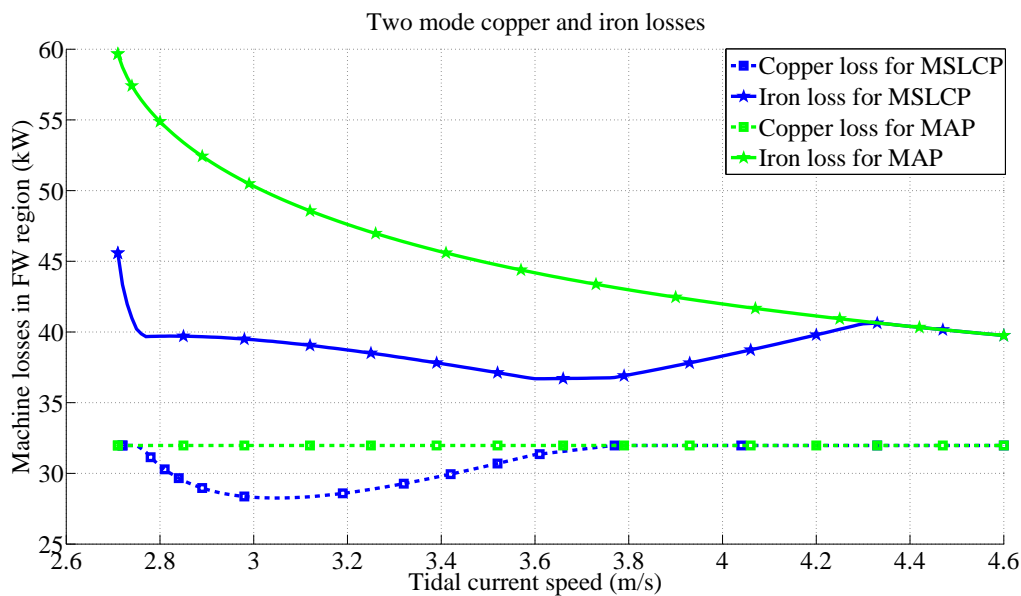
Figure 2.36 – Machine losses in FW region of MAP and MSLCP

2.7 Generators "A" and "B" cost performance comparison: MSL control in MPPT and MSLCP in FW region

In the last section, it has discussed the efficiency evolution for different control strategies. MSL control strategy can obtained the best system efficiency in MPPT and FW region (CP

mode). The results show that the system can't fulfill the completed range of CP control if the converter size are too small. In order to have full range constant power control, the converter size should big enough to have CPSR equal to $2.92(\frac{6.576}{2.252})$ for generator "A". The converter size has very strong influence to the system cost and efficiency(especially for FW region). In this section, the generator "A" and "B" full speed range efficiency are compared. Each generator has its own converter size (voltage and current limitation). The voltage limitation are the same (690 phase to phase RMS value) for the two generator. The current limitations are calculated to have full CP mode operation for each generator. Those currents are the minimum value to have CPSR equal to $2.92(\frac{6.576}{2.252})$.

From the Eq.2.127, it shows there are freedom of current and voltage combination to obtained the needed CPSR. Normally, in renewable energy MW range system, converter with $690V$ phase to phase RMS value is commonly used [80]. Therefore, the voltage limit is fixed to $563V$ ($\sqrt{2}\frac{690}{\sqrt{3}}$). Then the needed current limits are shown as Table. 2.10. The same process is applied to generator "B". The parameters of generator "B" is shown in Table. 2.9. It should be noted that generator "B" has 1% lower efficiency at rated speed than generator "A". We get the converter size for generator "B" as Table. 2.11 shown. As the inductance of generator "B" is $1mH$ less than generator "A", in order to obtain the same CPSR, the converter should be bigger than that of generator "A". We applied MSL to the two generator for full tidal speed range. For selected converter and machine system, MSL will has better efficiency than others control strategies. Fig. 2.37 shows the efficiency curve of the two generators. Generator "A" is the machine which has maximum efficiency at rated operating condition through preliminary design. However, in the MPPT region, it has smaller efficiency than the generator "B". In the FW region, the efficiency generator "B" is smaller than generator "A".

Symbol	Description	Value
ψ_{PMo}	Outer stator magnet flux linkage	$6.26Wb$
ψ_{PMi}	Inner stator magnet flux linkage	$5.85Wb$
L_{do}, L_{qo}	Outer stator *dq-axis* inductance	$5.72mH$
L_{di}, L_{qi}	Inner stator *dq-axis* inductance	$5.77mH$
R_{cuo}	Outer stator resistance	0.042Ω
R_{cui}	Inner stator resistance	0.044Ω
p	Pole pair	40

Table 2.9 – Control parameters of generator "B"

Stator	$\hat{V}_{max}(V)$	$\hat{I}_{max}(A)$	$S_{conv}(VA)$	Cost (k)€
o	563	758	6.4e5	77.7
i	563	681	5.75e5	72

Table 2.10 – Converter size to have complete CP range for generator "A". S_{conv} are the minimum apparent needed to have full range MSLCP control.

Stator	$\hat{V}_{max}(V)$	$\hat{I}_{max}(A)$	$S_{conv}(VA)$	Cost (k) €
o	563	891	7.5e5	86.8
i	563	801	6.76e5	80.7

Table 2.11 – Converter size to have complete CP range for generator "B". S_{conv} are the minimum apparent needed to have full range MSLCP control.
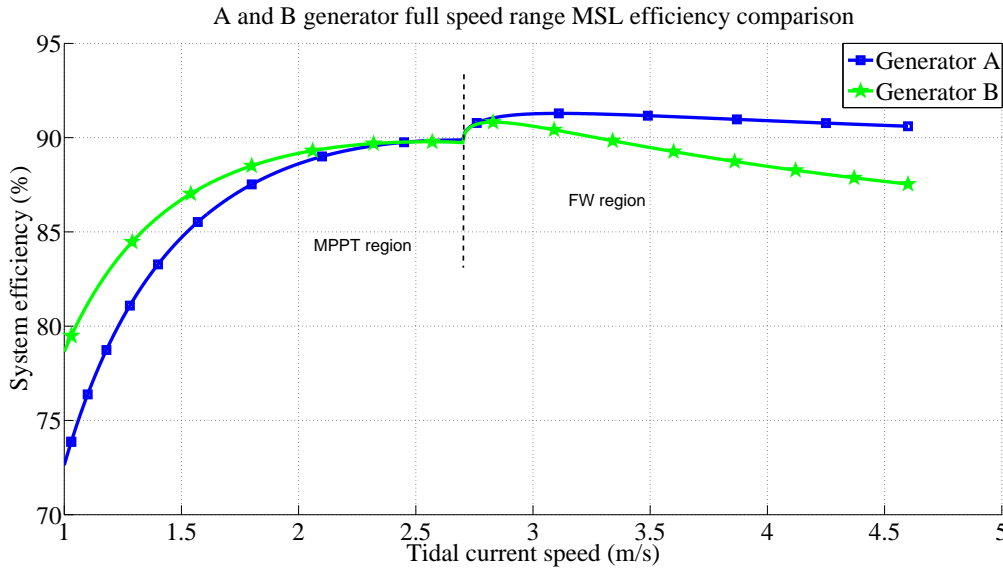
Figure 2.37 – Generator "A" and "B" efficiency comparison

From the efficiency curve, it is difficult to decide which machine is better. For a tidal farm which the majority time of one year is low speed tidal current , generator "B" may be a better solution for totally energy output of one year. The generator cost of "B" machine is $23k$€less than generator "A" shown in Fig. 2.7. However, the cost of converters for "B" machine is $18k$€more than that for generator "A". That means the total system cost of generator "B" is less $5k$€than the cost of generator "A" system. Therefore, through preliminary design, the generator which has maximum efficiency at rated operating condition may be a less cost effective solution. In order to find a cost effective solution for a specific tidal farm, the generator design should take into consideration the generator cost, converter cost, tidal current speed frequency into consideration to find cost effective solution [81]. In the next Chapter, an optimization generator design process will be presented which takes control strategy MSL and MSLCP, tidal speed frequency, converter cost into consideration for a full generator converter system operation circle. The objectives focus on maximizing the annual energy output and minimizing the system cost to improve the cost effective performance of tidal energy system.

2.8   Summary

In this chapter, firstly, an analytical preliminary generator design model is developed at the rated power condition. The external diameter of the generator is fixed at $3m$. Then, all the

generator parameters varies with the bore radius R_{so} depending on the fixed experience rules, such as the thickness of yoke equals to 30% of the pole pitch and air gap length equals to $2R_{so}/500$. The generator efficiency, cost, inductance and temperature variation are illustrated with the the variation of bore radius R_{so}. The active part cost and length of machine will decrease with the increasing of R_{so}. Therefore, the bigger R_{so} will result higher torque active mass density and higher torque volume density. However, when the generator R_{so} is bigger than a certain value, the generator efficiency decreases sharply. In order to comply with the thermal limitation, R_{so} can't be chosen too big or too small. In additional, bigger R_{so} leads the generator slot height and width ratio smaller. As a consequence, the inductance of machine will decrease with R_{so}. For direct drive fixed pitch tidal current turbine, flux weakening control is normally used to limit the turbine power when the operation speed is higher the rated value. Therefore, the flux weakening capability of machine should be taken into consideration. That means the inductance of machine should be selected properly. Too small inductance needs big size of converter to have enough flux weakening capability.

Secondly, the generator mathematical model is developed in dq-reference. The most common vector current control strategies both in MPPT and FW region are explained in detail. Then the control strategies are applied to the generator "A" which has maximum efficiency at rated power. In the MPPT region, MSL always has better efficiency than other control strategies. MSL strategy with constant power called MSLCP seems also to be the most appropriate one for FW region.

Thirdly, performances of generator "A" and another one having 1% lower efficiency at rated power are compared using MSL strategy. In MPPT region, generator "B" has better efficiency while in FW region generator "A" is better. Therefore, design a generator which has maximum efficiency at the rated power may not be good solution for a variable speed operation system such as tidal energy system. Furthermore, machine design should take full consideration of the converter cost and flux weakening capability for tidal current energy application. In addition, in order to finally design an effective generator-converter system for a specific tidal current site, the tidal current speed frequency should be included in the machine design process.

In the follow chapter, the Particular Swarm Optimization (PSO) algorithm is used to design a generator converter system which takes the tidal speed frequency into consideration for a specific tidal current site. The generator will be always operated with MSL control strategy to improve the system efficiency and the generator converter system has capability to provide the needed CPSR. The subject is to design the generator converter system which produce the energy with optimal system cost.

<div style="text-align: right; font-size: 3em; font-weight: bold;">3</div>

Joint optimization of DSCRPMG and converter for a specific tidal current energy farm

3.1 Introduction

Conventional machine design method is based on the experience rules of manufacturers. The designers start by heuristically selecting values of machine parameters, and then follow an iterative tuning process trying to achieve design objectives. Through the "try" process, it is difficult and time consuming to find an optimal set of machine design parameters which has high efficiency, low cost and suitable flux weakening capability. In addition, designing the generator for nominal operation condition may not be enough to find the high cost performance machine because the generator will not be operated at nominal condition in the majority time of its life circle for tidal current energy system. From the last chapter discussion, it is known that the converter can also influence the design of generator. The aim of this chapter is to present a method for tidal current energy generator optimization design taking into account the converter and tidal speed frequency to improve the performance of the electrical conversion chains.

For a given tidal farm site, the average tidal current speed can be predicted in long term. Therefore, the tidal current speed frequency is obtained. Each tidal current speed value has its corresponding turbine rotational speed and torque to achieve MPPT and power limitation (FW). That means the generator operation time for each tidal current speed and torque is known for one year. Knowing the system efficiency, the system annual energy output can be calculated.
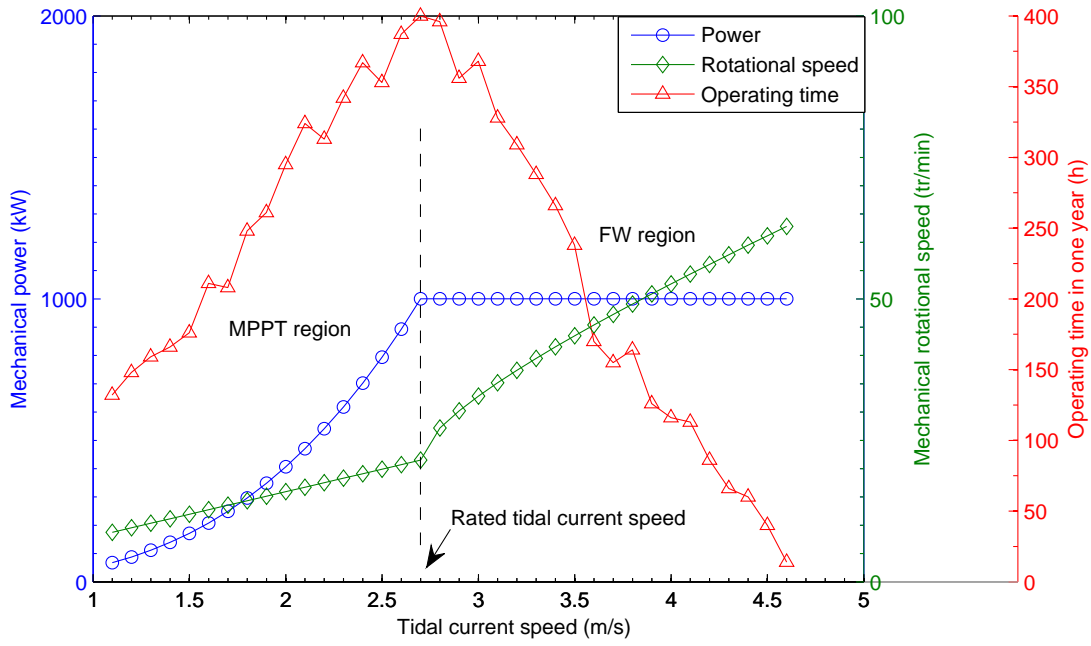
Figure 3.1 – Turbine operating points

The tidal current speed is discretized into N_{pts} operation points between the cut in speed and cut out speed. Then the fixed pitch turbine operation points can be shown in Fig. 3.1. The generator operation point can also be formulated as below:

$$\textbf{Operation} \quad \textbf{point} = (t_j, v_j)\underrightarrow{turbine}(t_j, T_j, \omega_{m,j})_{j\in[1;N_{pts}]} \tag{3.1}$$

where t_j is the operation point operating time in one year. v_j, T_j and $\omega_{m,j}$ are the tidal current speed, mechanical torque and mechanical rotational speed for operating point j respectively.

Generator optimization design is a compromise process as discussed in chapter 2. In many situation the objectives of the design conflict with one another. For example the high power density and low magnet volume [82]. One specification can't be improved without decreasing other performances. The complex relationship between many geometrical parameters makes the generator optimal design become a multi-objectives optimization problem. Some optimization algorithms are well applied to multi-objectives machine design problems, for example Genetic Algorithm (GA) and Particle Swarm Optimization (PSO) [83]. In this chapter, the DSCRPMG is optimized combining with the tidal operating point and control strategy to provide a high cost performance tidal energy generator converter system solution. In this thesis report, the PSO algorithm is used to realize the generator multi-objectives optimization. The two stators are parallel connected to the DC bus with two rectifiers, see Fig. 1.12.

3.2 Optimization objectives variables and constraints

Every optimization problem comprise of three parts: one or multi-objectives, a set variables, and constraints. For a randomly set of variable values, the objective functions can be calculated. Through comparing the objective values found by different sets of variables (minimum or maximum), the optimal set of variables are found. The calculation process should satisfy the constraints posed by mechanical, magnetic and electronic phenomenons in machine optimization problem.

A generalized formulation of an multi-objectives optimization problem is expressed as following [84, 85]:

$$
Problem \begin{cases} Min \quad F(x) = \begin{bmatrix} f_1(x) \\ f_2(x) \\ \vdots \\ f_b(x) \end{bmatrix} \\ g_i(x) \leq 0 \qquad i = 1, \cdots, l \\ h_j(x) = 0 \qquad j = 1, \cdots, m \\ x = [x_1, x_2, \cdots, x_n] \\ x_k^{min} \leq x_k \leq x_k^{max} \qquad k = 1, \cdots, n \end{cases} \tag{3.2}
$$

$F(x)$ is the objectives vector and there are b objective functions elements inside. Objective functions depend on the unknown parameters x. x is a n dimension vector containing the unknown parameters of the problem model. Each unknown parameters can be chosen between their corresponding minimum and maximum range. In electrical engineering, the unknown parameters can be both physical quantities (apparent power, induction, magnetic field...) and design parameters (machine geometrical dimensions, number of turns...). g_i and h_i are the inequality and equality constraints respectively which can represent the desired performances, such as system efficiency, power factor, temperature...

Pareto front curves represent the best approach to analyze multi-objective optimization problems [82, 86, 87]. It is formed by the set of Pareto optimal candidates and it also reflects the fact that it is not possible to reduce one of the objective function without increasing another objective. Pareto front curve is the best achievable compromise between the objective functions f1 and f2 according to the given specification. An example of Pareto front for two objectives (f_1 and f_2) is shown in Fig. 3.2 where the circles represent Pareto optimal points. The cross point represents a solution which is not a Pareto optimal solution since it is dominated by six circles.
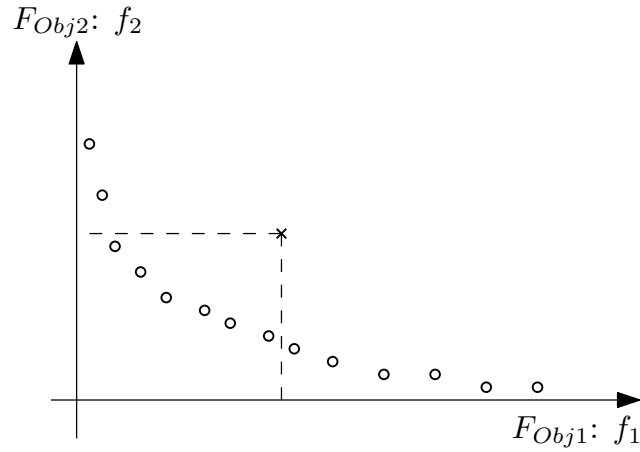
Figure 3.2 – Example of Pareto front optimal points (represented by circles) and a dominated point (represented by a cross).

3.2.1   Objectives

F_{Obj1}**: Maximize annual energy output**

For a selected tidal current energy site, the average tidal current speed is predictable. Based on the tidal current speed profile, the direct drive generator system operating point for one turbine characteristic can be decided. Each operating point, the generator needed torque, rotational speed and working time are known. The power harnessed by turbine will transfer to the electrical conversion chain through the shaft connection. The machine converter system will unavoidable to result some losses. The losses include copper losses, iron losses and converter losses (generator side). The mechanical losses are neglected in our optimization model. Only the generator side converter losses are taken into consideration. Therefore, the delivered electrical power for operating point j can be expressed as:

$$P_{elec,j} = T_j \omega_{m,j} - P_{cu,j} - P_{iron,j} - P_{conv,j} \tag{3.3}$$

As the two stators are parallel connected to two converters, the losses of converter $P_{conv,j}$ is the total loss of the two converters. Every turbine operating point has its operating time. Therefore, the rest energy which is transferred to DC bus in one year can be expressed by the following equation:

$$F_{Obj1}: \quad E_{elec} = \sum_{j=1}^{N_{pts}} P_{elec,j} t_j \tag{3.4}$$

The output energy quantity will directly influence the benefits of a tidal current energy project. Logically, the first objective is to maximize the annual energy output.

F_{Obj2}**: Minimize machine and converter cost**

Tidal current energy has been claimed as an attractive and advantageous resource for power generation in comparison with other renewable resources due to its predictable and high power density characteristics. However, the investment of tidal power plant construction is much higher than wind power even though some tidal projects have already reached a relatively mature stage in the last decade. Therefore, reduce the system investment cost is a valuable research subject for tidal plant projects. In this thesis report, the machine, machine supporting structure and converter cost are considered. Based on the generator and converter cost model Eq.2.79 and Eq.2.80 in last chapter, the total electrical conversion chain investment can be expressed as:

$$F_{Obj2}: \quad C_{TGC} = C_{generator} + C_{structure} + C_{convo} + C_{convi} \tag{3.5}$$

where C_{convo} and C_{convi} are the cost of converter for outer and inner stator respectively. C_{TGC} is the total cost of the system. Minimizing the generator and converter system cost is the second design objective of the optimization. $C_{structure}$ is the cost of machine supporting structure which can be approximately expressed as the equation below:

$$C_{structure} = \frac{1}{2} C_{str,ref} \left[(\frac{D_{ext}}{D_{ref}})^3 + (\frac{L}{L_{ref}})^3 \right] \tag{3.6}$$

This machine supporting structure cost equation was proposed by the doctor A.Grauers in 1996 [47] and cited by some paper [88, 89] . It is rare to find machine supporting structure cost model in literature. Of course, this machine supporting structure cost equation is only an approximate model and it is firstly applied to conventional single stator machine. Some times the real cost of machine supporting structure is uncountable, for example, when the machine diameter is above the maximum possible completely transportable value, it needs to assemble the pieces at the local offshore site of tidal energy farm. However, this cost model has its reasonable aspect that the structure cost and manufacturing difficulty will increase in relation with the machine diameter and length. It is logical to add the machine structure cost into the optimization model. It should be noted that the supporting structure cost is not considered in the machine preliminary design stage in last chapter. $C_{str,ref}$ is the reference cost of structure. D_{ref} and L_{ref} are the reference machine structure diameter and length. In this thesis, $C_{str,ref} = 20000€$, $D_{ref} = 2m$ and $L_{ref} = 1m$ are applied [47].

Final objective 1 $F_{obj,final1}$: Maximize revenue for 20 years

The investment cost and energy is a trade off problem. The machine converter system can't be optimized in one dimension (cost) without worsen in another (energy). There are set of possible candidate solutions known as Pareto front optimal solution. Choosing the final design solution from the Pareto front is a compromise task between the design objectives. In this

thesis, it is assumed that the tidal current speed will repeat every year for a 20-years period. Using the candidate solution points in Pareto front, the revenue for 20 years can be analyzed by post-calculation. It is also assumed that the turbine cost $C_{turbine}$ is $1M$€ [89] and the price of electricity (decided by electricity company like EDF) will not change for 20 years. Then, the revenue can be calculated as:

$$F_{obj,final1}: \quad R_{revenue} = 20E_{elec}P_{price/kWh} - C_{TGC} - C_{turbine} \tag{3.7}$$

There is a maximum revenue design solution in Pareto front. In all figures of this Chapter, the red point refers to the maximum revenue design solution.

Final objective 2 $F_{obj,final2}$: Minimum cost energy ratio €/kWh

Minimizing per kWh cost is another generally used method to decide the final design solution from the Pareto front which is defined as:

$$F_{obj,final2}: \quad Ratio = \frac{C_{TGC} + C_{turbine}}{E_{elec}} \tag{3.8}$$

It is also an important index to evaluate the cost performance in renewable energy system design [90–92]. Another final design solution choosing criteria is given out which the candidate generator results in minimum cost energy ratio. Minimum cost energy ratio means best cost performance. In all figures of this Chapter, the magenta point refers to the minimum cost energy ratio design solution.

3.2.2   Variables

In generator preliminary design process, some assumptions of machine geometry relationship have been taken such as the power ratio between the two stator and the thickness of yoke. In this Chapter, those parameters will be optimized. Fig. 2.1 shows the generator geometries except the length of machine. The machine external radius R is fixed as $1.5m$. Then the other geometries are design variables. Table. 3.1 lists all the design variables together. The variables design range are also indicated in this table.

The lower limit of power percentage of outer stator k_1 is 0.5 because of that normally the outer stator is bigger than inner stator. For the pole pairs variable, even number is taken in the variable range because it is assumed that the number of slot per pole per phase m equals to 1.25. In order to avoid the non-integer number of slots, the pole pairs number should be an even number. The geometry parameters vary continuously between the optimization range.

It should be addressed that the conductor number in one slot N_{sloto} and N_{sloti} in our optimization process is not integer. It is considered the windings are connected in series. Non-integer number of conductor is impossible realize. However, this problem can be adjusted

Table 3.1 – Optimization parameters.

Symbol	Description	Region	Unit
k_1	Rated power percentage of outer stator	[0.5;0.99]	-
p	Pole pairs	[2;200]	-
k_t	Teeth open ratio	[0.2;0.8]	-
R_{so}	Outer stator bore radius	[0.5;1.5]	m
h_{yokeo}	Thickness of outer stator yoke	[0.1;50]	cm
h_{sloto}	Height of outer stator slot	[0.1;50]	cm
l_g	Airgap length	[1;50]	mm
h_m	Thickness of magnet	[1;50]	mm
h_r	Thickness of cup rotor	[0.1;100]	cm
h_{yokei}	Thickness of inner stator yoke	[0.1;50]	cm
h_{sloti}	Height of inner stator slot	[0.1;50]	cm
L	Active machine length	[0.01;5]	m
N_{sloto}	Conductor number in one outer slot	[0.1;30;]	-
N_{sloti}	Conductor number in one inner slot	[0.1;30]	-
S_{convo}	Apparent power of the power converter for outer stator	[0.01;5]	MVA
S_{convi}	Apparent power of the power converter for inner stator	[0.01;5]	MVA

through post calculation with changing losses and inductance which is illustrated in Appendix. C.

The converter apparent power is also a parameter to be optimized. The machine phase to phase RMS voltage is fixed to $690V$. As consequence, the rated current can be calculated with the converter apparent power value. Therefore, the voltage limitation and the current limitation are:

$$\begin{cases} V_{ratedk} = \frac{690}{\sqrt{3}} \\ I_{ratedk} = \frac{S_{convk}}{3V_{ratedk}} \end{cases} \tag{3.9}$$

The apparent power is the image of the converter cost and it also indicates the power deliver capability. Hence, this parameter is very important to be optimized.

3.2.3 Constraints

The generator optimization design problem is based on an analytical model. The optimization algorithm randomly generate a set variable parameters in the variable range. This randomly set of parameters may not be realizable because of the mechanical or electrical limitation. Sometimes the limitation could be because the solution investment is too high and it is no longer reasonable. In order to reduce the variable search space, some constraints are introduced to obtain the realizable solution.

Total cost constraint

The total cost of the electrical conversion chain is limited. Because the system is no longer interesting for investment when the total cost exceed a certain value. The limit value is fixed as

$1M$€:

$$C_{TGC} \leq 1M€ \tag{3.10}$$

Geometry constraints

The physical geometries constraint can guarantee the machine optimization design solutions are realizable. The sum of outer stator bore radius, thickness of yoke and height of slot should not surpass the external radius:

$$R_{so} + h_{yokeo} + h_{sloto} \leq R \tag{3.11}$$

The radius of shaft should be bigger than a certain value. This value is fixed as zero. In fact, the radius of shaft can not be too small. However, it is really difficult to give out a real precise value of this limit. This constraint is expressed as follow:

$$\begin{cases} R_{shaft} = R_{so} - h_r - 2(l_g + h_m) - h_{yokei} - h_{sloti} \\ R_{shaft} \geq 0 \end{cases} \tag{3.12}$$

Furthermore, we also added the constraint of the ratio between thickness of yoke and pole pitch. This constraint can ensure that the calculation of flux density in yoke will be not totally wrong. In the mathematical analysis design model, we assume that the flux linkage in the yoke is half of the total flux linkage of one pole pitch. If the thickness of yoke is too big, the flux density near the surface of machine is almost 0. However, the flux density in the side near slots is much bigger than 0. Therefore, the iron losses model is no longer correct. In order to reduce the iron losses, the algorithm tends to relatively increase the thickness of yoke to reduce the flux density especially for the inner stator. Increasing the thickness of inner stator will decrease the inner stator average yoke flux density with only increasing the material of core and without changing the other performance. Approximately, this limitation is formulated as:

$$\begin{cases} h_{yokeo} \leq \tau_{po} \\ h_{yokei} \leq \tau_{pi} \end{cases} \tag{3.13}$$

In magnetic point of view, the smaller air gap length is better for the flux circuit. However, the air gap length can not be too small because of manufacture process and the running vibration. The minimum air gap length is expressed with the relation of bore radius as follow:

$$l_g \geq \frac{2R_{so}}{500} \tag{3.14}$$

Magnetic constraints

1. **Saturation**

   The magnetic field is created by the magnet and the armature current in a permanent magnet machine. The different machine part has different magnet field. For every type of core material there is a maximum flux density limitation. Below this limitation value, the flux density will remain in the linear domain. The core permeability will decrease sharply when the magnetic field surpass this value. For the core type M400-50A, the saturation of flux density is $1.4T$. This constraint can be express as follow:

$$\forall \quad \text{operation point } j, \quad \hat{B}_{x,j} \leq 1.4T \tag{3.15}$$

   where x represent different parts of the generator. In our generator model, the flux density is verified in five zones Fig. 2.1: the outer stator teeth, outer stator yoke, cup shape rotor, inner stator teeth and inner stator yoke. The generator phase currents will change with the operating point. Therefore, it should guarantee that for all operating point, there are no resultant flux density saturation come out.

2. **Demagnetization**

   The demagnetization phenomenon of the permanent magnets is a remarkable problem in permanent magnet machine application. The irreversible demagnetization of PM can reduces or sets to zero the flux density of PM, so as to cause the deterioration of the machine's performance. Hence, the machine designer should verify that the machine can be operated with no risk when it works normally or even in short circuit condition. The magnet demagnetization is usually caused by high temperature and high reverse armature flux density. In short circuit condition, all the phase current is used to weak the flux. Therefore, the demagnetization constraint are expressed in terms of flux density amplitude created by the stator short circuit current:

$$\begin{cases} \hat{B}_{armo,SC} \leq B_{eo} - B_d \\ \hat{B}_{armi,SC} \leq B_{eo} - B_d \end{cases} \tag{3.16}$$

   where $\hat{B}_{armo,SC}$ and $\hat{B}_{armi,SC}$ are the armature flux density under the Short Circuit (SC) condition. The SC current amplitude can be expressed as $\frac{\psi_{PM}}{L_s}$. The red curve in Fig. 2.20 shows the demagnetizing current limit. $\hat{B}_{armo,SC}$ and $\hat{B}_{armi,SC}$ are calculated as follow [89]:

$$\begin{cases} \hat{B}_{armo,SC} = \frac{3}{2}\frac{4}{\pi}\frac{\psi_{PMo}}{Lso}\frac{N_o}{2p}\frac{\mu_0}{l_{gefo}+h_m} \\ \hat{B}_{armi,SC} = \frac{3}{2}\frac{4}{\pi}\frac{\psi_{PMi}}{Lsi}\frac{N_i}{2p}\frac{\mu_0}{l_{gefi}+h_m} \end{cases} \tag{3.17}$$

B_d depends on the remanent flux density B_r, intrinsic coercive field H_c and the magnetic

permeability μ_{PM} and is given by:

$$B_d = B_r - \mu_{PM}H_c \tag{3.18}$$

The values of B_r, H_c and μ_{PM} are decided by the treated magnet. Their values are given in Table. 2.1.

Electrical constraints

In the last chapter, the converter current and voltage limitation circles which are introduced by the converter have been discussed. As the converter apparent power is an optimal variable parameter, the current limitation will change with the apparent power. Those constraints are made to ensure that the design solution of generator converter system will have the capability to deliver the power for every operation point. The voltage and current limitation principle are shown in Fig. 2.20 and they can be formulated as:

$$\forall \quad \text{operation point } i, \quad \begin{cases} \sqrt{v_{do,j}^2 + v_{qo,j}^2} \leq \sqrt{2}V_{ratedo} \\ \sqrt{v_{di,j}^2 + v_{qi,j}^2} \leq \sqrt{2}V_{ratedi} \end{cases} \tag{3.19}$$

$$\forall \quad \text{operation point } i, \quad \begin{cases} \sqrt{i_{do,j}^2 + i_{qo,j}^2} \leq \sqrt{2}I_{ratedo} \\ \sqrt{i_{di,j}^2 + i_{qi,j}^2} \leq \sqrt{2}I_{ratedi} \end{cases} \tag{3.20}$$

In addition, in order to achieve constant power control in flux weakening region, the constraints of CPSR are added for inner and outer stator. It assures that the generator converter system has the capability of constant power control for the maximum needed speed of turbine. This constraint is expressed as follow:

$$\begin{cases} CPSR_o \geq \frac{\omega_{m,cpm}}{\omega_{m,base}} \\ CPSR_i \geq \frac{\omega_{m,cpm}}{\omega_{m,base}} \end{cases} \tag{3.21}$$

The calculation of $CPSR_o$ and $CPSR_i$ are shown in Eq.2.127.

Winding temperature constraint

High temperature can cause various consequences, such as irreversible aging of insulation, part or full loss of magnetization of the magnets. For these reasons, the temperature rise (relative to ambient) must be forced to be below a limit value. A thermal model is presented in Chapter 2. The heating will be calculated based on the copper and iron losses. In the thermal model, the winding temperature is always higher than the iron temperature. Therefore, we will formulate this constraint with the temperature in winding. The thermal standard Class

F ($155°C$) is adopted. The ambient temperature is considered equal to $20°C$. The maximum winding temperature should be lower than $155°C$ for inner and outer stator:

$$\begin{cases} T_{cuo} \leq 155°C \\ T_{cui} \leq 155°C \end{cases} \qquad (3.22)$$

3.3 Optimization implementation

Fig. 3.3 shows the flow chart of the machine and converter system multi-objectives optimization process. Firstly, the machine geometries and converter apparent power are randomly generated in the region of their corresponding upper and lower boundary. Those randomly generated parameters may not be realizable from the mechanical point of view. The optimization algorithm will then regenerate another set value of the variables. Once the parameters satisfy the geometry constraints, the machine parameters can be calculated such as inductance, flux, mass.... From the generator active mass and converter apparent power, the cost of the system can be calculated. The machine is controlled with MSL control strategy which has discussed in the Chapter 2 for a certain turbine torque speed profile as shown in Fig. 3.1. For each operating point j, the *q-axis* current reference i_q can be obtained from the the needed torque. Then, the *d-axis* current reference i_d will be found by using the MSL control strategy. Then the electrical, magnetic and thermal constraints will be verified. If not all the operation points satisfy the constraints, the optimization algorithm will generate another set of machine and converter parameters once again. If all the operation points satisfy the constraints, it means that generator with this set of parameters is realizable and suitable for controlling this torque speed profile. The efficiency can be calculated for every operating points. As tidal current speed is predictable, the operating point work time t_j is known. Therefore, the energy for one year can be calculated. The annual energy is treated as the first objective. The algorithm will stop when it reaches a predefined stopping criteria which, normally, is simply the maximum number of allowed iterations. The maximum number of iteration should ensure the optimization achieve good convergence. After a certain value of iteration, the dominate Pareto front is obtained.

The number of particles in one swarm should be properly chosen. A big swarm size will generate variables in large scale of the search space for every iteration. If the allowed number of iteration is fixed, large number of particles will achieve a good optimization result. On the contrary, big size of particles increase the calculation complexity per iteration, therefore, more time needed for the same iteration. Theoretically, big size of swarm and bigger number of iteration will obtained more precise results if the time is available. However, in reality, after a certain size of swarm and a suitable number of iteration calculation, the result will have an acceptable convergence. The size of swarm and number of iteration can be treated as an optimization sensibility.
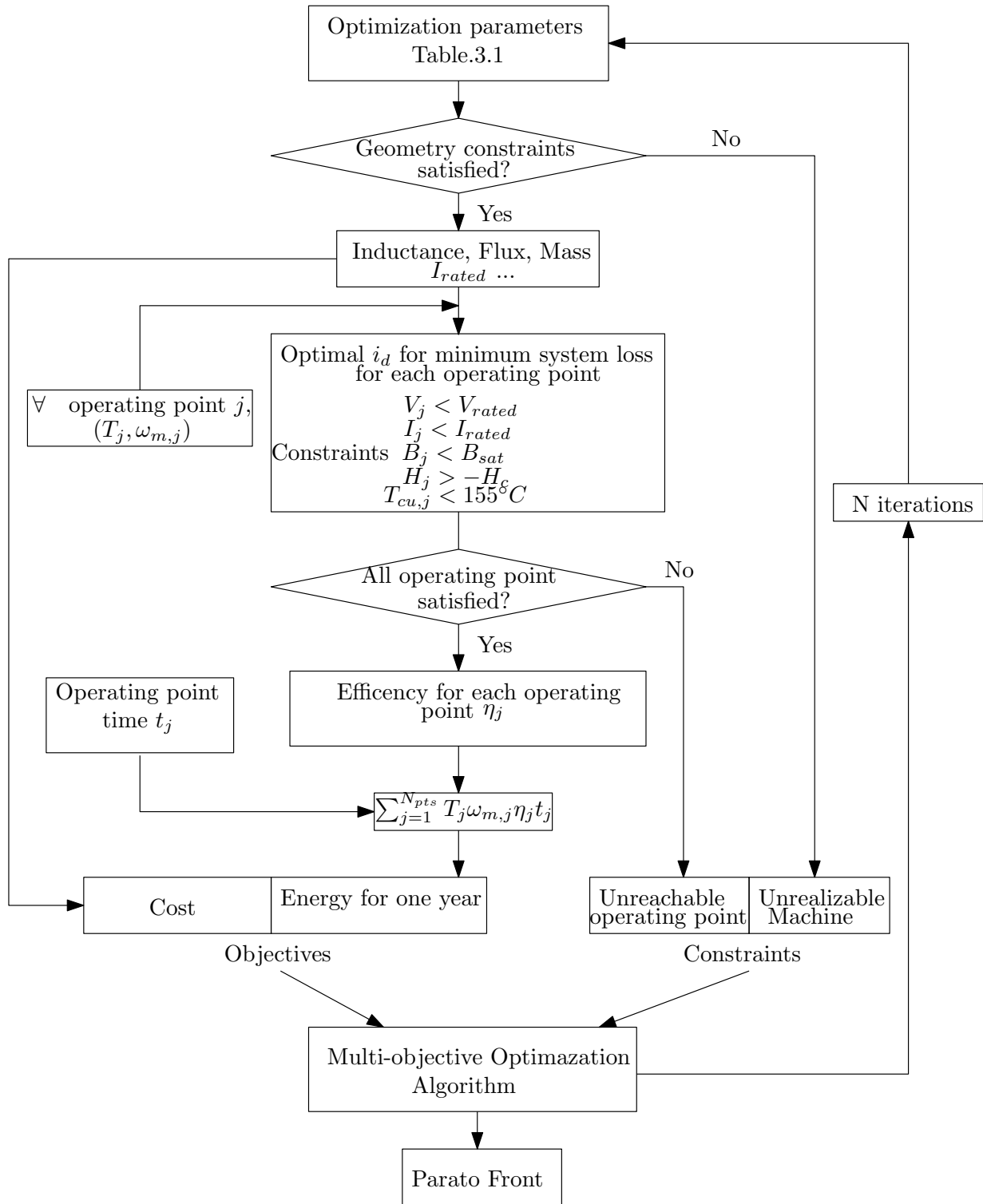
Figure 3.3 – Optimization flow chat

The most frequently used algorithms for multi-objective optimization are Non-dominated Sorting Genetic Algorithm (NSGAII) and Multiple Objective Particle Swarm Optimization (MOPSO). From the comparing research done before, it shows that MOPSO outperforms NS-GAII in many complex problem optimization. MOPSO has not only shorter convergence time but also higher precision [89, 93, 94]. The MOPSO program version which is used in this thesis

was implemented in Matlab by Doctor J. Aubry [89].

The principle of Particle Swarm Optimization is detailed in Appendix. B.

Some assumptions should be also emphasized in optimization design process:

— Two stators phase wingdings are star connected and independently connected to the DC-bus, line to line effective voltage $U = 690V$.

— Total rated power $P_n = 1MW$.

— Rated rotational speed $n = 21.5rpm$.

— Number of phase in each stator $q = 3$.

— Number of slot per pole per phase $m = 1.25$.

— Slot fill factor $k_f = 0.65$ [43].

— External stator radius $R = 1.5m$.

— The outer and inner PMs thickness are identical. The outer and inner air gap length also have the same value.

— Iron type M400-50A (saturation flux density $\hat{B}_s = 1.4T$) is used. Neodymium-Iron-Boron Magnets type is N35SH $B_r = 1.14T$ @80°C. Intrinsic coercive force $H_c = 876kA/m$.

— Iron lamination factor or stacking factor $k_{Fe} = 0.97$. Normally it is between 0.95 and 1 [44].

— Generator design and control are only based on the fundamental flux density harmonic.

Comparing to the assumption in preliminary design stage, the power factor becomes a result obtained by the optimization variable parameter S_{conv}. Teeth open ratio k_t also become an optimization variable parameter. The experience predefined rules, such as $h_{yoke} = 0.3\tau_p$, $h_r = 2h_{yoke}$ and $\hat{B}_g = 0.8T$, are no longer applied in the optimization process. In fact, those parameters becomes optimization variable parameters or results of optimization variable parameters.

3.4 Results analysis

3.4.1 Optimization parameters variation

The constant parameters used in the optimization process are the same as in preliminary design stage which are shown in Table. 2.1. This set of parameters are treated as reference parameters. The swarm size is fixed to 1000 and the number of iteration is 1500. In order to guarantee a good convergence, the algorithm will run the 10 times and then the 10 times results are merged into one final result. The following presented Pareto fronts are the final merged

result. The analytical design model is verified by Finite Element Analysis (FEA) method and it is discussed in Appendix. C.

Fig. 3.4 shows the Pareto front of the two objectives and four extreme solution generator shapes are also illustrated. In Fig. 3.4(a), the initial total cost varies with annual energy output. Every point in the Pareto front is one set of machine converter system parameter or called candidate design solution. This figure illustrate that the candidate design solution is a compromise result between the energy output and the investment. In the low energy output region, the total initial cost is also relatively low and vice versa. The cost always increase with the increasing of annual energy output. The annual energy output can be increased a lot without increasing too much of initial cost in the low energy region. However, in the high energy output region, the total initial cost increases much quicker than the annual energy output. From the discussion, it is known that higher energy output means higher initial cost and the increasing relationship is not linear. It seems like that in the low annual energy output region it prefers to increase a little cost to increase a lot annual energy output. In high energy output region, the increase of annual energy can't overcome the increase of initial cost.

The performance of generator "A" and "B" which has been discussed in Chapter 2 are also plotted in this figure. Using the parameters of those two generators, the annual energy output and investment cost can be calculated. The control strategy MSL is adopted in the full tidal speed range for the two generators. Those two generator are not optimal solutions. It confirms that generator "A" which has maximum efficiency at rated power has worse performance than the generator "B" which has 1% lower efficiency at rated power than generator "A". Generator "A" is $5000 \text{\euro}$ $(+1.3\%)$ more expensive and $40000kWh$ (-0.8%) less annual energy output than generator "B". It also proves that it is difficult to find a cost effective generator solution with designing generator only at rated power condition. For variable speed generator application, rated power and rated speed is only one operation point. The best efficiency generator for one point, usually, may not produce best energy output for the sum of all the operating points. Because the generator will not operate at rated condition point for the majority time for direct drive tidal energy application.

The four extreme design solutions in the Pareto front have the same external diameters and are represented in detail. 4 poles part are shown for each solution. From the shape of those machines, it can be seen that different design solutions have very different shape. The machine length are also very different, however they can't be illustrated in $2D$ picture. Some important parameters (more outer stator parameters) of the four solutions are given in the Table. 3.2 to help us to understand the machine shape. The lowest energy solution has bigger number of pole pairs. Therefore, there are much more slots than the other three solutions.

The final design solution $F_{obj,final1}$ and $F_{obj,final2}$ are shown with red point and magenta point respectively in all result figures in this chapter. Those design solutions are decided by the final objective function Eq.3.7 and Eq.3.8 respectively.
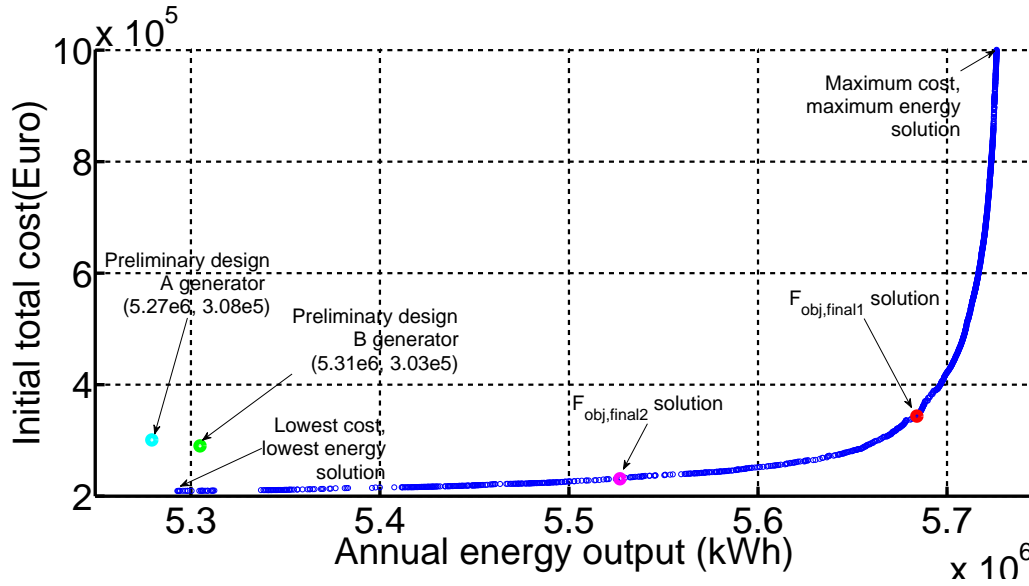
(a) Pareto front of optimization reference
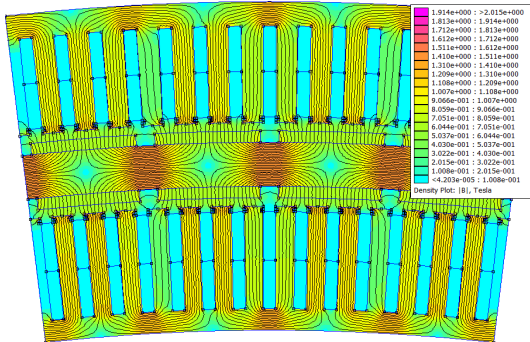
(b) Lowest investment solution
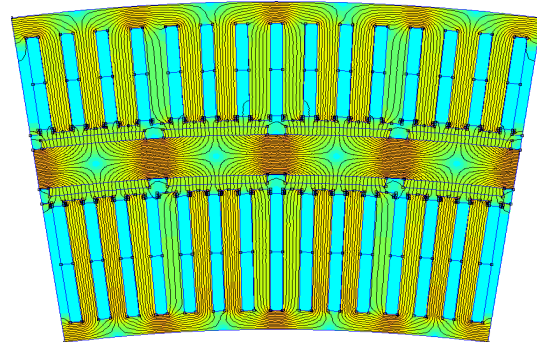
(c) $F_{obj,final2}$: Minimum €/kWh solution
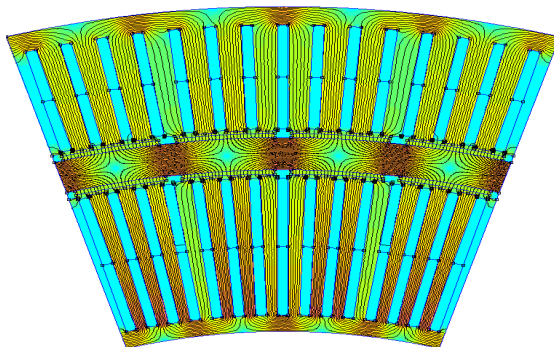
(d) $F_{obj,final1}$: Maximum revenue solution
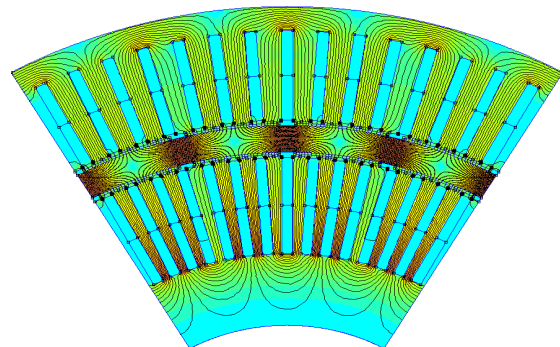
(e) Maximum energy solution

Figure 3.4 – Pareto front and four extreme solution generator shapes

Symbol	Lowest cost	$F_{obj,final2}$	$F_{obj,final1}$	Max E_{elec}
p	54	44	22	12
$R_{so}(m)$	1.415	1.390	1.251	1.150
$L(m)$	0.517	0.626	1.040	2.307
$h_{yokeo}(mm)$	17	20	36.8	73.5
$h_{sloto}(mm)$	63.5	86	208.4	272
$h_r(mm)$	31	38	65	82
$S_{convo}(MVA)$	0.6	0.62	0.67	2.96
$T/Mass(N.m/kg)$	62.9	39.3	12.2	4.24
$T/Volume(kN.m/m^3)$	121.6	100.5	60.4	27.2

Table 3.2 – The parameter changes of the lowest cost solution ("Traditional dimensioning generator"), $F_{obj,final2}$: minimum cost energy ratio, $F_{obj,final1}$: maximum revenue solution and maximum energy solution.

It is assumed that the price of electricity per kWh (0.14€/kWh) will not change for the 20 years and the tidal current annual energy output is the same for every year. The 20 years revenue variation with the two objectives are plotted as shown in Fig. 3.5. From the figure, it can be seen that there is best combination of annual energy output and initial cost to obtain maximum 20 years revenue. From the benefit point of view, the maximum energy design solution will not get the maximum revenue. The low investment may result the same revenue as the high investment. It is very interesting to analysis the Fig. 3.5(b). For every low initial cost solution (the left side of the maximum 20years revenue point), there is a higher cost design solution to get the same revenue. The benefit is a major concern for companies, hence, the design solution of the right side of after the red point are no longer interesting for investment any more. Because they need much more investment to get the same revenue.
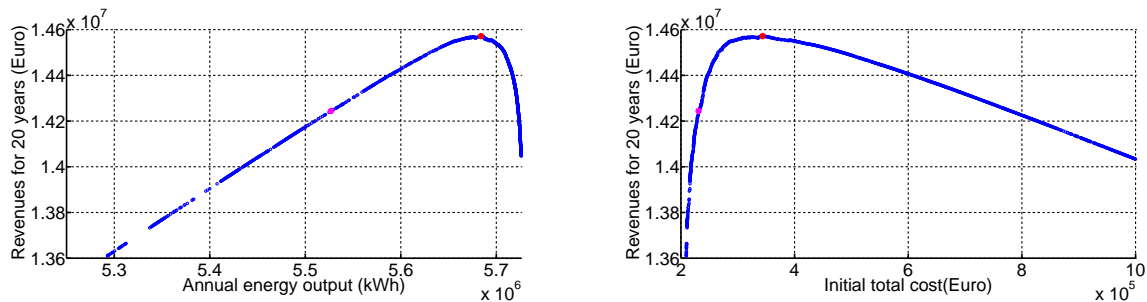
(a) Evolution of 20 years revenue vs. annual energy output

(b) Evolution of 20 years revenue vs. initial total cost

Figure 3.5 – Final objective 1: Evolution of 20 years revenue vs. objectives. Red point: maximize the 20 years revenue design solution; Magenta point: minimum cost energy ratio design solution.

Fig. 3.6 shows the variation of $F_{obj,final2}$ with the energy output and the investment. It is assumed that the $C_{turbine}$ equals to1M€. It shows that there is not so much variation of the cost energy ratio when the output energy is between $5.3 \times 10^6 kWh$ and $5.65 \times 10^6 kWh$. It is around 0.225€/kWh. When the output energy is very high, it increase sharply because of

the increasing in the initial total cost. From Fig. 3.6(b), it can be seen that the cost energy ratio increases almost linear with the initial total cost.
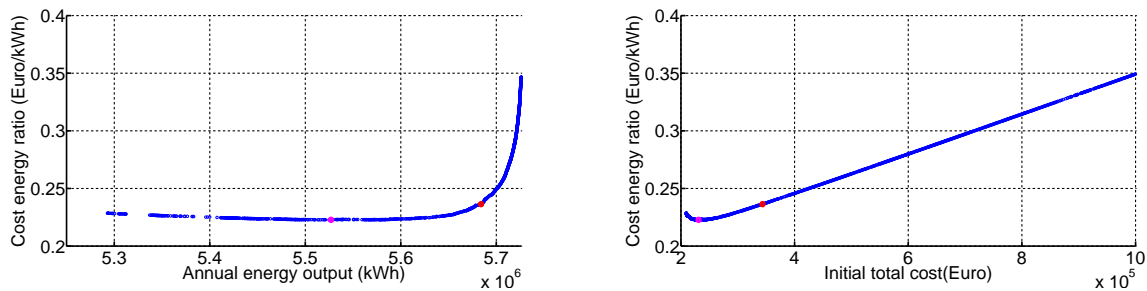
(a) Evolution of cost energy ratio $\in/kWh$ vs. annual energy output

(b) Evolution of cost energy ratio $\in/kWh$ vs. initial total cost

Figure 3.6 – Final objective 2: Cost energy ratio $\in/kWh$ vs. objectives. Red point: maximize the 20 years revenue design solution; Magenta point: minimum cost energy ratio design solution.

The Fig. 3.7 to 3.9 present the evolution of all the optimization parameters varying with function of the objectives. Every optimization parameter is plotted with annual energy output (left side) and the initial cost (right side). It is not so easy to justify clearly the changing of all optimization variables along the Pareto front. Because our optimization problem is strongly coupled with the tidal current speed, turbine characteristic, generator and converter models. Hence, it is really difficult to interpret all the optimization parameters variation. However, we can select some important parameter to analysis. The discrete variation caused by the discrete pole pair variation.

The outer stator power percentage k_1 varies between 0.54 and 0.61 which confirms that it is reasonable to design a double stator machine with bigger rated power for outer stator than that of inner stator. Otherwise, the cooling of inner stator will be a headache problem.

The pole pair number decreases with the annual energy output in Fig. 3.7(c). As the nominal torque is fixed by the turbine, and the machine torque varying with $p^2 L$ or $R^2 L$ [95], decreasing pole pair will cause increasing of machine length. Increasing of machine length L will leads to decreasing of machine bore radius R_{so}. Those relationship are confirmed by the optimization results. The pole pair number varies between 12 and 54. The rated rotational speed is $21.5 rpm$. The corresponding rated frequency is between $4.3 Hz$ and $19.35 Hz$. In the high energy output region, the pole pairs number is relatively low which may pose a problem of the converter commutation frequency. Typically, the lowest machine operating frequency is around $5 Hz$. Below $5 Hz$, the converter commutation output current harmonics can cause torque pulsations problem [96]. It means that the cut in speed operation frequency should be higher than $5 Hz$. In this thesis report, in order to see clearly the optimization variation, the limit constraint of pole pair is not applied. The cut in turbine rotational speed is $8.76 rpm$. It leads to the minimum pole pairs should be 36 to achieve the frequency limitation which the operating frequency should be

(a) Outer stator power percentage: k_1

(b) Outer stator power percentage: k_1

(c) Pole pair number: p

(d) Pole pair number: p

(e) Tooth open ratio: k_t

(f) Tooth open ratio: k_t

(g) Outer bore radius: R_{so}

(h) Outer bore radius: R_{so}
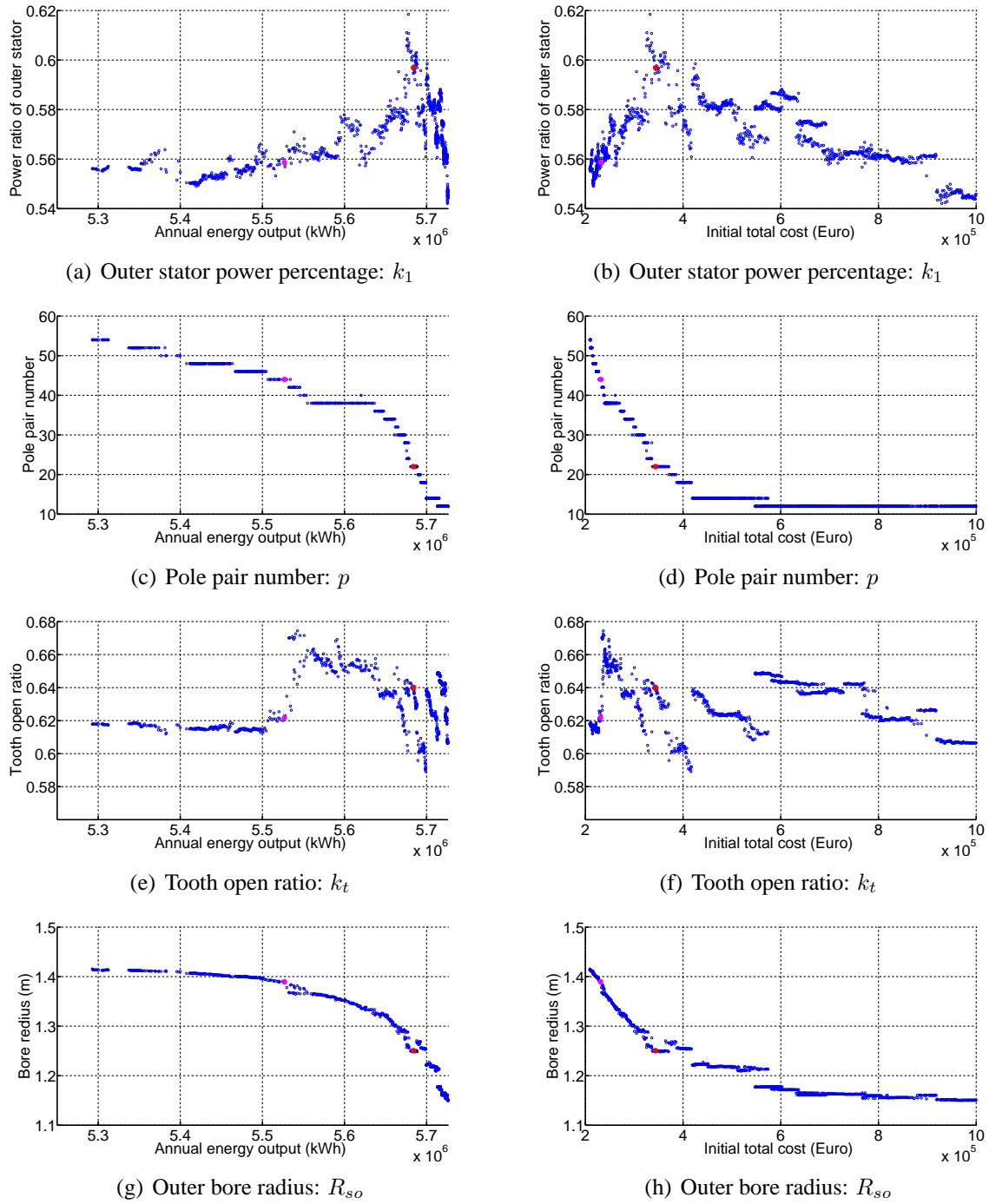
Figure 3.7 – Evolution of optimization parameters k_1, p, k_t and R_{so} vs. the two objectives. Red point: maximize the 20 years revenue design solution; Magenta point: minimum cost energy ratio design solution.

higher than $5Hz$. All in all, if the $5Hz$ constraint is used, the high energy region where the pole pair number is lower than 36 can't be selected.

The thickness of yoke of inner stator increases sharply in the high energy output region which is shown in Fig. 3.8(a) and Fig. 3.8(b). From the heat transfer point of view, it is better to have smaller inner yoke thickness. Form the efficiency point of view, it is better to increase the inner stator yoke thickness to decrease the flux density in yoke. Through decreasing the yoke

(a) Thickness of yoke: h_{yokeo} and h_{yokei}

(b) Thickness of yoke: h_{yokeo} and h_{yokei}

(c) Height of slot: h_{sloto} and h_{sloti}

(d) Height of slot: h_{sloto} and h_{sloti}

(e) Air gap length: l_g

(f) Air gap length: l_g

(g) Thickness of magnet: h_m

(h) Thickness of magnet: h_m
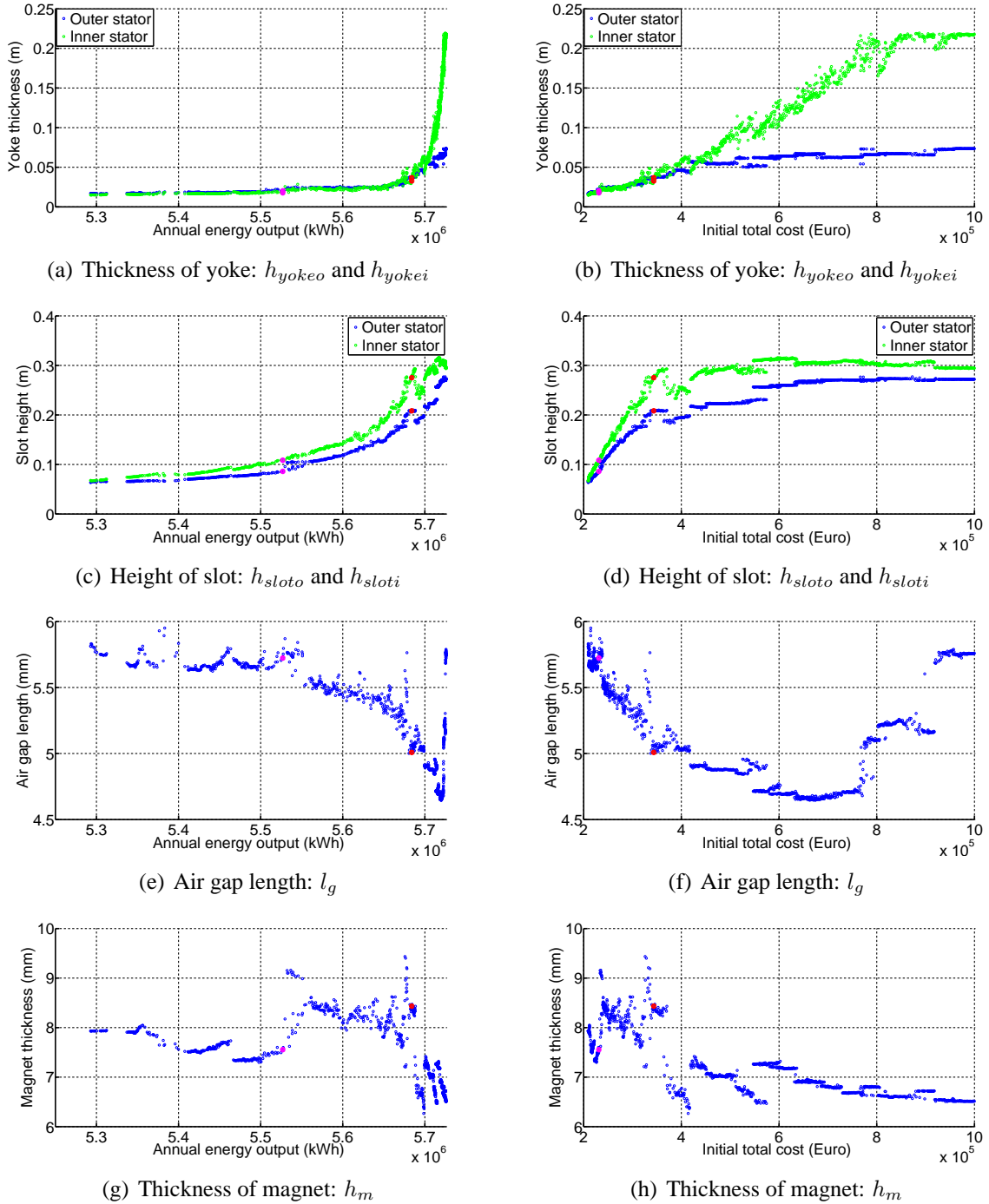
Figure 3.8 – Evolution of optimization parameters h_{yokeo} and h_{yokei}, h_{sloto} and h_{sloti}, l_g and h_m vs. the two objectives. Red point: maximize the 20 years revenue design solution; Magenta point: minimum cost energy ratio design solution.

flux density, the power efficiency can be increased even the mass of yoke is also increased. In the optimization process, increasing the inner yoke thickness is the final solution to increase the annual energy output. The length of generator also increased. The heat transfer surface will not have too much change comparing to the machine which has smaller inner yoke thickness. Therefore, if the cost and winding temperature don't reach their limit, increasing the inner stator thickness is good solution to increase the generator efficiency. For the yoke thickness of

(a) Thickness of rotor: h_r

(b) Thickness of rotor: h_r

(c) Generator length: L

(d) Generator length: L

(e) Number of conductor in one slot: N_{sloto} and N_{sloti} (f) Number of conductor in one slot: N_{sloto} and N_{sloti}

(g) Converter apparent power: S_{convo} and S_{convi}

(h) Converter apparent power: S_{convo} and S_{convi}
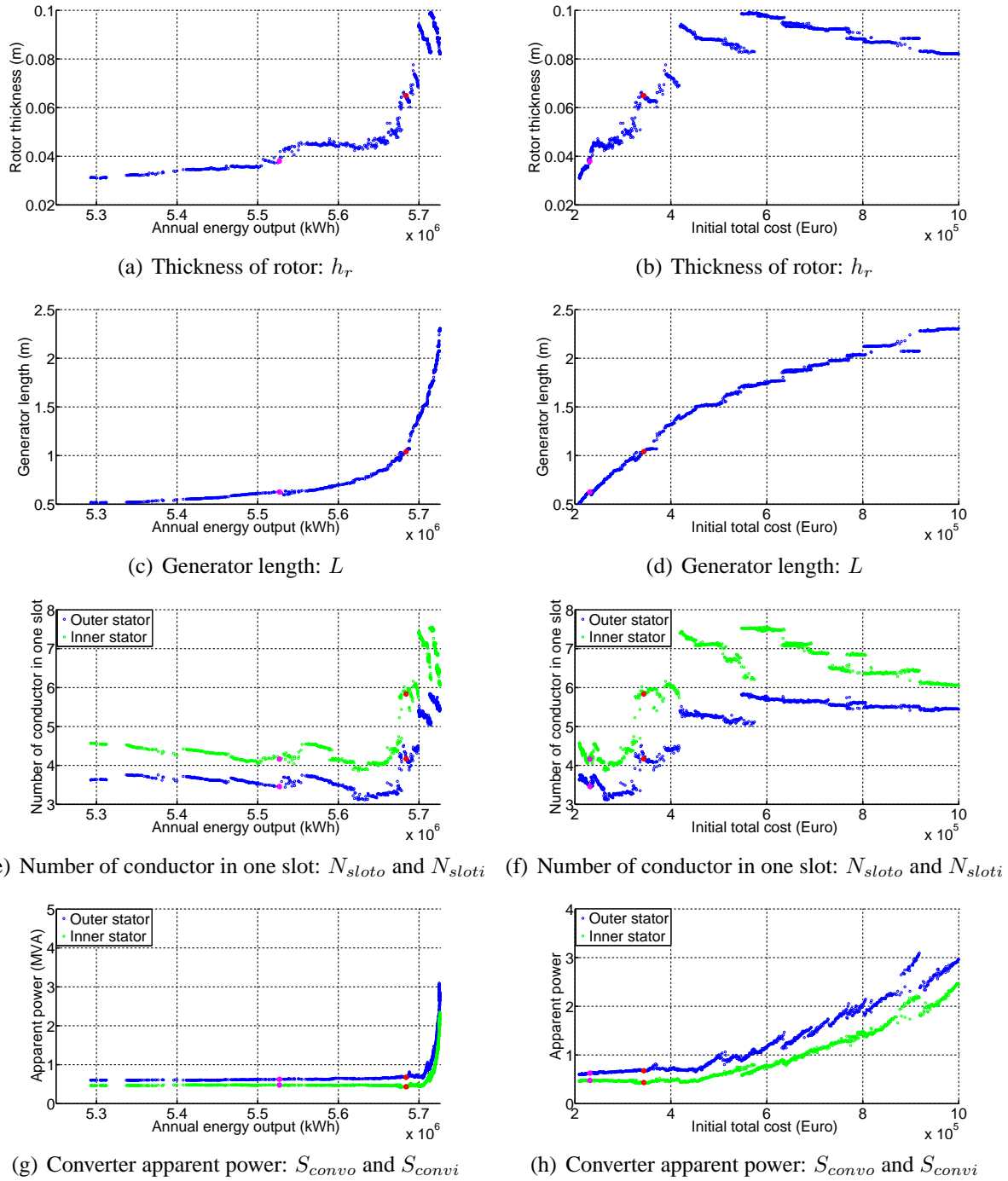
Figure 3.9 – Evolution of optimization parameters h_r and L, N_{sloto}, N_{sloti}, S_{convo}, S_{convi} vs. the two objectives. Red point: maximize the 20 years revenue design solution; Magenta point: minimum cost energy ratio design solution.

outer stator, it is not preferable to increase this thickness to increase the annual energy output. Because increasing the out stator yoke thickness will leads the bore radius decreasing. Hence, the outer yoke thickness can't increase in the same shape like the inner stator.

The height of inner slot is bigger than that of the outer stator which is shown in Fig. 3.8(c) and Fig. 3.8(d). It leads to a bigger inner inductance than inductance of outer stator. As the rated power of inner stator is smaller than rated power of outer stator, the apparent power of the

inner stator will be smaller than the outer stator. For the inner and outer stator converter, rated phase to phase voltages are fixed at $690V$. Therefore, inner stator has smaller rated current limit circle. The CPSR for the two stator should be bigger than $\frac{\omega_{m,cpm}}{\omega_{m,base}}$ which is 2.92 in our case. From the Eq.2.127, it can be deduced that the algorithm tends to have a bigger inductance value for a smaller current to satisfy the CPSR constraint.

The air gap length almost has the same evolution shape as the bore radius, see Fig. 3.8(e) and Fig. 3.7(g). Theoretically, the air gap length should be as small as possible. In our optimization model, a mechanical constraint of the air gap length is added which varies with the bore radius R_{so} as Eq.3.14 expressed. The magnet thickness is slightly bigger than the air gap length. The ratio between the magnet thickness and air gap length (h_m/l_g) varies between 1.3 and 1.6. For a given length of air gap, the magnet flux density increase very small with the increasing of magnet thickness. That means we increase the cost of magnet without increasing too much of flux density. The magnet thickness also is influenced by the ratio of magnet width and pole pitch β. Bigger magnet width and pole pitch ratio β can decrease the magnet thickness.

Table. 3.3 summarized some important parameters variation. It reveals the variation trends between those parameters. The investment cost increases with the annual energy output. Decreasing pole pair number can increase the energy output. However, the machine length will increase when the pole pair number is decreased. The optimized machines are big and heavy in the high energy output range. As a consequence, they are expensive.

Parameters	Range and Trends
Energy output (MWh)	5293 ↗ 5726
Investments (k€)	209.4 ↗ 1000
Power percentage k_1	0.54 ∼ 0.61
Pole pair p	54 ↘ 12
Bore radius $R_{so}(m)$	1.415 ↘ 1.150
Length $L(m)$	0.517 ↗ 2.307
h_m/l_g	1.3 ∼ 1.6
Rotor thickness $h_r(mm)$	31 ↗ 82
$S_{convo}(MVA)$	0.6 ↗ 2.96
$T/Mass(N.m/kg)$	62.9 ↘ 4.24
$T/Volume(kN.m/m^3)$	121.6 ↘ 27.2

Table 3.3 – Summarize of the optimized parameters variation trends

3.4.2 External parameters variation

In this section, the evolution of the generator magnetic-electronics performance parameters for the design candidate solutions will be discussed in detail, such as the torque active mass density, torque volume density, annual energy losses, cost of material, winding temperature. Those parameters can be used to verify the design solution through comparing the order of magnitude with the design standards in literature [10, 42, 47, 49, 50, 63, 97–100].
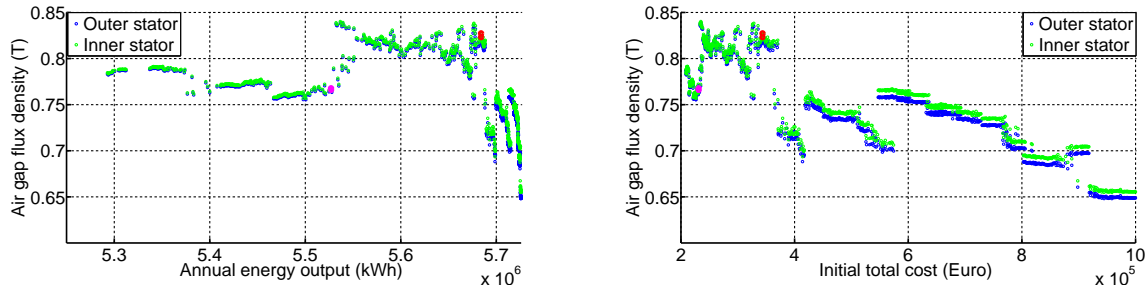
(a) Evolution of no load fundamental peak air gap flux density vs. annual energy output

(b) Evolution of no load fundamental peak air gap flux density vs. initial total cost

Figure 3.10 – Evolution of no load fundamental peak air gap flux density vs. objectives. Red point: maximize the 20 years revenue design solution; Magenta point: minimum cost energy ratio design solution.

Fig. 3.10 shows the evolution of the fundamental peak air gap flux density. The value between $0.65T \sim 0.85T$ is quit often selected in machine design. In the analytical machine design model, this value influenced by air gap length l_g , magnet thickness h_m and Carter's factor for a given magnet material type, see equations from Eq.2.10 to Eq.2.15. The maximum revenue design solution has the peak flux density around $0.82T$; the minimum cost per kWh design solution has the peak flux density around $0.76T$. Those value are very close to the standard values $0.8T \sim 1.05T$ for surface mounted PM machine design [42].

Fig. 3.11 shows the evolution of generator active mass and volume, torque active mass density and volume density. The mass and volume increase with the annual energy output and the initial total cost. The mass of the generator varies between $7ton$ and $104ton$. Mass below $20ton$ will be achieved for the majority energy output range. The heavy generators are no longer interesting for investment in the higher energy output region. As it is discussed before, the design solutions after the red point can never be good solutions because the same revenue can be obtained with the solutions before the red point. Therefore, the possible generator mass is below $36ton$. If the region with higher investment than the red point is not considered, the torque mass density varies between $12N.m/kg$ and $63N.m/kg$. The order of magnitude for generator mass and volume are reasonable comparing to the value given out in the literature for MW range machine [10, 97, 98]. The mass of maximum revenue design solution is 3 times of the minimum per kWh cost design solution ($36ton$ vs $11ton$). Although bigger mass has higher efficiency, it also caused some indirect investment, such as higher cost of transportation and installation. Compare to wind energy generator, the limitation of generator mass will be smaller for tidal energy generator because the generator is submerged in the water and buoyant materials are usually used for auxiliary system. It doesn't need to hoist the generator up to the top of tower. The main limitation is that it needs to design a strong enough support structure to fix the generator. It is difficult to chose an optimal machine from the Pareto front because there are a lot indirect investment values. The choice should result from a global technical

economical compromise in relation with the industrial environment.

The generator volume varies between $3.6m^3$ and $7.4m^3$ (red point). The torque volume density can achieve between $60kN.m/m^3$ and $120kN.m/m^3$. The torque volume density is slightly higher comparing with value in literature which is around $35 \sim 70kN.m/m^3$ for traditional single stator generator with external diameter equals to $3m$ [10, 97]. It confirms that double stator generator has the advantage of higher torque volume density than single stator generator. In the final section of this chapter, the detail comparison between the double stator PM generator and traditional single stator PM generator will be made.

Fig. 3.12 shows the maximum winding temperature for each candidate design solution. For a generator-converter solution system, each operating condition in torque speed profile there is one temperature in winding. Through comparing the winding temperature for every operating points, the maximum winding temperature is obtained. Usually, the maximum winding temperature is achieved when the generator-converter system operated at the rated point condition. The winding temperature decreases with the annual energy power increasing. The decreasing of winding temperature is caused by increasing the surface of heat transfer and decreasing of the power losses. The winding temperatures of maximum revenue design solution are around $32°C$ both in outer and inner stator. And for the minimum cost per kWh design solution, the maximum winding temperature of outer stator and inner stator are $82°C$ and $66°C$ respectively. For the design solutions with low cost, the maximum operation winding temperature is relatively higher than the high cost design solution. Low cost means less material used to design the machine. All the design solution will be operated for the same torque speed profile. Therefore, much less material machine is almost unavoidable to have smaller winding temperature for the same heat transfer coefficient. The inner stator winding temperature is not a problem for double stator machine design as the inner stator power is smaller than outer stator. Although the heat transfer surface for outer stator is bigger than inner stator, the outer stator winding temperature is slightly bigger than inner one. This is because the total power losses of outer stator is also much bigger than that of inner stator. The high cost design solution has less losses and bigger heat transfer surface than lower cost machine. It leads to relatively low winding temperature for the higher energy output solutions.

The lowest investment design solution has maximum winding temperature. It can be called "Traditional dimensioning generator" because designing a compact machine is usually the target in traditional machine design. This machine has the advantage of that it has less mass, smaller volume.

It is a really a complex task to build a very precise thermal model. Because the characteristic of the used iron material type and isolation paper also vary with the temperature. Furthermore, it is not so easy to calculated the real heat transfer surface and heat transfer coefficient. Therefore, the product of linear current load $A(kA/m)$ and current density $J(A/m^2)$ is used to evaluate the reasonable machine design for different cooling systems [42]. For example, for indirect air
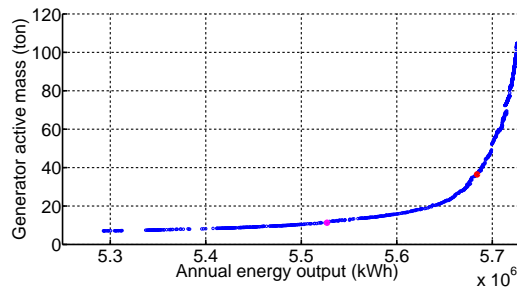
(a) Evolution of generator active mass vs. annual energy output
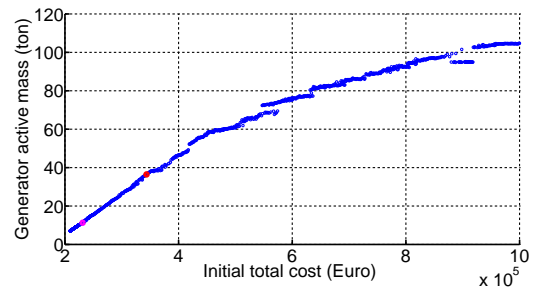
(b) Evolution of generator active mass vs. initial total cost
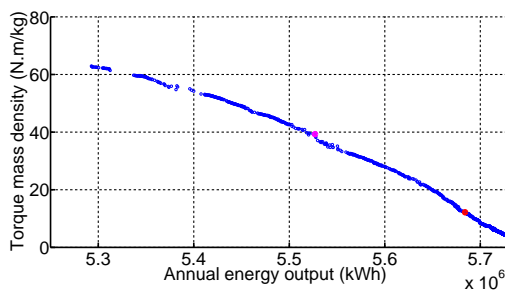
(c) Evolution of torque active mass density vs. annual energy output
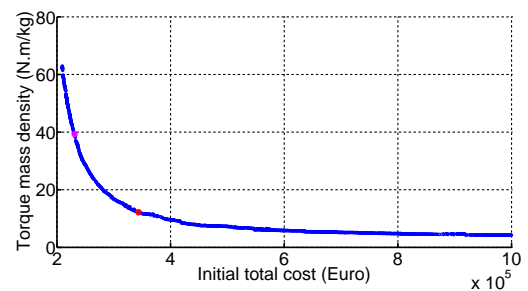
(d) Evolution of torque active mass density vs. initial total cost
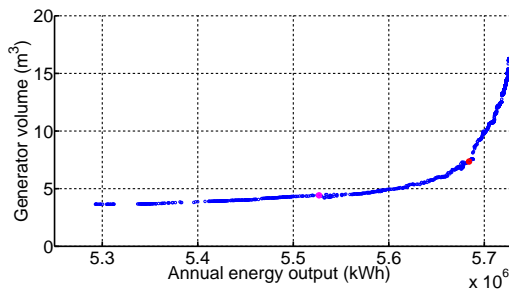
(e) Evolution of generator volume vs. initial total cost
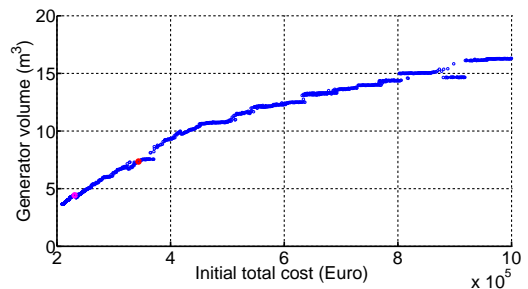
(f) Evolution of generator volume vs. initial total cost
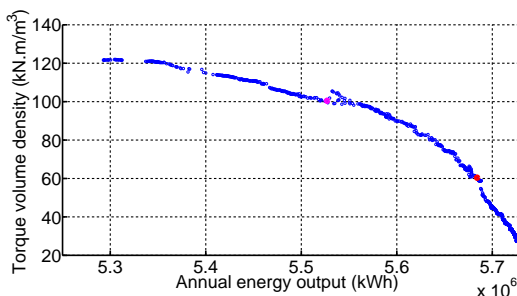
(g) Evolution of torque volume density vs. initial total cost
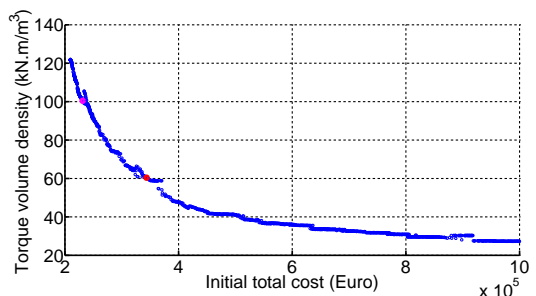
(h) Evolution of torque volume density vs. initial total cost

Figure 3.11 – Evolution of generator active mass and torque mass density, volume and torque volume density vs. objectives. Red point: maximize the 20 years revenue design solution; Magenta point: minimum cost energy ratio design solution.
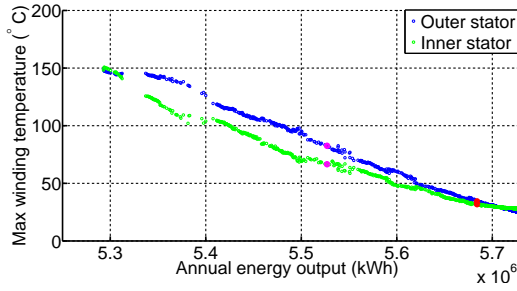
(a) Evolution of max operating winding temperature vs. annual energy output
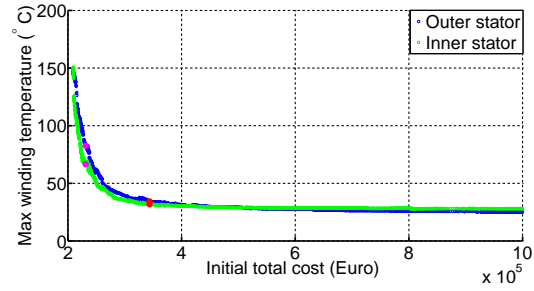
(b) Evolution of max operating winding temperature vs. initial total cost

Figure 3.12 – Evolution of max winding temperature vs. objectives. Red point: maximize the 20 years revenue design solution; Magenta point: minimum cost energy ratio design solution.
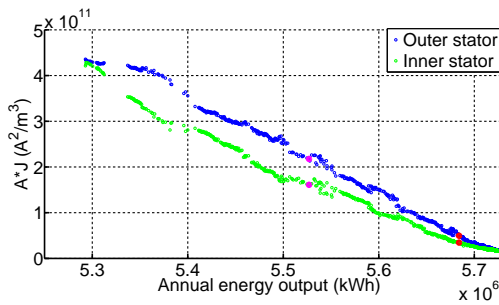
(a) Evolution of $A \times J$ vs. annual energy output
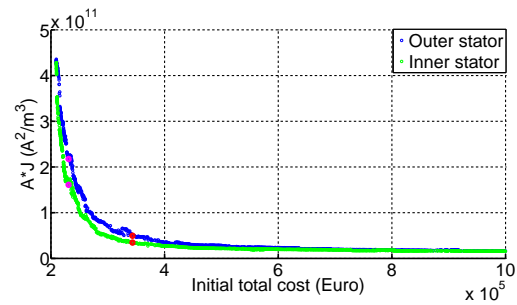
(b) Evolution of $A \times J$ vs. initial total cost

Figure 3.13 – Evolution of $A \times J$ vs. objectives. Red point: maximize the 20 years revenue design solution; Magenta point: minimum cost energy ratio design solution.

cooling system, the design range of the product $AJ(A^2/m^3)$ for surface mounted PM machine is $1.05 \times 10^{11}(A^2/m^3) \sim 4 \times 10^{11}(A^2/m^3)$. Fig. 3.13 shows the evolution of the $AJ(A^2/m^3)$ for every design candidate solution. The order of magnitude is in the normal design region. In the high cost region, the value of AJ is lower than $1.05 \times 10^{11}(A^2/m^3)$. That's because the machine is really big and heavy, the current density decreases shapely. Compare the figure Fig. 3.12 and Fig. 3.13, they have the same shape of varying trend. It confirms that the product of linear current load A and current density J is another important index of the machine thermal performance. This value could be a more useful index to evaluate the machine thermal performance than the thermal model. Because the thermal model is complex and depends on a lot of parameters and assumptions. On the contrary, the value AJ is easy to calculated.

Fig. 3.14 shows the evolution of annual energy losses and annual efficiency. From the annual energy losses figure, it can be seen that the converter losses haven't too much variation. The converter losses have strong relationship with the terminal voltage, current and power factor. The maximum terminal line to line voltage is fixed $690V$. The high energy high cost solution has bigger converter apparent power. Therefore, the maximum current is bigger than low cost solution. However, the power factor will decrease with the increasing of converter apparent power. Hence, the converter losses don't vary so strong. The copper loss decrease with the increasing of the cost. In the low annual energy low cost region, copper loss is the most important

(a) Evolution of annual power losses vs. annual energy output

(b) Evolution of annual power losses vs. initial total cost

(c) Evolution of annual efficiency vs. annual energy output

(d) Evolution of annual efficiency vs. initial total cost
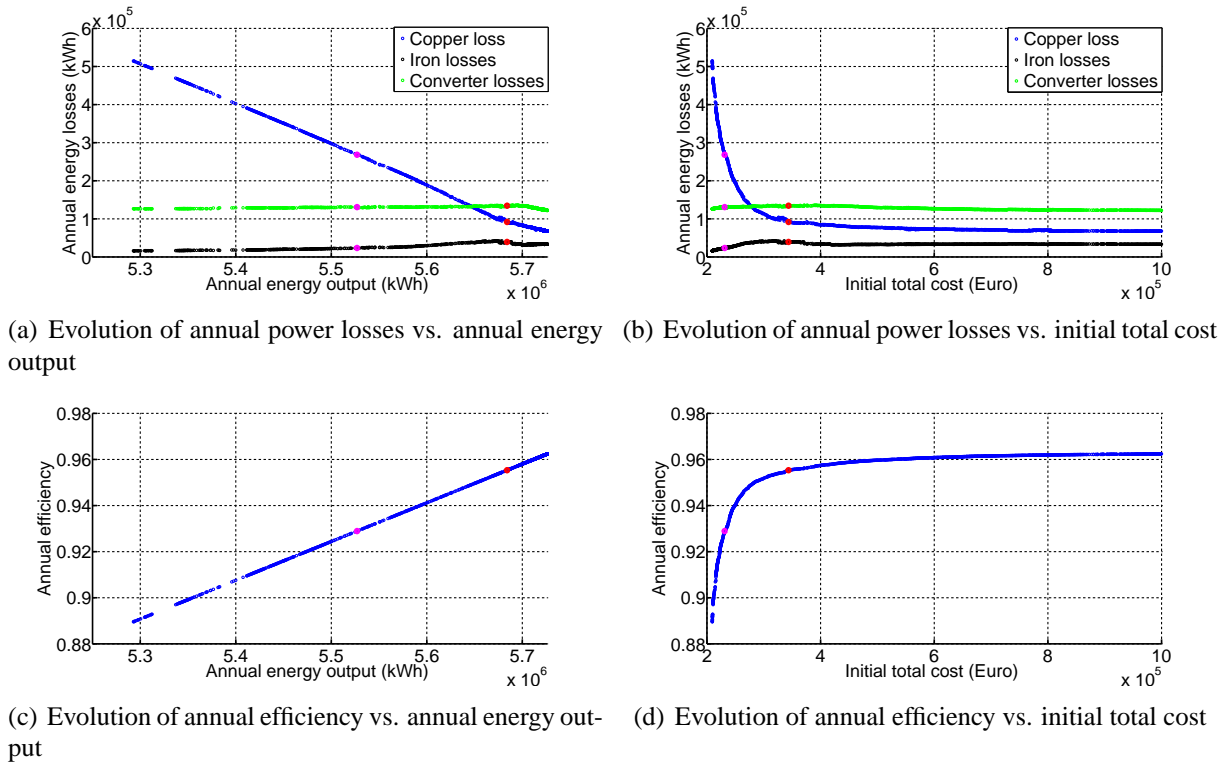
Figure 3.14 – Evolution of annual power losses and annual efficiency vs. objectives. Red point: maximize the 20 years revenue design solution; Magenta point: minimum cost energy ratio design solution.

part loss. The converter energy loss is bigger or equal to the iron energy loss.

The ratio between copper energy losses and iron energy losses for the lowest investment solution ("Traditional dimensioning generator"), minimum cost per kWh solution ($F_{obj,final2}$), and maximum 20 years revenue design solution ($F_{obj,final1}$) are 32, 11 and 2 respectively. The copper losses is always much bigger than iron losses. If machine design is based on one operating point, for example the rated power point, the maximum efficiency generator is obtained when the copper losses is equal to iron losses. However, when the generator is optimized with all the operating points, it seems that the optimal machine will be achieved with higher copper losses than iron losses. It confirms that copper loss is dominated in MW range generator wind or tidal energy application [49, 50, 98, 99].

The evolution of annual efficiency is also plotted as Fig. 3.14(c) and Fig. 3.14(d) shown. The annual energy efficiency is almost linear increasing with the annual energy output. That doesn't means we can increase the annual efficiency through increasing the annual energy output. From efficiency vs. cost figure, we can see that 96% is almost the efficiency limit for this tidal energy site. In the high cost region, the annual energy efficiency increase slightly when we increase the total cost. It is not reasonable to increase very small efficiency with double or triple the investment.

The ratio between $L_s I_{rated}$ and the magnet flux linkage ψ_{PM} is an import parameter to evaluate the flux weakening capability [63]. It is also called per unit reactance (X_{pu}). Bigger

X_{pu} means the machine has higher capability for flux weakening. When X_{pu} is equal or bigger than 1, theoretically, the machine can achieve infinite speed operation if there is no mechanical loss. When X_{pu} is smaller than 1, there exist a maximum speed that the generator can't produce any power. The maximum operation speed is calculated by the Eq.2.131. This ratio parameter should be designed normally smaller than 2 to avoid to big size of converter [47, 100]. Fig. 3.15 shows the evolution of this value for all candidate design solution. Comparing this figure with Fig. 3.9(g) and Fig. 3.9(h), it is confirmed that the ratio between L_sI_{rated} and ψ_{PM} has strong linear increase relationship with the converter apparent power. Bigger ratio between L_sI_{rated} and ψ_{PM} is better for flux weakening and worse for converter cost. It also means the system has very bad power factor. This ratio value is a compromise design result. This value can be chosen around 0.8 to get a good compromise and 0.8 is ratio of the majority annual energy output range as shown in the Fig. 3.15. When this ratio is about 0.8, one can get reasonable converter cost, power factor, efficiency and flux weakening capability.
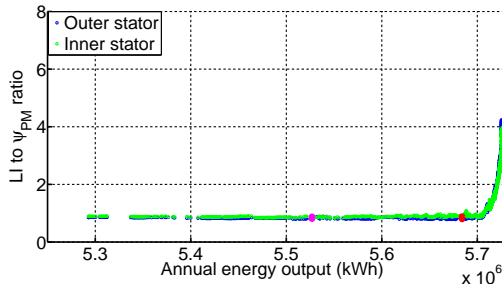
(a) Evolution of L_sI_{rated} to ψ_{PM} ratio vs. annual energy output
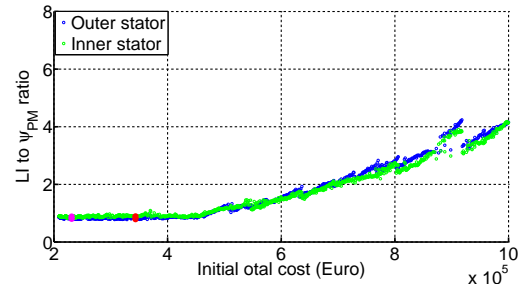
(b) Evolution of L_sI_{rated} to ψ_{PM} ratio vs. initial total cost

Figure 3.15 – Evolution of L_sI_{rated} to ψ_{PM} ratio vs. objectives. Red point: maximize the 20 years revenue design solution; Magenta point: minimum cost energy ratio design solution.
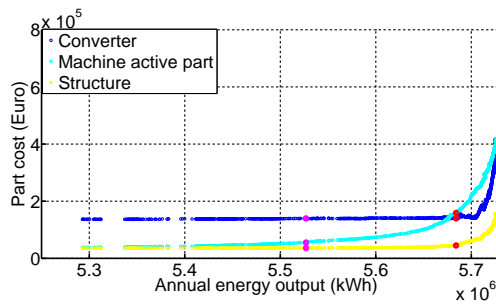
(a) Evolution of different part cost vs. annual energy output
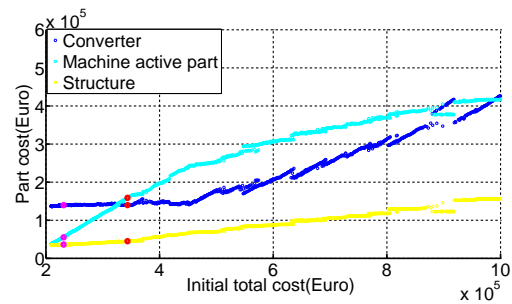
(b) Evolution of different part cost vs. initial total cost

Figure 3.16 – Evolution of different part cost vs. objectives. Red point: maximize the 20 years revenue design solution; Magenta point: minimum cost energy ratio design solution.

Fig. 3.16 shows the different part cost of the system. The converter cost is almost constant in the majority energy range. In the high energy output region, the converter cost increase shapely because of the converter apparent power increasing. The optimization algorithm prefer

the system has the possible minimum converter size to decrease the cost and to satisfy the constraints, such as the flux weakening capability. In the high energy high cost region, the program will search the possible solution to increase the annul energy output and the cost is will unavoidable increased. As it has been discussed before, the generator volume and the mass increase with the energy output. Therefore, the generator active material cost and structure cost increase with energy output increasing.

Table. 3.4 compares the optimization results with their corresponding values in literature. The corresponding values are obtained with conventional single stator PM machine. The order of magnitude of the optimization results and their corresponding values are very close. It confirms that the optimized generators are acceptable. The torque volume density is much higher than the corresponding value in literature. It is one of the most important advantages of DSCRPMG. The comparison between DSCRPMG and single stator PMSG will be emphasized at the end of this Chapter.

Parameters	Design Result Range	Literature Range	Notes
Peak flux density $\hat{B}_g$ (T)	$0.755 \sim 0.83$	$0.8 \sim 1.05$ [42]	PM surface mounted
$T/Mass(N.m/kg)$	$12 \sim 62.9$	$30 \sim 70$ [10, 97, 98]	Diameter $3m$
$T/Volume(kN.m/m^3)$	$60 \sim 120$	$35 \sim 70$ [10, 97]	Diameter $3m$
$A \times J(\times 10^{11}A^2/m^3)$	$0.5 \sim 4.2$	$1.05 \sim 4$ [42]	Indirect air cooling

Table 3.4 – Comparison between the optimization results and their corresponding values in literature.

3.5   Sensibility analysis

3.5.1   Sensibility of machine external radius

The reference external generator radius is set as $1.5m$. This value is approximately selected from the products for MW range of generator manufacture company ***The Switch*** [101]. In order to figure out the influence of different external diameter to the generator optimization, we increase the external radius 2 times of the reference radius, $R = 3m$. Fig. 3.17 shows some parameters comparison between the reference $R = 1.5m$ optimization and $R = 3m$. Fig. 3.17(a) is the Pareto front comparison between the two optimization situation. Before the annual output energy $5.71 \times 10^6 kWh$, in order to obtain the same annual energy output, The design solutions with $R = 3m$ will cost much more expensive than the reference $R = 1.5m$. It is better to design machine with smaller radius. In the high cost region, for the same investment, machine with bigger radius will produce more energy. Bigger radius machine has stronger capability to harness the energy. Then, the Pareto front without the cost of the structure is plotted as shown in Fig. 3.17(b). This figure indicates that bigger stator radius has always better performance than smaller radius generator if the cost of generator supporting structure
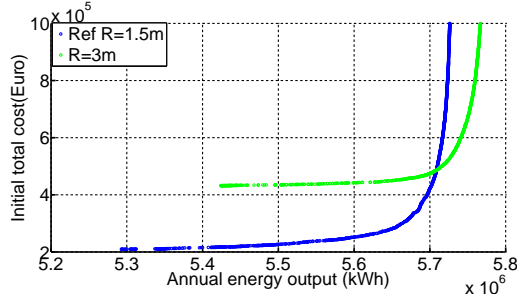
(a) Pareto front of reference $R = 1.5m$ and $R = 3m$
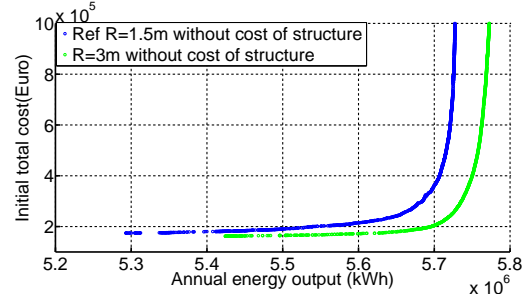
(b) Pareto front of reference $R = 1.5m$ and $R = 3m$ without the cost of structure
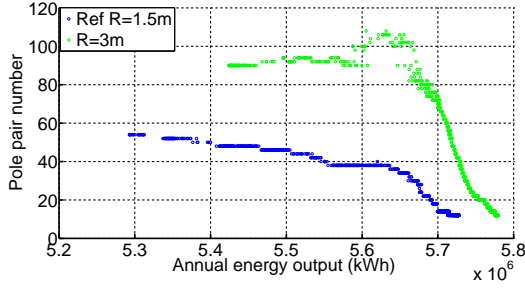
(c) Pole pair evaluation comparison
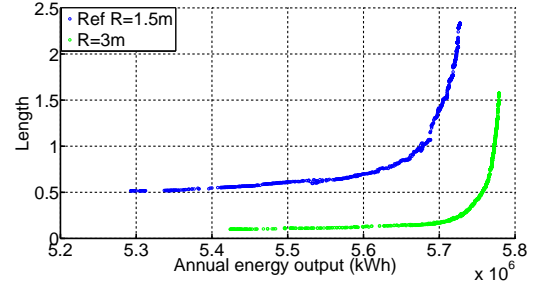
(d) Length evaluation comparison
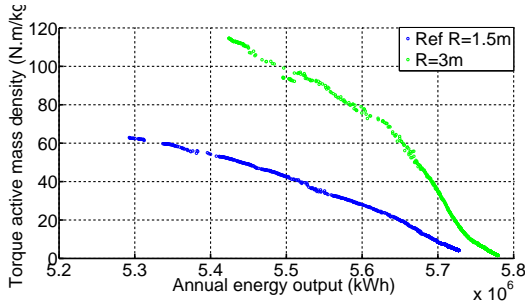
(e) Torque active mass density comparison
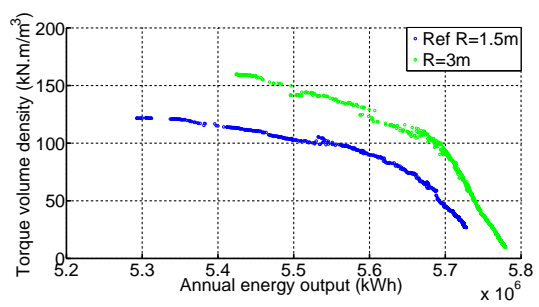
(f) Torque volume density comparison

Figure 3.17 – Sensibility comparison between external radius $R = 1.5m$ and $R = 3m$

is not considered. Comparing between Fig. 3.17(a) and Fig. 3.17(b), the cost of structure has big influence on the machine design selection. The structure cost is around 18% of the initial total cost for the reference $R = 1.5m$ optimization. Therefore, it is very important to take the structure cost into consideration to see the sensibility of the machine external radius.

The increasing of external radius will leads to bigger generator outer stator bore radius R_{so}. As it has been discussed before, bigger bore radius machine will cause smaller machine length. Smaller length needs more pole pair to produce the same torque. Those sensibility variations are confirmed by Fig. 3.17(c) and Fig. 3.17(d). In fact, the torque active mass density and machine torque volume density for $R = 3m$ machine design solution are bigger than $R = 1.5m$ as Fig. 3.17(e) and Fig. 3.17(f) shown. That's because when we increase the machine radius 2 times, the length of machine will decrease around 4 times to obtain the same torque. The machine torque has positive relationship with p^2L or R^2L [95].

From the above discussion, it is a little strange that a machine with smaller mass and smaller volume may result a higher supporting structure cost. This may be the drawback of the structure

cost model cost we used. However, it's really difficult to give out a machine structure cost model suitable for different radius. In total, it can be concluded that bigger external radius machine can have better efficiency than smaller external radius machine. The torque active mass density and torque volume density are bigger for bigger external radius machine. If the supporting structure cost is not considered, bigger diameter generator is a better solution. However, it can be envisaged that bigger diameter could not always be better choice. Therefore, it is reasonable to introduce the supporting structure cost model in the optimization process.

3.5.2   Sensibility of core material type

There are many kinds of core type which are use to machine. Different core type has its own characteristics, such as specific loss and magnetic saturation level. In order to research the influence of different core type for machine optimization design solutions, the generator is optimized with core type M800-65A which has bigger specific loss coefficient than the core type M400-50A. The same curve fitting method is used to find the loss coefficient as it has been done for M400-50A.
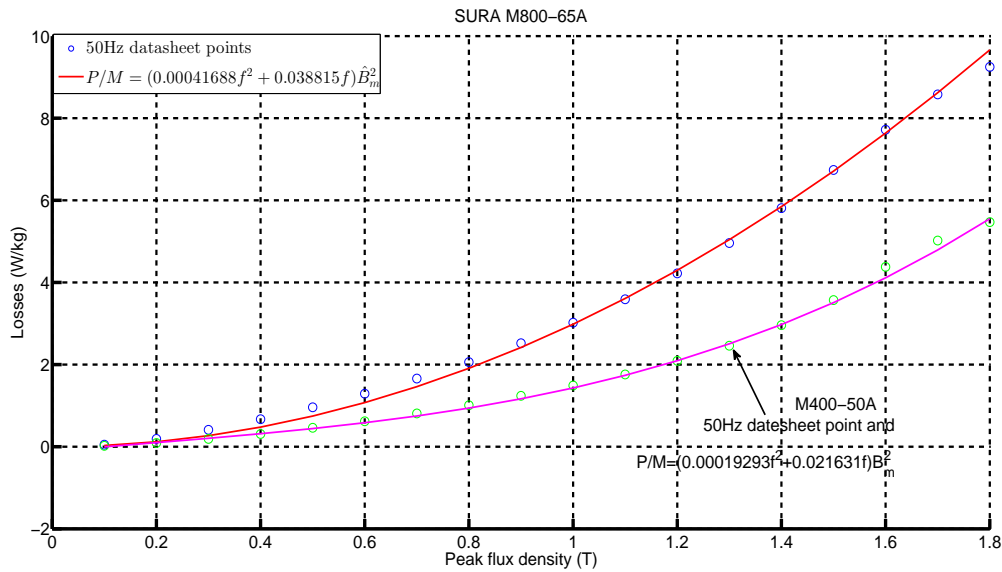
Figure 3.18 – SURA-M800-65A loss curve fitting

Fig. 3.18 shows the curve fitting of the core type M800-65A from the manufacture data sheet. The loss coefficients for M800-65A are found as $k_{ec} = 0.00041688 W/(kg.T^2.Hz^2)$ and $k_h = 0.038815 W/(kg.T^2.Hz)$. Those two values are almost double times of that of core type M400-50A ($k_{ec} = 0.00019293 W/(kg.T^2.Hz^2)$ and $k_h = 0.021631 W/(kg.T^2.Hz)$). Comparing to core type M400-50A, M800-65A may cause higher iron losses because of that it has higher loss coefficients.

Fig. 3.19 shows the optimization result comparison between the two core types. Blue curve the reference with obtained with M400-50A and greed curve is obtained with M800-65A. From

(a) Pareto fronts

(b) Material mass comparison

(c) Pole pair evaluation comparison

(d) Generator length evaluation comparison

(e) Annual iron loss evaluation comparison

(f) Annual copper loss evaluation comparison
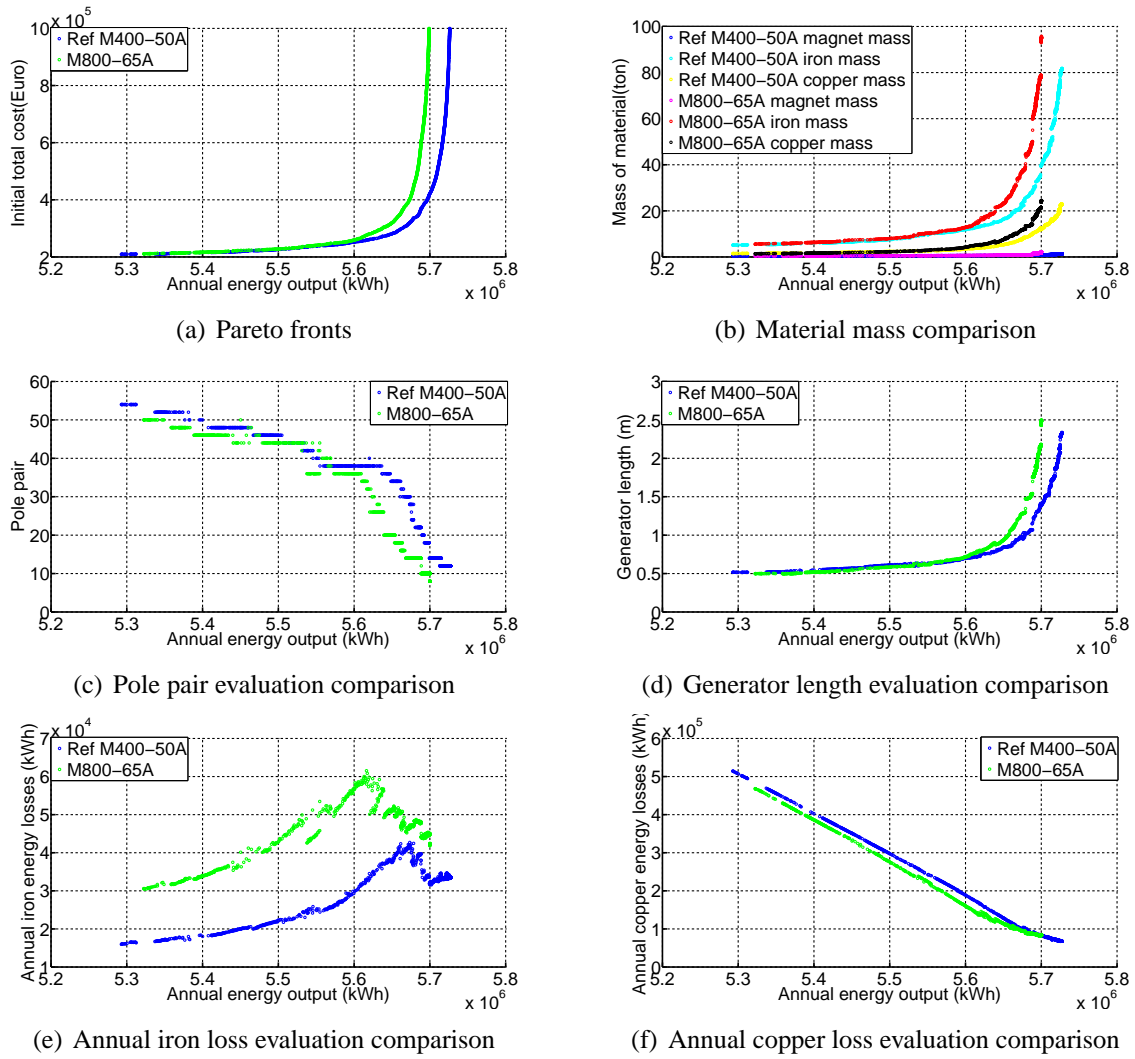
Figure 3.19 – Sensibility comparison between core type M800-65A and M400-50A

the Pareto front comparison, it is known that there is almost no difference for optimization design in low energy output region from the point of investment and energy output. However, for the high cost high energy region, optimization with core type M400-50A can have better energy output for the same investment. Fig. 3.19(b) shows the material used for the two material optimization. The magnet mass have not so much difference between the two core type optimization. However, the iron mass and copper mass has big difference in the region of high energy output. The iron mass and copper mass of M800-65A type are heavier than that of optimization for M400-50A. When the core loss coefficient is bigger, in order to have better efficiency, the algorithm tends to decrease the pole pair number to decrease the electrical frequency and finally to decrease the iron losses. The iron losses model is based on frequency, material mass and flux density. Decreasing the frequency has better effect for reducing the iron loss than decreasing the material mass because the iron losses has square relationship with frequency for eddy current loss part. Smaller number of pole pairs will lead to bigger length of machine. Those are confirmed by Fig. 3.19(c) and Fig. 3.19(d). The annual iron energy losses

and copper energy losses are also plotted in Fig. 3.19(e) and Fig. 3.19(f). Iron energy losses is always higher when the core material with higher loss coefficient is used. As the iron losses is already bigger, the optimization program will try to find to the solution which can decrease the copper loss. The bore radius R_{so} of M800-65A design solutions will smaller than M400-50A design solution in the bigger length region. Smaller bore radius and smaller number of slots will lead to a bigger slot surface. The current density will decrease and hence, the copper losses decrease even the mass of copper increase. The converter losses will also decrease as it has strong relationship with the current. The length increasing of M800-65A leads to a heavier and more expensive machine.

In conclusion, generator optimization design with higher loss coefficient core type will not have too much difference from the cost and energy point of view in the low investment and low energy output region. However, if the investment is large enough and the project needs to maximize the energy output, it is better to chose a core material with smaller loss coefficient.

3.5.3   Sensibility of material unit price: Magnet, Core and Copper

The machine design investment highly dependents on the unit price of the active material (iron, magnet, copper). However, their prices are always fluctuating with market.

The magnet price (Neodymium Metal) begun to rise since January 2009 and achieved its peak price in March 2011 (from 30\$/kg to 470\$/kg). Then the price fallen down to 80\$/kg in the year 2014 and shown stability since 2014. Magnet materials based on Rare Earth material compositions have seen significant cost increases over the last 6 years due to the mismatch between supply and demand for the basic raw materials, and production quotas imposed by the Chinese government [102].

Copper has traded between about 6.61\$/kg and 8.38\$/kg since the start of 2013. That's still a big drop from its record of 10.14\$/kg reached in April 2011 [103]. In 2015, the price of copper stay stable around 6.61\$/kg.

Electrical silicon steel sheet price varies between 0.62\$/kg and 1.06\$/kg in the last 5 years [104, 105]. This price is the cold rolled raw material price. In July 2015, this price is about 0.62\$/kg.

In this thesis, the reference price of magnet, copper, iron are 30€/kg, 6€/kg and 3€/kg respectively. The exchange rate between dollar and euro is 0.91 in July 2015. The used magnet price is smaller than the magnet market price in 2015. The used iron price is much bigger than the market. Copper price is coincident with the market price. However, the price sensibility result shows that the material price will not influence the machine dimensioning. The material price difference will not cause the machine material mass change.

In order to clearly see the difference influence caused by material price variation of the market, the price of materials are increased 5 times for each one. One of the magnet, copper

(a) Pareto front of magnet unit price 30€/kg and 150€/kg

(b) Material mass comparison between magnet unit price 30€/kg and 150€/kg

(c) Pareto front of iron unit price 3€/kg and 15€/kg

(d) Material mass comparison between iron unit price 3€/kg and 15€/kg

(e) Pareto front of copper unit price 6€/kg and 30€/kg

(f) Material mass comparison between copper unit price 6€/kg and 30€/kg
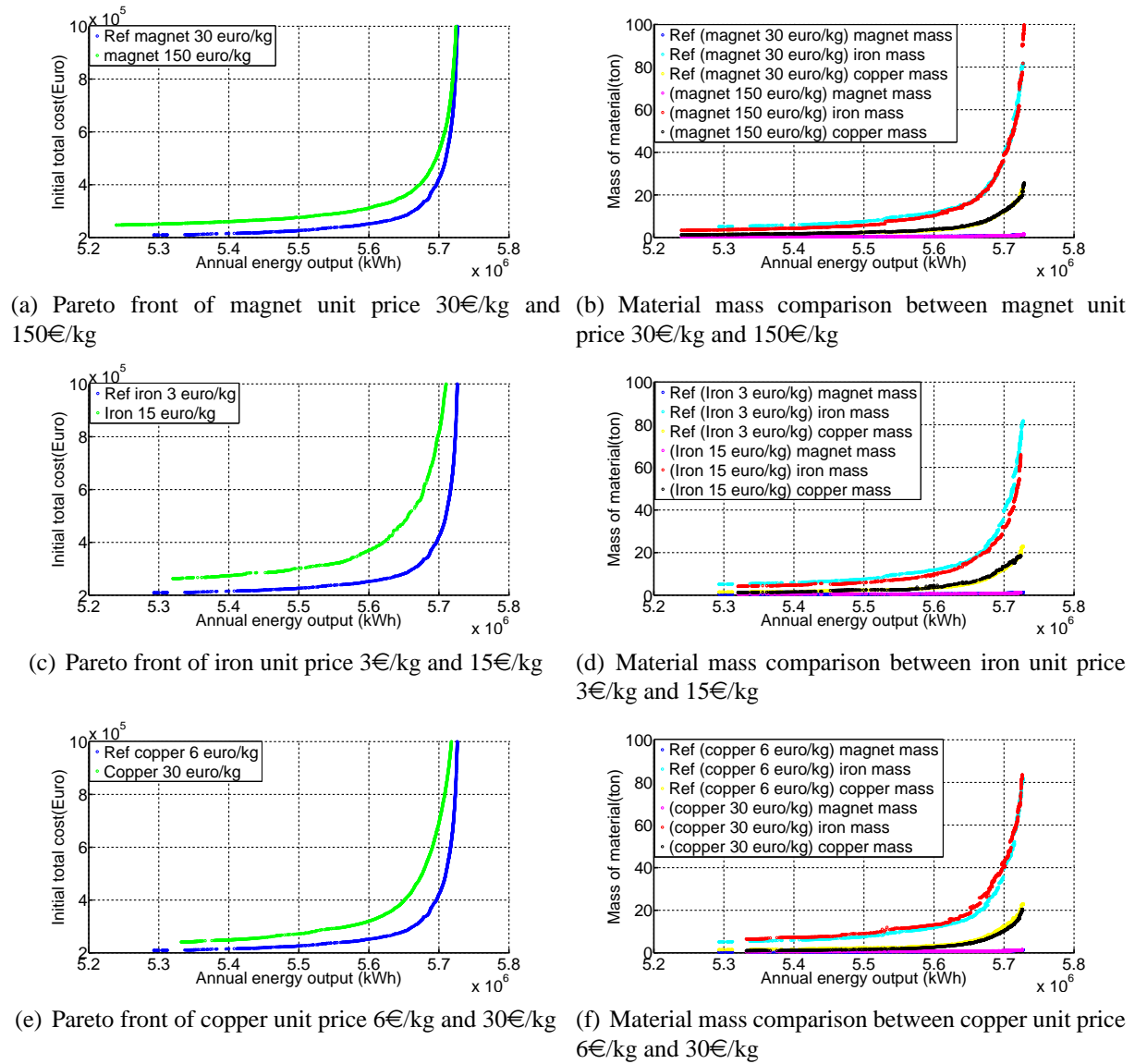
Figure 3.20 – Sensibility comparison between different material unit price

and iron price is changed to compare with the reference material price. Magnet price between $30€/kg$ and $150€/kg$, copper price between $6€/kg$ and $30€/kg$ and iron price between $3€/kg$ and $15€/kg$ are compared.

Fig. 3.20 shows the comparison results. The left side figures are the Pareto Front of the different material price optimization and the right side figures are the mass evolution of materials. When the price of materials increase 5 times, the initial total cost will increase to obtained the same annual energy output. However, from the material mass comparison in the right side figures, the price deference will not cause to much magnet, copper and iron mass variation. It means that the increased initial total cost are just caused by the increased material specific unit price. It indicates that the machine geometry optimization is "robust" and the price of the materials are not so important for the machine geometry optimization.

3.5.4   Sensibility of heat exchange coefficient

It is not easy to obtain the precise heat exchange coefficient h_c. According to the heat transfer theory, the following ranges of heat transfer coefficients for natural and forced convection can be obtained Table. 3.5 [50, 106]. For different cooling system, there is a heat exchange coefficient range.

Mode	Heat exchange coefficient $(W.m^{-2}.K^{-1})$
Air, free convection	Up to 15
Air, forced convection	50-300
Hydrogen gas, forced convection	100-1500
Oil, forced convection	500-2000
Water, forced convection	5000-20000
Water, boiling	2840-57000
Steam, condensing	5680-113000

Table 3.5 – Typical values of convection heat exchange coefficients.

In the reference optimization design process, h_c is assumed as $100(W.m^{-2}.K^{-1})$. In order to research the influence caused by different heat exchange coefficient value for the optimization, h_c is changed to $200(W.m^{-2}.K^{-1})$. The comparison of the optimization results of the two heat exchange coefficients are shown in Fig. 3.21. The Pareto front of the two heat exchange coefficients are almost coincident. $h_c = 200(W.m^{-2}.K^{-1})$ has more low annual energy output solutions than $h_c = 100(W.m^{-2}.K^{-1})$ as the red ellipse region shown. Bigger heat exchange coefficient has better capability to evacuate the heat. Therefore, good cooling system permit the generator has more power losses. Logically, better cooling system will have higher cost. However, because there is no cost model of cooling system in our optimization model, the variation of heat exchange coefficients will just influences the design possible solution region. Bigger heat exchange coefficient value optimization can obtain lower annual energy output region. It means the generator can be designed more compact for better cooling system. Fig. 3.21(b) indicates the maximum winding operation temperature is smaller for $h_c = 200(W.m^{-2}.K^{-1})$. In fact, the power losses and heat transfer surface are the same for optimization with $h_c = 100(W.m^{-2}.K^{-1})$ and $h_c = 200(W.m^{-2}.K^{-1})$ when their Pareto front are coincident. Heat exchange coefficient just influences lowest annual energy output solution where the winding temperature constraint is achieved.

Table. 3.6 illustrates the sensibility index of the some constant parameters (external radius R, core type, active material unit price and heat transfer coefficient h_c). The two optimization objectives are very sensible to the external radius R. Bigger R is better for generator efficiency. However, the supporting structure cost will increase which leads to the initial investment increase. Different core type has different specific core losses coefficient. Therefore, the energy output is sensible to the core type. The active material unit price have very small influence to the energy output. The total cost will be directly influenced. However, in fact, the mass of each

(a) Pareto front of heat exchange coefficient $h_c = 100(W.m^{-2}.K^{-1})$ and $h_c = 200(W.m^{-2}.K^{-1})$

(b) Winding maximum temperature comparison between heat exchange coefficient $h_c = 100(W.m^{-2}.K^{-1})$ and $h_c = 200(W.m^{-2}.K^{-1})$
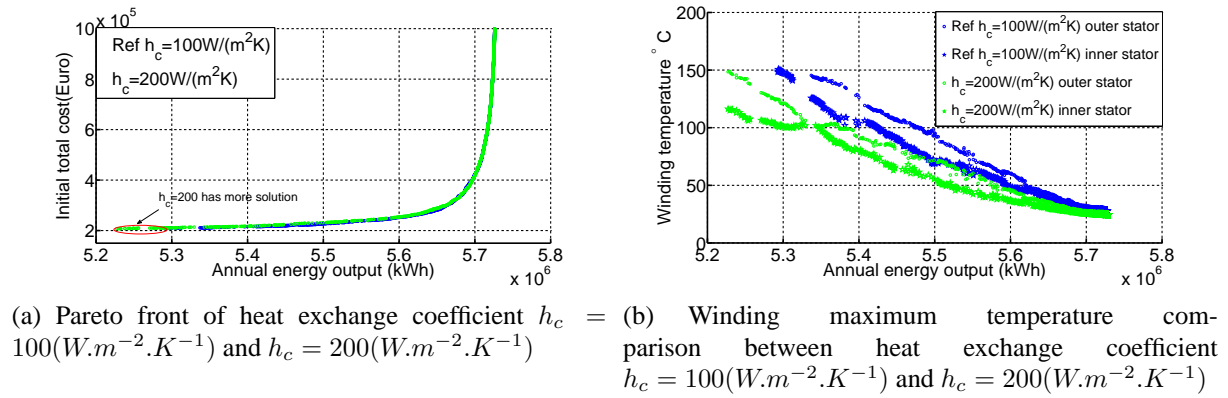
Figure 3.21 – Sensibility comparison between different heat exchange coefficient

active material is almost not changed. The heat transfer coefficient h_c has smallest sensibility to the two objectives. Bigger h_c leads to more compact machine and less efficient generator. As the cost model has no relationship with h_c, the initial investments are almost not influenced.

Parameters	Sensibility index	
	Energy output	Investment
External diameter R	★★★	★★★
Core type	★★	★
Material unit price (PM, Cu, Iron)	☆	★★
Heat exchange coefficient h_c	☆	☆

Table 3.6 – Sensibility index of external diameter R, core type, material unit price and heat exchange coefficient h_c.

3.6 Single stator and double stator PM generator comparison

In this section, a conventional single stator generator (PMSG) is optimized to replace the double stator generator to extract the tidal current energy. Then, the cost performance between single stator generator and the double stator generator optimized before are compared. The three phase winding of the single stator are connected to one set of back to back converter. The optimization process is the same as double stator optimization. The tidal current speed and frequency, turbine power curve characteristics and MSL control strategy are also introduced into the optimization process. The objectives are also the annual energy output and the system cost. The needed constant parameter (such as the rated voltage) can be found in Table. 2.1.

Single stator generator structure is different with double stator generator, therefore, the optimization variable parameters will be different. Fig. 3.22 shows the structure of conventional single stator PM generator. The external radius is equal to $R = 1.5m$ which is the same as
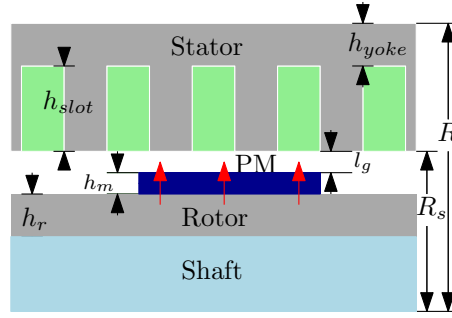
Figure 3.22 – Conventional single stator PM generator structure

the double stator generator. The structure of single stator machine is simpler than double stator machine. Hence, the optimization variable parameters will be less than double stator generator. Table. 3.7 shows the variable parameters and their optimization range. There are totally 11 parameters to be optimized. The machine phase to phase RMS voltage is also keep as $690V$.

Table 3.7 – Single stator generator optimization parameters.

Symbol	Description	Region	Unit
p	Pole pairs	[2;200]	-
k_t	Teeth open ratio	[0.2;0.8]	-
R_s	Stator bore radius	[0.5;1.5]	m
h_{yoke}	Thickness of stator yoke	[0.1;50]	cm
h_{slot}	Height of stator slot	[0.1;50]	cm
l_g	Airgap length	[1;50]	mm
h_m	Thickness of magnet	[1;50]	mm
h_r	Thickness of rotor	[0.1;100]	cm
L	Active machine length	[0.01;5]	m
N_{slot}	Conductor number in one slot	[0.1;30]	-
S_{conv}	Apparent power of the power converter	[0.01;5]	MVA

The constraints are similar to the constraints which we used for double stator generator optimization, such as mechanic, electrical, magnetic constraints. For all the operating point in full tidal current speed range, the single stator machine should not have magnet saturation come out and have the full capability of flux weakening.

Fig. 3.23 show some interesting comparison between single stator and double stator generator optimization design. From the Pareto front curve Fig. 3.23(a), it is know that single stator generator needs slightly less investment than double stator generator design for the same annual energy output. That's because double stator need more material to build the generator. In another words, double stator machine is heavier than single stator machine for the same energy output. Then, the evolution of the torque active mass density for the two type generator are shown in Fig. 3.23(b). It confirms that single stator generator optimization evolution has higher torque active mass density. However, the torque volume density evolution, we find that double stator has much more better torque volume density than single stator generator as Fig. 3.23(c) shown. The torque volume density of double stator generator is around 65% more than that

of single stator for the majority energy output region. In high energy high cost design solution region, the double stator generator torque volume solutions are slightly bigger than single stator. However, this design region is no longer a cost effective solution for renewable energy application. The torque active mass density of double stator decrease approximately 1% than single stator for the same energy output design solution.

(a) Pareto fronts of DSPMSG and SPMSG

(b) Torque active mass density

(c) Torque volume density
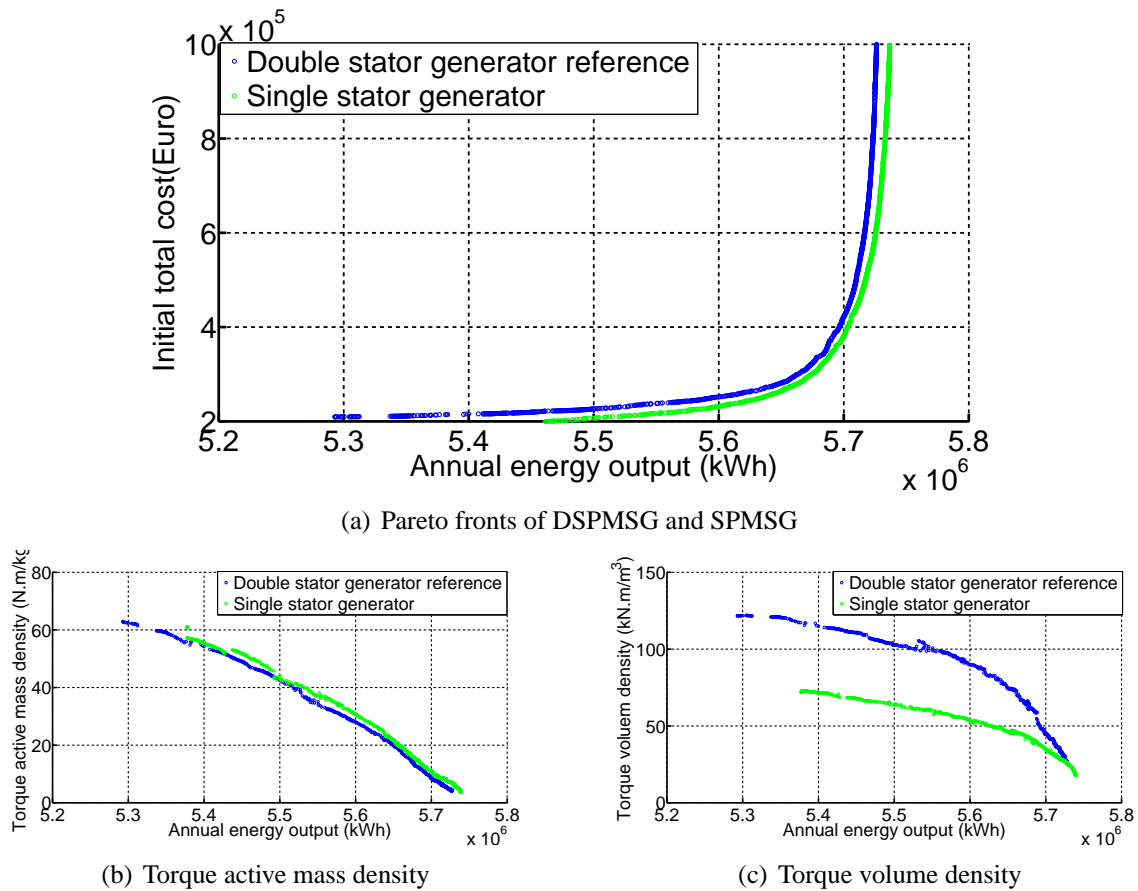
Figure 3.23 – Double stator and single stator PM generator optimization evolution comparison.

Generally, DSCRPMG has much higher torque volume density than single stator PM generator which is around 65% higher. However, DSCRPMG is around 1% heavier than single stator generator. That indicates double stator machine is very interesting for the applications which has strict volume limitation. For instance, electrical vehicle application [107]. For high MW range wind energy application, generator mass becomes the main limitation. For this high MW wind energy application, double stator machine is no longer be a better solution comparing to single stator machine. Because its mass is heavier than single stator machine and heavier machine may cost higher cost of tower or impossible to support the nacelle. However, for tidal current energy application, double stator PM generator solution could be a comparative solution comparing with single stator PM generator. Firstly, the high torque volume density can reduce a lot the current fluid weakening effect [108–110]. High torque volume density machine means the machine has smaller volume for the same output torque. In wind energy, the wind flow can pass easily when the nacelle is very small. When the nacelle is very big, the turbulence
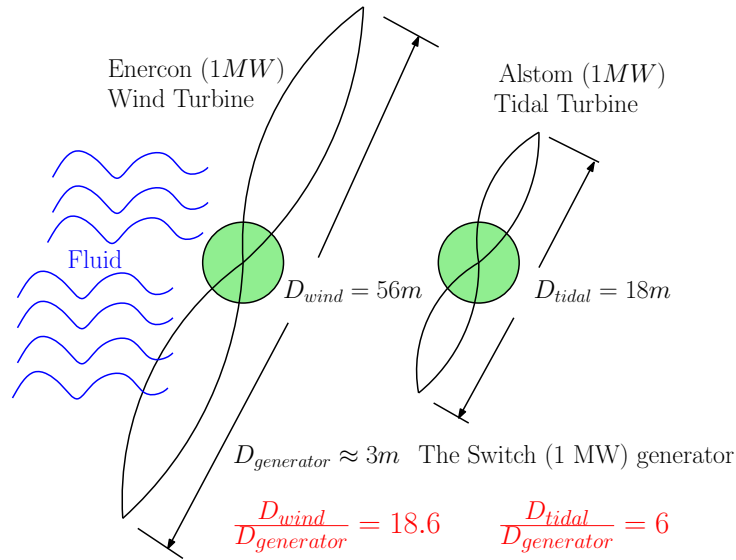
Figure 3.24 – Ratio between blade diameter and generator diameter for wind turbine and tidal current turbine.

phenomenon will come out. It will reduce the blades kinetic energy and the life time of the blade. In tidal energy, this weak effect will be more obvious than wind energy because the tidal turbine blade radius is much smaller than wind turbine blades. Fig. 3.24 illustrated the different turbine blades diameter and generator diameter ratios for wind energy and tidal current energy in a simple way. The water density is 820 times higher than air density, therefore, the tidal turbine blade radius is much smaller than wind turbine blade radius. As we can see from figure, the ratio between blade diameter and generator diameter of tidal energy system is 6 and that of wind energy system is 18.6. When this ratio value is smaller, the flow weak effect cause by the nacelle is stronger. That means is it is much more interesting to design compact generator for tidal energy comparing to wind energy [111]. Therefore, double stator generator is suitable for tidal energy application to reduce the fluid weak effect and turbulence. Secondly, double stator machine has higher redundancy than single stator machine as it has two stator which can be parallel connected to the DC bus. When one stator has problem, the other stator can operated independently to continually produce the power. Based on the two advantages comparing to single stator machine, double stator generator could be hopeful selection for tidal energy application. In the next chapter, the system control for the double stator generator under health condition and fault condition will be discussed.

3.7   Summary

In this chapter, a multi-objectives DSCRPMG optimization design method which takes into account the control strategy, converter losses, operation condition and tidal current frequency is presented. This method can be also applied to other variable speed drive system, such as wind energy and electrical vehicle. The torque speed profile and operating time should be known.

MSL control strategy and MSLCP control strategy are applied in the MPPT region and FW region respectively to calculate the *d-axis* current reference i_d. Two objectives are maximizing the annual energy output and minimizing the initial total cost (including generator and converter cost). It is difficult to increase the energy output without increasing the initial total cost. Multi-objectives DSCRPMG optimization design method provides a set of generators solutions with different energy output and investment which are presented in form of Pareto front. The final generator design choice is strongly depending on the selection criteria. For the one which needs really compact generator, lowest cost and energy output generator may be a good solution. Two other choosing criteria are also given which are minimum cost per kWh and maximum 20 years revenue.

Comparing to the preliminary machine design, the considerations are much comprehensive in optimization design process. In order to draw the Pareto front, a multi-objectives Particular Swarm Optimization algorithm is used to optimize 16 parameters. The machine-converter model and the control strategy are those presented in chapter 2. The Pareto front is a useful guide to choose a structure because it gives available compromises between the investment and the extracted energy. However the choice is not obvious. It is the reason why two secondary criteria are defined to choose a particular machine one the Pareto front. The first one $F_{obj,final1}$ is calculated by the difference between the revenue in 20 years and costs including the turbine one estimated to $1M€$. The second one, $F_{obj,final2}$ is determined by the ratio of costs and extracted energy in one year.

Pre-designed machine of chapter 2 are logically dominated by the optimized Pareto front. One might think that the best machine is the most compact, with high poles number and at thermal limit. However things are not so simple. For example, the machine chosen with $F_{obj,final2}$ leads to a very slight increase of the investment while the extracted energy is significantly enhanced.

Variations of various optimized parameters on Pareto front are presented in order to outline some design rules. For example, the number of pole pair is included between 12 and 54; the external stator extracts about 57% of the full power, the *p.u.* reactance is very close to 80%. Moreover, parameters of inner and outer machines are quite similar.

A sensitivity study is achieved on some geometrical parameters, cooling characteristic, core type and costs of active material. For example, it is shown that increasing the outer diameter results in better annual efficiency but step up the investment or that the active material price has a minor influence on the dimensioning.

To conclude this chapter, a comparison is realized between the double stator machine and a classical single stator machine. It points out that the double stator machine allows a clean torque per volume improvement ($+65\%$) with for counterpart a slight mass torque diminution (-1%). The proposed DSCRPMG allows to reduce dimensions of the direct drive generator and then to soften its impact on fluid flow. As a matter of fact, contrariwise to wind power system, the

diameter of direct drive generator is non negligible vs turbine size. Another plus of our machine is its natural redundancy and magnetic independence between outer an inner stator.

<div style="text-align: right; font-size: 3em; font-weight: bold;">4</div>

Control of a DSCRPMG in health and fault conditions

4.1 Introduction

It has been proved in last chapter that DSCRPMG has much higher torque volume density than single stator PMSG. In this chapter, the study will mainly focus on the control and fault tolerant performance comparison between PMSG and DSCRPMG. In order to research the performance of the generators in fault conditions, the control system of PMSG and DSCRPMG for health normal operation condition should be firstly build.

Fig. 4.1 and Fig. 4.2 shows the PMSG and DSCRPMG tidal energy system topology. For DSCRPMG system, the two stators are connected in parallel to the same DC-bus. The generator side and grid side are separated by a back to back converters. Generator side converter control is used to control the rotational speed to achieve MPPT or FW. The grid side converter is used to control the DC-bus voltage as a constant value to deliver all the generator power to the grid. The grid side control system is the same for the PMSG and DSCRPMG. The generator side control systems are separately designed for the two generator systems.

The generators are modeled with Simscape (Matlab) toolbox. Simscape provides a possibility to connect Simulink, Simpowersystem in the same simulation. It has the advantage of customizing personal model block. Using Simscape to model the machine, the generator or motor operation mode can be easily changed which only needs to change the load torque direction (positive or negative). The initial machine state is also easily set up. The DSCRPMG modeling codes are given in Appendix. D. PMSG and DSCRPMG parameters are obtained from the ma-
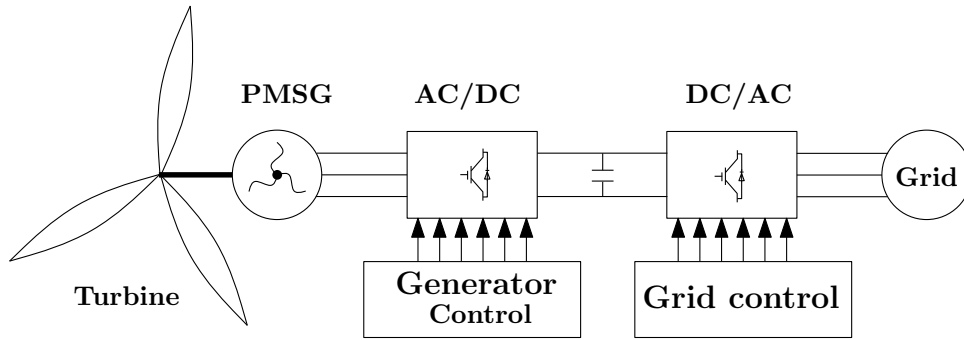
Figure 4.1 – PMSG system
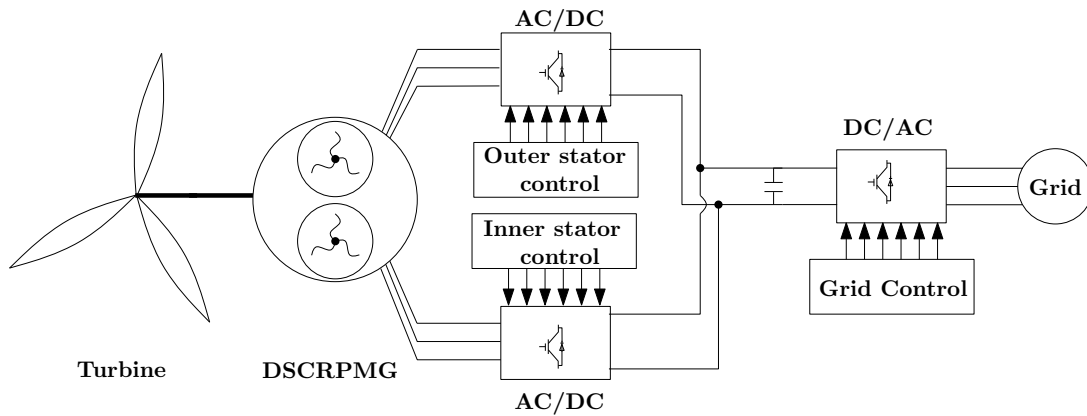
Figure 4.2 – DSCRPMG system

chine optimization and they are the solution which minimize the cost per kWh ratio solution in chapter 3. The generator parameters and controller parameters used in the simulation are shown in Appendix. E.

Open circuit fault is considered in this thesis because this kind of fault is the most frequently fault in renewable energy application [112, 113]. In order to avoid losing control, the control structure should be reconfigured. In literature, four leg converter topology is normally used in PMSM fault tolerant control [114–116]. However, they increased the number of the power electronics devices. Furthermore, the machine neutral point is connected with the four leg converter which may cause torque ripple even in health condition [117]. Therefore, the machine design should reduce electromotive force (emf) zero-sequence component as low as possible. In DSCRPMG fault tolerant control, once one stator has failure, the other stator can be used to compensate the torque ripple caused by the faulty stator. The faulty control reconfiguration of DSCRPMG is between the two stator current loop control system. Hence, the fault tolerant control of DSCRPMG will not need the fourth converter leg to connect the neutral point of machine.

Three fault control strategies are proposed for DSCRPMG system. All of them have better fault tolerant performance than single stator PMSG. In order to obtain fault tolerant control capability, the generator design and converter selection should permit big current pass through.

In the following the fault tolerant performance and phenomenon will be compared and detailed.

4.2   Gird side converter control design

The grid side converter control is focused on the topics: DC-bus voltage control, active and reactive power delivered tor the grid and to ensure the high quality power needed by the grid codes. The control structure contains two cascaded loops are shown in Fig. 4.3. The inner loops control the grid currents or grid power and the outer loops control the DC-link voltage and the reactive power. The current loops are responsible of the power quality, thus harmonic compensation can be added to the action of the current controllers to improve it. The outer loops regulate the power flow of the system by controlling the active and reactive power delivered to the grid. In tidal or wind energy application, in order to transfer the maximum available power to the grid from the DC-bus, the voltage of the DC-bus should be control at a constant value. Constant DC-bus voltage value can be achieved by directly control the voltage or control the capacitor energy.
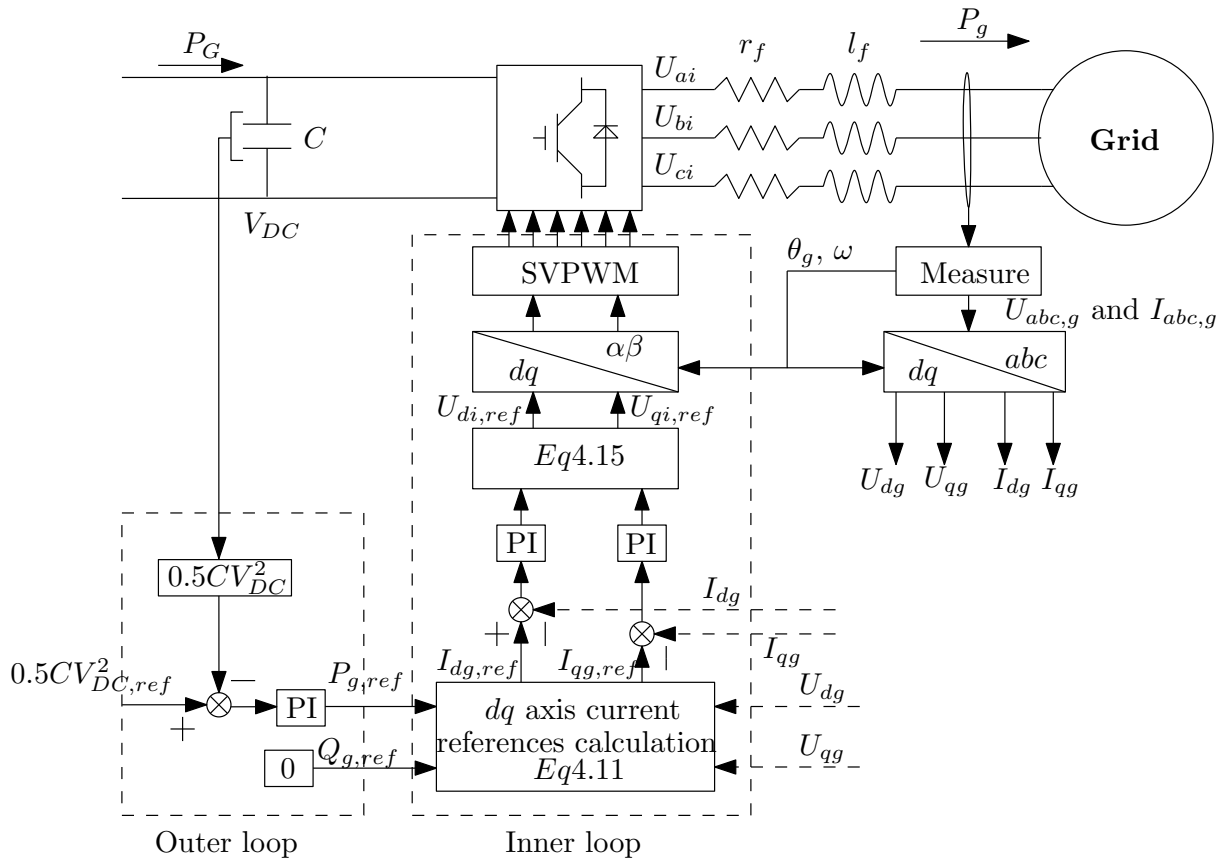
Figure 4.3 – Control structure of the grid side converter

The grid side model is given by:

$$
\begin{bmatrix} U_{ai} \\ U_{bi} \\ U_{ci} \end{bmatrix} = -l_f \frac{d}{dt} \begin{bmatrix} I_{ag} \\ I_{bg} \\ I_{cg} \end{bmatrix} - r_f \begin{bmatrix} I_{ag} \\ I_{bg} \\ I_{cg} \end{bmatrix} + \begin{bmatrix} U_{ag} \\ U_{bg} \\ U_{cg} \end{bmatrix}
\tag{4.1}
$$

By applying Park transformation matrix $\mathbf{T}_{abc \to dq0}$ to the two side of the above equation, the *dq axis* grid model can be obtained as:

$$
\begin{bmatrix} U_{di} \\ U_{qi} \end{bmatrix} = -l_f \begin{bmatrix} \frac{dI_{dg}}{dt} \\ \frac{dI_{qg}}{dt} \end{bmatrix} + \begin{bmatrix} -r_f & l_f\omega \\ -l_f\omega & -r_f \end{bmatrix} \begin{bmatrix} I_{dg} \\ I_{qg} \end{bmatrix} + \begin{bmatrix} U_{dg} \\ U_{qg} \end{bmatrix}
\tag{4.2}
$$

The frequency ω can be detected using PLL block [118]. The *dq axis* current and voltage are decoupled. This characteristic provides an effective means for the independent control of the active power and reactive power of the system. The grid side active power and reactive power can be calculated by the follow equation:

$$
\begin{cases} P_g = \frac{3}{2}(U_{dg}I_{dg} + U_{qg}I_{qg}) \\ Q_g = \frac{3}{2}(U_{qg}I_{dg} - U_{dg}I_{qg}) \end{cases}
\tag{4.3}
$$

Q_g is fixed to zero to achieve unity power factor control. Negative or positive value of reactive power can be used to obtain leading or lagging power factor operation respectively.

The DC-bus power is the power difference between generator side and grid side. It can be expressed as:

$$
\frac{d}{dt}(\frac{1}{2}CV_{dc}^2) = P_G - P_g
\tag{4.4}
$$

where P_g is grid side active power, P_G is generator side power. The grid side converter losses are neglected in this model. Since the DC-bus voltage is constant, the generator power can be totally transferred to the grid side.

The needed DC-bus voltage reference should be determined with the consideration of the system transients and possible grid voltage variations [80]. Assume that when the inverter operates under the rated conditions, the modulation index m_a is 0.8. The DC-bus voltage reference should be fixed as:

$$
V_{dc} = \frac{\sqrt{2}\sqrt{3}U_{ai}}{m_a} = \frac{\sqrt{6}}{0.8} = 3.06pu \quad (U_{ai} = 1pu)
\tag{4.5}
$$

This value will gives about 20% voltage margin for adjustment during the transients and grid voltage variations.

4.2.1 Outer loop control design

The available energy in DC-bus can be expressed as:

$$y_{dc} = \frac{1}{2}CV_{dc}^2 \qquad (4.6)$$

Then, the derivation of this variable will give out the power of DC-bus which is the power difference between the generator side and grid side. It is expressed by the following equation:

$$\dot{y}_{dc} = P_G - P_g \qquad (4.7)$$

The control low given by Eq.4.8 governs the evolution of the error of energy to obtain an asymptotic convergence to zero ($\epsilon_{dc} = y_{dc,ref} - y_{dc}$). This equation expresses the principle of a PI controller. The integral part is introduced to ensure zero error in the steady state and to compensate for modeling errors [119].

$$\dot{\epsilon}_{dc} + (2\xi\omega_{dc})\epsilon_{dc} + \omega_{dc}^2 \int \epsilon_{dc} = 0 \qquad (4.8)$$

where ω_{dc} represents the desired cutoff frequency of the energy controller. This dynamic is placed in such a manner to ensure the control objective and to avoid interaction with the internal current loops. ξ is the damping factor set between 0.7 and 1. By developing the equation Eq.4.8, the derivative of the energy can be expressed as follows:

$$\dot{y}_{dc} = \dot{y}_{dc,ref} + (2\xi\omega_{dc})\epsilon_{dc} + \omega_{dc}^2 \int \epsilon_{dc} = G_{PI,dc} \qquad (4.9)$$

$\dot{y}_{dc,ref} = 0$ because the reference DC-bus voltage is constant. $G_{PI,dc}$ is the output of the outer loop PI controller. Since the equations Eq.4.7 and Eq.4.12 are equivalent, the active power reference is:

$$P_{g,ref} = P_G - G_{PI,dc} \qquad (4.10)$$

P_G cane be treated as a disturbance in the point view of control. The reactive power reference $Q_{g,ref}$ is fixed to zero to operate at unity power factor.

For the synthesis of *dq* reference currents of the inner loop, active and reactive power are calculated by the external controller. Thus, by solving the Eq.4.3, the *dq axis* reference current are given by the following equation:

$$\begin{cases} I_{dg,ref} = \frac{U_{dg}P_{g,ref}+U_{qg}Q_{g,ref}}{\frac{3}{2}(U_{dg}^2+U_{qg}^2)} \\ I_{qg,ref} = \frac{U_{qg}P_{g,ref}-U_{dg}Q_{g,ref}}{\frac{3}{2}(U_{dg}^2+U_{qg}^2)} \end{cases} \qquad (4.11)$$

4.2.2 Inner loop control design

For the control of the converter-side currents (inner current loop), PI controllers are used. The control low given by Eq.4.12 governs the evolution of the errors of current for *dq axis* to obtain an asymptotic convergence to zero ($\epsilon_{idg} = i_{dg,ref} - i_{dg}$ and $\epsilon_{iqg} = i_{qg,ref} - i_{qg}$).

$$\begin{cases} \dot{\epsilon}_{idg} + (2\xi\omega_{idg})\epsilon_{idg} + \omega_{idg}^2 \int \epsilon_{idg} = 0 \\ \dot{\epsilon}_{iqg} + (2\xi\omega_{iqg})\epsilon_{idg} + \omega_{iqg}^2 \int \epsilon_{iqg} = 0 \end{cases} \tag{4.12}$$

where

$$\begin{cases} \dot{\epsilon}_{idg} = \frac{di_{dg,ref}}{dt} - \frac{di_{dg}}{dt} \\ \dot{\epsilon}_{iqg} = \frac{di_{qg,ref}}{dt} - \frac{di_{qg}}{dt} \end{cases} \tag{4.13}$$

It is known that $\frac{di_{dg,ref}}{dt} = 0$ and $\frac{di_{qg,ref}}{dt} = 0$. From Eq.4.13 and Eq.4.13, it can deduce that:

$$\begin{cases} \frac{di_{dg}}{dt} = (2\xi\omega_{idg})\epsilon_{idg} + \omega_{idg}^2 \int \epsilon_{idg} = G_{PI,dg} \\ \frac{di_{qg}}{dt} = (2\xi\omega_{iqg})\epsilon_{idg} + \omega_{iqg}^2 \int \epsilon_{iqg} = G_{PI,qg} \end{cases} \tag{4.14}$$

$\frac{di_{dg}}{dt}$ and $\frac{di_{qg}}{dt}$ can be calculated from Eq.4.2. The left side of the two equations are the output of PI controller ($G_{PI,dg}$ and $G_{PI,qg}$). ω_{idg} and ω_{iqg} represent the desired cutoff frequency of the *dq axis* current controller. They are equal ($\omega_{idg} = \omega_{iqg}$). ξ is the damping factor set between 0.7 and 1. Combining with Eq.4.2, the Eq.4.14 can be rewritten as:

$$\begin{bmatrix} U_{di,ref} \\ U_{qi,ref} \end{bmatrix} = -l_f \begin{bmatrix} G_{PI,dg} \\ G_{PI,qg} \end{bmatrix} + \begin{bmatrix} -r_f & l_f\omega \\ -l_f\omega & -r_f \end{bmatrix} \begin{bmatrix} I_{dg} \\ I_{qg} \end{bmatrix} + \begin{bmatrix} U_{dg} \\ U_{qg} \end{bmatrix} \tag{4.15}$$

The first part of left side of the above equation are the output of the PI controllers by multiplying $-l_f$. In fact, $G_{PI,dg}$ and $G_{PI,qg}$ can be express with PI controller form:

$$\begin{bmatrix} G_{PI,dg} \\ G_{PI,qg} \end{bmatrix} = K_{pg} \begin{bmatrix} \epsilon_{idg} \\ \epsilon_{iqg} \end{bmatrix} + K_{ig} \begin{bmatrix} \int \epsilon_{idg} dt \\ \int \epsilon_{iqg} dt \end{bmatrix} \tag{4.16}$$

where $K_{pg} = 2\xi\omega_{idg}$ and $K_{ig} = \omega_{idg}^2$ are the proportional and integrate coefficient of the grid side converter current PI controller. It should be noticed that the third term in the right-hand side allows compensating coupling terms between d and q axes. In practice, l_f and r_f are not known exactly and may vary during the operation. However, the coupling due to the parameters uncertainties are not considered and assume that it is effectively rejected by the current controllers. The controller parameters can be tuned by pole-placement technique or directly by selecting the cutoff frequency ω_{idg}. The cutoff frequency for inner current loop should be more than 10 times bigger than the cutoff frequency of outer energy loop controller.

4.2.3 Grid side control simulation results

In order to verify the grid side control, a simple simulation model is build in Simulink(Matlab) as shown in Fig. 4.4. The turbine generator side is modeled by a controlled current source. A step source block is used to model the generator power variation. The parameters used in this simulation are:

— The effective line line voltage and frequency at the connection point: 690V/50Hz;

— The filter parameters: $l_f = 1mH$, $r_f = 0.01\Omega$;

— The DC-bus capacitor: $C = 20mF$;

— Controller parameters: Damping ratio $\xi = 0.707$, natural frequency for the outer loop $\omega_{dc} = 150rad/s$, natural frequency for the inner power loop $\omega_{idg} = 2000rad/s$.

— The switching frequency: $f_{pwm} = 5kHz$.
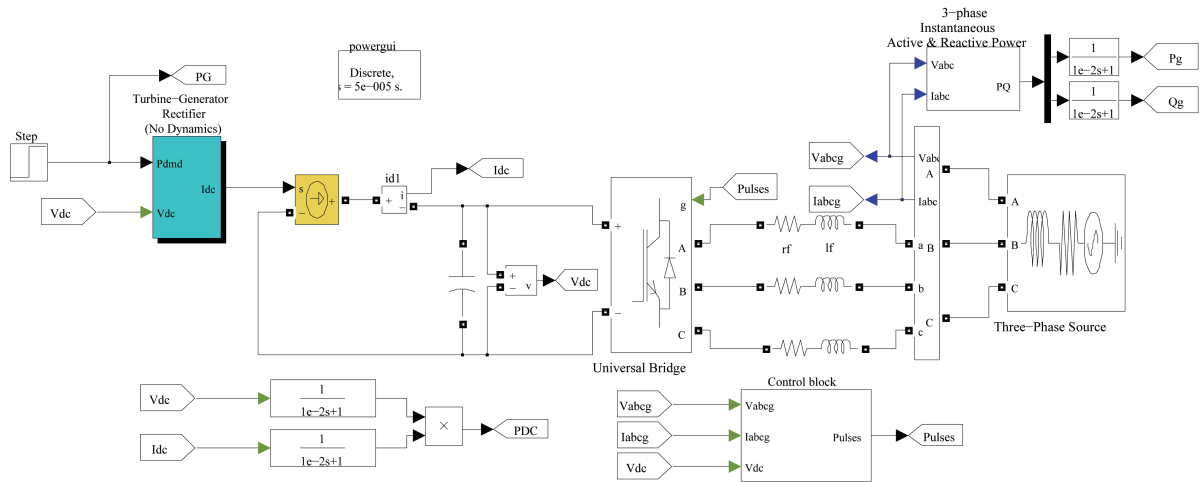
Figure 4.4 – Grid side control simulink blocks

Fig. 4.5 shows the simulation results. The generator power modeled with a controlled current source and it steps from $0.5MW$ to $1MW$ at $0.5s$. The grid side power P_g follows the generator power. The grid side power is a little smaller than the generator side power P_G because of the losses of filter. When the generator power is doubled, the grid side current also increases two times. The reactive power always keep at zero to obtained unity power factor control. The DC-bus voltage reference is fixed as 1200V (decided by Eq.4.5). The DC-bus voltage V_{dc} follows the reference even the transferred power doubled after a short period transition. The grid side voltage always keep at 690V phase to phase voltage and the current amplitude is almost doubled. This figure confirms that the grid side controller is well tuned.
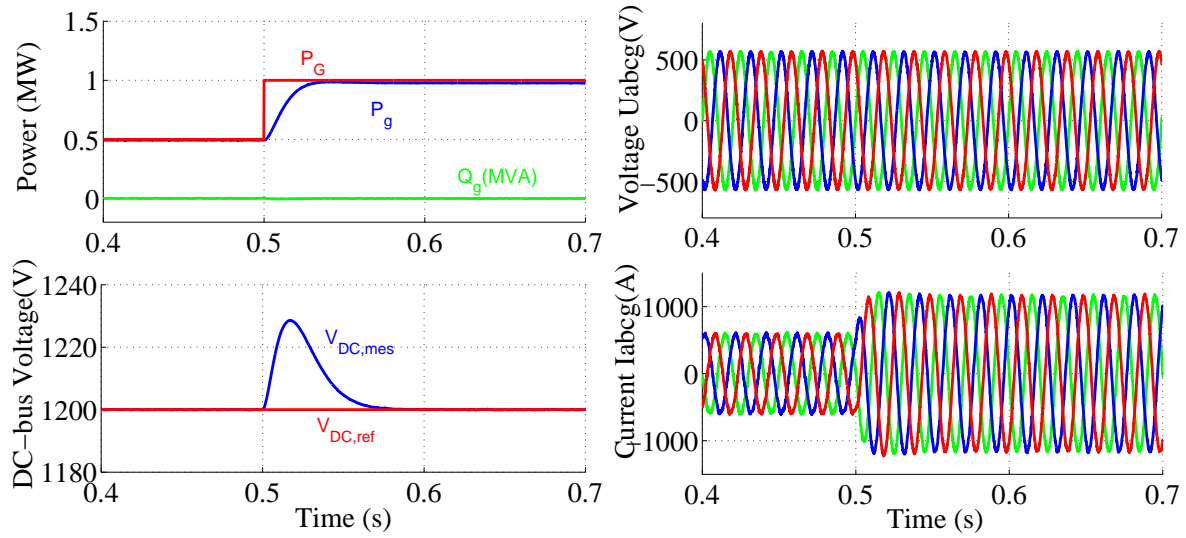
Figure 4.5 – Grid side control simulation results

4.3 Generator side control in normal condition

4.3.1 Control structure of PMSG

The PMSG dynamic model is given in the *dq axis* frame as follow:

$$\begin{cases} V_d = R_s I_d + L_d \frac{dI_d}{dt} - \omega_e L_q I_q \\ V_q = R_s I_q + L_q \frac{dI_q}{dt} + \omega_e L_d I_d + \omega_e \psi_{PM} \\ T_e = \frac{3}{2} p [\psi_{PM} I_q + (L_d - L_q) I_d I_q] \\ T_e = T_L + J \frac{d\omega_m}{dt} + f \omega_m \end{cases} \tag{4.17}$$

The main objective of the generator side control is to obtain the desired rotational speed to achieve the MPPT for direct drive turbine. In order to achieve the desired speed, the generator electrical torque should be controlled. For surface mounted PM generator, the *dq axis* inductances are the same ($L_d = L_q$). The electrical torque is proportional to the *q axis* current I_q. Therefore, control the torque is finally achieved by controlling the *q axis* current I_q. Fig. 4.6 shows the generator side converter control scheme. A cascaded control structure with an inner current control loop and outer speed control loop is employed. The speed reference $\omega_{m,ref}$ depends on the tidal current speed and turbine characteristics. The *d axis* current reference is calculated and dependent on the used control strategies which are discussed in the Chapter 2. In this thesis, MSL is applied to provide $I_{d,ref}$ with a look up table. To have a completely independent control of the *d* and *q axis,* it is necessary to add terms of compensation which are
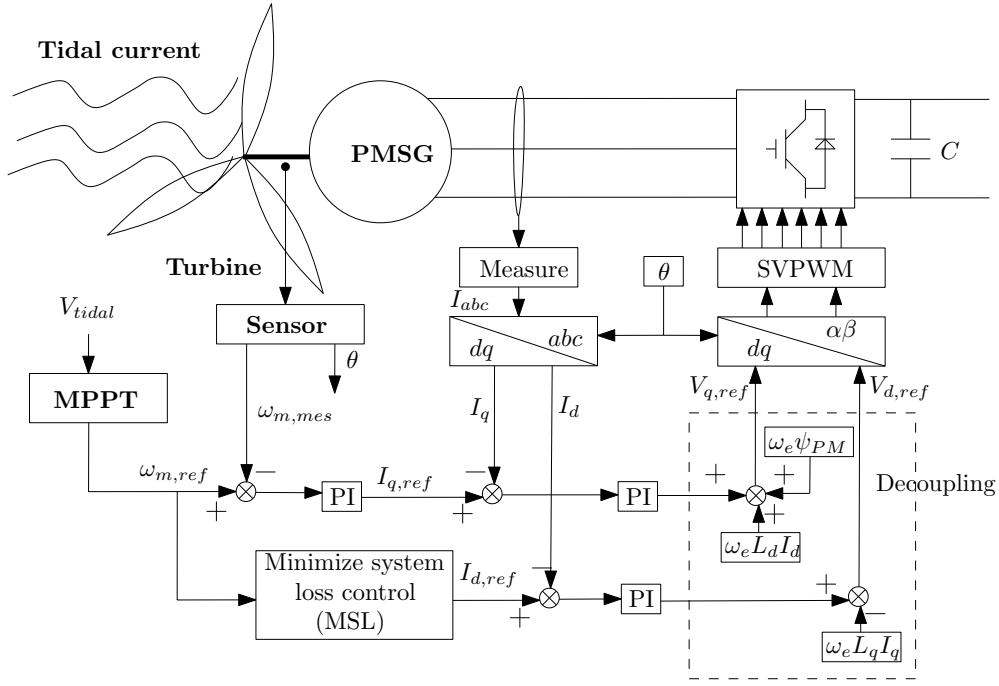
Figure 4.6 – Control scheme of PMSG side converter

called decoupling in the figure. PI controllers are used for both the speed and current control loops.

PMSG inner current loop controller design

1. *q-axis* current controller design

   The *q-axis* current controller is firstly designed. This current loop is presented as Fig. 4.7. The rectifier is modeled as a first order transfer function ($\frac{1}{0.5T_{pwm}s+1}$) with a time constant $0.5T_{pwm}$, $T_{pwm} = \frac{1}{f_{pwm}}$ and where f_{pwm} is the switching frequency [118].
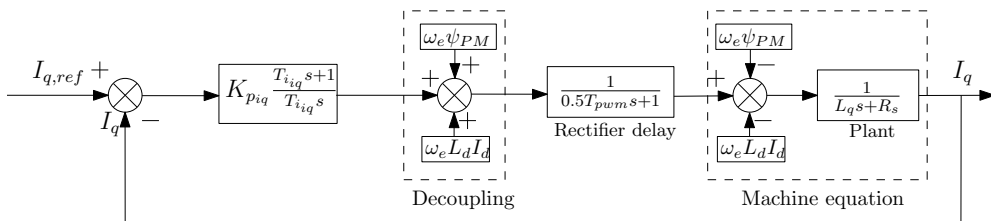
Figure 4.7 – *q-axis* current control loop

The transfer function of PI controller is:

$$G_{PI,q}(s) = K_{p_q}\frac{T_{i_q}s + 1}{T_{i_q}s} \tag{4.18}$$

where K_{p_q}: proportional gain of the q-axis current controller; T_{i_q}: integral time of the q-axis current controller.

The machine equation transfer function can be equivalently represented as $\frac{K}{\tau_q s+1}$ with $K = \frac{1}{R_s}$ and $\tau_q = \frac{L_q}{R_s}$.

Then, the open loop transfer function of *q axis* current loop is:

$$G_{oq}(s) = K_{p_q} \frac{T_{i_q}s + 1}{T_{i_q}s} \frac{1}{0.5T_{pwm}s + 1} \frac{K}{\tau_q s + 1} \qquad (4.19)$$

The dominant pole of the system is compensated by the PI controller through imposing time constant of controller equals to τ_q ($T_{i_q} = \tau_q$). Then, the *q axis* current open loop transfer function becomes:

$$G_{oq}(s) = K_{p_q} \frac{1}{T_{i_q}s} \frac{1}{0.5T_{pwm}s + 1} K \qquad (4.20)$$

Using the Optimal Modulus (OM) criterion, the proportional gain of the PI controller, K_{p_q} , can be calculated [120]. The standard transfer of a second order system to use OM criterion is expressed as:

$$G_{OM}(s) = \frac{1}{2\tau s(\tau s + 1)} \qquad (4.21)$$

Comparing Eq.4.20 and Eq.4.21, it finds:

$$\frac{K_{p_q}K}{T_{i_q}} = \frac{1}{2T_{pwm}} \qquad (4.22)$$

Therefore,

$$\begin{cases} K_{p_q} = \frac{T_{i_q}}{KT_{pwm}} \\ T_{i_q} = \frac{L_q}{R_s} \end{cases} \qquad (4.23)$$

2. *d-axis* current controller design

   The *d-axis* current control loop structure is illustrated as Fig. 4.8.
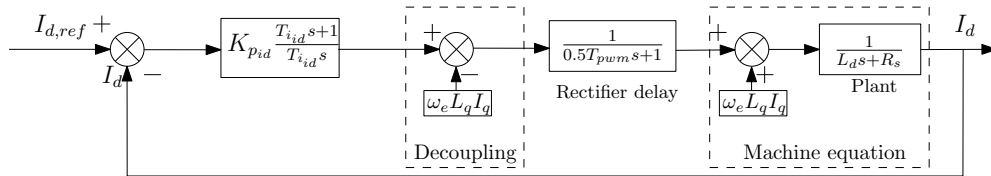
Figure 4.8 – *d-axis* current control loop

The *d-axis* control structure is the same as the *q-axis* control structure. The decoupling components are different. However, they don't influence the controller parameters design. Using the same method as *q-axis* current controller design, the *d-axis* current controller

parameters can be obtained as follow:

$$\begin{cases} T_{i_d} = \tau_d = \frac{L_d}{R_s} \\ K_{p_d} = \frac{T_{i_d}}{KT_{pwm}} \end{cases} \tag{4.24}$$

In fact, for PM surface mounted generator, as the *dq-axis* inductance are the same, the parameters of *dq-axis* current control loop are the same.

The parameters of single stator PMSG and the controller parameters are shown in the Appendix. E. Fig. 4.9 shows the Bode diagram of the inner current open loop. The designed PI controller leads to a phase margin PM= $65.5°$ at $724Hz$. Therefore, the inner current loop is stable.
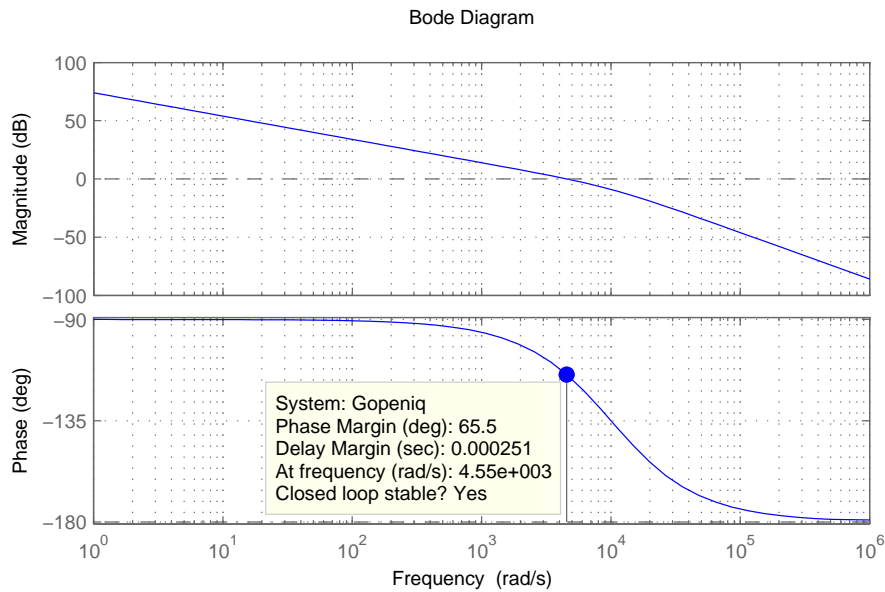
Figure 4.9 – Bode diagram of the *q-axis* current loop

PMSG outer speed loop controller design

The control scheme of the outer speed loop is shown in Fig. 4.10. T_L is the load torque
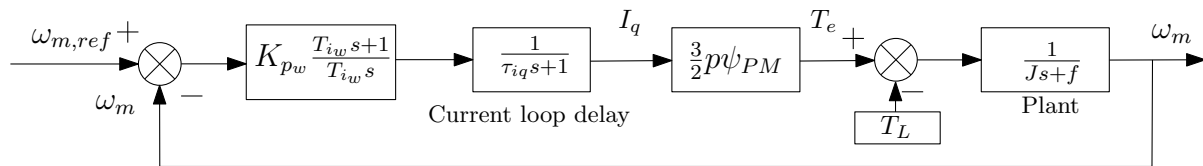
Figure 4.10 – Speed control loop of PMSG

given by the tidal turbine. The speed loop consists the elements as follow:

— PI speed controller to cancel the static error of the speed.
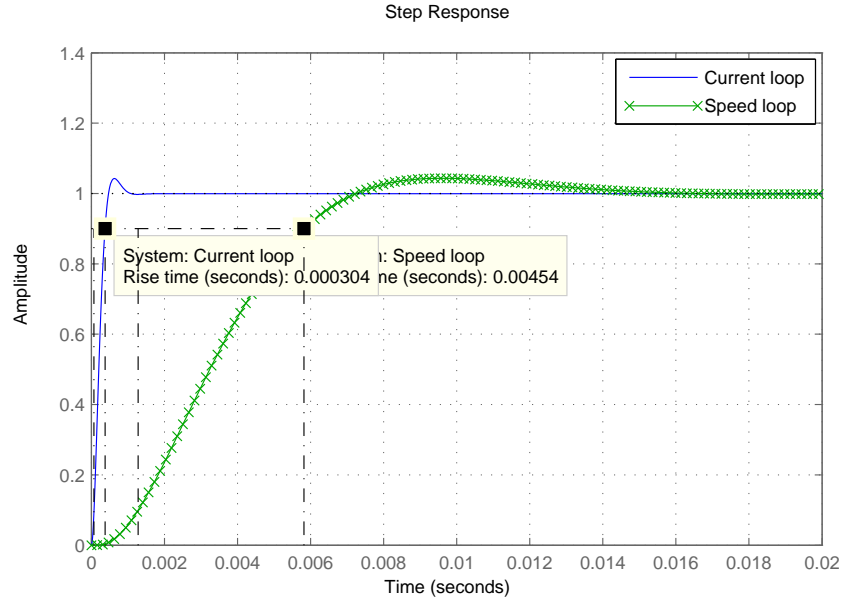
Figure 4.11 – Step response of inner current and speed control loop of PMSG

— The *q axis* current close control loop is modeled as a first order transfer function which equals to $\frac{1}{\tau_{iq}s+1}$, where the time constant $\tau_{iq} = \frac{T_{i_{iq}}}{K_{i_{iq}}K}$.

— The relationship between *q axis* current and electrical torque.

— The generator mechanical equation transfer function.

The load torque T_L is a disturbance from the point of view of the controller. In controller tuning, friction coefficient f is neglected as it is very small. Then, the open speed control loop transfer function can be expressed as:

$$G_{ow}(s) = K_{pw}\frac{T_{i_w}s + 1}{T_{i_w}s}\frac{1}{\tau_{iq}s + 1}K_T\frac{1}{Js} \tag{4.25}$$

where $K_T = \frac{3}{2}p\psi_{PM}$. The Optimum Symmetric Method (OSM) is used to tuning the speed loop controller [118,120]. The standard form of the open loop transfer function of the Optimum Symmetric Method is:

$$G_{OSM}(s) = \frac{K_1K_PT_Is + K_1K_P}{s^2(T_1T_Is + T_I)} \tag{4.26}$$

The speed open loop transfer function can be represented as a similar transfer function to the standard OSM transfer function:

$$G_{ow}(s) = \frac{\frac{K_T}{J}K_{pw}T_{i_w}s + \frac{K_T}{J}K_{pw}}{s^2(\tau_{iq}T_{i_w}s + T_{i_w})} \tag{4.27}$$
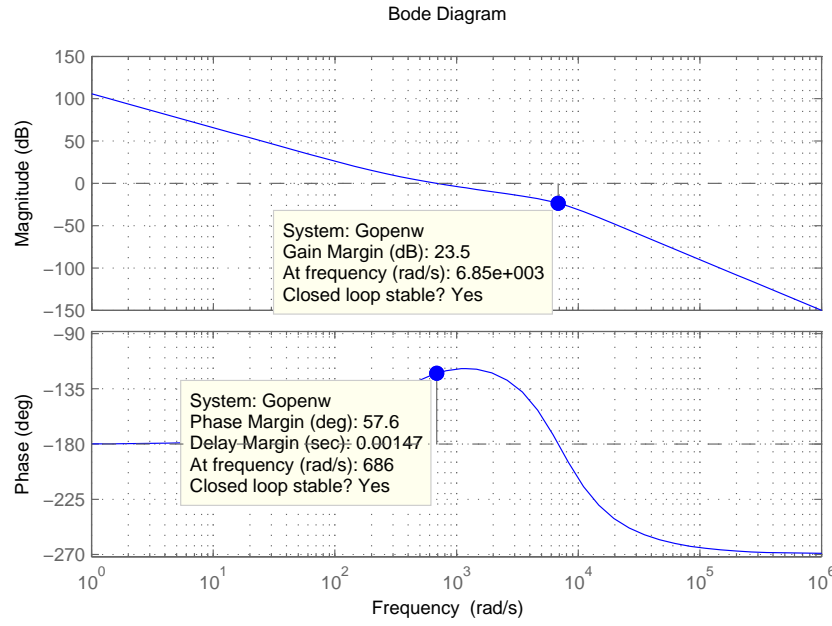
Figure 4.12 – Bode diagram of the speed control loop of PMSG

Using the tuning rule of OSM, the speed PI controller parameters can be obtained:

$$\begin{cases} T_{i_w} = 4T_1 = 4\tau_{iq} \\ K_{p_w} = \frac{1}{2K_1 T_1} = \frac{1}{2\frac{K_T}{J}\tau_{iq}} \end{cases} \tag{4.28}$$

The step response of the speed control loop is shown in Fig. 4.11. The rising time of the speed control loop is $4.54ms$ and it is 15 times of the inner current loop rising time which is $0.304ms$. The current loop response much quickly than the speed loop. Fig. 4.12 show the Bode diagram of the speed control open loop. The obtained PI controller leads to a gain margin of GM$= 23.5(dB)$ at $6850Hz$ and a phase margin, PM$= 57.6°$ at $686Hz$. Therefore, the speed close control loop system is stable.

4.3.2 Control structure of DSCRPMG

The DSCRPMG rotational reference frame model is deduced in the Chpater 2 as Eq.2.96, Eq.2.98, Eq.2.99 and Eq.2.100 expressed. The two stator have its independent *dq axis* voltage equation. The total electrical torque of the generator is the sum of the torque produced by the outer and inner stator. The mechanical equation of the double stator generator is the same as single stator generator.

Fig. 4.13 shows the generator side control system of DSCRPMG. The two stators are separately controlled by two set of control systems. Generator rotational speed is controlled to achieve MPPT. Each stator has its own inner *dq axis* current control loop. Five PI controllers are used in this control system. They are outer speed control loop controller, outer stator I_{do}
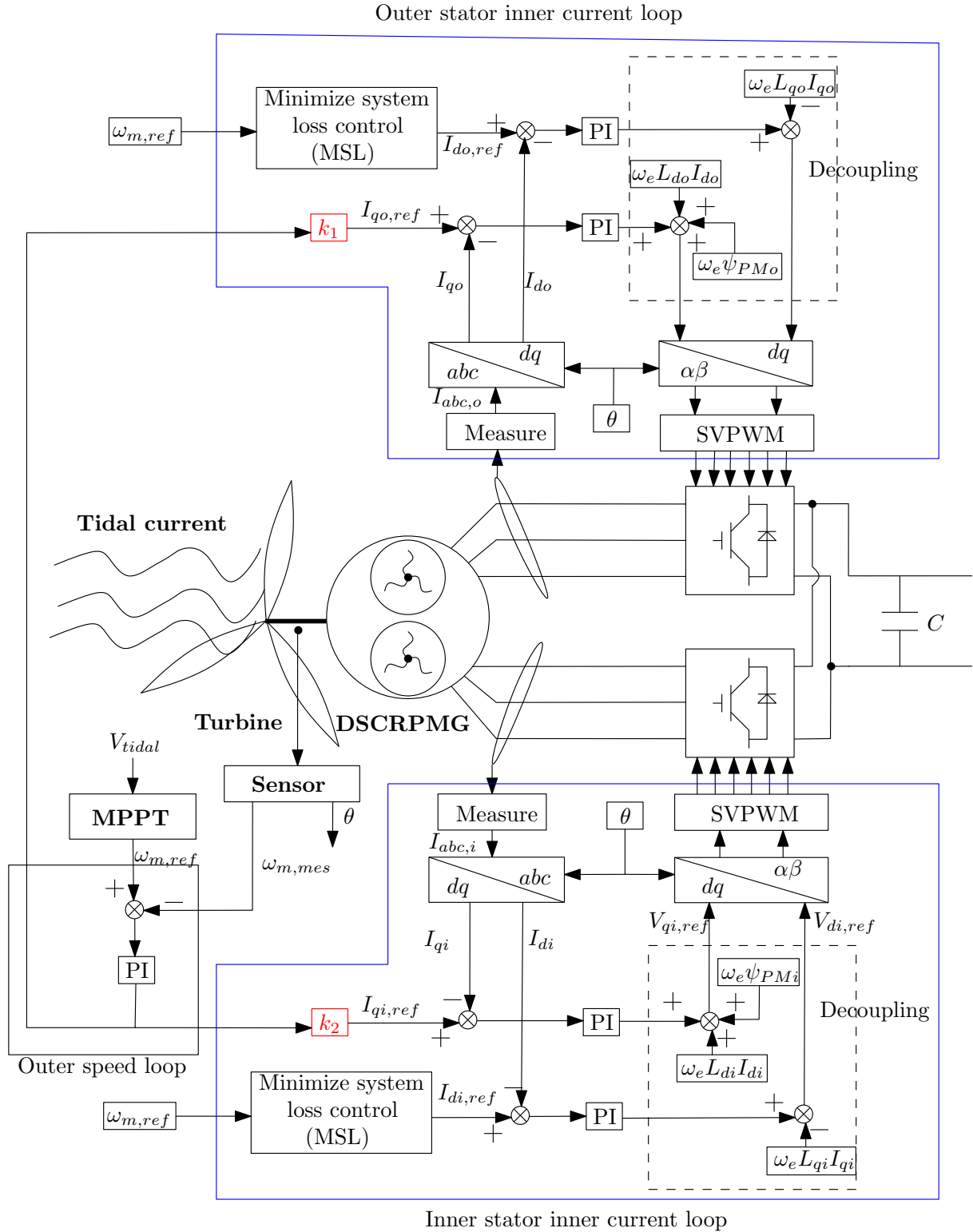
Figure 4.13 – Control scheme of DSCRPMG side converter. k_1 is the outer stator power percentage of the total power; k_2 is the inner stator power percentage of the total power.

and I_{qo} current controllers and inner stator I_{di} and I_{qi} current controllers. Comparing to single stator PMSG control scheme Fig. 4.6, the speed control loop has the same structure. The current control loop structure is also the same as single stator machine except there exists coefficients k_1 and k_2 in the outer and inner *q-axis* current loop respectively. k_1 and k_2 represent the power (or torque) percentage of each stator. They can be expressed as:

$$\begin{cases} k_1 = \frac{T_{eo}}{T_e} \\ k_2 = \frac{T_{ei}}{T_e} \end{cases} \tag{4.29}$$

The values of k_1 and k_2 are decided through the machine design. Because the *dq-axis* inductance in each stator are equal ($L_{do} = L_{qo}$, $L_{di} = L_{qi}$), the *dq-axis* current PI controller are the same for each stator.

Inner current loop controller design of DSCRPMG

The same tuning method has been taken as we have done for single stator PMSG current loop controller design before. Therefore, the detail of the current controller design for DSCRPMG will not be detailed.

1. PI controller for outer stator.

   The transfer function of outer stator PI controllers are expressed as below:

   $$\begin{cases} G_{PI_{do}}(s) = K_{p_{do}} \frac{T_{i_{do}}s+1}{T_{i_{do}}s} \\ G_{PI_{qo}}(s) = K_{p_{qo}} \frac{T_{i_{qo}}s+1}{T_{i_{qo}}s} \end{cases} \tag{4.30}$$

   where,
   $T_{i_{do}} = T_{i_{qo}} = \frac{L_{do}}{R_{cuo}}$.
   $K_{p_{do}} = K_{p_{qo}} = \frac{T_{i_{do}}}{K_o T_{pwm}}$, and $K_o = \frac{1}{R_{cuo}}$.

2. PI controller for inner stator.

   The transfer function of inner stator PI controllers are expressed as below:

   $$\begin{cases} G_{PI_{di}}(s) = K_{p_{di}} \frac{T_{i_{di}}s+1}{T_{i_{di}}s} \\ G_{PI_{qi}}(s) = K_{p_{qi}} \frac{T_{i_{qi}}s+1}{T_{i_{qi}}s} \end{cases} \tag{4.31}$$

   where,
   $T_{i_{di}} = T_{i_{qi}} = \frac{L_{di}}{R_{cui}}$.
   $K_{p_{di}} = K_{p_{qi}} = \frac{T_{i_{di}}}{K_i T_{pwm}}$, and $K_i = \frac{1}{R_{cui}}$.

Outer speed loop controller design of DSCRPMG

The speed control loop structure is presented by Fig. 4.14. In this figure:
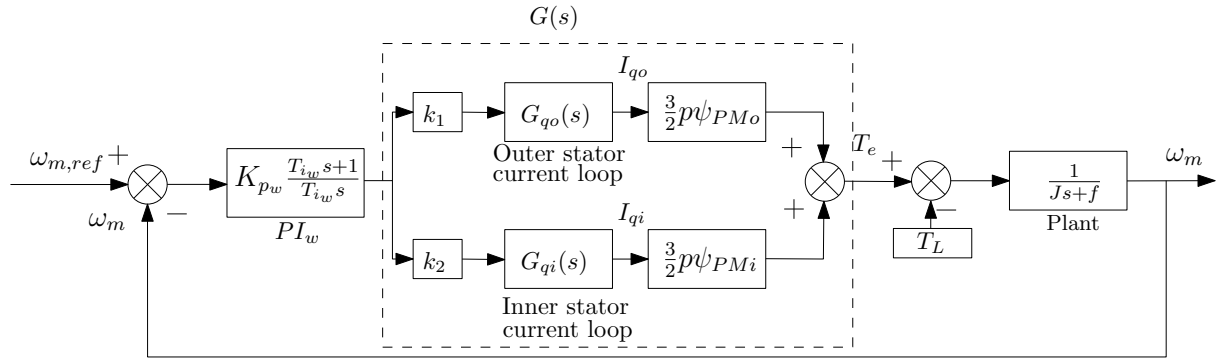
Figure 4.14 – Speed control loop structure of DSCRPMG

T_e: Total electrical torque produced by outer and inner stator.

T_L: Tidal turbine torque.

$G_{qo}(s)$: The equivalent transfer function outer stator *q axis* current close control loop. It is assumed that $G_{qo}(s) = \frac{1}{\tau_{qo}s+1}$, where $\tau_{qo} = \frac{T_{i_{do}}}{K_{p_{do}}K_o}$.

$G_{qi}(s)$: The equivalent transfer function inner stator *q axis* current close control loop. It is assumed that $G_{qi}(s) = \frac{1}{\tau_{qi}s+1}$, where $\tau_{qi} = \frac{T_{i_{di}}}{K_{p_{di}}K_i}$.

$G(s)$ is the equivalent transfer function of the two parallel *q axis* current control loop of DSCRPMG. It can be expressed as:

$$G(s) = K_{To}G_{qo}(s) + K_{Ti}G_{qi}(s) \tag{4.32}$$

where $K_{To} = k_1 \frac{3}{2}p\psi_{PMo}$ and $K_{Ti} = k_2 \frac{3}{2}p\psi_{PMi}$. $G(s)$ can be rewritten as below:

$$G(s) = \frac{K_{To} + K_{Ti}}{\tau_{ec}s + 1} \tag{4.33}$$

where $\tau_{ec} = \tau_{qo} + \tau_{qi} - \frac{\tau_{qo}K_{Ti}+\tau_{qi}K_{To}}{K_{To}+K_{Ti}}$.

The turbine torque T_L is treated as a disturbance for controller design. The friction coefficient f is neglected as it is very small. Finally, the transfer function of the open speed control loop of DSCRPMG is obtained:

$$G_{ow}(s) = \frac{\frac{K_{To}+K_{Ti}}{J}K_{pw}T_{i_w}s + \frac{K_{To}+K_{Ti}}{J}K_{pw}}{s^2(\tau_{ec}T_{i_w}s + T_{i_w})} \tag{4.34}$$

Using the tuning rule of OSM, the speed PI controller parameters of DSCRPMG can be obtained:

$$\begin{cases} T_{i_w} = 4\tau_{ec} \\ K_{pw} = \frac{1}{2\frac{K_{To}+K_{Ti}}{J}\tau_{ec}} \end{cases} \tag{4.35}$$

The step response of current loop and the speed control loop are shown in Fig. 4.15. The rising time of the speed control loop is $7.09ms$ and it is 10.5 times of the inner current loop

rising time which is $0.672ms$. The current loop response much quickly than the speed loop. Fig. 4.16 show the Bode diagram of the speed control open loop. The obtained PI controller leads to a gain margin of GM= $21.2(dB)$ at $4330Hz$ and a phase margin, PM= $33.9°$ at $808Hz$. Therefore, the speed close control loop system is stable.
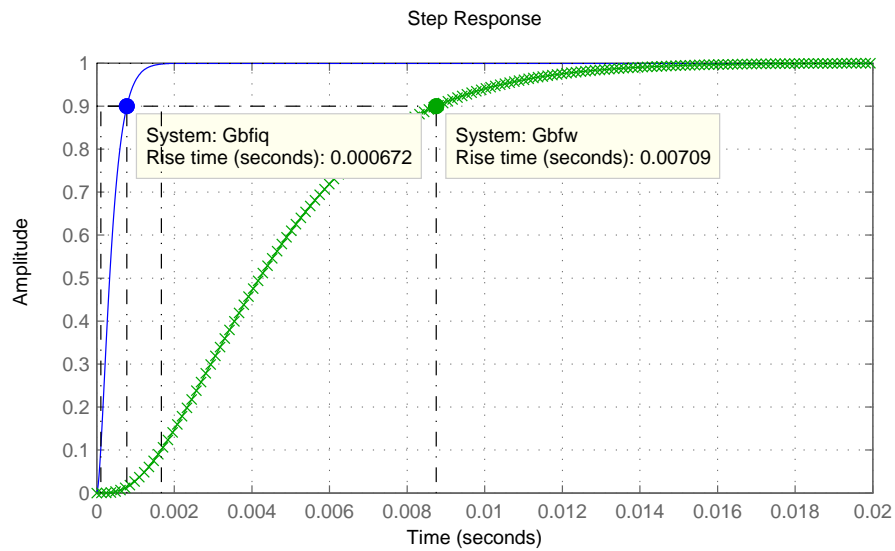
Figure 4.15 – Step response of inner current loop and outer speed loop
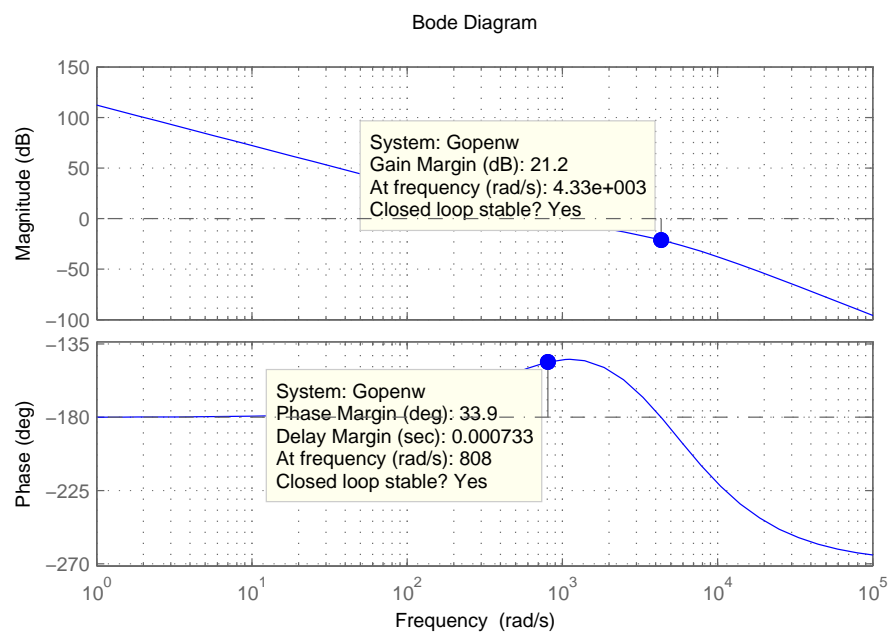
Figure 4.16 – Bode diagram of the speed control loop of DSCRPMG

4.3.3   Simulation results of generator (PMSG and DSCRPMG) side control in normal conditions

In this section, the generator (PMSG and DSCRPMG) systems operated in constant rated tidal speed condition ($2.7m/s$) are firstly presented. The corresponding rated generator rotational speed is $21.5rpm$ and rated torque is $0.44MN.m$. Then, the generator (PMSG and DSCRPMG) system performances for variable tidal speed condition are also studied and compared.

Fig. 4.17 and Fig. 4.18 present the simulation results of PMSG and DSCRPMG system under constant tidal speed condition receptively. Comparing the two figures, it can be seen that both single stator PMSG and DSCRPMG system can well follow the speed reference and produce the needed rated torque without oscillations. The total torque of DSCRPMG T_e is produced by the sum of outer stator torque T_{eo} and inner stator torque T_{ei}. The inner stator torque is smaller than the outer stator torque ($k_1 > k_2$). Therefore, the inner stator current amplitude is smaller than outer stator. The phase currents of single stator PMSG are much bigger than the currents of outer or inner stator of DSCRPMG.

The results indicate that the parameters of controller are well tuned for the two generator system.
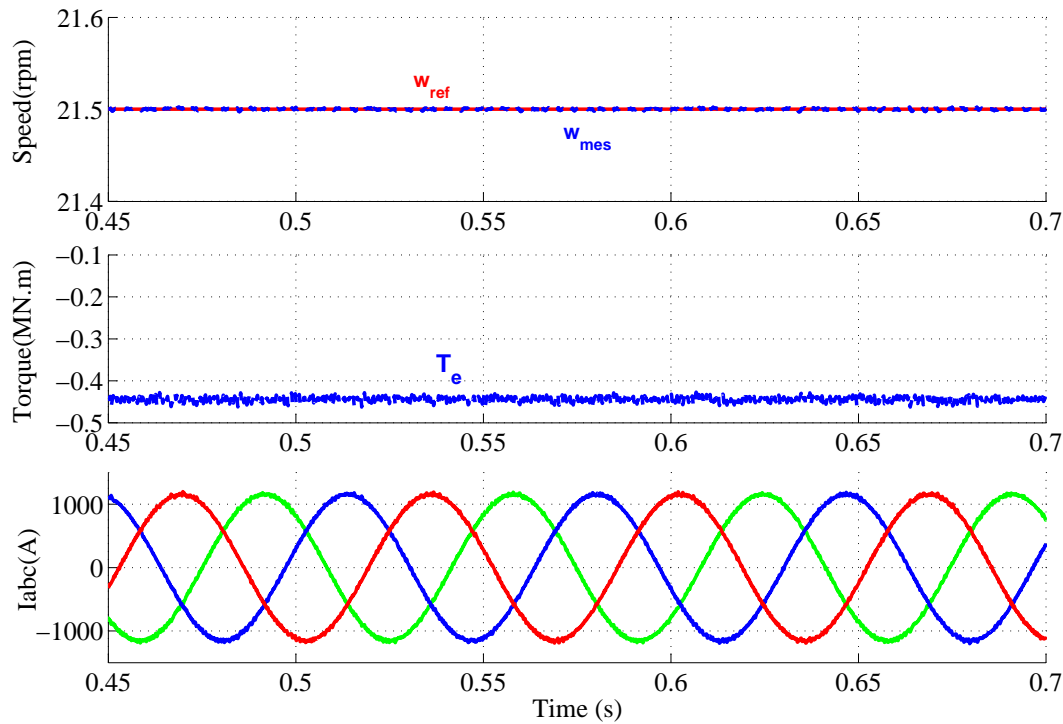
Figure 4.17 – PMSG in healthy condition
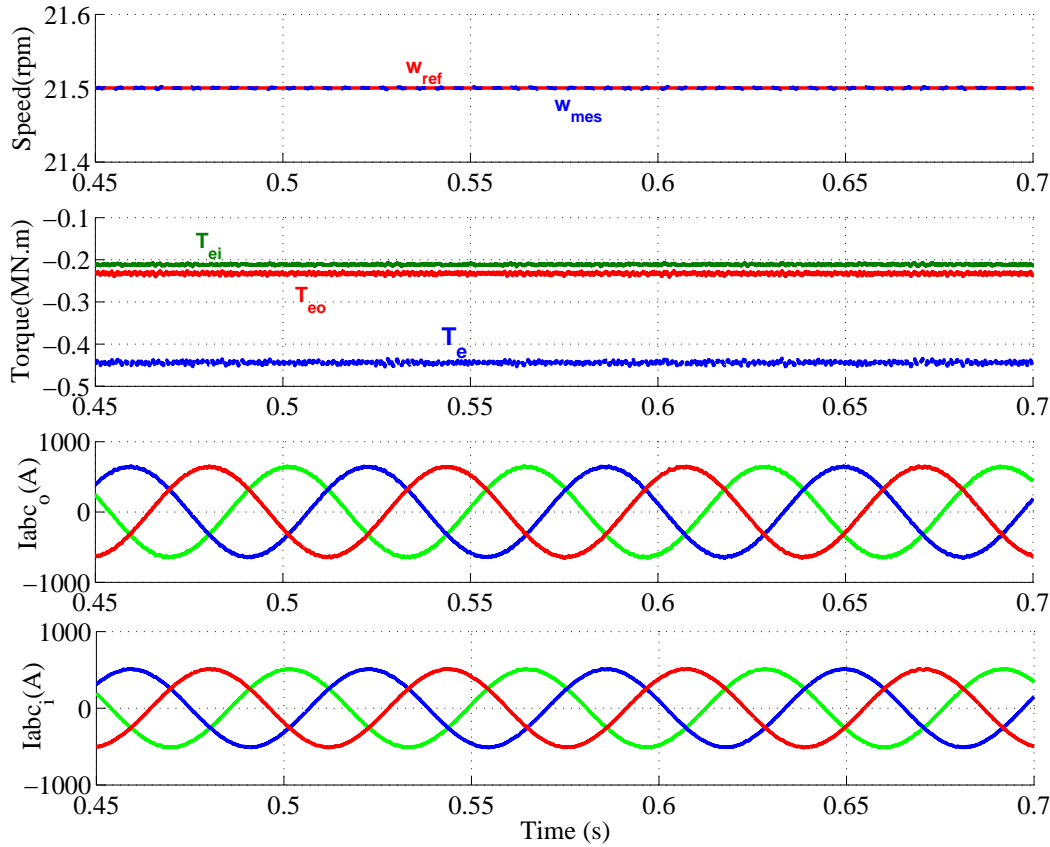
Figure 4.18 – DSCRPMG in healthy condition

The control verifications of the single stator PMSG and DSCRPMG in variable speed condition are shown in Fig. 4.19 and Fig. 4.20 respectively. The tidal current speed is modeled as a oscillation sinusoidal curve. The frequency is around $0.3Hz$ which is much bigger than real tidal current speed frequency. For much slow variation tidal current energy system, the control system design has the capability to satisfy the control goals. When tidal speed is bigger the rated value, the rational speed should be accelerated to keep the turbine power at the power limitation (rated power). The torque is decreased in flux weakening region. For generator operation, the torque and power is negative which means the generator provides power to the grid.

Analysis and comparing the two figures, some conclusion can be drawn:

— The speed reference is followed very good in the two generators.

— It can be said that there is almost no performance difference between PMSG and DSCRPMG in health condition.

— The phase currents of single stator PMSG are nearly doubled comparing to DSCRPMG. That is because each stator of DSCRPMG provides around half of the total rated power ($1MW$) and the rated phase voltage is the same for PMSG and DSCRPMG.

— The difference of power and torque between the generator and turbine are caused by the turbine acceleration and deceleration in Fig. 4.19(b) and Fig. 4.20(b). When tidal current speed is lower than the rated value $2.7m/s$, the generator rotational speed increase or decrease with tidal current speed with the same ratio to achieve MPPT control. When tidal current is bigger than $2.7m/s$, the torque of generator will immediately decrease and then the rotational speed will increase. From the turbine characteristics, for each tidal current speed above the rated value, there is a corresponding rotational speed which will keep the turbine harness the rated power. The turbine torque will decreased. Therefore, the generator needs to provide smaller torque in high rotational speed (above rated speed). It can be achieved by control d-axis current reference as a negative value to decrease the flux linkage of generator which is called flux weakening. For constant speed operation, the power and torque between the generator and turbine will be equal.

— MSL control strategy is used, therefore, the d axis currents are always non-zero and negative both in PMSG and DSCRPMG system. When tidal current is bigger than $2.7m/s$, d axis currents are near to zero. Because for the machine choosing here, copper losses are more important, MSL control strategy is very close to ZDC control.

— Outer stator current is bigger than inner stator current because the rated power of outer stator is bigger than inner stator ($k_1 > k_2$).

— The *dq-axis* currents follow the reference very good both in PMSG and DSCRPMG systems.
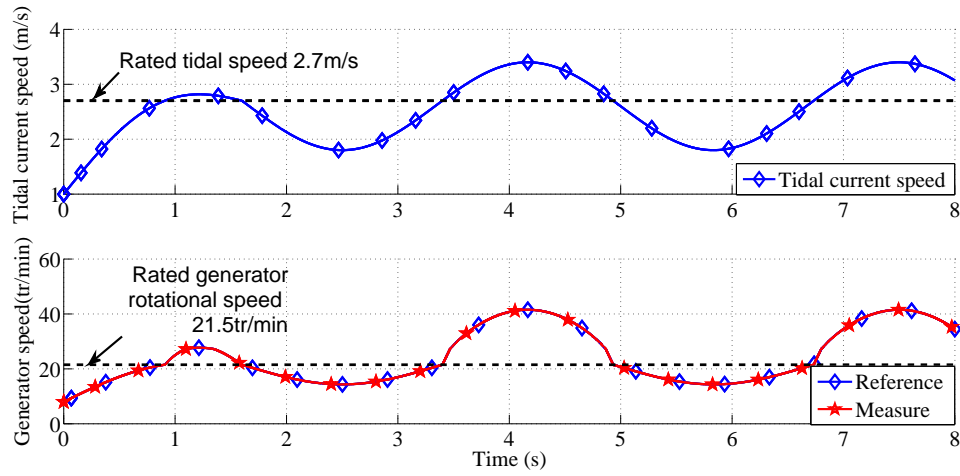
(a) Tidal current speed, generator reference and measured speed
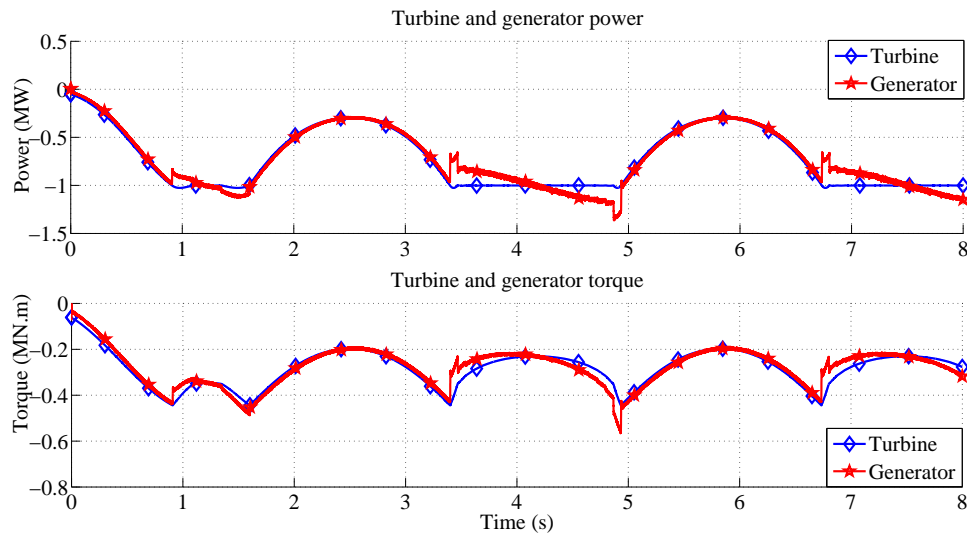
(b) Power, torque of turbine and generator
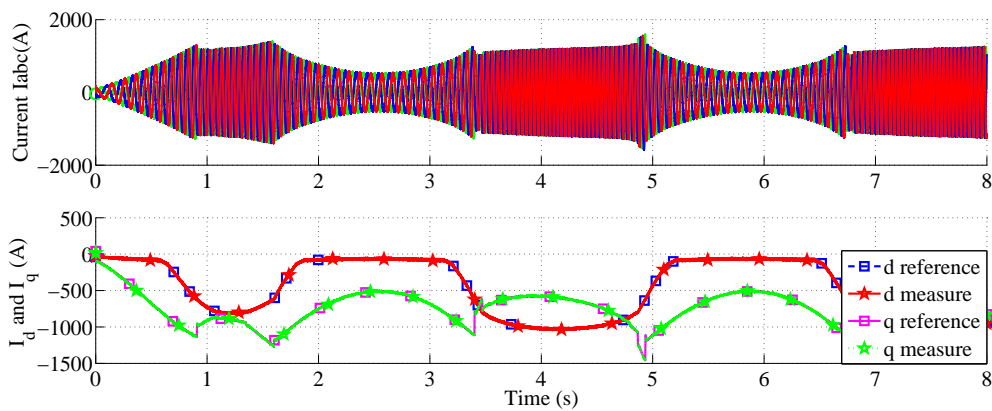
(c) Three phase current and dq axis reference and measured current

Figure 4.19 – PMSG operation simulation in health and variable speed conditions
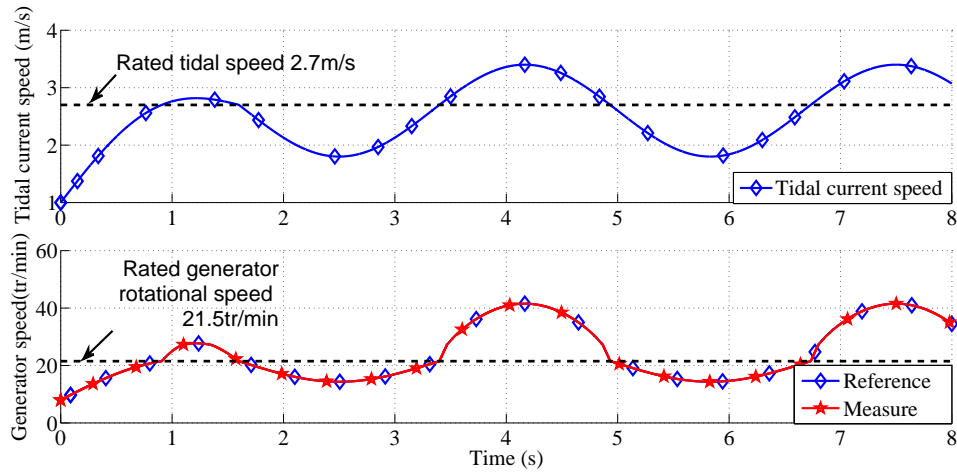
(a) Tidal current speed, generator reference and measured speed
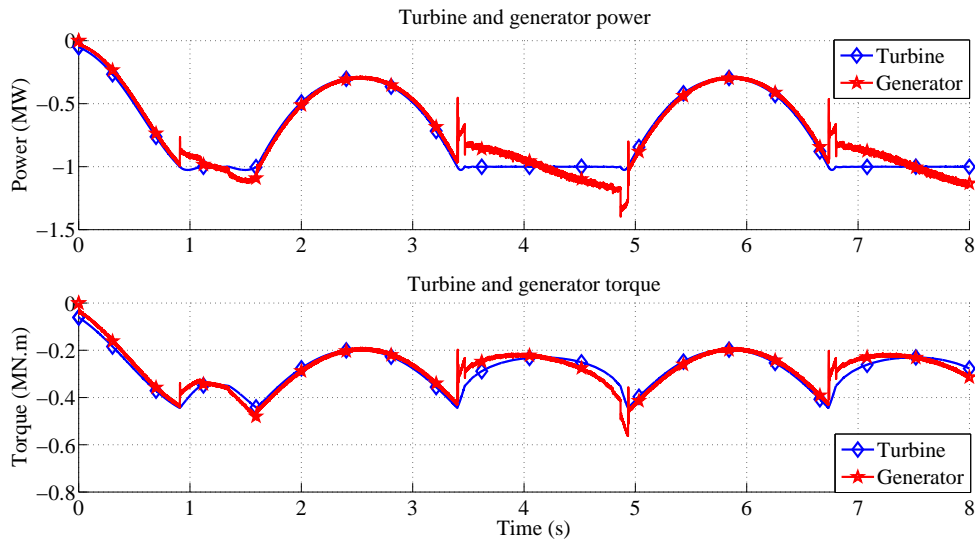
(b) Power, torque of turbine and generator
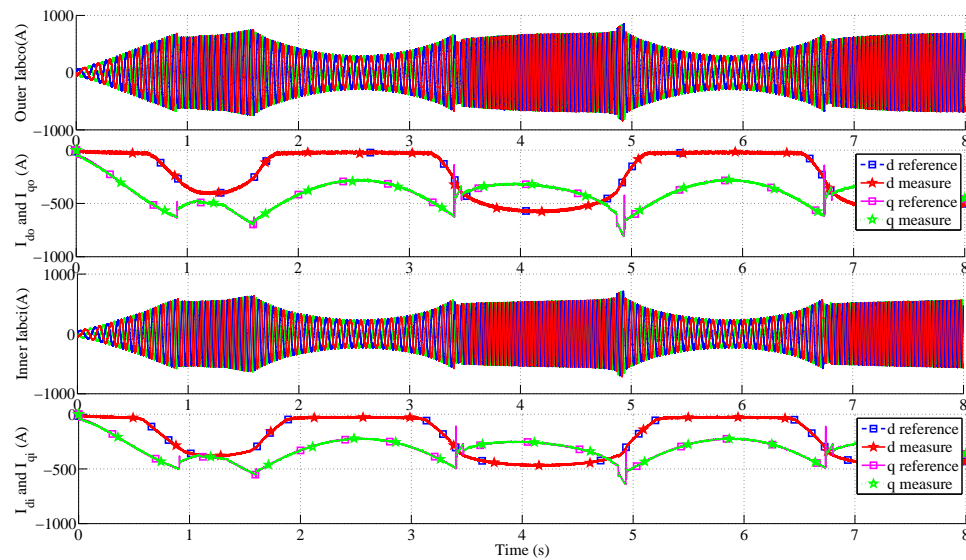
(c) Outer and inner stator current and dq axis reference and measured current

Figure 4.20 – DSCRPMG operation simulation in health condition and variable speed conditions

4.4 PMSG and DSCRPMG control in fault conditions

In most industrial applications, it is very important to continually operate the machine when there is a tolerable fault came out. The failures normally occur in the following components: machine, capacitors, power converter, and sensors. Among them, the most frequent faults are caused by power converter, which are usually related to semiconductor or control circuit failures. It is reported that such faults are attributed to 60% of the power system failures (26% of printed circuit boards failures, 21% of semiconductor failures, and 13% of solder failures) in wind energy system [112, 121, 122]. In this thesis, the research failure is focused on the one phase open circuit fault which is usually caused by converter. In order to realize fault condition control, fast fault diagnosis and analysis are needed [123, 124]. Once the fault condition come out, the reference of *dq axis* current should be changed or the converter topology should be changed to avoid the system losing control [125, 126]. The PI controller parameters will not be changed. Open circuit fault operation of PMSM is firstly treated. For DSCRPMG, three control methods are detailed for the fault control operation.

To realize the default of one phase open circuit, one bridge semiconductors of the rectifier which is directly connected to a phase of outer stator will be disabled. They are illustrated in Fig. 4.21. Hence, the current of the default phase (phase a) is zero. In order to clearly present and compare the difference performance between the PMSG and DSCRPMG, it is assumed that the fault situation happened at the nominal operation point.

(a) PMSG (b) DSCRPMG
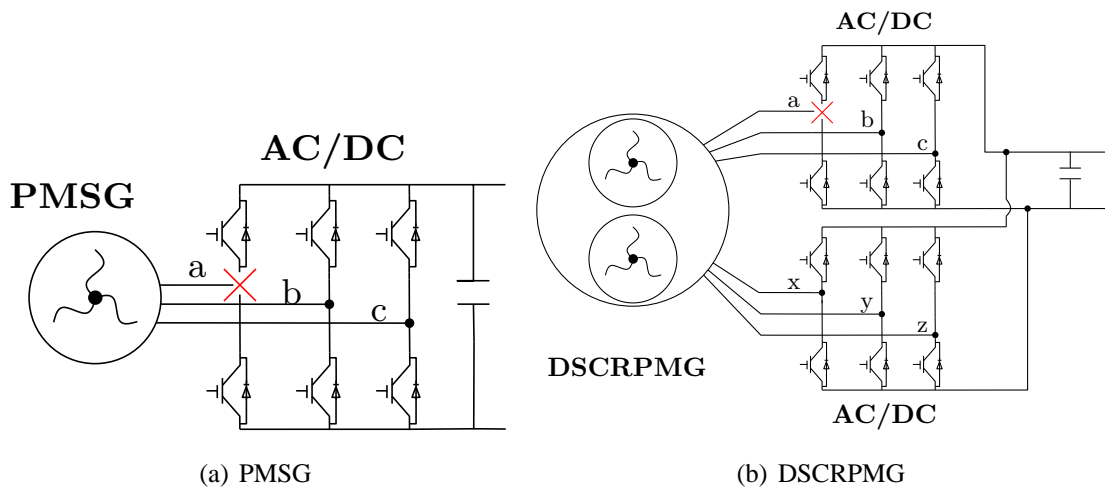
Figure 4.21 – Open circuit fault illustration

Fault tolerant control may trigger serious damage to the converter protection system (such as over current and DC bus over voltage protection). For the aim of continuity operation, the generator and converter should be designed over sizing to avoid the secondary faults due to excessive stress imposed by current and voltage. It will increase the investment of the system. Furthermore, reconfiguration of the system needs more devices. Diagnose and monitoring system are also needed for the fault tolerant control. In this thesis report, only the phenomenon and

performance of open circuit fault control are addressed both in PMSG and DDSCRPMG.

For simplifying the simulation, in the fault tolerant control, the *d-axis* current reference will be fixed as zero instead of using MSL control and the speed will be considered as constant.

4.4.1   Control of PMSG in the condition of open circuit fault

In the case of one phase open circuit fault of single stator PMSG, it is considered that this phase is disconnected and there is no current. Therefore, the system configuration is changed comparing to the health condition. If the control strategy doesn't change, the system will loss control and diverges which may cause serious damage for the system if the system protection is not so strong. In the situation of fault, one can disconnect the system and shunt down the system directly. However, it is not so easy to repair the system in a short time for tidal energy system [127]. Shunt down the system means losing energy. In order to increase the annual energy output, the generator should be controlled under acceptable fault conditions. Through changing the control strategy, the torque and speed oscillation can be reduced to an acceptable level for the system. To have continuity of service in case of default, the system must be controlled to have a mean torque as close as possible to the request value.

It is assumed that the generator phase A is disconnected ($i_a = 0$). And assuming that the neutral point of the generator is not connected, it has:

$$i_a + i_b + i_c = 0 \Rightarrow i_c = -i_b \tag{4.36}$$

It means that the B, C phase current are in reverse direction.

The new PMSM current model becomes:

$$\begin{cases} i_a = 0 \\ i_b = I_m \cos(\theta) \\ i_c = -I_m \cos(\theta) \end{cases} \tag{4.37}$$

where I_m is the current amplitude. Applying the park transformation $\mathbf{T}_{abc \to dq0}$ (see Eq.2.90) to Eq.4.37, the new *dq axis* currents are obtained:

$$\begin{bmatrix} i_d \\ i_q \end{bmatrix} = \mathbf{T}_{abc \to dq0} \begin{bmatrix} i_a \\ i_b \\ i_c \end{bmatrix} = \frac{\sqrt{3}}{3} I_m \begin{bmatrix} \sin(2\theta) \\ 1 + \cos(2\theta) \end{bmatrix} \tag{4.38}$$

It can be seen that the measured *dq axis* currents are no longer constant after the park transformation under the phase open circuit fault condition. Their frequency are two times of the ABC phase currents. Therefore, in order to follow this dynamics, the *dq axis* current reference i_d^* and i_q^* should be consequently modified. The reconfiguration control structure is shown in
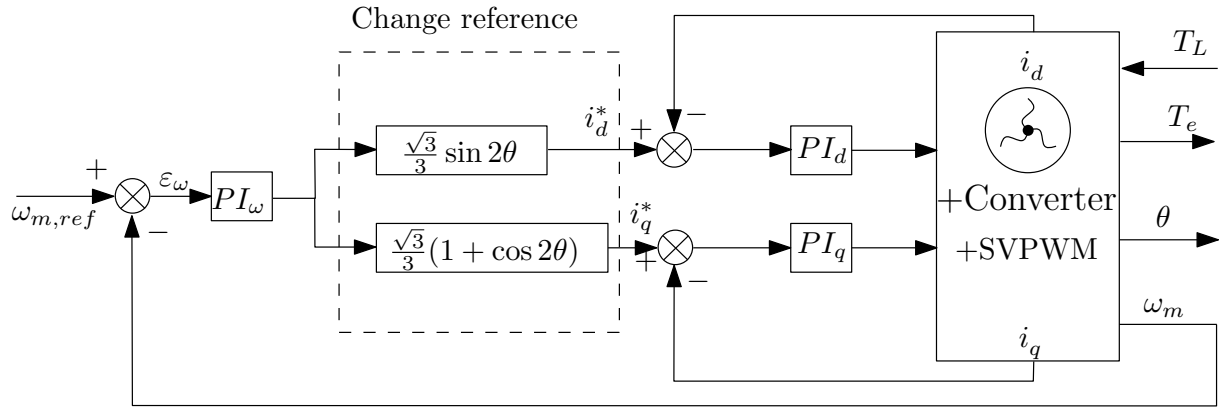
Figure 4.22 – Vector control strategy of PMSG under open circuit fault condition

Fig. 4.22.

The generator electrical torque under fault condition is:

$$T_e = \frac{3}{2}p\psi_{PM}i_q = \frac{3}{2}p\psi_{PM}\frac{\sqrt{3}}{3}I_m(1 + \cos(2\theta)) \tag{4.39}$$

It consists of two components in fault condition which are: Average torque part and torque ripple part. For the same *q axis* current amplitude under health and fault condition, the average torque produced in fault condition is much smaller than that in health condition. The ratio is:

$$\frac{T_{e_{fault}}}{T_{e_{health}}} = \frac{\frac{3}{2}p\psi_{PM}\frac{\sqrt{3}}{3}I_m}{\frac{3}{2}p\psi_{PM}I_m} = \frac{\sqrt{3}}{3} \approx 0.58 \tag{4.40}$$

It means that, in open circuit fault condition, the generator can produce only 58% of the torque under health condition with the same current.

Fig. 4.23 shows the test simulation results of PMSG both in health condition and in fault condition. It should be noted that the PI controller should add anti-windup in fault condition to avoid system losing control. From the result figure, some conclusion can be drawn:

— The dq axis current become sinusoidal and the frequency is two times of the phase current frequency.

— The speed has oscillation cause by the open circuit fault. The speed oscillation varies around $\pm 9.3\%$ at $30Hz$ of the average speed (speed reference).

— The torque oscillation is around $\pm 100\%$ at $30Hz$. And the mean value is the needed turbine torque ($0.44MN.m$).

(a) Speed and torque in health condition

(b) Speed and torque in fault condition

(c) Currents in health condition

(d) Currents in fault condition
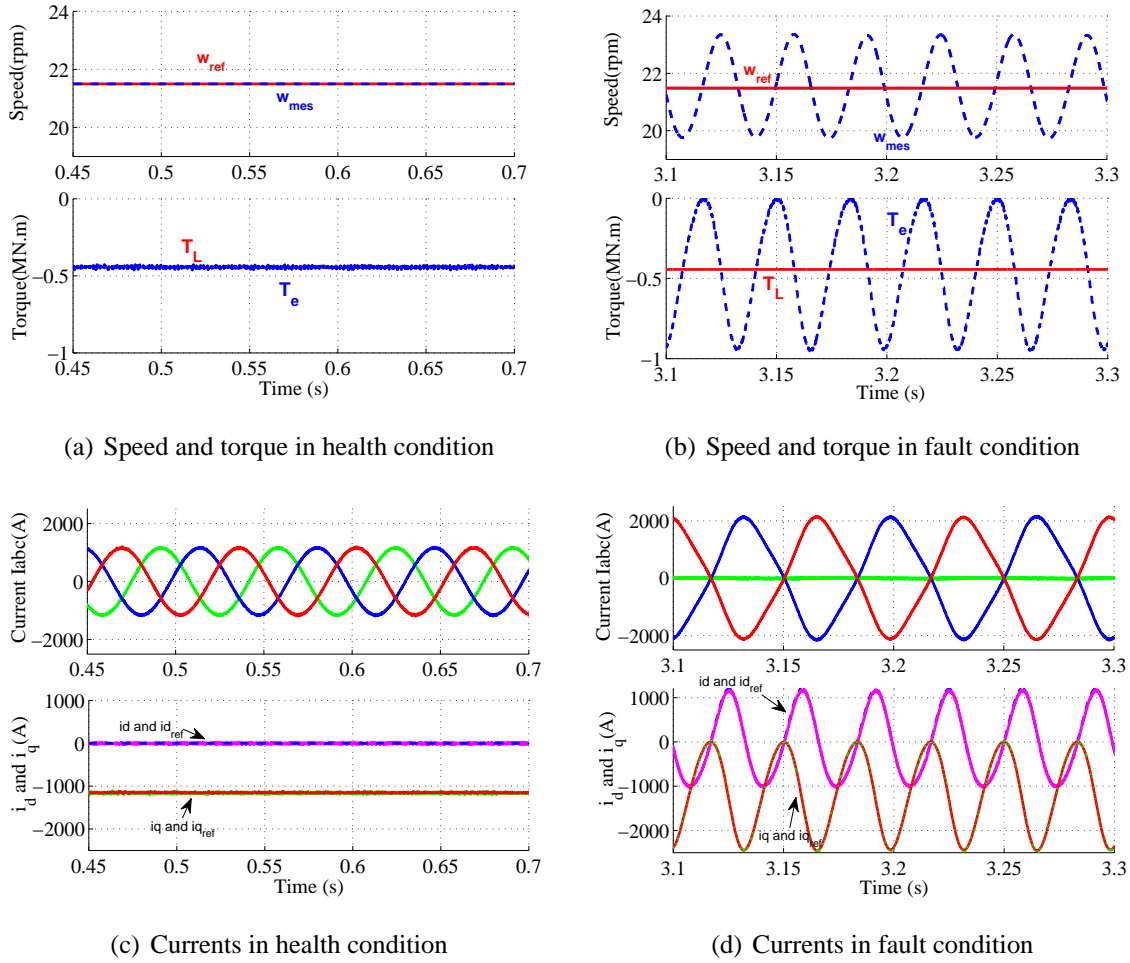
Figure 4.23 – Single stator performance in health and open circuit fault control.

4.4.2   Control of DSCRPMG in the condition of open circuit fault

DSCRPMG can be used to minimize the torque and speed oscillation caused by the faulty stator because they can be compensated with the other healthy stator. In the situation of losing one phase of the outer stator, three control strategies are used to minimize the oscillation of torque and speed. They are:

1. Control the generator by shunting down the faulty stator (Losing one phase, then disconnecting the faulty stator).

2. Control the generator by changing the faulty stator current control references to ensure continuity of service.

3. Control the generator by high pass filter based compensator or torque estimator.

The idea of the three methods is that: firstly, once there is open circuit come out in one stator, the faulty stator will be disconnected completely to the DC bus. As a consequent, the source of torque and speed oscillation is removed from the system. The DSCRPMG is operated as a single stator generator. The healthy stator needs to produce the total load torque(turbine

torque). Hence, the currents of the healthy stator will be doubled (because of $k_1 < k_2$). It may cause thermal problem of the healthy stator. Secondly, the faulty stator will continually keep in service to produce part of torque. However, the torque and speed oscillations are relatively big because the faulty stator will produce an oscillated torque. Finally, in order to reduce the torque and speed oscillations, a high pass filter based compensator or torque estimator are designed to extract the torque oscillation current single and then inject it to the healthy stator current loop. Through doing that, the healthy stator can produce a torque which has inverse form comparing to the faulty stator torque form. Therefore, the total generator torque and speed oscillations will be remedial.

Method 1: Control the generator by shunting down the faulty stator

In this method, the faulty stator is disconnected to the DC bus. The generator is operated with only the health inner stator as a single stator machine. Therefore, the needed total torque is all produced by the inner stator. As there are no faulty current existed in the DSCRPMG, the torque speed performances in the faulty condition are almost the same as healthy condition.

The test simulation results is shown in Fig. 4.24. Before time $0.5s$, the system operated in health condition. At time $0.5s$, the outer stator is disconnected to the DC-bus.

The results indicate that:

— The three phase currents of the faulty stator are zero. Therefore, the outer stator doesn't produce any torque.

— The currents of inner health stator is increased to produce the power which outer stator can't produce. The torque T_e is equal to inner stator torque T_{ei}. The currents of inner stator will increase $\frac{K_{To}+K_{Ti}}{K_{Ti}}$ times. In our case, this value is equal to 2.1. That means the inner stator current will increase 2.1 time of the rated current value to provide the total rated torque. The machine should have the capability operated with this current level in fault condition. This is strongly depended on the machine design.

— After $0.025s$ transient period, the torque and speed follows the reference as in health condition. There is no torque and speed oscillation. The system operates as a single stator generator system.

This method can perfectly eliminate the torque and speed oscillation. However, the temperature of winding should be carefully verified because the phase currents increased more than 2 times. Big current can cause high power losses which may lead to high temperature in windings. The researched DSCRPMG is selected from the Pareto-front in the Chapter 3 with the criteria $F_{obj,final2}$. The wingding temperatures of this machine are $82°C$ and $66°C$ for inner stator and outer stator windings respectively Fig. 3.12 at rated operation condition. That means this machine has a big margin to operated in a over-rated current condition.
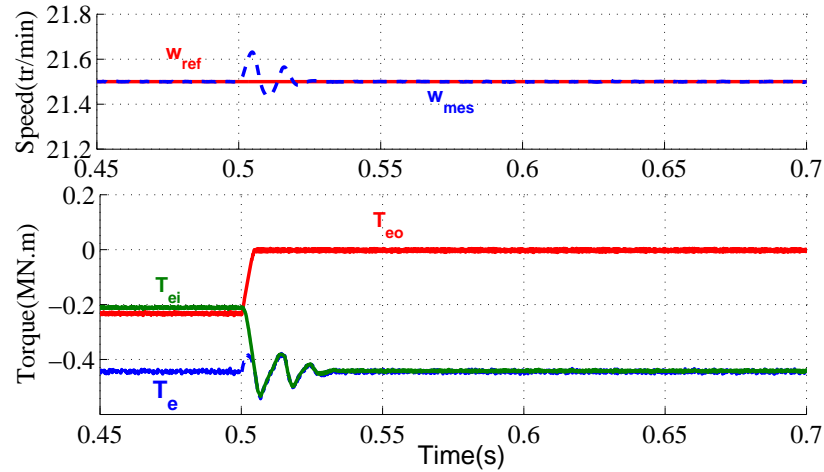
(a) Speed and torque
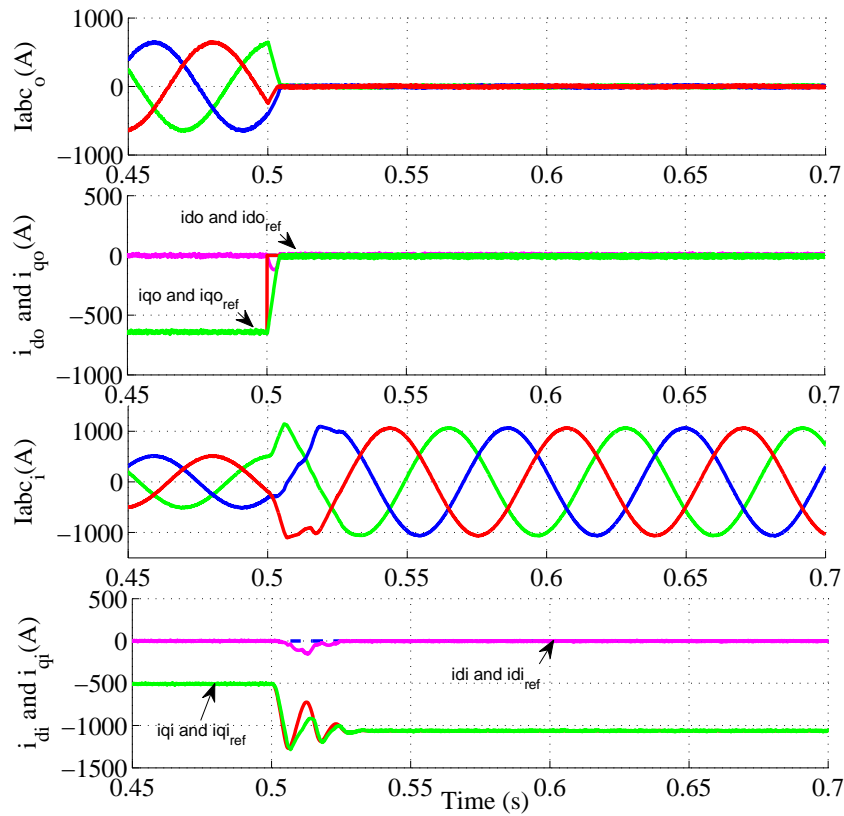
(b) Currents

Figure 4.24 – Method 1: Fault control method through shunting down the fault stator

Fig. 4.25 shows the outer and inner stator winding temperature variation surface which varies with the generator rotational speed and phase current amplitude. The green planes of the figure are the limitation of winding temperature which equal to $155°C$ (Class F). The winding temperatures increase with generator rotational speed and phase current both for inner and outer stator. The winding temperatures increase more dominated with current than speed because the copper losses is much important than iron losses in this machine. Inner stator winding temperature is bigger than outer stator. When the phase current is $1000A$ and rotational speed is

$21.5tr/min$, outer stator winding temperature is still below the green limitation plane. How-ever, the inner stator is too heat and it is bigger than $155°C$. That means this machine is not suitable for this strategy with outer stator open circuit fault because the needed inner stator phase current are bigger than $1000A$ in fault condition. On the contrary, if the open circuit fault is happened in inner stator phase winding, this method can be applied to the outer stator to provide the total torque.

(a) Outer stator   (b) Inner stator
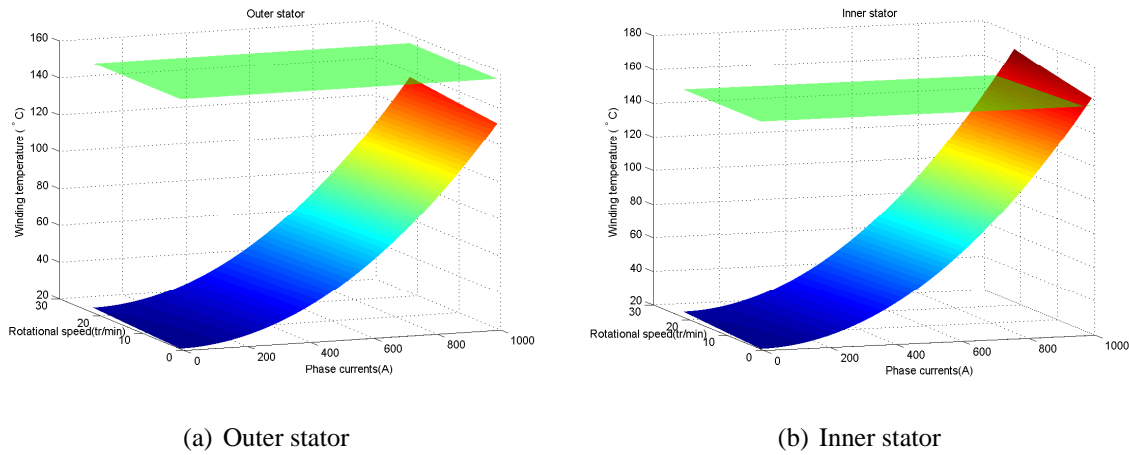
Figure 4.25 – Winding temperatures variation with the speed and current of the selected DSCRPMG.

For the researched case, in order to avoid serious current situation happened, the torque reference should be reduced to avoid inner stator winding bigger than the limitation in fault condition, i.e for torque $0.35MN.m$, the inner stator will not have thermal problem for this machine.

The generators which has low cost and low energy output in Fig. 3.4 can't be used for fault tolerate control for the methods provided in this thesis because they are compact and has small current tolerate margin. For those machines, the load torque should be reduced to avoid serious damage in the situation of fault or completely shutdown.

Method 2: Control the generator by changing the faulty stator current control references

In the first method, the faulty stator is removed out from the system completely and then it produce no torque. In this section, the faulty stator will continually in operation to produce torque. In order to avoid the faulty stator losing control, the faulty stator (outer stator) *dq axis* current references will be changed like it have been done for single stator PMSG open circuit fault tolerant control. The control structure of the inner stator has no change. The inner stator *dq axis* current references are still the output of the PI speed controller. For the outer stator who loses one phase, its *dq axis* measure currents will start oscillation as it has been discussed for

PMSG. Similar to Eq.4.38, the *dq axis* current reference of outer stator can be expressed as:

$$\begin{bmatrix} i_{do}^* \\ i_{qo}^* \end{bmatrix} = \frac{\sqrt{3}}{3} I_{mo} \begin{bmatrix} \sin(2\theta) \\ 1 + \cos(2\theta) \end{bmatrix} \tag{4.41}$$

where I_{mo} is the current reference which is the output of the speed controller.

The total electrical torque is :

$$T_e = \frac{3}{2} p \psi_{PMi} i_{qi}^* + \frac{3}{2} p \psi_{PMo} \frac{\sqrt{3}}{3} I_{mo} (1 + \cos(2\theta)) \tag{4.42}$$

This equation shows that the total torque of DSCRPMG also has oscillation.

The control structure is shown in Fig. 4.26. Only the outer stator current references are modified as it has been done for single stator fault control.
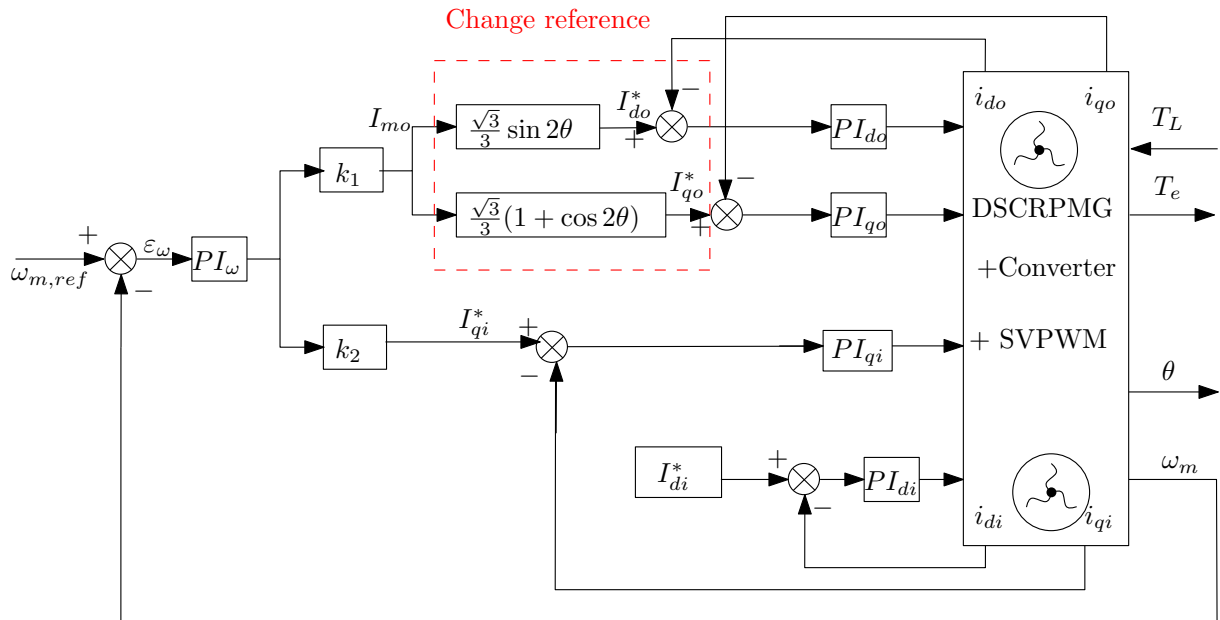
Figure 4.26 – Control structure of of DSCRPMG in fault condition: Modify the current reference of the failure stator

The test simulation results are shown in Fig. 4.27. From this figure, some conclusion can be drawn:

— The oscillation frequency of the *dq axis* current of outer stator is two times of the stator phase currents.

— There is also some speed oscillation ($\pm 3.7\%$), but much more smaller than that of single stator PMSG fault control.

— The torque oscillation is between $-0.28 MN.m$ (-37%) and $-0.71 MN.m$ ($+60\%$) around the average torque $0.44 MN.m$ which is the generator rated torque. The torque oscillation is not symmetric (unlike PMSM faulty control performance). This because the inner

stator and the outer stator torque (T_{ei} and T_{eo}) has a phase angle difference which is not equal to 0 or π.
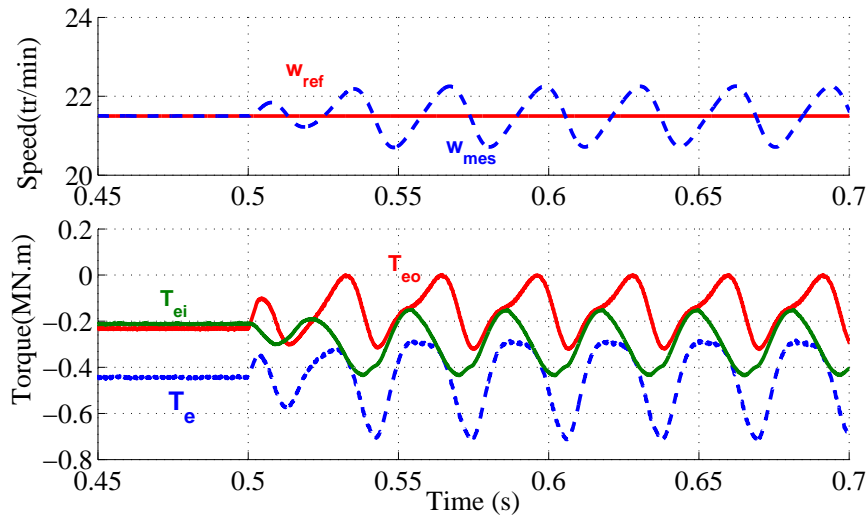
(a) Speed and torque
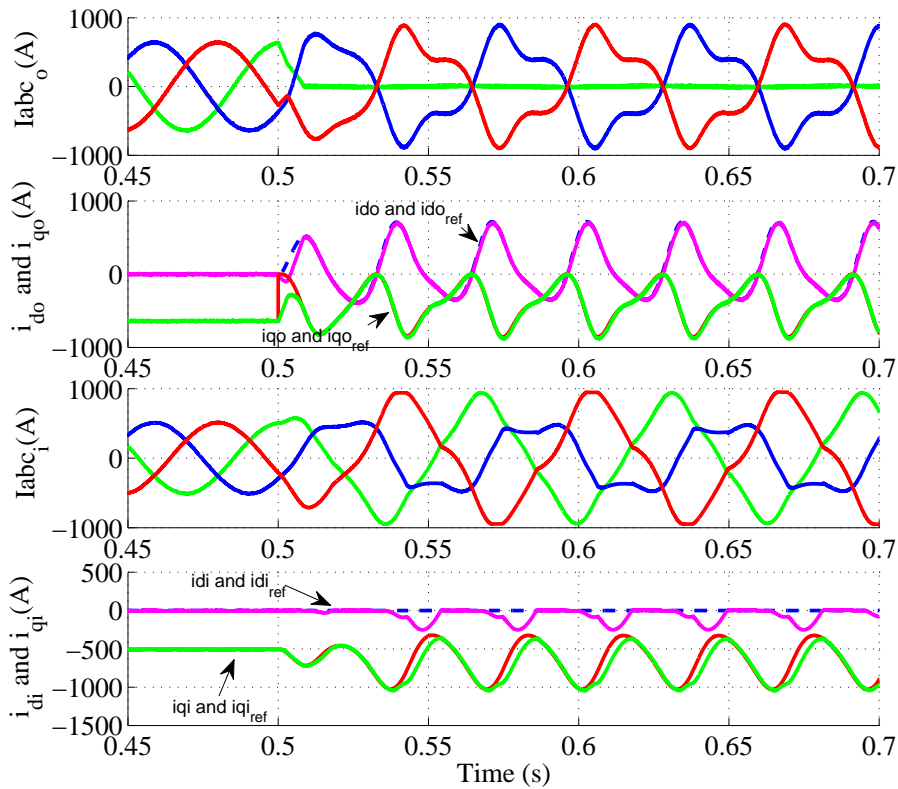
(b) Currents

Figure 4.27 – Method 2: Faulty control method through only modifying the faulty stator current control references

— The two phase currents I_{bo} and I_{co} of outer stator which has open circuit problem are in opposite and $I_{ao} = 0$. However, B and C phase currents are not sinusoidal any more.

— Both the inner and outer stator phase currents are increased to satisfy the needed torque

because the outer stator torque producing capability decreased. When the outer stator produced a small torque (i.e. when $cos(2\theta) = -1$), the control system will generate a big current reference for inner health stator to provide big torque to compensate the outer stator losing torque. The oscillation of torque and speed lead the inner stator q axis current non constant. The inner health stator currents become unbalanced. A and C phase currents amplitude of inner stator are almost doubled.

The healthy stator can help the faulty stator to produce the torque. Therefore, the oscillation of torque and speed is much smaller than single stator PMSG fault control.

In this method, the outer and inner stator maximum phase currents are near $1000A$. Outer stator windings are acceptable to have $1000A$. Inner stator has two phase currents near $1000A$ and the other one phase current keeps at the rated level. The three phase currents of inner stator are unbalanced. Fig. 4.25 is plotted with balanced three phase currents assumption. It is difficult to calculate the iron losses for unbalanced current condition. If the iron losses is not considered in this method, the winding temperatures may not be a problem for the researched machine case. The winding temperature limitation is less strong than the first method because of less copper losses.

Method 3: Control the generator by changing the two stator current references with compensator or estimator

The second method fault tolerant control can keep the faulty stator continually in service. However, this method has torque and speed oscillations. For the aim of canceling the torque and speed oscillation, two methods are proposed in this section which inject the oscillation current to the healthy stator current control loop with high pass filter based compensator or torque estimator. The outer stator *dq-axis* current references are modified as the second method to avoid the system diverging.

(A) **High pass filter based compensator.**
To cancel the faulty stator torque ripples, a high pass filter based compensator is proposed to extract the oscillation current, see Block2 in Fig. 4.28. This compensator superpose an appropriate compensating signal to the q-axis current loop of the healthy stator so that the modified control rejects the torque ripples caused by the faulty stator. The injected compensating current $i_{qo,comp}$ to the inner stator (healthy stator) q-axis current reference can be expressed as:

$$i_{qo,comp} = \frac{s}{s + 2\pi f_c} k_c i_{qo} \tag{4.43}$$

where k_c is the compensating gain whose value is set to 0.8. The filter cutoff frequency f_c is set to be sufficiently smaller than the torque oscillating frequency at the rated operation. Hence, f_c is fixed to 5 Hz.
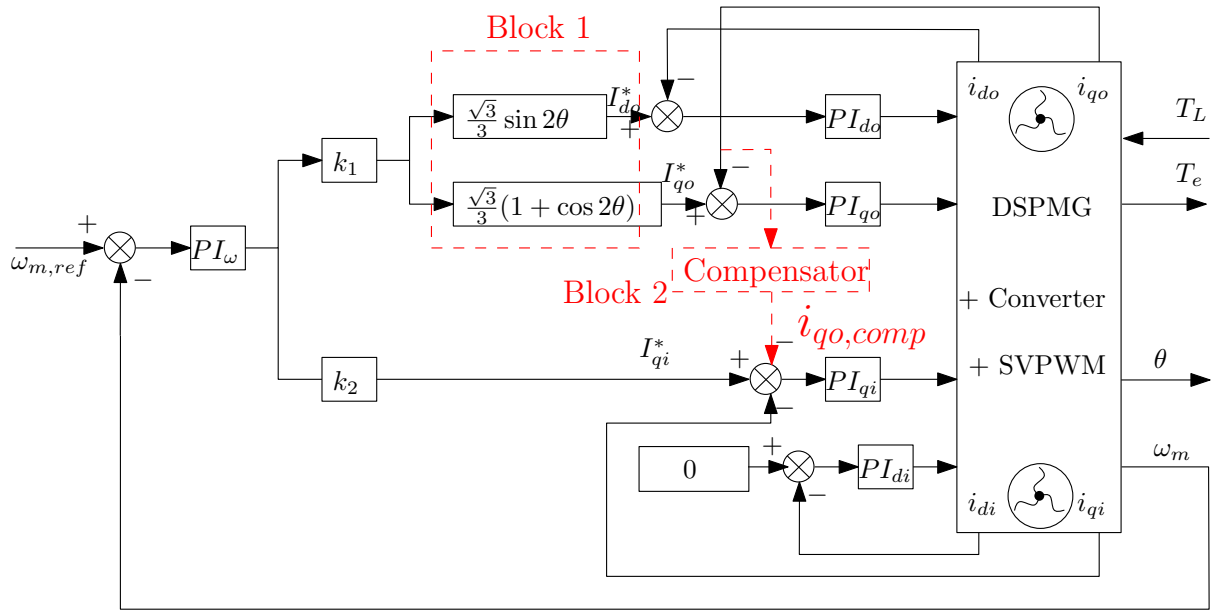
Figure 4.28 – Proposed fault control diagram using high pass filter based compensator.

The simulation results are shown in Fig. 4.29. Some conclusions from the figure can be drawn:

— The oscillation frequency of the *dq axis* current of outer stator is two times of the stator phase currents.

— The speed is oscillated around the speed reference about 0.1% after the open circuit fault is come out.

— The torque oscillation is very small ($\pm 5\%$) and can be treated as the same in health condition. When the outer stator torque T_{eo} reduced, the inner stator will increase to compensate the torque which outer stator can't produce. They have inverse variation form.

— This torque and speed oscillations are significantly reduced with the use of the proposed compensator

— The phase current amplitude of the inner stator increased to compensate the torque decreasing of the faulty stator. The relative phase current increases bigger than the other phases: when phase A of outer stator is open, the phase A of inner stator increase bigger than the other two. The inner stator currents become unbalanced. The phase current amplitude of the faulty stator will not change. There is no winding temperature problem for the faulty stator. Because there is just one phase current which is around $1000A$ in inner stator, the winding temperature problem is less important than the method 1.
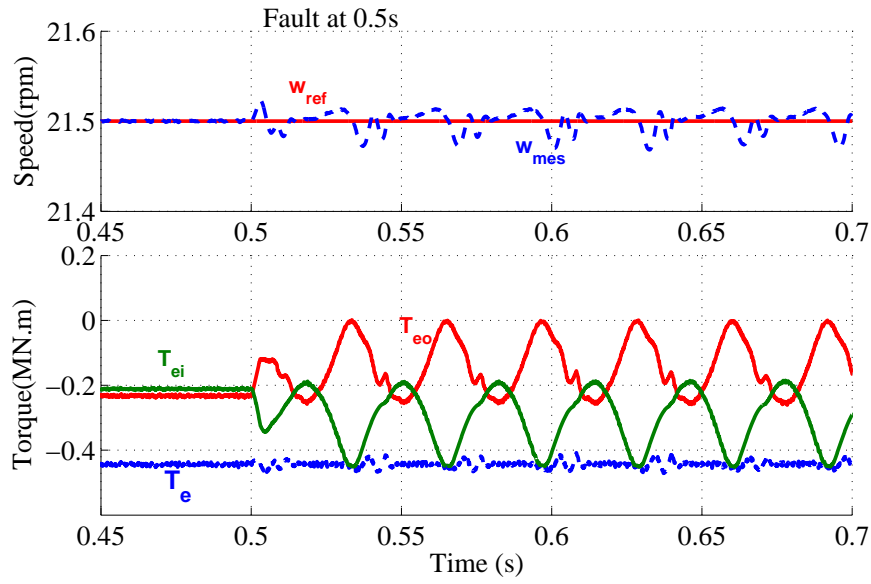
(a) Speed and torque
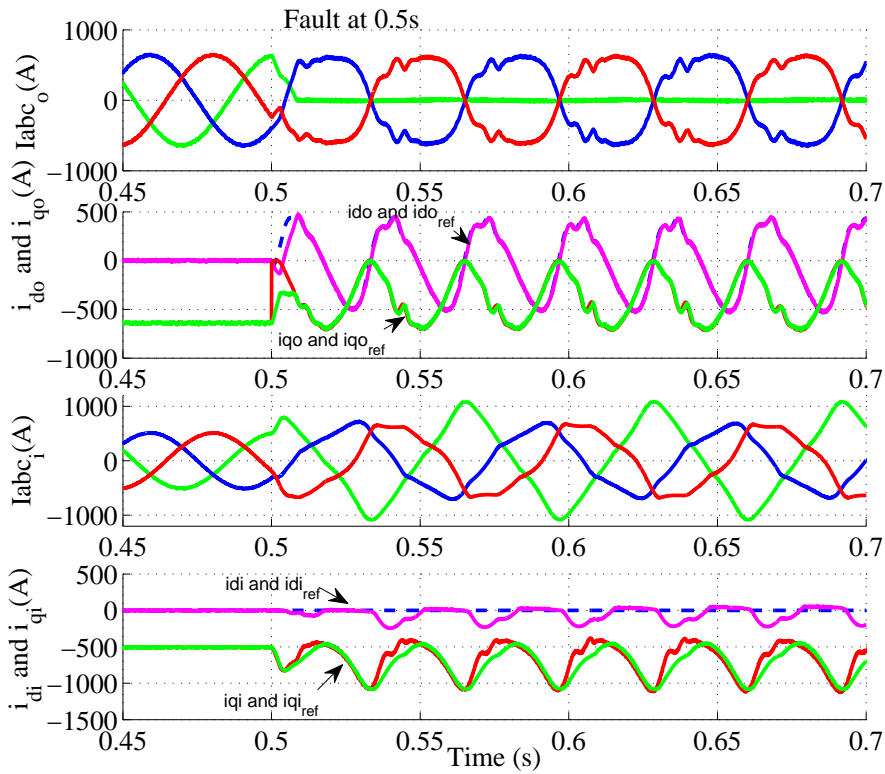
(b) Currents

Figure 4.29 – Method 3: Fault control method by modifying outer stator current references and using high pass filter based compensator

(B) **Torque estimator.**

In this part, a new fault tolerant control method which has very small torque and speed oscillation and smaller winding temperature problem comparing to method 1 and method 2 is proposed.

The control system structure is shown in Fig. 4.30. Firstly, the outer stator dq axis current reference are modified like method 1. Secondly, a torque estimator is used to calculate the oscillation current Δi_q which will be added to the speed controller output of inner q axis current control loop. This Δi_q can lead the generator produce a torque ΔT_e in the reference to compensate the oscillation torque.
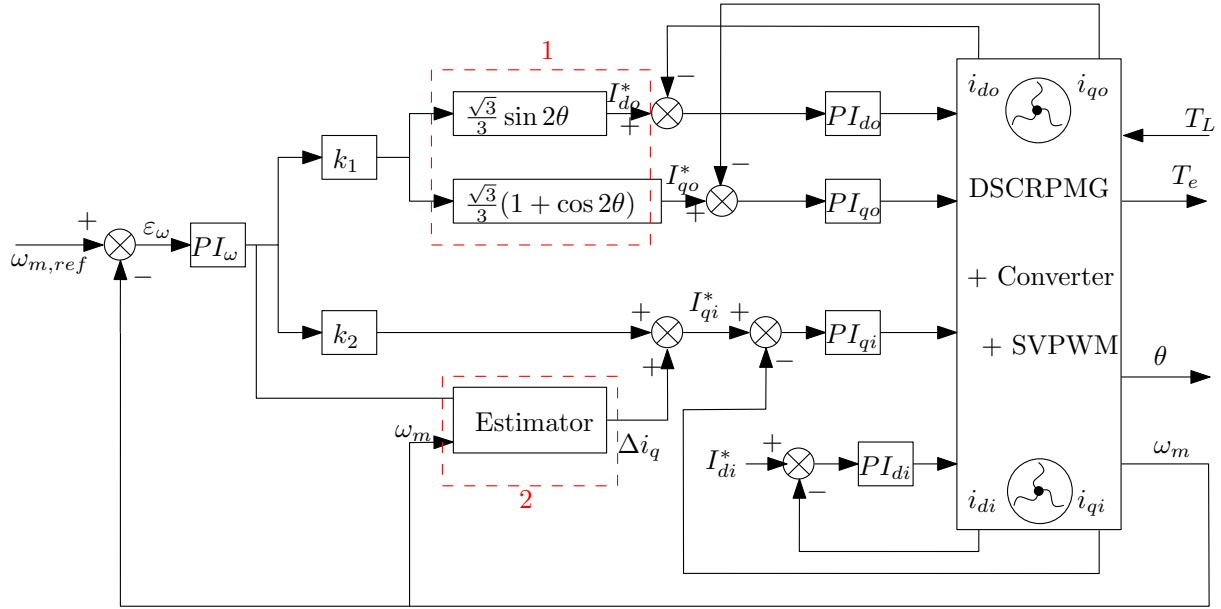
Figure 4.30 – Proposed fault control diagram using torque estimator.

The mechanical equation of the generator and turbine system can be expressed as follow:

$$J\frac{d\omega_m}{dt} + f\omega_m = \prec Te \succ -\Delta T_e - T_L \tag{4.44}$$

where:

ΔT_e: the oscillation of torque.

$\prec Te \succ$: the average electrical torque.

The the oscillation of torque ΔT_e can be treated as a disturbance which is added to the turbine torque.

$$T'_L = \Delta T_e + T_L \tag{4.45}$$

The corresponding oscillation current is:

$$\Delta i_q = \frac{\prec Te \succ -\hat{T}'_L}{K_{To} + K_{Ti}} \tag{4.46}$$

where $K_{To} = k_1 \frac{3}{2}p\psi_{PMo}$ and $K_{Ti} = k_2 \frac{3}{2}p\psi_{PMi}$. This current can compensate the torque oscillation caused by the fault outer stator.

The method of the estimator design is based on the mechanical model of the generator [128]. The PI controller is used to estimate the disturbance torque and converge it to the

real turbine torque. The topology of the estimator is shown in Fig. 4.31.
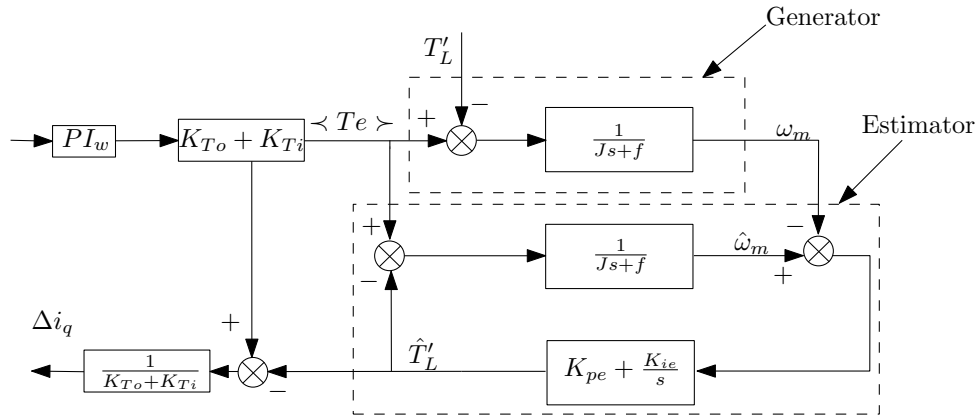
Figure 4.31 – Estimator structure

The transfer function between the estimated torque and the real torque is:

$$\frac{\hat{T}'_L}{T'_L} = \frac{1 + \frac{K_{pe}}{K_{ie}}s}{1 + \frac{K_{pe}+f}{K_{ie}}s + \frac{J}{K_{ie}}s^2} \tag{4.47}$$

where K_{pe} and K_{ie} are the proportional coefficient and integrate coefficient of the PI controller of the estimator.

$$\begin{cases} K_{pe} = 2\xi\omega_n J - f \\ K_{ie} = J\omega_n^2 \end{cases} \tag{4.48}$$

The choice of the damping ratio ξ and natural frequency ω_n must quick enough so as to the regulation loop current i_{qi} will not be affected by the time required to estimate. In this thesis, $\xi = 0.707$ and $\omega_n = 8000 rad/s$

The simulation result is shown in the Fig. 4.32.

The results can be concluded as follow:

— The speed follows the reference very good with oscillation around $\pm 0.1\%$ after the open circuit fault is come out.

— The torque oscillation is very small ($\pm 4.5\%$). When the outer stator torque T_{eo} reduced, the inner stator will increase to compensate the torque which outer stator can't produce. They have inverse variation form.

— The phase current amplitude of the inner stator increased for compensating the torque decreasing of the outer stator which has open circuit fault. The relative phase current increases bigger than the other phases: when phase A of outer stator is open, the phase A of inner stator increase bigger than the other two. The inner stator currents become unbalanced. The phase current amplitude of the faulty stator will not change. There is no winding temperature problem for the faulty stator. Because

there is just one phase current which is around $1000A$ in inner stator, the winding temperature problem is less important than method 1.

— The outer stator *dq axis* current oscillation frequency is 2 times of the phase current.
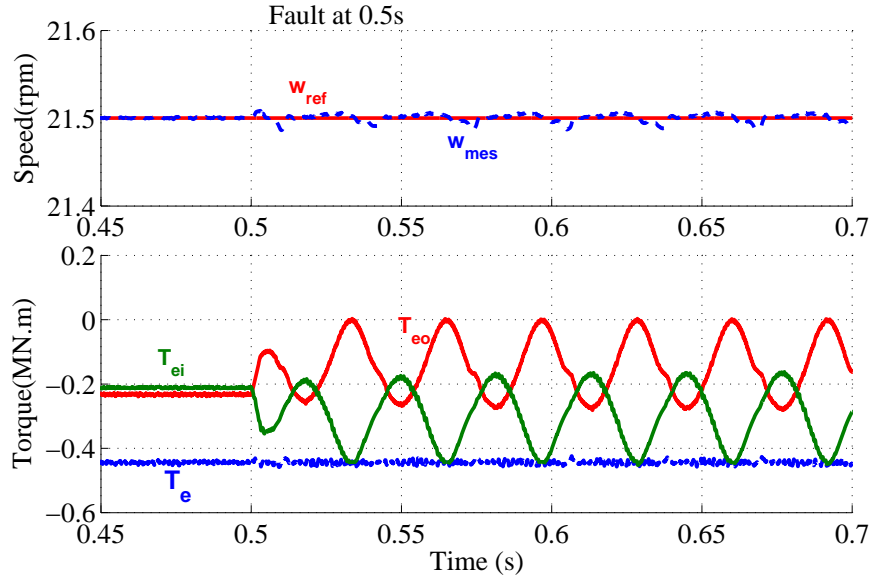
(a) Speed and torque
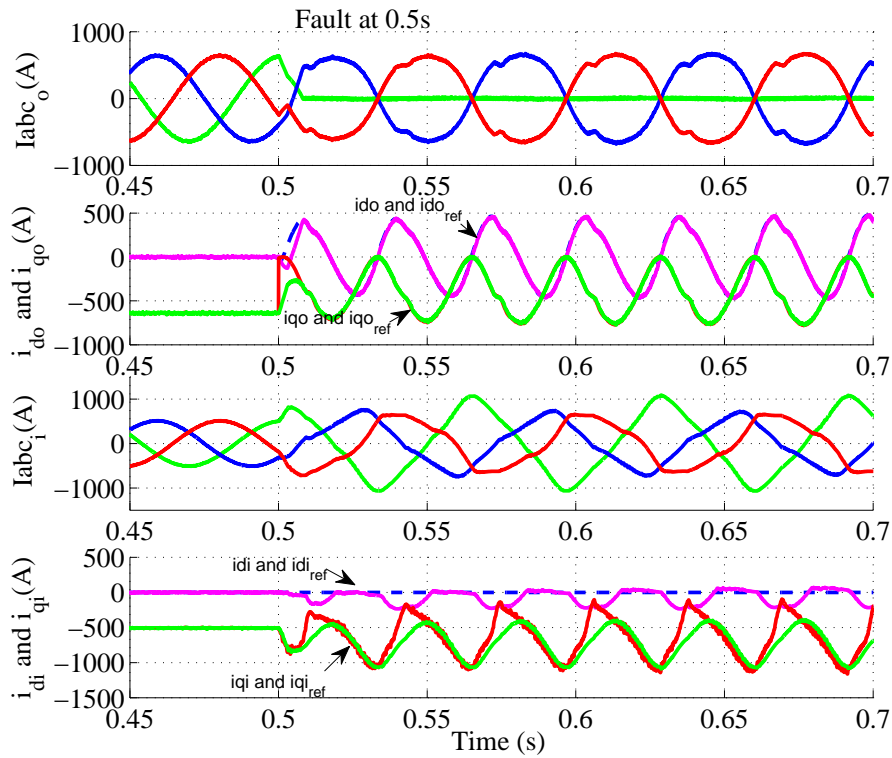
(b) Currents

Figure 4.32 – Method 3: Fault control method by modifying outer stator current references and using torque estimator

This figure confirms that this method is useful since the torque ripples are estimated.

However, it should be noted this method ensures the filtering of the torque, but at the same time the currents of the healthy stator will have more harmonics (due to the reference which is added with a torque ripple current Δi_q).

Comparing to high pass filter based compensator, the performance of the two methods can be regarded as the same. It seems like that torque estimator has slightly better performance. However, the parameter of the high pass filter k_c and f_c are not optimized.

4.4.3   Comparison between the faulty control methods

In this section, the comparison of the open circuit fault tolerance performance is made between PMSG and DSCRPMG. Table. 4.1 shows the generator performance under faulty condition. DSCRPMG gained an overwhelming advantage under faulty condition comparing to PMSG no matter which control method is used.

Generator	M	Oscillation rate		WTL	RI
		Speed	Torque		
PMSG	1	$\pm 9.3\%$	$\pm 100\%$	😐😕	Easy, Anti-windup PI
DSCRPMG	1	$\approx 0\%$	$\approx 0\%$	😐😕	Easy
	2	$\pm 3.7\%$	$+60\%, -37\%$	😕	Easy, Anti-windup PI
	3	$\pm 0.1\%$	$\pm 4.5\%$	🙂	Compensator or torque estimator

Table 4.1 – Fault tolerant control performance comparison. M: Method. WTL: Winding Temperature Limit. RI: Reconfiguration Implement

In PMSG, the method changing the current reference is used. The system can still be controlled. However, the torque and speed oscillation are serious.

In DSCRPMG, three methods are used to decrease the torque and speed oscillation under faulty condition. The first method which stop the faulty stator directly can perfectly reduce the torque and speed oscillation. This because the faulty stator which leads torque and speed oscillation is disconnected to the DC-bus. In order to satisfy the needed torque, the inner stator current is increased to provide the total torque. This current increase the power losses and may cause thermal problem of the generator. Therefore, in order to obtained fault control without reducing the load torque, the machine should be specially designed (over-size or strong cooling system).

In the other two methods, the third method can reduce the torque and speed oscillation sharply. This method is the prefer one for DSCRPMG open circuit fault control because it has very small torque and speed oscillation. Furthermore, it has smaller winding temperature problem comparing to method 1 and method 2. DSCRPMG has the advantage of that, once one stator has fault, the other stator can provide compensation to keep the performance.

4.5 Summary

This chapter is dedicated to the control system design and open circuit fault tolerant control of PMSG and DSCRPMG. The health condition operation are firstly analyzed. Generator side and grid side control systems are separately designed. Generator side control for each stator of DSCRPMG is similar to the PMSG control especially for the inner current control loop. In DSCRPMG control system, the q axis current for inner and outer stator are obtained from the speed controller output which then multiply the corresponding torque ratio k_1 and k_2 of each stator. In the health operation condition, PMSG and DSCRPMG has almost the same performance for the same tidal current profile.

In open circuit fault control, PMSG system needs to change to control reference to avoid losing control if the machine neutral point is not accessible. The *dq axis* currents are not constant value any more and they oscillate with two times frequency of the phase current frequency. The amplitude of the phase currents should increase $\sqrt{3}$ times to provide the same torque as in health condition. This will cause the stress of the machine isolation, demagnetizing and low efficiency problem. It should be considered in the machine design stage.

Three methods of open circuit fault tolerant control for DSCRPMG system are discussed. As this machine inherently has two stators and the total machine torque is produced by the sum of the two stator torque, the healthy stator can produce more torque to compensate the faulty stator losing torque. The oscillation currents in faulty stator can be injected to the health stator current control loop by high pass filter based compensator or torque estimator. Hence, the torque oscillation caused by the faulty stator can be mitigated by the healthy stator through producing a inverse oscillated torque. The compensator and torque estimator are used to calculate the current ripple Δi_q and then this current is injected to the health stator *q axis* current control loop. The torque and speed oscillation are remedial and the fault tolerant performance is almost like in health condition. The winding temperature thermal problem is less important in the third method. Therefore, DSCRPMG is more suitable for fault tolerant operation than PMSG no matter which method is used.

<div style="text-align: right; font-size: 3em; font-weight: bold;">5</div>

Conclusions & perspectives

5.1   Conclusions

In this thesis, the research mainly focuses on multi-objective optimization design and open circuit fault tolerant control of a DSCRPMG for tidal current energy application. The DSCRPMG is optimized for a full torque speed profile decided by turbine characteristics combining with control strategy, converter size and losses, every operation point frequency for a choosing tidal site. The open circuit fault tolerant control is realized by taking the inherent advantage of DSCRPMG that once one stator has defect, the other healthy stator can compensate the torque and speed oscillation caused by the fault stator.

In Chapter 1, a comprehensive state of art of tidal energy extracting is presented. Tidal current energy basic theory and two tidal current speed modeling methods (called HAM and practical model SHOM) are explained in detail. As many interesting go to tidal current energy research in the recent years, some pre-commercial and prototypes of tidal turbine have achieved success. Those up to date pre-commercial tidal turbine are reviewed in classification of turbine form (horizontal, vertical, ducted and oscillating hydrofoil turbine). The possible tidal current energy generator system choices are discussed. Some introductions of the DSCRPMG are given at the last part of this Chapter.

In Chapter 2, firstly, an analytical preliminary DSCRPMG design model based on semi-experimental thumb rules is developed at the rated power condition. The external parameters such as inductance, emf, system losses and particularly the curve of efficiency are deduced. Two generators are chosen from this efficiency curve to research the system investment and annual energy output for a given torque speed profile and operation frequency. The first one is

the generator which has maximum efficiency at the rated power. The other one is the generator which has 1% less efficiency. In order to choose the suitable and high efficiency machine control strategy, a comprehensive commonly applied machine vector current control strategies (such as ZDC, CMF and MML) are studied. An appropriate control strategy MSL minimizing all system losses (converter and machine) which has the best system efficiency for the full torque speed profile is proposed. The results shows that the generator which has 1% less efficiency at rated power condition has better cost effective than the maximum efficiency generator. It has less investment and more annual energy output. Therefore, it is difficult to obtain a high cost effective generator through designing a generator at rated power condition using experience rules for variable speed drive energy system. In order to design a high cost effective generator, optimization tool should be applied.

In Chapter 3, a multi-objectives PSO is adopted to design a cost effective DSCRPMG converter system for tidal current energy application. 16 variable parameters including DSCRPMG geometry parameters and converter size parameters are optimized under mechanical, magnetic, electrical and thermal constraints. The two optimization objectives are maximizing the annual energy output and minimizing the investment. The investment includes generator material, generator supporting structure and converter costs. For a given torque speed profile of a selected tidal farm site, the operation time in one year for each operation point is predictable. Applying the MSL control to every operation point of the torque speed profile allows to calculate the annual energy output.

Two criteria are provided to select the final design solution from the Pareto front which can maximize the 20 years revenue and minimize the cost energy ratio $€/kWh$. The optimization model is validated through comparing analytical results and FEA results of the selected machine in Pareto front. Some parameters sensibilities such as iron material type, material specific cost, generator outer diameter and heat transfer coefficient are analyzed and compared with the reference Pareto front.

The same optimization process is applied to single stator PMSG. Comparing with the optimization solutions for DSCRPMG, the torque volume density of DSCRPMG is around 65% higher than single stator PMSG in the majority solutions for the same annual energy output. The price to pay for increasing the torque volume density is that the mass of DSCRPMG is 1% heavier than the mass of single stator PMSG. Increasing 1% mass to reduce 65% volume is really valuable in the application which needs compact machine.

In Chapter 4, control systems of PMSG and DSCRPMG are designed and simulated both in health condition and open circuit condition. In healthy condition, the performances of PMSG and DSCRPMG are almost the same. In open circuit fault control, the reconfiguration of control system is needed to avoid the system losing control. DSCRPMG has much better performance than PMSG in fault condition. The torque is produced by the sum of the two stator torques. Therefore, once one stator has defected, the other stator can produce an inverse oscillation

torque to compensate default. Three methods control for DSCRPMG system are proposed to assure continuity of service or to minimize torque oscillations. The comparison results indicate that methods based on a torque estimator or an appropriate high pass filter lead to the best results. Performances which are almost like in health condition can be achieved; speed oscillations are very lower while torque oscillation does not exceed 5%.

5.2   Perspectives

Some improvements and ideas for the future research in this field are outlined as follows:

— The thermal model used in this thesis is a simple model. In the future work, a more sophisticated and precise thermal model can be used in the optimization process to reduce the winding temperature error.

— For a selected tidal energy farm, the rated tidal current speed can be added to the optimization variable parameter. Through optimizing this parameter, the designer can evaluate which rated power of generator is better for the selected tidal energy farm.

— Study shift angle between external and internal stators to reduce the cogging and/or torque ripple

— Only open circuit failure is discussed in this thesis report. In the future work, the short circuit, sensor failure and ground faults should be researched in DSCRPMG system.

— Consideration of the tidal turbine model in the entire conversion chain study, from the resource to the grid integration.

— Investigation of other converter topologies for fault tolerant studies to fulfill continuity of service.

— Experimental validation of fault tolerant control of DSCRPMG should be carried out.

Appendices

A

Converter losses model

In this appendix chapter, the IGBT converter losses model which is already developed by Semikron are presented [129]. The detail formulation is deduced in this reference or in some other literature [130, 131]. IGBT and diode power losses in converter, as well as power losses in any semiconductor component, can be mainly divided in two groups:

1. Conduction losses (P_{cond})

2. Switching losses (P_{sw})

The total converter loss is:

$$P_{conv} = P_{cond} + P_{sw} \tag{A.1}$$

The sinusoidal type pulse width modulation is considered in the losses calculation model. The losses of generator side IGBTs and diodes are considered.

A.1 Conduction losses

The average conduction losses of IGBT or diode can be expressed as bellow:

$$P_{cond,x} = V_{o,x} I_{avr,x} + R_{d,x} I_{rms,x}^2 \tag{A.2}$$

where $I_{avr,x}$ and $I_{rms,x}$ are the average current and the effective RMS current of the devices. The subscribe x means IGBT or Diode. $V_{o,x}$ is the on state zero-current collector-emitter voltage and $R_{d,x}$ is collector-emitter on-state resistance. $V_{o,x}$ can be read directly from the specific IGBT Data-sheet. In this thesis, it is considered that $V_{o,IGBT} = 2V$ and $V_{o,Diode} = 1.7V$.

The collector-emitter on-state resistance $R_{d,x}$ is scaled by the converter rated current value I_{rated}. For bigger rated current device, the manufacture contact surface between the collector and emitter will bigger. Therefore, it is considered those resistance values has inversely proportional relation to the rated current I_{rated}. The expression of those value are [89]:

$$R_{d,IGBT} = \frac{1.5}{I_{rated}\sqrt{2}} \tag{A.3}$$

$$R_{d,Diode} = \frac{1.04}{I_{rated}\sqrt{2}} \tag{A.4}$$

The average current and the effective RMS current in Eq.A.2 should be calculated separately for IGBT and diode. They can be expressed as follow:

$$I_{avr,IGBT} = \hat{I}_{amplitude}\left(\frac{1}{2\pi} + \frac{m}{8}\cos\varphi\right) \tag{A.5}$$

$$I^2_{rms,IGBT} = \hat{I}^2_{amplitude}\left(\frac{1}{8} + \frac{m}{3\pi}\cos\varphi\right) \tag{A.6}$$

$$I_{avr,Diode} = \hat{I}_{amplitude}\left(\frac{1}{2\pi} - \frac{m}{8}\cos\varphi\right) \tag{A.7}$$

$$I^2_{rms,Diode} = \hat{I}^2_{amplitude}\left(\frac{1}{8} - \frac{m}{3\pi}\cos\varphi\right) \tag{A.8}$$

where $\hat{I}_{amplitude}$ is the amplitude of phase current. It can be calculated from *dq-axis* current i_d and i_q. m is the modulation index which can be understood as the voltage utilization of the converter. It can be calculate as:

$$m = \frac{2\hat{V}_{amplitude}}{U_{DC}} \tag{A.9}$$

where $\hat{V}_{amplitude}$ is the amplitude of phase voltage. It can be also calculated from *dq-axis* current i_d and i_q Eq.2.111. $U_{DC} = 1200V$ in our case.

The power factor $\cos\varphi$ depends on the generator operating point and is calculated as:

$$\cos\varphi = \frac{P_{elec}}{\frac{3}{2}\hat{V}_{amplitude}\hat{I}_{amplitude}} \tag{A.10}$$

The total conduction losses is:

$$P_{cond} = 6(P_{cond,IGBT} + P_{cond,Diode}) \tag{A.11}$$

A.2   Switching losses

The average switching power losses is proportional to the current and switching frequency. The following equation can be used to approximately calculate the average switching power

losses [89]:

$$P_{sw} = 6(f_c B_{sw} \frac{\hat{I}_{amplitude}}{\pi})$$

(A.12)

where f_c is the carrier PWM frequency which is $2kHz$ in this thesis. B_{sw} is coefficient of the components. It is assumed that B_{sw} is constant and equals to $3mJ.A^{-1}$.

B

Principle of particle swarm optimization

PSO algorithm is evolutionary computation technique which was inspired by the social behavior of bird flocking and fish schooling [132]. It was translated in a simple way, the behavior of a group of bees. Each group of bees, or each swarm is composed of many particles moving at each iteration in the search space. The displacement of a particle is expressed as a function bellow:

$$\vec{x}_i^{t+1} = \vec{x}_i^t + \vec{v}_i^{t+1} \tag{B.1}$$

where $\vec{x}_i^t$ represent the i_{th} particle position in one iteration. The next position of this particle is the sum of the local position and speed velocity vector $\vec{v}_i^{t+1}$. This velocity vector is the heart of the PSO algorithm. It drives the optimization process and reflects both the own experience knowledge and the social experience knowledge from the all particles. The expression of velocity vector $\vec{v}_i^{t+1}$ is:

$$\vec{v}_i^{t+1} = \omega \vec{v}_i^t + \varphi_1 c_1 (\vec{x}_{pbest_i} - \vec{x}_i^t) + \varphi_2 c_2 (\vec{x}_{gbest_i} - \vec{x}_i^t) \tag{B.2}$$

The velocity vector update equation in Eq.B.2 has three major components:

— $\omega \vec{v}_i^t$: This component is sometimes referred to as **inertia**. It let the particle has a tendency to continue in the same direction it has been traveling. This component can be scaled by a constant as in the modified versions of PSO. It should be noted that there is no inertia weight ω for the first version PSO. It serves to decreasing the overall searching time.

— $\varphi_1 c_1 (\vec{x}_{pbest_i} - \vec{x}_i^t)$: This component is a linear attraction towards the best position $\vec{x}_{pbest_i}$ ever found by a certain particle. It called as **cognitive component**.

— $\varphi_2 c_2 (\vec{x}_{gbest_i} - \vec{x}_i^t)$: The last component is a linear attraction towards the best position

$\vec{x}_{gbest_i}$ found by any particle whose corresponding fitness value is the global best. This part expresses the "cooperation" or "social knowledge". It called as **social component**.

The coefficient c_1 and c_2 are two random number in the interval $[0, 1]$. φ_1 and φ_2 are two positive value called **acceleration coefficients** which will effect the speed of convergence. The values of ω, φ_1 and φ_2 should be properly chosen to guarantee that the particles' velocities do not grow to infinity.

In each iteration, every individual in the swarm is moved into a new position where a new fitness value is calculated. The fitness value is compared to the best recorded position of both the individual and the swarm. If a better position is found, then the memory of better position will be updated. This work will repeat until the algorithm reaches a predefined stopping criteria which, normally, is simply the maximum number of allowed iterations.

C

Analytical model validation by FEMM

C.1   Flux density, torque and inductance verification

In this section, three special machine design solutions which are obtained by the two final objectives ($F_{obj,final1}$ and $F_{obj,final2}$) criteria and the lowest investment solution ("Traditional dimensioning generator") are selected to verify the analytical model with Finite Element Analysis (FEA) method. The software Finite Element Method Magnetics (FEMM) will be used to realize the finite element analysis. This software is free and easily interfaced with Matlab through a toolbox available online. To reduce the computation time, we simulate 2 pole pair part of the complete generator. The three generator parameters are shown in the Table. C.1. Using those parameters, the generator geometer shape can be drawn in the software.

In FEMM, the number of conductor in one slot should be a integer value. Therefore, the number of conductor N_{slot} we obtained through optimization can't be applied to the simulation. The non-integer conductor number value is obtained with the assumption that the conductor are connected in series. However, we can realize the generator with coil windings connected in parallel. The rated current for each parallel circuit will be I_{series}/n_a. I_{series} is the rated current obtained with all conductor connected in series. n_a is the number of parallel winding circuit in one phase. The number of conductor in one slot increase n_a times. That means the surface of each conductor will decrease $1/n_a$ times as before when the conductors are connected in series. The rated current also decrease $1/n_a$ times in each conductor. Therefore, the current density will not change. The copper volume will also not change. Hence, the loss of the copper is the same like before. The total inductance of the generator of one stator is equal to $1/n_a$ times of the one parallel inductance. The total inductance calculation has the same principle as the

Table C.1 – Parameters of the three generators.

Symbol	Lowest cost	$F_{obj,final2}$	$F_{obj,final1}$
p_{ratio}	0.55	0.56	0.59
p	54	44	22
k_t	0.61	0.62	0.64
$R_{so}(m)$	1.415	1.389	1.250
$h_{yokeo}(cm)$	1.7	2.0	3.7
$h_{sloto}(cm)$	6.4	8.6	20.8
$l_g(mm)$	5.8	5.7	5.0
$h_m(mm)$	7.9	7.6	8.4
$h_r(cm)$	3.1	3.8	6.5
$h_{yokei}(cm)$	1.5	1.8	3.3
$h_{sloti}(cm)$	6.8	10.8	27.5
$L(m)$	0.517	0.625	1.04
N_{sloto}	3.62	3.45	4.17
N_{sloti}	4.56	4.16	5.83
$S_{convo}(MVA)$	0.60	0.62	0.67
$S_{convi}(MVA)$	0.46	0.47	0.43
$T/Mass(N.m/kg)$	62.9	39.3	12.2
$T/Volume(kN.m/m^3)$	121.6	100.5	60.4

calculation of total resistance with many parallel circuit.

Table. C.2 shows the number of conductor in one slot after the post calculation. As the number of pole pairs of the three machine are 54, 44 and 22, the corresponding 9, 11 and 11 parallel circuit can be used to obtained the some performance as the all the conductor connected in series. The EMF produced by each parallel circuit is equal to the EMF before we do post calculation with all coil connected in series. The number of parallel circuit n_a should be a integer value which can be calculated by the number of pole pairs divided with a multiple number of 2. Because we need 2 pole pairs to have the integer number of slot with number of slot per pole per phase $m = 1.25$. Therefore, 2 pole pairs part of the machine is the smallest unit part to evaluated the machine performance. For example, for machine with 44 pole pairs, we can have 22 (44/2) or 11 (44/(2*2)) parallel circuits.

Table C.2 – Series non-integer conductor number change to integer conductor number

		Series	Parallel	No. of parallel circuit n_a
Lowest E_{elec}	N_{sloto}	3.62	3.45*9=31.05≈32	9
	N_{sloti}	4.56	4.56*9=41.04≈40	9
$F_{obj,final2}$	N_{sloto}	3.45	3.45*11=37.95≈38	11
	N_{sloti}	4.16	4.16*11=45.75≈46	11
$F_{obj,final1}$	N_{sloto}	4.17	4.17*11=45.87≈46	11
	N_{sloti}	5.83	5.83*11=64.13≈64	11

Fig. C.1, Fig. C.2 and Fig. C.3 illustrated the simulation characteristics of the lowest energy output machine, minimum cost per kWh machine and maximum revenue machine respectively.

(a) Lowest cost

(b) Torque variation (Analytical rated torque $444kN.m$, relative error 3.6%)

(c) No load outer air gap flux density (Analytical value in Fig. 3.10 is $0.77T$, relative error 1.3%)

(d) No load inner air gap flux density (Analytical value in Fig. 3.10 is $0.78T$, relative error 1.3%)
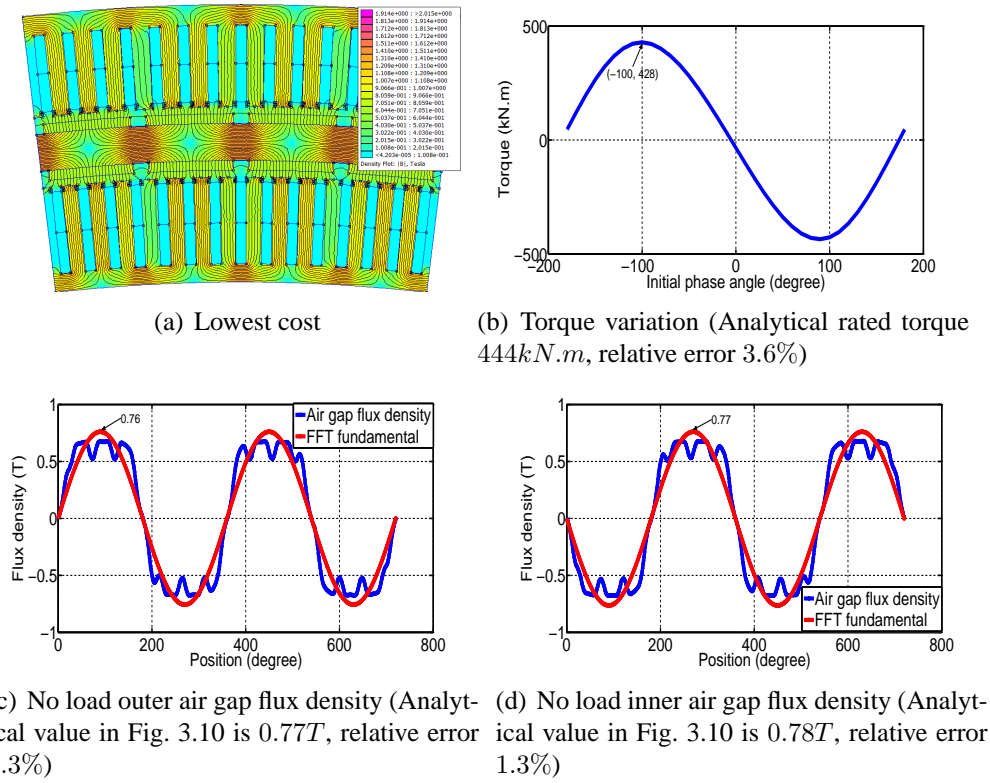
Figure C.1 – Lowest investment design solution

(a) $F_{obj,final2}$

(b) Torque variation (Analytical rated torque $444kN.m$, relative error 1.6%)

(c) No load outer air gap flux density (Analytical value in Fig. 3.10 is $0.76T$, relative error 1.3%)

(d) No load inner air gap flux density (Analytical value in Fig. 3.10 is $0.77T$, relative error 1.3%)
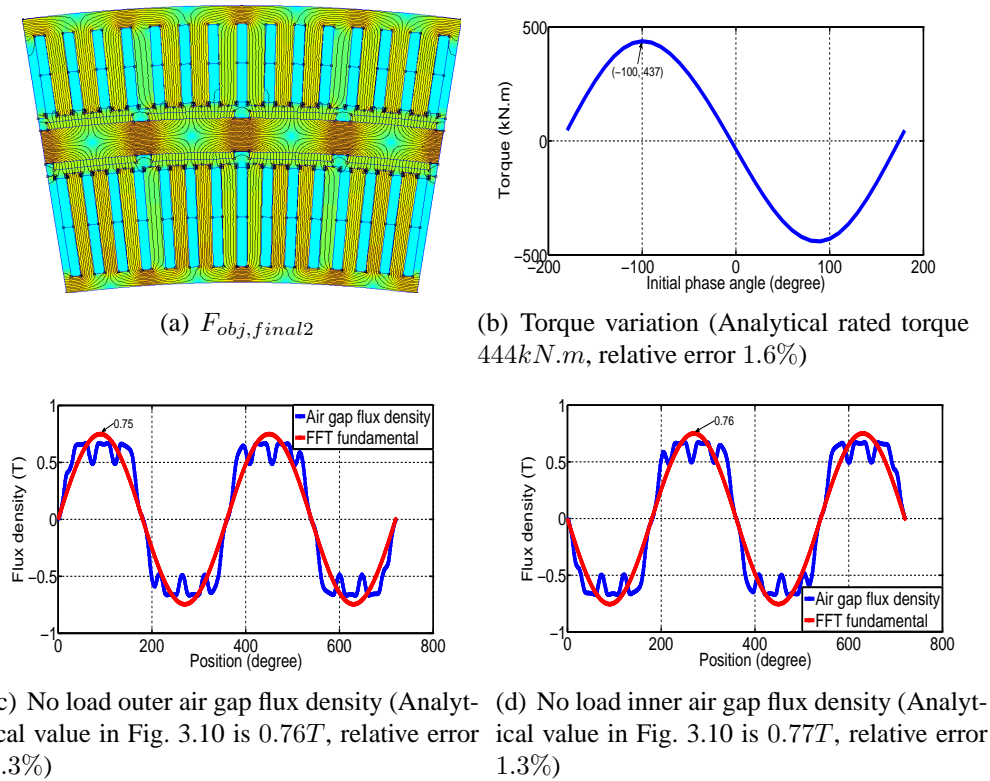
Figure C.2 – $F_{obj,final2}$ design solution

(a) $F_{obj,final1}$

(b) Torque variation (Analytical rated torque $444kN.m$, relative error 2.7%)

(c) No load outer air gap flux density (Analytical value in Fig. 3.10 is $0.82T$, relative error 0.6%)

(d) No load inner air gap flux density (Analytical value in Fig. 3.10 is $0.827T$, relative error 0.8%)
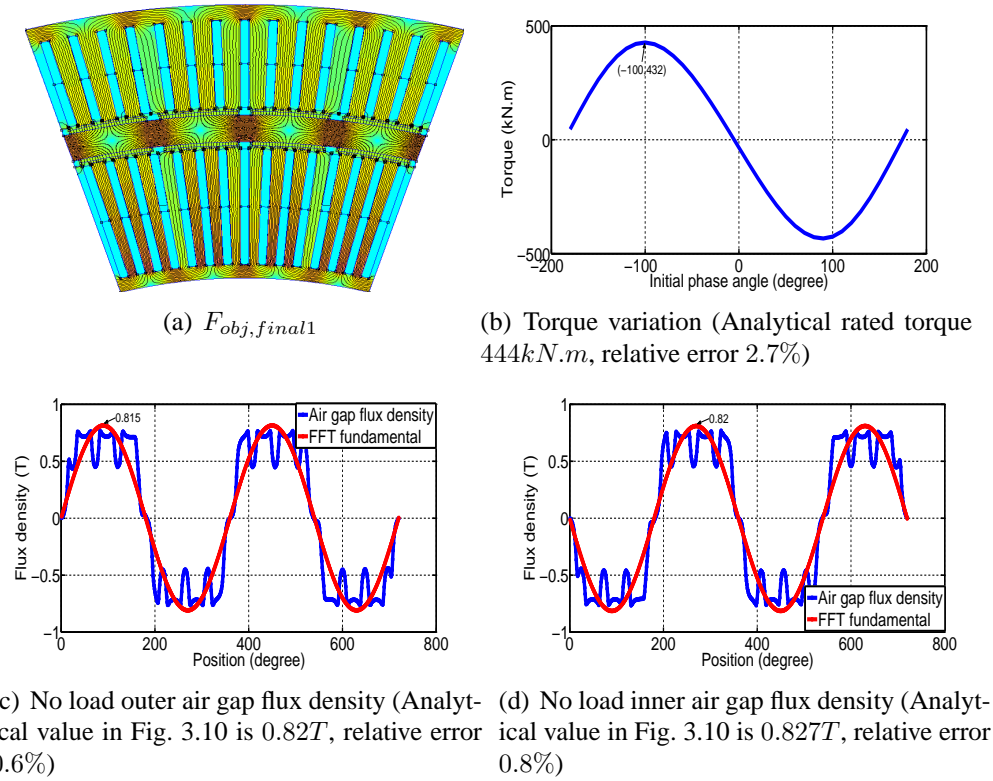
Figure C.3 – $F_{obj,final1}$ design solution

For each generator, the torque capability and no load air gap flux density are shown. The blue curve in the flux density figure is the FEA air gap density. Then we use Fast Fourier Transformation (FFT) to get the fundamental harmonic part which showed in red curve. The peak value of the fundamental harmonic flux density has around $0.01T$ difference between the analytical calculation. The relative error are around 1% for the three machines FEA air gap flux density is always smaller than the analytical calculation method. The inner air gap flux density is a little bigger than outer stator air gap flux density even they have the same mechanical air gap length l_g and magnet thickness h_m. That is because the inner air gap Carter's factor (see Chapter 2) is a little smaller than that of outer stator. Therefore, the effective air gap length of inner stator is smaller than that of outer stator. Smaller effective air gap length will result bigger air gap flux density for the same magnet thickness.

In order to verify the torque capability of the generator, the currents are applied into the phase winding in the simulation. The amplitude of the current for inner and outer are equal to $\frac{1}{11}$ of the maximum *q axis* current of inner and outer stator in analytical method. Because we need to keep the total phase current is the same as current when there is just one series circuit. The maximum *q axis* currents are obtained when the machine is operated in rated condition. We vary the initial phase angle of the two three phase current. Three phase currents are balance sinusoid current. From the torque variation figure in Fig. C.1, Fig. C.2 and Fig. C.3, it is known that the generator obtained maximum torque when the initial phase angle equal to $-100°$. When the initial phase angle is equal to $-100°$, the resultant armature flux linkage vector is $90°$ before

the magnet flux linkage. In vector current control, when the current vector is in the same phase with EMF vector, the control method is called ZDC control strategy (see Chapter 2). If we want to increase the torque for other initial phase angle, the amplitude of current should be increased. For example, constant mutual flux control strategy. The obtained torques for the two machines are little smaller than the analytical model. That may caused by the air gap flux density. The flux density in FEA is already smaller than the analytical model. Therefore, the torques are reasonable to be a little smaller than analytical model. However, the relative error between FEA and analytical model is acceptable.

The inductance difference between the analytical model and FEA are also compared. The results are shown in the Table. C.3. From the comparison, it is known that the inductance will not change after the post calculation with 9 parallel circuit for lowest energy machine and 11 parallel circuit for the other two. The relative error is acceptable and hence it is considered that the optimization analytical model is acceptable.

Symbol	Description	Analytical calculation	FEMM	Relative error
Lowest cost				
L_{so}	Outer stator inductance	$5.8mH$	$5.5mH$	5.1%
L_{si}	Inner stator inductance	$9.6mH$	$9.0mH$	6.2%
$F_{obj,final2}$				
L_{so}	Outer stator inductance	$5.8mH$	$5.7mH$	3.4%
L_{si}	Inner stator inductance	$9.7mH$	$9.4mH$	3.1%
$F_{obj,final1}$				
L_{so}	Outer stator inductance	$10.5mH$	$10.1mH$	3.8%
L_{si}	Inner stator inductance	$23.8mH$	$22.9mH$	3.8%

Table C.3 – Lowest cost, $F_{obj,final2}$ and $F_{obj,final1}$ solution inductance comparison between analytical method and finite element method

The relative error of the inductance and torque for lowest energy output machine is bigger than the other two machine. That is caused by the non-integer conductor post calculation as Table. C.2 shown. The machine is designed with double layer winding, therefore, even number of conductor is needed. The lowest energy output machine has bigger winding error comparing to the other two machine. In reality, this error can be decreased with slightly changing the length of the machine.

C.2   Post calculation of non-integer number of conductor per slot

The optimization variable of number of conductor per slot N_{slot} is non-integer in the optimization process. It is assumed the phase winding are connected in series. It is impossible to realize the machine with non-integer number of conductor in reality. However, this non-integer

number of conductor can be post calculated and changed to bigger integer number with a certain number of parallel circuit. This changing will not lead too much changing of the generator performance.

Taking $F_{obj,final2}$ generator as a example, $N_{sloto} = 3.45$ and $N_{sloti} = 4.16$. Pole pair number is 44. In order to realize the machine with winding in series, the best approach to realize the machine is $N_{sloto} = 4$ and $N_{sloti} = 4$. Even number is needed for double layer machine. However, those value will lead to $16\%(0.55/3.45)$ error of voltage for outer stator and $4\%(0.16/4.16)$. In the post calculation stage, using $N_{sloto} = 38$ ($11 \times 3.45 = 37.95$) and $N_{sloti} = 46$ ($11 \times 4.16 = 45.75$) to get the same voltage if the winding coil is connected with 11 parallel circuit rather than all in series. The parallel circuits number depends on the number of pole pair and it can be any integer value of $\frac{p}{W}$, where W is a even number $(2, 4, 6, ...)$. The errors of the voltage are 0.1% $(0.05/37.95)$ and 0.5% $(0.25/45.75)$ for outer and inner stator respectively. Obviously, through connecting the winding in parallel, the voltage error is reduced. If the optimization parameter varies with integer value. There is no voltage error between series and parallel winding machine. However, integer number optimization will cause discontinues Pareto front results or even can't find the solutions if the terminal voltage is fixed too small. In bigger number of pole pair machine design, it will have bigger number of slot when the number of slot per pole per phase is not very small. Therefore, if all slot has integer number of conductors and they are connect in series, it will lead to a big value of EMF and the number of conductor in one slot is very small. Small number of conductor will lead the big conductor cross section surface. In real machine design, the skin effect of the conductor will come out for big conductor cross section surface.

It is very important to note that it needs to assume that the slot fill factor k_f will not change. Assuming the cross section surface of conductor is S_1 when $N_{sloto} = 3.45$ and S_2 when $N_{sloto} = 38$. The relation between S_1 and S_2 is:

$$S_1 = 11S_2 \tag{C.1}$$

Fig. C.4 shows the illustration and comparison for non-integer conductor post calculation of outer stator. The power will not change. The current in each parallel circuit is $\frac{1}{11}$ of the total current. Therefore, the current density will not change in the conductor. Because of the total cross section surface and length of conductor don't change, the copper volume for one phase will also not change. Consequently, the copper losses will be the same as before the post calculation because copper losses can also expressed as $P_{cu} = J^2 V$ [133]. The inductance for each parallel circuit is 11 times bigger than the inductance before post calculation. From the inductance calculation section 2.2.1, in those equations, the pole pair and slot number will be 11 times smaller. It will lead 11 times bigger inductance. However, the total inductance of the 11 parallel circuit is $\frac{1}{11}$ of each parallel inductance value. Therefore, the inductance will not

change.
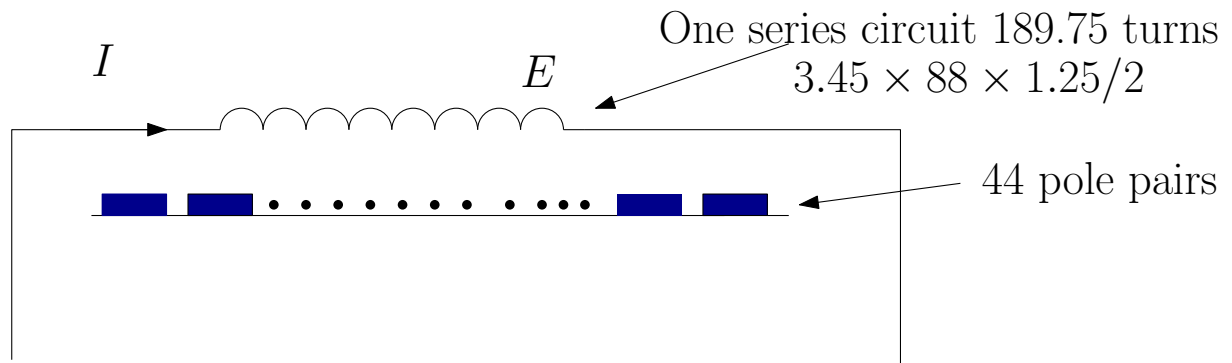
(a) Original $N_{sloto} = 3.45$ in series
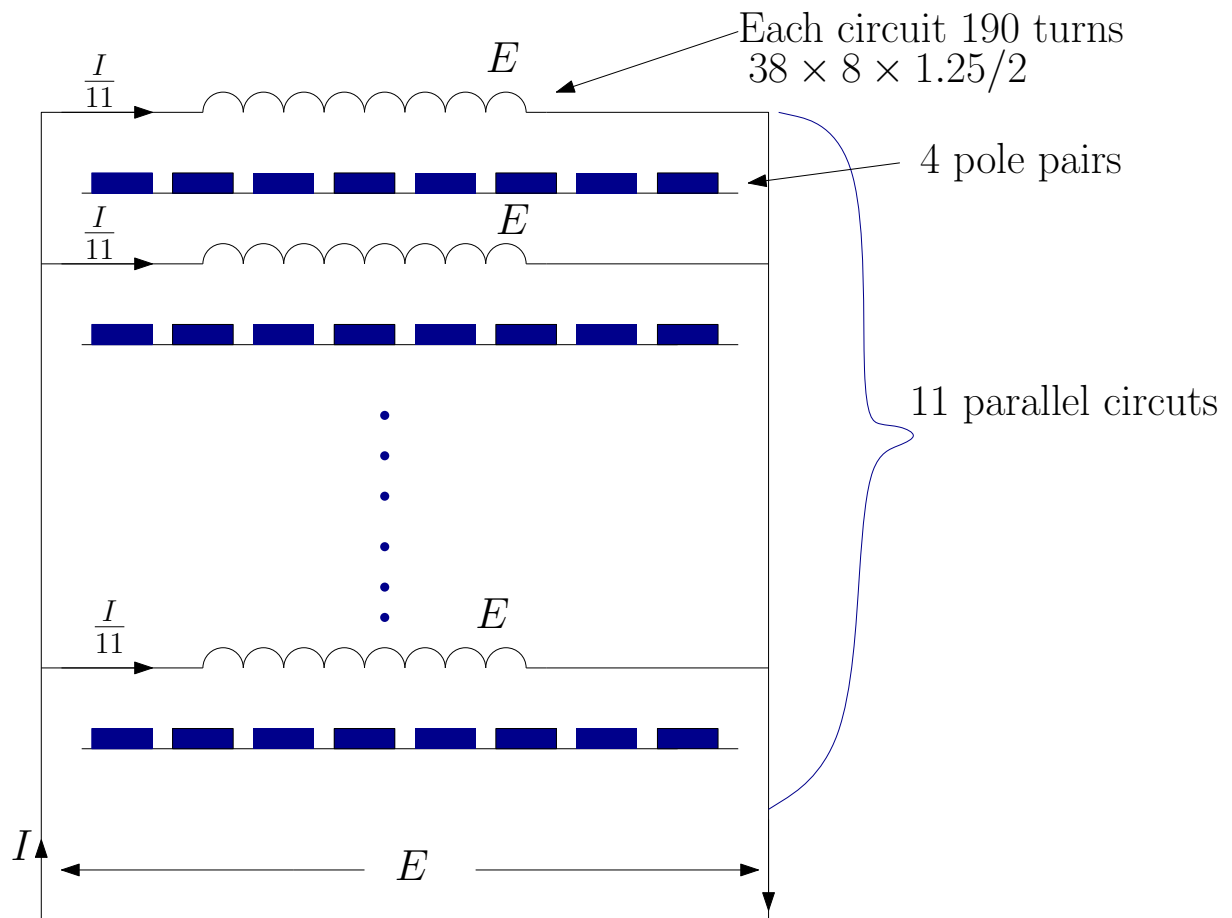
(b) After post calculation $N_{sloto} = 38$ with 11 parallel circuits

Figure C.4 – Simple illustration and comparison for non-integer conductor post calculation

D

Generator Simscape codes

D.1   DSCRPMG code

```
1  component  DSPMG_jian
2  % Double  Stator  Permanent  Magnet  Synchronous  Machine
3  % This  block  models  a  double  stator  permanent  magnet  synchronous  motor.  The
      two  stators  are  controlled  in  parallel.
4  % Matlab  version  R2011b
5  % 21/04/2015  Jian  ZHANG.
6
7  parameters
8        nPolePairs  =  {44, '1'};            % Number  of  pole  pairs
9        outer_pm_flux_linkage  =  {5.5, 'Wb'};    % Outer  stator  permanent
    magnet  flux  linkage
10       inner_pm_flux_linkage  =  {6.3, 'Wb'};    % Inner  stator  permanent
    magnet  flux  linkage
11       Ldo  =  {0.0058, 'H'};               % Outer  stator  d−axis  inductance
    , Ldo
12       Ldi  =  {0.0096, 'H'};               % Inner  stator  d−axis  inductance
    , Ldi
13       Lqo  =  {0.0058, 'H'};               % Outer  stator  q−axis  inductance
    , Lqo
14       Lqi  =  {0.0096, 'H'};               % Inner  stator  q−axis  inductance
    , Lqi
15       Rso  =  {0.039, 'Ohm'};              % Outer  stator  resistance  per
    phase , Rso
16       Rsi  =  {0.047, 'Ohm'};              % Inner  stator  resistance  per
```
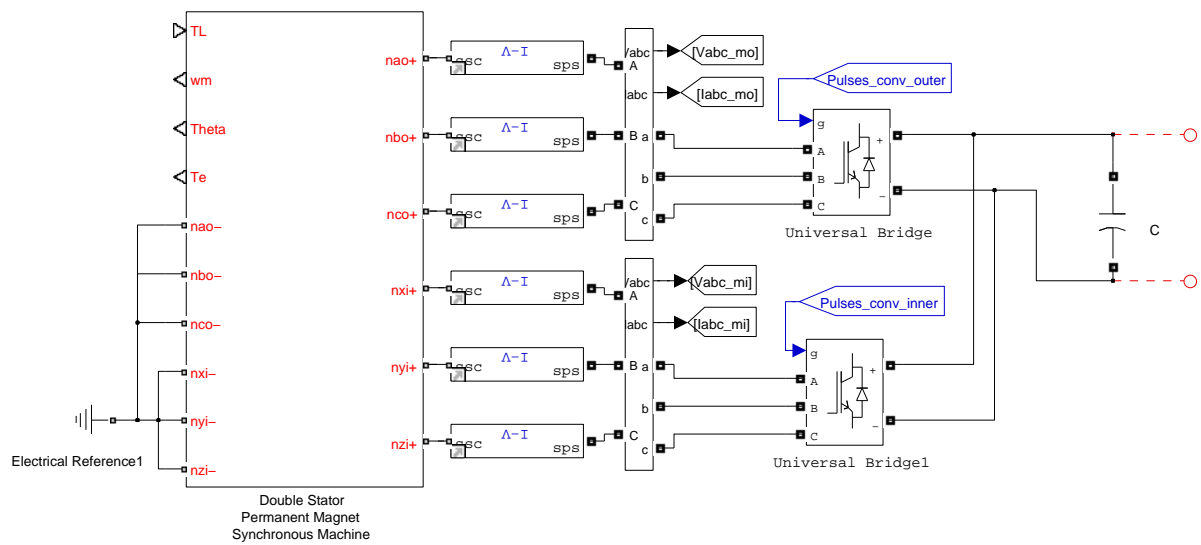
Figure D.1 – Simscape DSCRPMG model connect with Simpowersystem

Figure D.2 – DSCRPMG parameters setting mask

```matlab
    phase, Rsi
        J  = {1.3131e4, 'kg*m^2'};               % Inertia, J
        f  = {0.5, 'N*m*s'};                  % Viscous damping, f
        initial_outer_currents={[0 0], 'A'};      % Initial outer currents,
    [ido iqo]
        initial_inner_currents={[0 0], 'A'};      % Initial outer currents,
    [idi iqi]
        angular_position0={0,'deg'};         %Initial rotor angle
        angular_velocity0={0,'rad/s'};       %Initial rotor velocity
    end

    parameters (Hidden=true)
        shift_3ph = { [0,-2*pi/3,2*pi/3], 'rad' };
        mat={[1/2, 1/2, 1/2], '1'};
    end
    inputs
        TL = { 0, 'N*m' }; % TL: left
    end

    outputs
        mechanical_velocity = { 0, 'rad/s' }; % wm: left
        mechanical_angle = { 0, 'rad' }; % Theta: left
        Electrical_torque = { 0, 'N*m' }; % Te: left
    end

    nodes
        vaop= foundation.electrical.electrical;  % nao+: right
        vaon= foundation.electrical.electrical;  % nao-: left
        vbop= foundation.electrical.electrical;  % nbo+: right
        vbon= foundation.electrical.electrical;  % nbo-: left
        vcop= foundation.electrical.electrical;  % nco+: right
        vcon= foundation.electrical.electrical;  % nco-: left

        vxip= foundation.electrical.electrical;  % nxi+: right
        vxin= foundation.electrical.electrical;  % nxi-: left
        vyip= foundation.electrical.electrical;  % nyi+: right
        vyin= foundation.electrical.electrical;  % nyi-: left
        vzip= foundation.electrical.electrical;  % nzi+: right
        vzin= foundation.electrical.electrical;  % nzi-: left
    end

    variables
        % Mechanical
        angular_position = {0, 'rad'}; % Rotor angle
        angular_velocity= {0, 'rad/s'}; % Rotor angular velocity
        torque = {0, 'N*m'}; % torque
```

```matlab
        % Outer stator currents
        iao = {0, 'A' }; % Phase currents a
        ibo = {0, 'A' }; % Phase currents b
        ico = {0, 'A' }; % Phase currents c
        % Outer Stator voltages
        vao = {0, 'V' }; % Phase voltages a
        vbo = {0, 'V' }; % Phase voltages b
        vco = {0, 'V' }; % Phase voltages c

        % Inner stator currents
        ixi = {0, 'A' }; % Phase currents x
        iyi = {0, 'A' }; % Phase currents y
        izi = {0, 'A' }; % Phase currents z
        % Inner Stator voltages
        vxi = {0, 'V' }; % Phase voltages x
        vyi = {0, 'V' }; % Phase voltages y
        vzi = {0, 'V' }; % Phase voltages z


        % Outer stator currents
        i_do = {0, 'A'}; % Outer d-axis current
        i_qo = {0, 'A'}; % Outer q-axis current
        i_0o = {0, 'A'}; % Outer 0-axis current
        % Inner stator currents
        i_di = {0, 'A'}; % Inner d-axis current
        i_qi = {0, 'A'}; % Inner q-axis current
        i_0i = {0, 'A'}; % Inner 0-axis current

    end

    function setup
    through(iao,vaop.i,vaon.i);
    across(vao,vaop.v,vaon.v);
    through(ibo,vbop.i,vbon.i);
    across(vbo,vbop.v,vbon.v);
    through(ico,vcop.i,vcon.i);
    across(vco,vcop.v,vcon.v);

    through(ixi,vxip.i,vxin.i);
    across(vxi,vxip.v,vxin.v);
    through(iyi,vyip.i,vyin.i);
    across(vyi,vyip.v,vyin.v);
    through(izi,vzip.i,vzin.i);
    across(vzi,vzip.v,vzin.v);
```

```matlab
106        i_do=initial_outer_currents(1);
107        i_qo=initial_outer_currents(2);
108        i_di=initial_inner_currents(1);
109        i_qi=initial_inner_currents(2);
110        angular_position=angular_position0;
111        angular_velocity=angular_velocity0;
112    end
113
114
115    equations
116        let
117
118            electrical_angle = nPolePairs*angular_position;
119            % Set up Park's transform
120            abc2dq = (2/3)*[cos(electrical_angle) cos(electrical_angle-2*pi
   /3) cos(electrical_angle+2*pi/3);
121                           -sin(electrical_angle) -sin(electrical_angle-2*
   pi/3) -sin(electrical_angle+2*pi/3);
122                                       mat];
123
124            vdq0o= abc2dq*[vao vbo vco]';
125            v_do=vdq0o(1);
126            v_qo=vdq0o(2);
127
128            vdq0i= abc2dq*[vxi vyi vzi]';
129            v_di=vdq0i(1);
130            v_qi=vdq0i(2);
131            % Outer stator Flux linkages
132            psi_do = i_do*Ldo + outer_pm_flux_linkage;
133            psi_qo = i_qo*Lqo;
134
135            % Inner stator Flux linkages
136            psi_di = i_di*Ldi + inner_pm_flux_linkage;
137            psi_qi = i_qi*Lqi;
138
139        in
140
141            %Outer stator current relationship
142            [ i_do; i_qo ; i_0o]== abc2dq*[iao ibo ico]';
143            iao+ibo+ico == 0;
144            %Inner stator current relationship
145            [ i_di; i_qi ; i_0i]== abc2dq*[ixi iyi izi]';
146            ixi+iyi+izi == 0;
147            % Electric to mechanical rotation
148            angular_velocity == angular_position.der;
149
```

```matlab
150            % Outer Electrical equations
151            v_do == i_do*Rso + i_do.der*Ldo - nPolePairs*angular_velocity*
       psi_qo;
152            v_qo == i_qo*Rso + i_qo.der*Lqo + nPolePairs*angular_velocity*
       psi_do;
153            % Inner Electrical equations
154            v_di == i_di*Rsi + i_di.der*Ldi - nPolePairs*angular_velocity*
       psi_qi;
155            v_qi == i_qi*Rsi + i_qi.der*Lqi + nPolePairs*angular_velocity*
       psi_di;
156
157            % Mechanical equation
158            torque == 3/2*nPolePairs*(i_qo*psi_do - i_do*psi_qo)+3/2*
       nPolePairs*(i_qi*psi_di - i_di*psi_qi);
159
160            torque== TL+J*angular_velocity.der+f*angular_velocity;
161
162            % Output ports
163            Electrical_torque==torque;
164            mechanical_velocity==angular_velocity;      % wm
165            mechanical_angle==angular_position;          % theta
166        end
167     end
168
169 end
```

E

Control parameters

E.1 Optimized DSCRPMG parameters (Generator choosing from the Pareto front in Chater 3 with criteria $F_{obj,final2}$)

Symbol	Description	Value
ψ_{PMo}	Outer stator magnet flux linkage	$5.5Wb$
ψ_{PMi}	Inner stator magnet flux linkage	$6.3Wb$
L_{do}, L_{qo}	Outer stator *dq-axis* inductance	$5.8mH$
L_{di}, L_{qi}	Inner stator *dq-axis* inductance	$9.6mH$
R_{cuo}	Outer stator resistance	0.039Ω
R_{cui}	Inner stator resistance	0.047Ω
p	Pole pair	44
Controller parameters		
Speed loop	$K_p = 42486, K_i = 2.6 \times 10^7$	
Outer stator current loop	$K_p = 14.5, K_i = 100$	
Inner stator current loop	$K_p = 24, K_i = 120$	

Table E.1 – Optimized DSCRPMG parameters and relatively controller parameters which are used to test the fault control.

E.2 Optimized PMSG parameters and corresponding controller parameters (Generator choosing from the Pareto front in Chater 3 with criteria $F_{obj,final2}$)

Symbol	Description	Value
ψ_{PM}	Magnet flux linkage	$6.1Wb$
L_d, L_q	*dq-axis* inductance	$4.2mH$
R_{cu}	Stator resistance	0.019Ω
p	Pole pair	42
Controller parameters		
Speed loop	$K_p = 17000, K_i = 4.3 \times 10^6$	
Current loop	$K_p = 21, K_i = 95$	

Table E.2 – Optimized PMSG parameters and relatively controller parameters which are used to test the fault control.

E.3 Grid side control parameters and torque estimator parameters

DC-bus voltage	$V_{dc} = 1500V$
DC-bus capacitor	$C = 130mF$
Filter parameters	$l_f = 1mH, r_f = 0.01\Omega$
Controller parameters	
Outer energy loop	$K_p = 700, K_i = 250000$
Inner power loop	$K_p = 7000, K_i = 25 \times 10^6$
Estimator parameters	
Estimator	$K_p = 1.5 \times 10^8, K_i = 8.4 \times 10^{11}$

Table E.3 – Grid side control parameters and torque estimator parameter.

List of publications

1. J. Zhang, L. Moreau, P.E. Guillerm, M. Machmoum, "State of the Art in Tidal Current Energy Extracting Technologies," International Conference on Green Energy, March 2014

2. J. Zhang, L. Moreau, M. Machmoum, "Optimal Control Strategies of a Double Stator Permanent Magnet Generator Applied in Tidal Current Energy Extracting," Symposium de Génie Electrique (SGE14): EF-EPF-MGE 2014, July 2014, ENS Cachan, France.

3. J. Zhang, L. Moreau, J. W. Guo, M. Machmoum, "Electromagnetic Structure Limits and Control of a Double Stator Permanent Magnet Generator for Tidal Energy Applications," IEEE International Power Electronics and Application Conference and Exposition, November 2014.

4. J. Zhang, L. Moreau, M. Machmoum, "Stratégies de commande optimale d'une génératrice à aimants permanents à double stator appliquée à l'extraction d'énergie des courants marins," La Revue 3EI, Avril 2015.

5. J. Zhang, A. Houari, A. Seck, L. Moreau, M. Machmoum, "Fault Tolerant Control of a Double Stator Permanent Magnet Generator in Tidal Current Energy System," IEEE International Conference on Industrial Technology, March 2016. ***Submitted***

Bibliography

[1] http://homepages.spa.umn.edu/~llrw/a1001_f07/tides.jpg. On-line; accessed 1-Sep-2015.

[2] T. J. Hammons, "Tidal power in the UK and worldwide to reduce greenhouse gas emissions," *International Journal of Engineering Business*, 2011.

[3] I. Bryden and G. T. Melville, "Choosing and evaluating sites for tidal current development," *Proceedings of the Institution of Mechanical Engineers, Part A: Journal of Power and Energy*, vol. 218, pp. 567–577, 2004.

[4] L. S. Blunden and a. S. Bahaj, "Initial evaluation of tidal stream energy resources at Portland Bill, UK," *Renewable Energy*, vol. 31, pp. 121–132, 2006.

[5] S. Benelghali, *On multiphysics modeling and control of marine current turbine systems*. PhD thesis, Université De Bretagne Occidentale, 2009.

[6] S. Love, *Tidal current turbine farms in scotland : A channel model approach to determine power supply profiles and the potential for embedded generation*. PhD thesis, University of Strathclyde, 2005.

[7] H. Chen, *Modeling and control of a marine current energy conversion system using a doubly salient permanent magnet generator*. PhD thesis, Université de Nantes, 2014.

[8] http://www.shom.fr/. Online; accessed 1-Sep-2015.

[9] Z. Zhou, F. Scuiller, J. F. Charpentier, M. E. H. Benbouzid, and T. Tang, "Power smoothing control in a grid-connected marine current turbine system for compensating swell effect," *IEEE Transactions on Sustainable Energy*, vol. 4, no. 3, pp. 816–826, 2013.

[10] L. Moreau, *Modélisation, conception et commande de genratrices à réluctance variable basse vitesse*. PhD thesis, Université de Nantes, 2005.

[11] J. Zhang, L. Moreau, and M. Machmoum, "State of the art in tidal current energy extracting technologies," in *International Conference on Green Energy ICGE*, pp. 1–7, 2014.

[12] A. I. Winter, "Speed regulated operation for tidal turbines with fixed pitch rotors," in *Oceans '11*, pp. 1–8, 2011.

[13] http://mreworldmap.com/mre-map. Online; accessed 1-Sep-2015.

[14] http://verdantpower.com. Online; accessed 1-Sep-2015.

[15] `http://www.alstom.com/microsites/power/products-services/` `renewables/ocean-energy/`. Online; accessed 1-Sep-2015.

[16] `http://www.hammerfeststrom.com/products/tidal-turbines`. Online; accessed 1-Sep-2015.

[17] `http://www.marineturbines.com`. Online; accessed 1-Sep-2015.

[18] `http://www.tidalstream.co.uk`. Online; accessed 1-Sep-2015.

[19] `http://www.tocardo.com`. Online; accessed 1-Sep-2015.

[20] `http://www.atlantisresourcescorporation.com`. Online; accessed 1-Sep-2015.

[21] `http://www.sabella.fr`. Online; accessed 1-Sep-2015.

[22] `http://www.voith.com/en/products-services/hydro-power/` `ocean-energies/tidal-current-power-stations--591.html`. Online; accessed 1-Sep-2015.

[23] C. Belloni, *Hydrodynamics of ducted and open-centre tidal turbines*. PhD thesis, University of Oxford, 2013.

[24] J. Hardisty, *The analysis of tidal stream power*. John Wiley & Sons, 2009.

[25] `http://www.lunarenergy.co.uk/`. Online; accessed 1-Sep-2015.

[26] `http://www.openhydro.com/home.html`. Online; accessed 1-Sep-2015.

[27] `http://www.cleancurrent.com`. Online; accessed 1-Sep-2015.

[28] `http://www.gcktechnology.com/GCK/pg2.html`. Online; accessed 1-Sep-2015.

[29] `http://www.bluenergy.com/`. Online; accessed 1-Sep-2015.

[30] `http://www.biopowersystems.com/biostream.html`. Online; accessed 1-Sep-2015.

[31] J. A. Baroudi, V. Dinavahi, and A. M. Knight, "A review of power converter topologies for wind generators," *Renewable Energy*, vol. 32, pp. 2369–2385, 2007.

[32] S. Benelghali, M. E. H. Benbouzid, and J. F. Charpentier, "Generator systems for marine current turbine applications: A comparative study," *IEEE Journal of Oceanic Engineering*, vol. 37, pp. 554–563, 2012.

[33] D. Bang and H. Polinder, "Review of generator systems for direct-drive wind turbines," *European Wind Energy*, pp. 1–11, 2008.

[34] L. Moreau, M. E. Zaim, and M. Machmoum, "Electromagnetic design optimization of a low speed Slotted Switched Reluctance Machine using genetic algorithm," *2012 XXth International Conference on Electrical Machines*, no. 2, pp. 233–237, 2012.

[35] N. Harkati, L. Moreau, M. E. Zaim, and J. F. Charpentier, "Low speed doubly salient permanent magnet generator with passive rotor for a tidal current turbine," *Proceedings of 2013 International Conference on Renewable Energy Research and Applications, ICRERA 2013*, no. October, pp. 528–533, 2013.

[36] A. Dieng, *Modélisation dynamique et commande d'un ensemble « génératrice synchrone pentaphasée à FEM non sinusoïdale – convertisseur AC/DC tolérant aux défauts »*. PhD thesis, Université de Nantes, 2014.

[37] A. Dieng, M. F. Benkhoris, M. A. Ahmed, and J. C. L. Claire, "Fault-tolerant control of 5-phase PMSG for marine current turbine applications based on fractional controller," in *The International Federation of Automatic Control*, 2014.

[38] F. Chai, S. Cui, and S. Cheng, "Performance analysis of double-stator starter generator for the hybrid electric vehicle," *IEEE Transactions on Magnetics*, vol. 41, no. 1, pp. 484–487, 2005.

[39] S. Niu, *Design, control and application of double-stator permanent magnet brushless machines*. PhD thesis, University of HongKong, 2009.

[40] C. Liu, *Design , analysis , control and application of permanent-magnet hybrid brushless machines*. PhD thesis, University of HongKong, 2009.

[41] S. Niu, K. T. Chau, and C. Yu, "Quantitative comparison of double-stator and traditional permanent magnet brushless machines," *Journal of Applied Physics*, vol. 105, no. 2009, pp. 4–7, 2009.

[42] J. Pyrhönen, T. Jokinen, and V. Hrabovcová, *Design of rotating electrical machines*. John Wiley & Sons, 2014.

[43] S. Djebarri and J. F. Charpentier, "Comparison of direct-drive PM generators for tidal turbines," in *Electronics and Application Conference and Exposition (PEAC)*, pp. 474–479, 2014.

[44] Y. Duan, *Method for design and optimization of surface mount permanent magnet machines and induction machines*. PhD thesis, Georgia Institute of Technology, 2010.

[45] R. Krishnan, *Permanent magnet synchronous and mrushless DC motor drives*. John Wiley & Sons, 2010.

[46] J. Saint-Michel, "Bobinage des machines tournantes à courant alternatif," tech. rep., Techniques de l'ingénieur - D3420, 2001.

[47] A. Grauers, *Design of direct-driven permanent-magnet generators*. PhD thesis, Chalmers University, 1996.

[48] L. Qinghua, *Analysis, design and control of permanent magnet synchronous motors for wide-speed operation*. PhD thesis, National University of Singapore, 2005.

[49] V. Ruuskanen, *Design aspects of megawatt-range direct-driven permanent magnet*. PhD thesis, Lappeenranta University of Technology, 2011.

[50] Y. Alexandrova, *Wind turbine direct-drive permanent-magnet generator with direct liquid cooling for mass reduction*. PhD thesis, Lappeenranta University of Technology, 2014.

[51] S. Andersen, *Design and optimization of gearless drives using multi-physics approach*. PhD thesis, Technical University of Denmark, 2012.

[52] J. F. Gieras and M. Wing, *Permanent magnet motor technology: design and applications*, vol. 113. Marcel Dekker AG, second edi ed., 2002.

[53] "Alternateurs installation et maintenance," tech. rep., Leroy Somer, 2011.

[54] A. Krings, *Iron losses in electrical machines - Influence of material properties , manufacturing processes , and inverter operation*. PhD thesis, KTH School of Electrical Engineering, 2014.

[55] A. Krings and J. Soulard, "Overview and comparison of iron loss models for electrical machines," *Journal of Electrical Engineering*, vol. 10, pp. 162–169, 2010.

[56] S. B. A. Cogent, "Non oriented electrical steel," tech. rep., 2013.

[57] N. Bernard, F. Martin, and M. El-Hadi Zaïm, "Design methodology of a permanent magnet synchronous machine for a screwdriver application," *IEEE Transactions on Energy Conversion*, vol. 27, no. 3, pp. 624–633, 2012.

[58] J. Nerg and V. Ruuskanen, "Lumped-parameter-based thermal analysis of a doubly radial forced-air-cooled direct-driven permanent magnet wind generator," *Mathematics and Computers in Simulation*, vol. 90, pp. 218–229, 2012.

[59] S. Nategh, *Thermal analysis and management of high-performance electrical machines*. PhD thesis, KTH School of Electrical Engineering, 2013.

[60] A. Rezzoug and M. El-Hadi Zaïm, *Non-conventional electrical machines*. John Wiley & Sons, 2013.

[61] M. El-Hadi Zaïm, "Conception de machines electriques," tech. rep., Polytech de Nantes, 2014.

[62] J. Aubry, H. Ben Ahmed, and B. Multon, "Sizing optimization methodology of a surface permanent magnet machine-converter system over a torque-speed operating profile: Application to a wave energy converter," *IEEE Transactions on Industrial Electronics*, vol. 59, no. 10, pp. 2116–2125, 2012.

[63] B. Multon, J. Lucidarme, and L. Prévond, "Analyse des possibilités de fonctionnement en régime des désexcitation des moteurs à aimants permanents," *Journal de Physique III*, vol. 5, pp. 623–640, 1995.

[64] F. Zhao, T. A. Lipo, and B. Kwon, "Dual-stator interior permanent magnet vernier machine for torque density and power factor improvement," tech. rep., University of Wisconsin Madison, 2014.

[65] Y. Wang, M. Cheng, M. Chen, Y. Du, and K. Chau, "Design of high-torque-density double-stator permanent magnet brushless motors," *IET Electric Power Applications*, vol. 5, no. August 2010, p. 317, 2011.

[66] G. Junwei, "Modelling of high torque multi air gap permanent magnet synchronous generator for wind turbine applications," tech. rep., Université de Nantes.

[67] N. P. Quang and J.-A. Dittrich, *Vector control of three-phase AC machines: System development in the practice*. 2008.

[68] W. Leonhard, *Control of electrical drives*. Springer, 2001.

[69] J. Zhang, L. Moreau, and M. Machmoum, "Optimal control strategies of a double stator permanent magnet generator applied in tidal current energy extracting," in *Symposium de Génie Electrique*, vol. 2, pp. 8–10, 2014.

[70] S. Kim, Y. D. Yoon, S. K. Sul, and K. Ide, "Maximum torque per ampere (MTPA) control of an IPM machine based on signal injection considering inductance saturation," *IEEE Transactions on Power Electronics*, vol. 28, no. 1, pp. 488–497, 2013.

[71] S. Morimoto, Y. Takeda, T. Hirasa, and K. Taniguchi, "Expansion of operating limits for permanent magnet motor by current vector control considering inverter capacity," *IEEE Transactions on Industry Applications*, vol. 26, no. 5, pp. 866–871, 1990.

[72] S. Morimoto, Y. Tong, Y. Takeda, and T. Hirasa, "Loss minimization control of permanent magnet synchronous motor drives," *IEEE Transactions on Industrial Electronics*, vol. 41, no. 5, pp. 511–517, 1994.

[73] W. Qiao, L. Qu, and R. G. Harley, "Control of IPM synchronous generator for maximum wind power generation considering magnetic saturation," *IEEE Transactions on Industry Applications*, vol. 45, no. 3, pp. 1095–1105, 2009.

[74] C. Mademlis, J. Xypteras, and N. Margaris, "Loss minimization in surface permanent-magnet synchronous motor drives," *IEEE Transactions on Industrial Electronics*, vol. 47, no. 1, pp. 115–122, 2000.

[75] M. Hauck, I. Munteanu, A. I. Bratcu, S. Bacha, and D. Roye, "Operation of grid-connected cross-flow water turbines in the stall region by direct power control," *IEEE Transactions on Industrial Electronics*, vol. 58, no. 4, pp. 1132–1140, 2011.

[76] Z. Zhou, *Modeling and power control of a marine current turbine system with energy storage devices*. PhD thesis, Université de Bretagne Occidentale, 2014.

[77] R. Dutta, L. Chong, and M. F. Rahman, "Analysis of CPSR in motoring and generating modes of an IPM motor," *2011 IEEE International Electric Machines and Drives Conference, IEMDC 2011*, no. 2, pp. 1474–1479, 2011.

[78] G. Pellegrino, E. Armando, and P. Guglielmi, "Direct-flux vector control of IPM motor drives in the maximum torque per voltage speed range," *IEEE Transactions on Industrial Electronics*, vol. 59, no. 10, pp. 3780–3788, 2012.

[79] H. Liu, Z. Q. Zhu, E. Mohamed, Y. Fu, and X. Qi, "Flux-weakening control of nonsalient pole PMSM having large winding inductance, accounting for resistive voltage drop and inverter nonlinearities," *IEEE Transactions on Power Electronics*, vol. 27, no. 2, pp. 942–952, 2012.

[80] B. Wu, Y. Liang, N. Zargari, and S. Kouro, *Power conversion and control of wind energy systems*. John Wiley & Sons, 2011.

[81] J. Zhang, L. Moreau, J. Guo, and M. Machmoum, "Joint optimization of electromagnetic structure and control of a double stator permanent magnet generator for tidal energy applications," in *Electronics and Application Conference and Exposition*, no. 1, 2014.

[82] C. Coello, G. Lamont, and D. Veldhuizen, *Evolutionary algorithms for solving multi-objective problems*. Springer, 2007.

[83] E. L. Engevik, *Optimal design of tidal power generator using stochastic optimization techniques*. PhD thesis, Norwegian University of Science and Technology, 2014.

[84] S. Brisset, "Démarches et outils pour la conception optimale des machines electriques," tech. rep., 2007.

[85] B. S. N'Tshuika, *Optimisation de gammes : Application à la conception des machines synchrones à concentration de flux*. PhD thesis, Université de Grenoble, 2011.

[86] J. Linder and S. Lindkvist, *Interactive multiobjective optimization*. PhD thesis, Chalmers University of Technology, 2011.

[87] J. Persson, *Efficient optimization of complex products: A simulation and surrogate model based approach*. PhD thesis, Linköping University, 2015.

[88] H. Li and Z. Chen, "Design optimization and evaluation of different wind generator systems," *Electrical Machines and Systems, 2008. ICEMS 2008. International Conference on*, pp. 2396–2401, 2009.

[89] J. Aubry, *Optimisation du dimensionnement d'une chaîne de conversion électrique directe incluant un système de lissage de production par supercondensateurs. Application au houlogénérateur SEAREV.* PhD thesis, Ecole Normale Supérieure de Cachan, 2011.

[90] J. Aubry, M. Ruellan, H. Ben Ahmed, and B. Multon, "Minimization of the kWh cost by optimization of an all-electric chain for the SEAREV Wave Energy Converter," *Pro-

ceedings of the 2nd International Conference on Ocean Energy (ICOE 2008), pp. 1–7, 2008.

[91] IRENA, "Renewable power generation costs," Tech. Rep. January, IRENA, 2012.

[92] P. Schwabe, S. Lensink, and M. Hand, "IEA wind task 26," tech. rep., IEA, 2011.

[93] T. D. Souza, E. Goldbarg, and M. Goldbarg, "Comparing PSO and NSGAII for the biobjective oil derivatives distribution problem," *Evolutionary Computation (CEC), 2010 IEEE Congress on*, 2010.

[94] A. C. Godínez, L. E. M. Espinosa, and E. M. Montes, "An experimental comparison of multiobjective algorithms: NSGA-II and OMOPSO," *Proceedings - 2010 IEEE Electronics, Robotics and Automotive Mechanics Conference, CERMA 2010*, pp. 28–33, 2010.

[95] B. Multon, H. B. Ahmed, M. Ruellan, and G. Robin, "Comparaison du couple massique de diverses architectures de machines tournantes synchrones à aimants," *Revue de l'Electricité et de l'Electronique*, vol. -, p. 85, 2006.

[96] B. Drury, *The control techniques drives and controls handbook*. IET, second ed., 2009.

[97] M. R. Dubois, *Optimized permanent magnet generator topologies for direct-drive wind turbines*. PhD thesis, Delft University, 2004.

[98] S. Djebarri, *Contribution à la modélisation et à la conception optimale de génératrices à aimants permanents pour hydroliennes*. PhD thesis, Université de Bretagne Occidentale, 2015.

[99] V. Ruuskanen, P. Immonen, J. Nerg, and J. Pyrhönen, "Determining electrical efficiency of permanent magnet synchronous machines with different control methods," *Electrical Engineering*, vol. 94, pp. 97–106, 2012.

[100] A. Grauers and P. Kasinathan, "Force density limits in low-speed PM machines due to temperature and reactance," *IEEE Transactions on Energy Conversion*, vol. 19, no. 3, pp. 518–525, 2004.

[101] `http://www.theswitch.com/wind-power/`. Online; accessed 1-Sep-2015.

[102] "Rare earth ore prices stable," Tech. Rep. January, Integrated Magnetics, 2015.

[103] F. Majestic, "Gold, silver and copper prices report 2015,"

[104] SteelBenchmarker, "Price history tables and charts USA," tech. rep., SteelBenchmarker.

[105] `http://www.metalprices.com/p/SteelBenchmarkerFreeChart`. Online; accessed 1-Sep-2015.

[106] A. Binder, "Lecture notes on large generators and high power drives. Chapter 2: Heating and cooling of electrical machines.".

[107] K. T. Chau, *Electric vehicle machines and drives: Design, analysis and application*. John Wiley & Sons Singapore Pte.Ltd., 2015.

[108] B. Sanderse, "Aerodynamics of wind turbine wakes: Literature review," tech. rep., Energy research Centre of the Netherlands (ECN), 2009.

[109] L. M. Tossas and S. Leonardi, "Wind turbine modeling for computational fluid dynamics," Tech. Rep. July, NREL, 2013.

[110] F. Zahle and N. Sorensen, "Characterization of the unsteady flow in the nacelle region of a modern wind turbine," *Wind Energy*, vol. 14, pp. 271–283, 2011.

[111] M. Arnold, F. Biskup, D. Matha, and P. W. Cheng, "Simulation of rotor-foundation-interaction on tidal current turbines with computational fluid dynamics," 2013.

[112] K. Fischer, T. Stalin, H. Ramberg, J. Wenske, and R. Karlsson, "Investigation of converter failure in wind turbines Investigation of converter failure in wind turbines," Tech. Rep. November, Elforsk report 12:58, 2012.

[113] A. Gaeta, G. Scelba, and A. Consoli, "Modeling and control of three-phase PMSMs under open-phase fault," *IEEE Transactions on Industry Applications*, vol. 49, no. 1, pp. 74–83, 2013.

[114] F. Meinguet and J. Gyselinck, "Control strategies and reconfiguration of four-leg inverter PMSM drives in case of single-phase open-circuit faults," *2009 IEEE International Electric Machines and Drives Conference, IEMDC '09*, no. 2, pp. 299–304, 2009.

[115] N. Bianchi, S. Bolognani, M. Zigliotto, and M. Zordan, "Innovative remedial strategies for inverter faults in IPM synchronous motor drives," *IEEE Transactions on Energy Conversion*, vol. 18, no. 2, pp. 306–314, 2003.

[116] O. Wallnark and O. Carlson, "Post-fault operation of fault-tolerant inverters for PMSM drives," in *Power Electronics and Applications*, pp. 1–10, 2005.

[117] F. Meinguet, X. Kestelyn, E. Semail, and J. Gyselinck, "Fault detection, isolation and control reconfiguration of three-phase PMSM drives," *Proceedings - ISIE 2011: 2011 IEEE International Symposium on Industrial Electronics*, pp. 2091–2096, 2011.

[118] D. Mehrzad, J. Luque, and M. C. Cuenca, "Vector control of pmsg for wind turbine applications," tech. rep., Aalborg University, 2009.

[119] A. Houari, *Contribution à l'étude de micro-réseaux autonomes alimentés par des sources photovoltaïques*. PhD thesis, Université de Lorraine, 2012.

[120] R. C. Panda, *Introduction to PID controllers – Theory , tuning and application to frontier areas*. InTech, 2012.

[121] N. M. A. Freire, *Fault-tolerant permanent magnet synchronous generator drives for wind turbine applications*. PhD thesis, Université de Coimbra, 2013.

[122] F. Spinato, P. Tavner, G. van Bussel, and E. Koutoulakos, "Reliability of wind turbine subassemblies.," vol. 3, no. January 2008, pp. 387–401, 2009.

[123] H. Yu, Z. Liu, and S. Cui, "Research on fault analysis and diagnosis of PMSM in HEV," *2011 International Conference on Electrical Machines and Systems*, pp. 1–4, 2011.

[124] J. O. Estima and A. J. M. Cardoso, "A new approach for real-time multiple open-circuit fault diagnosis in voltage-source inverters," *IEEE Transactions on Industry Applications*, vol. 47, no. 6, pp. 2487–2494, 2011.

[125] F. Meinguet, *Fault-tolerant permanent-magnet synchronous machine drives fault detection and isolation, control recon guration and design considerations*. PhD thesis, Université Libre de Bruxelles, 2012.

[126] M. S. Nejad, *Architectures d'alimentation et de commande d'actionneurs tolérants aux défauts: régulateur de courant non linéaire à large bande passante*. PhD thesis, Institut National Polytechnique de Lorraine, 2007.

[127] Dti, "Economic viability of a simple tidal stream energy capture device," tech. rep., 2007.

[128] M. O. Hamiti, *Réduction des ondulations de couple d' une machine synchrone à réluctance variable* . PhD thesis, Université Henri Poincaré, Nancy-I, 2009.

[129] Semikron, "Power electronics teaching system principle for sizing power converters," tech. rep., 2008.

[130] J. Regnier, *Conception de systèmes hétérogènes en génie électrique par optimisation évolutionnaire multicritère*. PhD thesis, Institut National Polytechnique de Toulouse, 2003.

[131] D. Graovac and M. Pürschel, "IGBT power losses calculation using the data-sheet parameters," Tech. Rep. January, Infineon, 2009.

[132] J. Kennedy and R. Eberhart, "Particle swarm optimization," *Neural Networks, 1995. Proceedings., IEEE International Conference on*, vol. 4, pp. 1942–1948 vol.4, 1995.

[133] J. Denies, H. B. Ahmed, F. Glineur, and B. Dehez, "Study of a topology optimization tool associating a hybrid algorithm with a Voronoï-based formalism for the design of electromagnetic devices," *Electrical Machines (ICEM), 2010 XIX International Conference on*, vol. 1348, 2010.

Thèse de Doctorat

ZHANG JIAN

Dimensionnement optimisé et stratégies de commande d'une génératrice synchrone à aimants permanents à double stator pour application hydrolienne

Optimization design and control strategies of a double stator permanent magnet generator for tidal current energy application

Résumé

Les travaux présentés dans cette thèse portent sur l'étude, le dimensionnement optimisé et la commande d'une chaîne de conversion d'énergie hydrolienne à base de machine synchrone à aimants permanents à deux stators (DSCRPMG). Les concepts de turbines hydroliennes, les projets existants et les structures électrotechniques usuelles sont d'abord présentés. Un système d'entraînement direct avec une turbine à pas fixe est retenu. Le modèle analytique de la machine synchrone à deux stators est élaboré et différentes stratégies de commande sont testées (commande à facteur de puissance unitaire, à flux constant ou à couple maximal). Une approche originale minimisant la fois les pertes de la machine mais aussi celles du convertisseur est proposée conduisant à un meilleur rendement sur l'ensemble de la plage de vitesse (zone MPPT et régime défluxé) tout en respectant les contraintes de tenue en tension et thermiques du système. Une optimisation multi-objectif de l'investissement et de l'énergie extraite par l'ensemble de la chaîne de conversion est réalisée pour une durée d'exploitation de 20 ans avec prise en compte des probabilités d'apparition de vitesse du courant marin. Il en résulte que la machine double stator donne une nette amélioration du couple volumique en contrepartie d'une légère dégradation du couple massique comparée à la machine synchrone classique. Enfin l'accent est mis sur la commande de la chaine de conversion en mode normal ou en mode défaut, en particulier le cas de l'ouverture d'une phase du stator externe. Différentes stratégies sont étudiées pour assurer une continuité de service et minimiser les ondulations de couple montrant ainsi les possibilités offertes par la DSCRPMG.

Abstract

The work presented in this thesis concerns the study of sizing, optimization and control of double stator permanent magnet generator (DSCRPMG) system for tidal current energy application. Turbine concepts, relative projects and usual chain of tidal energy conversion are first presented. A direct drive system with fixed pitch turbine is used. The analytical model of the DSCRPMG is developed and different control strategies are tested (unity power factor control, constant flux and maximum torque per ampere control). An original approach minimizing both losses of the machine and the converter is proposed, leading to improve the system efficiency over the whole speed range (MPPT and flux weakening regions) taking into account voltage and thermal constraints. A multi-objective optimization of investment and energy extracted by the entire conversion chain is performed for an operating period of 20 years, taking into account the occurrence of the sea current speed probabilities. As a result, the double stator machine gives a clear improvement in torque density despite a slight degradation of the mass torque compared to the conventional single stator synchronous machine. Finally emphasis is placed on the control of the conversion chain under normal mode or fault conditions, particularly for open circuit fault of the outer stator. Different strategies are designed to ensure continuity of service and minimize torque ripples, showing the possibilities offered by the DSCRPMG.

Mots clés

Energie hydrolienne, machine synchrone à double stator, optimisation multiobjectif, commande, mode défluxé, continuité de service, tolérance aux défauts.

Key Words

Tidal current energy, double stator permanent magnet machine, control strategies, multi-objectives particle swarm optimization, fault tolerant, torque ripple.